

## **INFORMATION TO USERS**

**This manuscript has been reproduced from the microfilm master. UMI films the text directly from the original or copy submitted. Thus, some thesis and dissertation copies are in typewriter face, while others may be from any type of computer printer.**

**The quality of this reproduction is dependent upon the quality of the copy submitted. Broken or indistinct print, colored or poor quality illustrations and photographs, print bleedthrough, substandard margins, and improper alignment can adversely affect reproduction.**

**In the unlikely event that the author did not send UMI a complete manuscript and there are missing pages, these will be noted. Also, if unauthorized copyright material had to be removed, a note will indicate the deletion.**

**Oversize materials (e.g., maps, drawings, charts) are reproduced by sectioning the original, beginning at the upper left-hand corner and continuing from left to right in equal sections with small overlaps.**

**Photographs included in the original manuscript have been reproduced xerographically in this copy. Higher quality 6" x 9" black and white photographic prints are available for any photographs or illustrations appearing in this copy for an additional charge. Contact UMI directly to order.**

**ProQuest Information and Learning  
300 North Zeeb Road, Ann Arbor, MI 48106-1346 USA  
800-521-0600**

**UMI<sup>®</sup>**



## **NOTE TO USERS**

**This reproduction is the best copy available.**

UMI<sup>®</sup>



**ELECTROKINETIC TRANSPORT AND FLUID MOTION IN  
MICROANALYTICAL ELECTROLYTE SYSTEMS**

by  
Thomas L. Sounart

---

A Dissertation Submitted to the Faculty of the  
DEPARTMENT OF CHEMICAL AND ENVIRONMENTAL ENGINEERING  
In Partial Fulfillment of the Requirements  
For the Degree of  
DOCTOR OF PHILOSOPHY  
WITH A MAJOR IN CHEMICAL ENGINEERING  
In the Graduate College  
THE UNIVERSITY OF ARIZONA

2001

**UMI Number: 3040130**

**UMI<sup>®</sup>**

---

**UMI Microform 3040130**

**Copyright 2002 by ProQuest Information and Learning Company.  
All rights reserved. This microform edition is protected against  
unauthorized copying under Title 17, United States Code.**

---

**ProQuest Information and Learning Company  
300 North Zeeb Road  
P.O. Box 1346  
Ann Arbor, MI 48106-1346**

THE UNIVERSITY OF ARIZONA ©  
GRADUATE COLLEGE

As members of the Final Examination Committee, we certify that we have read the dissertation prepared by Thomas L. Sounart

entitled Electrokinetic Transport and Fluid Motion in  
Microanalytical Electrolyte Systems

and recommend that it be accepted as fulfilling the dissertation requirement for the Degree of Doctor of Philosophy

James C. Baygents  
James C. Baygents

6 Dec 2001  
Date

Roberto Guzman  
Roberto Guzman

12/06/01  
Date

Eduardo A. Saez  
Eduardo A. Saez

12/6/01  
Date

\_\_\_\_\_  
Date

\_\_\_\_\_  
Date

Final approval and acceptance of this dissertation is contingent upon the candidate's submission of the final copy of the dissertation to the Graduate College.

I hereby certify that I have read this dissertation prepared under my direction and recommend that it be accepted as fulfilling the dissertation requirement.

James C. Baygents  
Dissertation Director James C. Baygents

6 Dec 2001  
Date

### STATEMENT BY AUTHOR

This dissertation has been submitted in partial fulfillment of requirements for an advanced degree at The University of Arizona and is deposited in the University Library to be made available to borrowers under rules of the Library.

Brief quotations from this dissertation are allowable without special permission, provided that accurate acknowledgment of source is made. Requests for permission for extended quotation from or reproduction of this manuscript in whole or in part may be granted by the head of the major department or the Dean of the Graduate College when in his or her judgment the proposed use of the material is in the interests of scholarship. In all other instances, however, permission must be obtained from the author.

SIGNED: \_\_\_\_\_

A handwritten signature in black ink, written over a horizontal line. The signature is cursive and appears to read "Thomas J. Anderson".

## ACKNOWLEDGEMENTS

First of all, I would like to thank Dr. James Baygents for serving as my dissertation director. His guidance, critical review, and great intellect have provided me with outstanding graduate research training. Second, I would like to thank my committee, including Drs. Eduardo Saez, Roberto Guzman, Robert Arnold, and Wendell Ela, for their examination of this dissertation and/or my knowledge of chemical and environmental engineering fundamentals. Although these examinations were difficult and sometimes painful, they were educational. I wish also to thank Paul Safier and Eric Case for rushing data to me so that I could assemble the final copy of this dissertation. I thank God for giving me the desire and ability to reach this goal, and I thank my parents for teaching me values that encourage achievement, but always in perspective and always with humility. Finally, I owe my deepest gratitude to my wife, Dawn, for her selfless, unwavering support of my protracted academic pursuits. My words can never be enough to thank her for the sacrifices she has quietly made.

## DEDICATION

**This dissertation is dedicated to my beautiful daughter, Kaiessa, who has blessed my life with infinite joy since the day we met just 10 months ago.**

## TABLE OF CONTENTS

LIST OF TABLES . . . . .	8
LIST OF FIGURES . . . . .	9
ABSTRACT . . . . .	12
<b>CHAPTER 1. INTRODUCTION . . . . .</b>	<b>14</b>
1.1. Scope . . . . .	14
1.2. Analytical Separations . . . . .	20
1.2.1. Basic Modes of Separation . . . . .	20
1.2.2. Analyte Stacking . . . . .	24
1.3. Microfluidic Processes . . . . .	28
1.3.1. Advantages . . . . .	28
1.3.2. Electrokinetics . . . . .	29
1.4. Simulation of Microanalysis Processes . . . . .	31
1.4.1. Electric Field Strengths Used in Practice . . . . .	34
1.4.2. Electrically-Driven Flows . . . . .	36
1.5. Present Study . . . . .	37
<b>CHAPTER 2. SUPPRESSION OF NUMERICAL OSCILLATIONS . . . . .</b>	<b>41</b>
2.1. Flux-Corrected Transport (FCT) . . . . .	41
2.2. Poorly Buffered Systems . . . . .	43
<b>CHAPTER 3. 2-D ELECTRICALLY-DRIVEN TRANSPORT: PROTOTYPE PROBLEM . . . . .</b>	<b>45</b>
3.1. Problem Formulation . . . . .	48
3.1.1. Balance laws . . . . .	48
3.1.2. Initial and boundary conditions . . . . .	51
3.2. General 2-D Simulation Method . . . . .	53
3.2.1. Stokes flow . . . . .	53
3.2.2. Numerical approach . . . . .	55
3.3. Results and Discussion . . . . .	56
3.3.1. Electroosmotic pumping . . . . .	56
3.3.2. Analyte stacking . . . . .	75
3.4. Concluding Remarks . . . . .	84
<b>CHAPTER 4. LUBRICATION APPROXIMATIONS . . . . .</b>	<b>87</b>
4.1. Scale Analysis . . . . .	91
4.1.1. Charge Balance . . . . .	92

## TABLE OF CONTENTS—Continued

4.1.2. Navier-Stokes Equations . . . . .	96
4.1.3. Component Mass Balances . . . . .	98
4.2. Approximation for $\mathbf{E}(\mathbf{x},t)$ . . . . .	98
4.2.1. Approximation for $E_a$ ( $(h/b)^2\Gamma \ll 1$ , $(h/b)^3Pe\Gamma \ll 1$ ) . . . . .	99
4.2.2. Approximation for $E_t$ ( $(h/b)^2\Gamma \ll 1$ , $(h/b)^3Pe\Gamma \ll 1$ ) . . . . .	100
4.3. Approximation for $\mathbf{v}(\mathbf{x},t)$ . . . . .	102
4.3.1. Approximation for $u$ ( $(h/b)^2 \ll 1$ , $(h/b)Re \ll 1$ ) . . . . .	102
4.3.2. Approximation for $v$ and $\Psi$ ( $(h/b)^2 \ll 1$ , $(h/b)Re \ll 1$ ) . . . . .	103
4.3.3. Further Simplification ( $(h/b)^2\Gamma \ll 1$ , $(h/b)Re \ll 1$ ) . . . . .	104
4.4. Results and Discussion . . . . .	106
4.4.1. $\gamma < 1$ , Buffer A ( $\Delta\omega_c/\omega_c \ll 1$ ), $(h/b_0)^2 \ll 1$ . . . . .	108
4.4.2. $\gamma < 1$ , Buffer A ( $\Delta\omega_c/\omega_c \ll 1$ ), $h/b_0 = O(1)$ . . . . .	117
4.4.3. $\gamma < 1$ , Buffer B ( $\Delta\omega_c/\omega_c \sim 1$ ) . . . . .	119
4.4.4. $\gamma > 1$ , Buffer B . . . . .	130
4.5. Concluding Remarks . . . . .	135
CHAPTER 5. 2-D ANALYTE TRANSPORT USING LUBRICATION APPROXIMATIONS FOR $\mathbf{v}$ AND $\mathbf{E}$ . . . . .	<b>137</b>
5.1. Approximate Formulation . . . . .	138
5.2. Results and Discussion . . . . .	143
5.3. Concluding Remarks . . . . .	150
CHAPTER 6. 1-D MACROTRANSPORT REPRESENTATION OF SOLUTE CONSERVATION . . . . .	<b>151</b>
6.1. Macrotransport Approximation . . . . .	154
6.2. Evaluation . . . . .	159
6.2.1. Buffer A . . . . .	159
6.2.2. Buffer B . . . . .	165
6.3. Dispersion in Simple FASS Experiments . . . . .	170
6.4. Concluding Remarks . . . . .	175
CHAPTER 7. SUMMARY AND FUTURE STUDIES . . . . .	<b>178</b>
APPENDIX A. SIMULATION OF ELECTROPHORETIC SEPARATIONS BY THE FLUX-CORRECTED TRANSPORT METHOD . . . . .	<b>185</b>
APPENDIX B. SIMULATION OF ELECTROPHORETIC SEPARATIONS: EFFECT OF NUMERICAL AND MOLECULAR DIFFUSION ON pH CALCULATIONS IN POORLY BUFFERED SYSTEMS . . . . .	<b>202</b>
REFERENCES . . . . .	<b>212</b>

## LIST OF TABLES

TABLE 3.1.	Buffer, amino acid, and solvent ion properties . . . . .	57
TABLE 3.2.	Protein properties . . . . .	58
TABLE 4.1.	Dimensionless groups for 2-D simulations . . . . .	108
TABLE 5.1.	Approximation errors for analyte concentrations . . . . .	147
TABLE 6.1.	Dimensionless groups for 1-D simulations . . . . .	161
TABLE 6.2.	The critical dimensionless group for solutes in 1-D simulations .	161
TABLE 6.3.	Buffer, analyte, and solvent ion properties . . . . .	172

## LIST OF FIGURES

FIGURE 1.1. Schematic of MBE . . . . .	20
FIGURE 1.2. Schematic of ZE . . . . .	21
FIGURE 1.3. Schematics of ITP and IEF . . . . .	23
FIGURE 1.4. Illustration of FASS . . . . .	26
FIGURE 3.1. Sketch of prototype configuration and initial conditions . . . . .	47
FIGURE 3.2. Streamlines for $\gamma = 1/5$ . . . . .	59
FIGURE 3.3. Streamlines and $ \hat{v} $ in upstream zone boundary for $\gamma = 1/5$ . . . . .	61
FIGURE 3.4. Conductivity field for $\gamma = 1/5$ . . . . .	62
FIGURE 3.5. Contours of constant $\Phi$ for $\gamma = 1/5$ at $\tau = 5$ . . . . .	63
FIGURE 3.6. Electric field for $\gamma = 1/5$ . . . . .	64
FIGURE 3.7. Analyte concentration fields for $\gamma = 1/5$ at $\tau = 2.2$ . . . . .	66
FIGURE 3.8. Analyte concentration fields for $\gamma = 1/5$ at $\tau = 5$ . . . . .	68
FIGURE 3.9. Cross-sectionally averaged analyte concentrations for $\gamma = 1/5$ . . . . .	69
FIGURE 3.10. Sketch of more general electroosmotic pumping configuration . . . . .	70
FIGURE 3.11. Peak position and variance in electroosmotic pumping . . . . .	72
FIGURE 3.12. Peak variance at values of $l$ for $1/\gamma = 10$ . . . . .	74
FIGURE 3.13. Streamlines and $ \hat{v} $ in upstream zone boundary for $\gamma = 2$ . . . . .	76
FIGURE 3.14. Maximum fluid speed for $\gamma = 2$ and $1/5$ . . . . .	77
FIGURE 3.15. Conductivity field for $\gamma = 2$ . . . . .	79

LIST OF FIGURES—*Continued*

FIGURE 3.16. Electric field for $\gamma = 2$ . . . . .	80
FIGURE 3.17. Cross-sectionally averaged analyte concentrations for $\gamma = 2$ . . . . .	82
FIGURE 3.18. Peak variance and height in FASS . . . . .	85
FIGURE 4.1. Definition sketch for approximate theory . . . . .	88
FIGURE 4.2. Initial streamlines for buffer A, $\gamma = 1/10$ . . . . .	109
FIGURE 4.3. Initial streamlines in upstream zone boundary . . . . .	110
FIGURE 4.4. Initial axial velocity profiles in upstream zone boundary . . . . .	112
FIGURE 4.5. Fluid speed approximation error $\varepsilon$ in upstream zone boundary . . . . .	114
FIGURE 4.6. Conductivity field in upstream zone boundary . . . . .	115
FIGURE 4.7. Axial derivative of slip velocity in upstream zone boundary . . . . .	116
FIGURE 4.8. Initial streamlines for $h/b_0 = 2$ . . . . .	117
FIGURE 4.9. Initial Axial velocity profiles for $h/b_0 = 2$ . . . . .	118
FIGURE 4.10. Time dependence of $\varepsilon$ for buffer A . . . . .	120
FIGURE 4.11. Streamlines, conductivity, and potential for $h/b_0 = 2$ at $\tau_s = 2$ . . . . .	121
FIGURE 4.12. Conductivity contours for buffer B, $\gamma = 1/10$ . . . . .	122
FIGURE 4.13. $E_t$ contours for buffer B, $\gamma = 1/10$ . . . . .	123
FIGURE 4.14. Conductivity contours for buffer B, $\gamma = 1/10$ . . . . .	125
FIGURE 4.15. Streamlines for buffer B, $\gamma = 1/10$ . . . . .	126
FIGURE 4.16. $E_t$ contours for buffer B, $\gamma = 1/50$ . . . . .	127
FIGURE 4.17. Streamlines for buffer B, $\gamma = 1/50$ . . . . .	128
FIGURE 4.18. Time dependence of $\varepsilon$ for buffer B, $\gamma < 1$ . . . . .	129

LIST OF FIGURES—*Continued*

FIGURE 4.19. Time dependence of $\varepsilon$ buffer B, $\gamma > 1$ . . . . .	131
FIGURE 4.20. Time evolution of streamlines for buffer B, $\gamma = 5$ . . . . .	132
FIGURE 4.21. Streamlines, conductivity, and $E_t$ for buffer B, $\gamma = 5$ . . . . .	133
FIGURE 4.22. Streamlines for buffer B, $\gamma = 2$ , $E_0 = 720$ V/cm . . . . .	134
FIGURE 5.1. Analyte concentrations for buffer A, $\gamma = 1/10$ , $h/b_0 = 1/6$ . . . . .	144
FIGURE 5.2. Analyte concentrations for buffer A, $\gamma = 1/10$ , $h/b_0 = 2$ . . . . .	146
FIGURE 5.3. Analyte concentrations for buffer B, $\gamma = 1/50$ . . . . .	148
FIGURE 5.4. Analyte concentrations for buffer B, $\gamma = 2$ . . . . .	149
FIGURE 6.1. $\langle C \rangle$ for buffer A, $\gamma = 1/5$ . . . . .	160
FIGURE 6.2. $\langle \sigma \rangle$ for buffer A, $\gamma = 1/5$ . . . . .	163
FIGURE 6.3. $\langle E_x \rangle$ for buffer A, $\gamma = 1/5$ . . . . .	164
FIGURE 6.4. $\langle C \rangle$ , $\langle \sigma \rangle$ , and $\langle E_x \rangle$ for buffer A, $\gamma = 5$ . . . . .	166
FIGURE 6.5. $\langle C \rangle$ , $\langle \sigma \rangle$ , and $\langle E_x \rangle$ for buffer B, $\gamma = 1/50$ . . . . .	168
FIGURE 6.6. $\langle C \rangle$ , $\langle \sigma \rangle$ , and $\langle E_x \rangle$ for buffer B, $\gamma = 5$ . . . . .	169
FIGURE 6.7. Burgi and Chien [36] peak variance data for PTH-Arg . . . . .	171
FIGURE 6.8. Simulated dispersion of ARG and high-field zone for buffer C . . . . .	173
FIGURE 6.9. Dispersion coefficient vs. $t$ . . . . .	174
FIGURE 6.10. Simulated ARG peak variances vs. $\gamma$ . . . . .	176

## ABSTRACT

Electrically-driven separation schemes, such as zone electrophoresis (ZE), isotachopheresis (ITP) and isoelectric focusing (IEF), are used profoundly to fractionate mixtures of charged compounds for preparative and particularly analytical applications. Inherent to the separation process is the development of local variations in the electrical conductivity, pH, electric field, etc. One-dimensional, quantitative descriptions of the spatio-temporal evolution of these variations, and their role in the separation process, have been developed over the past two decades. These descriptions lend significant insight into the electromigrational behavior of analytes and buffer components. Nevertheless, because they are one-dimensional, such descriptions omit important effects of electrokinetic fluid motion. The fluid motion arises naturally in the context of the separation scheme, and affects the evolving spatial gradients associated with the separation process. One-dimensional simulations have also been plagued by numerical limitations associated with advection-dominant transport in regions of sharp concentration gradients. In this dissertation, the numerical difficulties are resolved, and a general two-dimensional model of electrokinetic separations is presented. Because the balance laws account for coupling of the velocity field to the ion transport, a variety of processes important to both microfluidic manipulations and analytical separations can be considered. High-ionic strength electroosmotic pumping and field-amplified sample stacking are examined in detail. It is demonstrated that unsteady fluid eddies disperse the gradients in the field variables, and this limits the

efficacy of microanalysis processes.

Scaling arguments suggest that, at least for simple geometries, approximate solutions to the general model are possible. Semi-analytic approximations are constructed for the fluid velocity  $\mathbf{v}$  and electric field  $\mathbf{E}$ , and the parameter space over which they apply is defined. These approximations reduce simulation times by about two thirds, and provide general information on the dominant physics in microanalysis processes. The scale analysis and simulation results demonstrate that although cross-sectional conductivity gradients meet or exceed those in the axial direction, the electric field is essentially unidirectional. Also, at sufficiently high electric field strengths (ca. several hundred V/cm), nonlinear electrohydrodynamic stresses begin to influence the fluid motion. Finally, if the electrical stresses are negligible, the semi-analytic solutions for  $\mathbf{v}$  and  $\mathbf{E}$  permit 1-D macrotransport representations of the solute transport. Effective 1-D simulations yield cross-sectionally averaged values for the field variables in orders of magnitude less simulation time than 2-D simulations.

## CHAPTER 1

# INTRODUCTION

### 1.1 SCOPE

Electrokinetic phenomena stem from the motion of ionic solutions near charged surfaces. Electrokinetic motion in aqueous electrolytes was first investigated by Reuss [52] in 1809, who observed, upon application of an electric field, the movement of suspended clay particles (electrophoresis) and, in separate experiments, the electrically-driven motion of water through a bed of quartz sand (electroosmosis). The discovery of other electrokinetic effects ensued [132], and their importance in many chemical and biochemical processes is now apparent [132, 84]. For example, the diverse applications of modern colloid science, including ceramic fabrication, oil recovery, food processing, and paint and ink technology, owe much to our understanding of electrokinetics [84]. Electroosmosis—fluid motion induced by an applied electric field—has been used extensively to measure interfacial electrical properties [32, 96, 99, 129, 110, 115, 141] and recent interest in the phenomenon revolves around analytical separations [88, 100, 24], environmental remediation [127, 95], microelectromechanical systems (MEMS) [31], and transdermal drug-delivery schemes [70, 117, 131]. Electrophoresis—the translation of a charged particle in an applied electric field—is used to measure particle charge and mobility [22, 46, 62, 112, 164, 162], and is one of the most widely used techniques for fractionating mixtures of charged compounds, particularly for analyti-

cal applications [93, 102, 156]. Various schemes employing this mechanism have been developed [19, 73, 102, 111] to separate components ranging from monatomic ions [102, 125] to colloidal particles [65, 116, 124, 16] and living cells [148, 149]. Electrophoresis is the predominant method used to separate and analyze molecules of biological significance, such as proteins and nucleic acids [73, 93, 102, 113, 156].

Many recent advances in microscale chemical analysis are predicated on the broad utility of electrophoretic separations, and have stimulated continued development of methods and instrumentation. Narrow bore capillaries ( $O(10\text{--}100\ \mu\text{m i.d.})$ ) are routinely used in conventional capillary electrophoresis (CE) instruments [153, 7], and electrophoresis in similar sized channels etched on microchips is a rapidly emerging technology [31, 63, 50]. Improved heat dissipation in these microscale systems has permitted the use of electric field strengths on the order of hundreds to thousands of V/cm without loss of resolution due to thermal instabilities [31, 7, 50]. Separation column lengths and time scales in conventional capillary electrophoresis instruments are typically tens of centimeters [7, 5, 6] and minutes to tens of minutes [31, 7, 5, 6], respectively. In planar microdevices, they range from millimeters to centimeters [31, 63, 50] and milliseconds to seconds [31, 50, 90], respectively.

The potential advantages of miniaturization extend far beyond faster separations and more compact instrumentation. Electrophoretic separations on microchips have been multiplexed [160], permitting analysis of up to 96 samples simultaneously. The “lab-on-a-chip” concept offers the possibility of integrating multiple chemical-analysis processes on a single microchip [63, 37], with the ultimate goal of replacing an entire

laboratory with a miniature instrument. Fabrication of microscale mechanical pumps with sufficient flow control to integrate these processes has proven difficult, and this has stimulated the development of alternative pumping mechanisms. One attractive option is electroosmosis, which arises naturally when potential gradients are imposed along narrow channels, and is routinely used to mobilize the carrier fluid in CE. It is thus a natural choice for microfluidic systems, which typically require applied potential gradients for electrophoretic separations.

Given the importance of electrokinetic motion to the development of microfluidic devices and the importance of microfluidics in analytical chemistry, a detailed understanding of the relevant electrokinetic transport processes is clearly desirable. Numerical simulations can contribute significantly to this understanding by providing insight to microscale processes not amenable to experimental investigation. They can also be used as design tools to optimize novel systems [57]. Early numerical studies of analytical separations were restricted to one dimension and plagued by numerical difficulties associated with high Peclet number advection of sharp gradients in the field variables. Numerical improvements progressed slowly over the last decade, but (prior to our work) a general method for simulation of analytical separations at electrical fields strengths typically used in practice, had not been demonstrated. Moreover, 2-D simulations of microfluidic processes have been limited to linear systems wherein steady velocity fields and potential gradients obtain in uniform conductivity buffers.

In many microanalytical processes, including most separations, ion transport is nonlinearly coupled to fluid motion in nonuniform electrolytes. It is the purpose of

this dissertation to investigate several of these processes through the development of theories and dynamic simulations. As will be discussed, this involves the use of numerical techniques, first developed for hyperbolic conservation laws, to solve the nonlinear balance laws of the electrophoresis model. The general effectiveness of one such numerical method, Flux-Corrected Transport (FCT), is demonstrated on 1-D, time-dependent problems. It is shown that FCT yields converged solutions (in minutes to hours) to problems that are impractical to solve using previously-published schemes. It is further revealed that egregious numerical errors can result when high-field methods such as FCT and upwinding are applied to simulations of electrophoresis in poorly buffered systems. The cause of such errors is explained, and algorithms to prevent them are presented. Regions of sufficiently poor buffering to cause the errors are not uncommon in electrophoretic separations [113, 130, 145, 147], so without this understanding, many processes could not be examined by dynamic simulation. The 1-D model is then extended to two dimensions. 2-D simulation results are presented that characterize the unsteady fluid motion and ion transport in heterogeneous electrolytes, and quantify the impact of electroosmotic dispersion on the performance of some important microfluidic processes. A quantitative understanding of analyte dispersion mechanisms in microfluidic systems is important because dispersion often limits process performance, and the results of this dissertation demonstrate that fluid circulation in the vicinity of the spatial nonuniformities must be considered to evaluate analyte dispersion.

Electrically-driven microfluidic processes in nonuniform electrolytes had not been

simulated prior to the work of this dissertation in part because of the computational challenges involved. At electric field strengths of hundreds to thousands of V/cm, sharp gradients in the field variables form locally and fine meshes and/or flux limiter techniques are required for convergence. Moreover, two linear elliptic PDE's, and a system of nonlinear algebraic equations and parabolic PDE's must be solved simultaneously at each point in a 3-D (or 4-D) spatiotemporal computational domain. The application of FCT to the electrophoresis model has permitted simulation of some processes, but many more complicated systems remain intractable. Adaptive, nonuniform grids may improve computational efficiency enough to conquer these systems, but many challenges to the development of such algorithms for electrophoresis simulations exist. An alternative approach to computational development is to seek approximations to the problem formulation that simplify the calculation without excising the essential physics and chemistry. In this dissertation, approximate, semi-analytic solutions for the electrolyte velocity  $\mathbf{v}$  and electric field  $\mathbf{E}$  are constructed, and the parameter space over which such approximations are useful is delineated. With these approximate solutions, the computational expense devoted to calculating  $\mathbf{v}$  and  $\mathbf{E}$  (as much as 80% of the total simulation time) is virtually eliminated. Similar approximations for the pH, the calculation of which consumes most of the remaining simulation time, may be possible. This would reduce simulation times by at least an order of magnitude over that required to solve the full problem, and would permit simulation of many more complicated electrolyte systems.

The approximations for  $\mathbf{v}$  and  $\mathbf{E}$  have also inspired Taylor-Aris macrotransport

approximations [33] for the solute conservation, that have led to an effective 1-D representation of the problem in terms of cross-sectionally averaged values. Effective 1-D simulations predict solutal migration and dispersion in orders of magnitude less simulation time, and can therefore be used to investigate a wide variety of processes and conditions. In addition to extending the capabilities of electrophoresis simulations, the approximations developed in this dissertation provide general information, that cannot be provided by individual experiments or simulations, on the dominant physics in microanalysis processes.

The literature review that follows begins with some background on electrophoretic separation techniques in §1.2. The basic modes of separation are described, and a class of preconcentration techniques called sample or analyte stacking is discussed. Stacking has garnered increasing interest among analytical chemists in the last decade, as a method to improve detection limits in miniaturized systems. Background on the development of microfluidic systems is then provided in §1.3, followed by a review of numerical simulations of electrokinetic transport processes in §1.4. The review begins with an abridged history of electrokinetic theory in the context of electrophoretic separations, followed by a discussion of the numerical problems encountered in simulations at high electric field strengths. A survey of the research on 2-D simulations of electroosmotic motion is then presented, and the Introduction is closed with an overview of the dissertation research in §1.5.

## 1.2 ANALYTICAL SEPARATIONS

### 1.2.1 BASIC MODES OF SEPARATION

The variety of electrophoretic methods precludes the use of any rigid system to classify the techniques. At a fundamental level, however, most employ one of four basic modes—moving boundary electrophoresis (MBE), zone electrophoresis (ZE), isotachopheresis (ITP), and isoelectric focusing (IEF) [113]. These are described schematically in Figs. 1.1–1.3. In MBE, which has become essentially obsolete, a sample

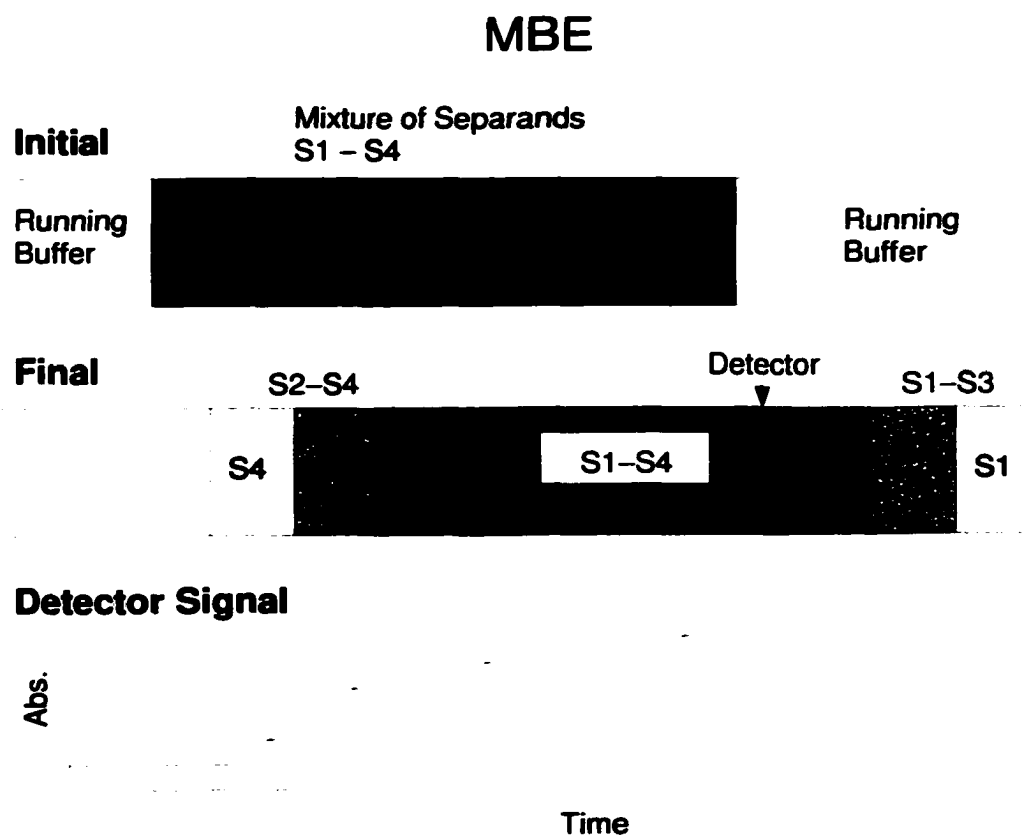


FIGURE 1.1. Schematic of MBE. The electrophoretic mobility  $\mu^e$  of the separands decreases from S1 to S4, and all are cationic.

mixture is dissolved in buffer and injected into the separation column as a zone that occupies most of the column. The sample zone is bounded on both ends by uniform buffer that extends into reservoirs at the column ends. An electric potential difference is applied across the column, and the charged components of the mixture migrate electrophoretically at different speeds. This results in the formation of distinct zones of unique composition, fore and aft of the initial sample zone, from which the concentrations of the ions in the sample can be deduced after passing the zones through a detector. ZE, which has essentially replaced MBE, differs from MBE only by the

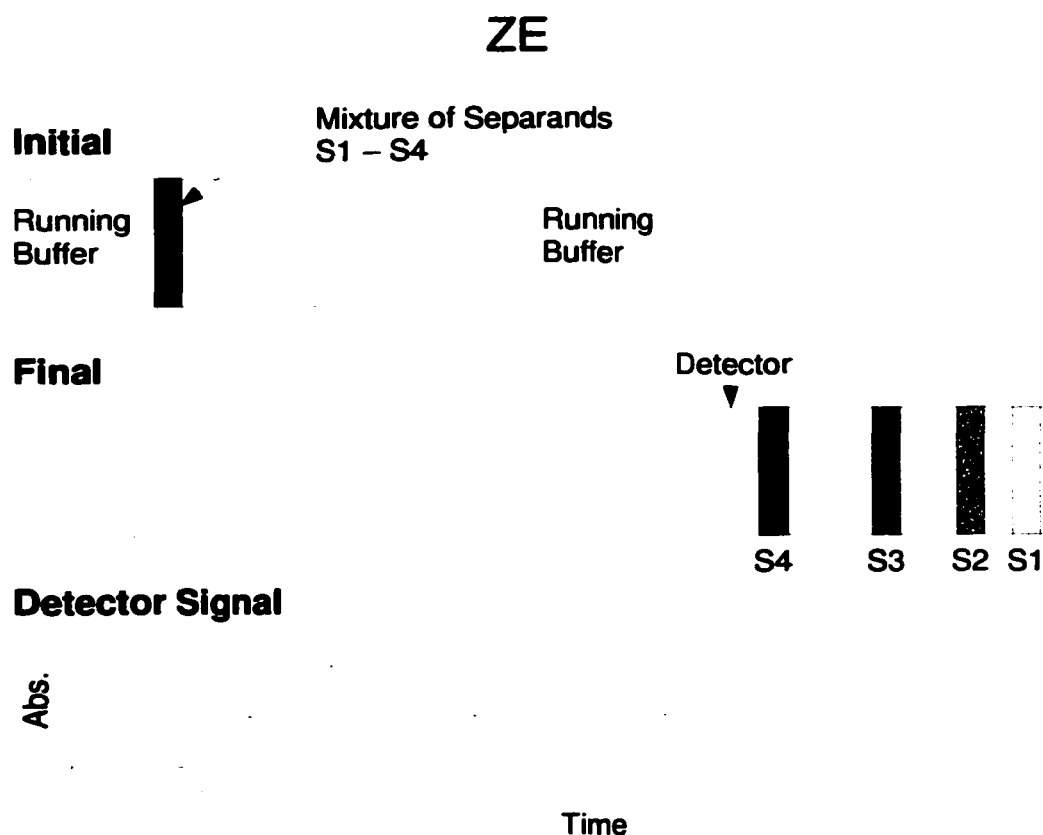
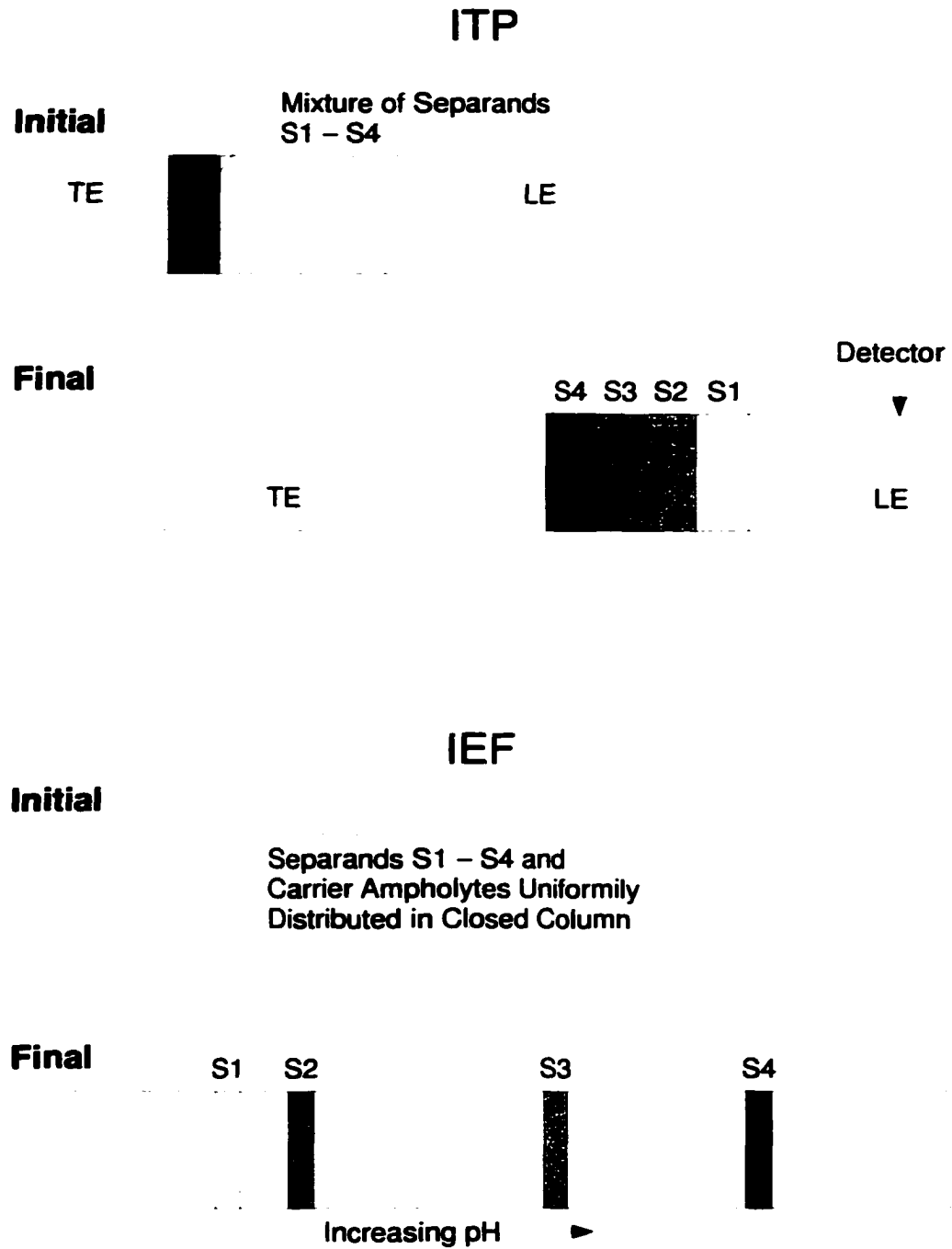


FIGURE 1.2. Schematic of ZE. The electrophoretic mobility  $\mu^e$  of the separands decreases from S1 to S4, and all are cationic.

length of the initial sample zone  $L_s$ . In ZE, this zone is typically two orders of magnitude shorter than the column length  $L_c$ , permitting complete separation of each component into isolated zones bounded by running buffer, that are measured as each in turn is eluted at the detector.

ITP differs from ZE by the choice of running buffer leading and trailing the initial sample zone. In ITP, the leading electrolyte (LE) and trailing electrolyte (TE) of the sample mixture are chosen with a higher and lower electrophoretic mobility  $\mu^e$ , respectively, than those of the ions in the sample. With these initial conditions, the sample constituents are separated into a train of zones that migrate at the same speed, i.e. isotachophoretically, sandwiched between the leading and trailing electrolytes. The advantage of this mode is that, because conservation of charge forces the electric field to decrease, zone to zone, from the trailing to the leading electrolyte, the component zone boundaries are self-sharpening (the diffusive fluxes are opposed by electromigrational fluxes in the zone boundaries). This reduces dissipation of the sample zones by diffusion, and thereby improves the resolution of the separation.

While MBE, ZE, and ITP separate charged particles by mobility, IEF separates them by isoelectric point (pI), and is therefore only useful for amphoteric compounds such as proteins and amino acids. In IEF, an electric potential difference is applied across the length of a column, causing ampholytes to migrate in a pH gradient until they reach their pI. The pH gradient is established by a buffer comprised of ampholytes—called carrier ampholytes because they carry the current and the pH [113]—with a spectrum of pI's. Classically, IEF has been conducted in closed columns



**FIGURE 1.3.** Schematics of ITP and IEF. ITP:  $\mu^e$  of LE  $>$   $\mu^e$  of S1–S4  $>$   $\mu^e$  of TE; after separation, all ions migrate at constant (isotachophoretic) speed. IEF:  $\mu^e$  of the separands is zero in the final (steady) state; pI increases from S1 to S4. Carrier ampholytes form pH gradient upon application of electric field.

to force the most basic and acidic carrier ampholytes to concentrate at the cathode and anode, respectively. This process is essential, as it drives the formation of the pH gradient. However, in the last decade, IEF has been accomplished in open capillaries by bounding the carrier ampholyte buffer by a strong base and acid, respectively, on the cathodic and anodic ends of the capillary. Like ITP, IEF has the advantage of forming self-sharpening zone boundaries; amphoteric analytes concentrate, or focus, at their pI until the electromigrational fluxes toward the pI are balanced by diffusive fluxes away from it.

These separation modes do not adequately describe separations that combine electrophoresis with other techniques such as chromatography. For example, capillary electrochromatography (CEC) [7, 43] and micellar electrokinetic chromatography (MEKC) [7, 114] essentially combine ZE with chromatographic mechanisms, and separate components on the basis of their electrophoretic mobilities and their affinities for another (stationary) phase. Thus, electrochromatographic methods permit components of similar mobilities (including neutral species) or affinities to be resolved.

### 1.2.2 ANALYTE STACKING

As microscale analysis has advanced in the last decade, the need to improve analyte detection has become evident. The short optical path lengths in microcolumns are insufficient for UV detection—used in most commercial capillary electrophoresis

devices—of components of low concentration in many applications [77, 155]. To improve the limits of detection, research has focussed on (i) improved detection methods [34, 50, 71, 77, 107] and (ii) on-column sample concentration [13, 34, 71, 77, 121]. The latter, also called analyte or sample stacking, is particularly appealing since it can be implemented without modification of standard instrumentation; analyte stacking can be realized simply by an appropriate selection of buffers. Stacking occurs when the analytes in the initial sample are concentrated in narrower zones during separation [154]. This process is inherent in IEF where analytes are stacked at their pI, whereas in ITP and ZE, stacking will occur only for specific buffer configurations.

Several methods for sample stacking in ZE have been investigated [155]. In most methods, analytes are stacked when the running buffer is diluted in the sample zone. Conservation of charge then requires a higher electric field in the sample zone than in the running buffer. As a result, analytes must slow down as they migrate electrophoretically out of the initial sample zone, and thus concentrate at the run buffer/sample zone boundary [154] as illustrated in Fig. 1.4. Methods employing this mechanism are generally called field-amplified sample stacking (FASS) or ionic strength mediated stacking, and the simplest of such methods is sometimes called simple stacking. In simple FASS, a diluted sample zone of length  $L_s \sim 10^{-2}L_c$  is introduced to the column, and the separation is conducted according to a typical ZE protocol. This method, which has been used to analyze a variety of compounds [36, 14, 92, 147, 120, 104], is straightforward to implement and requires no modification of standard procedures. The level of stacking realized by this method is,

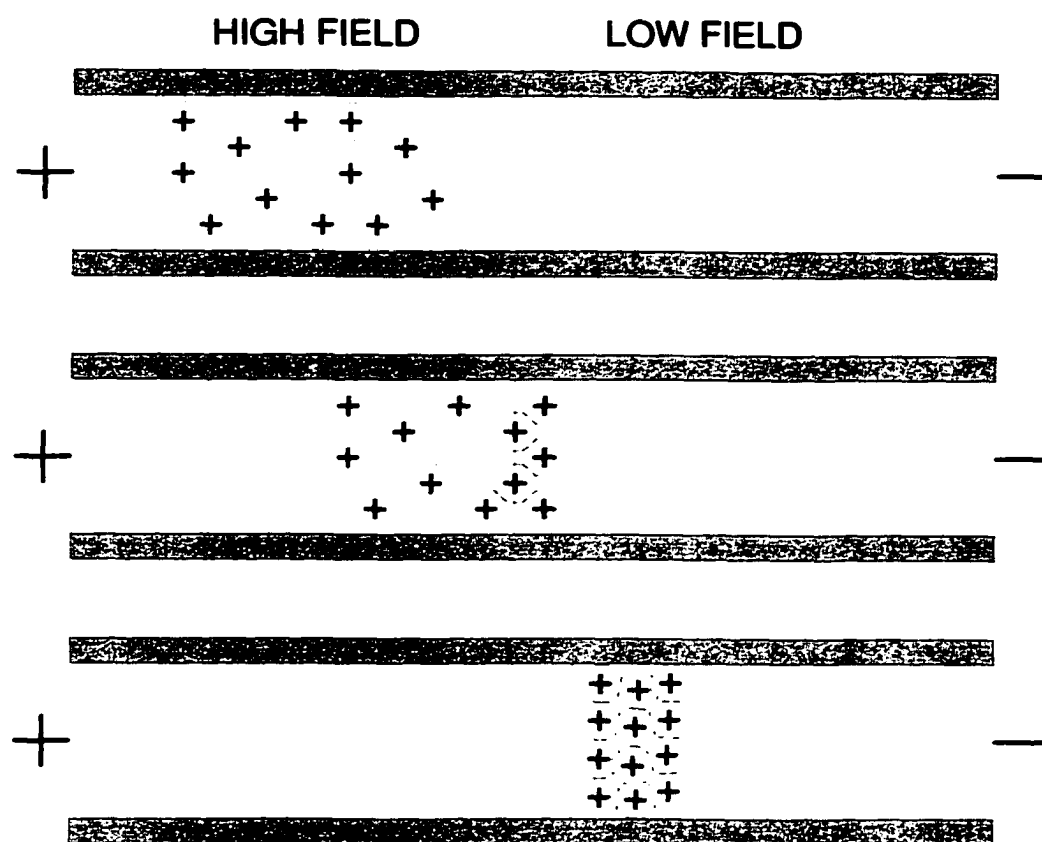


FIGURE 1.4. Illustration of FASS mechanism for cations [154]

however, limited by the small mass of sample injected in the column; the analytes reach a stacking limit when they are concentrated into zones that are narrower than the characteristic dispersion length for the separation [36]. Higher concentrations are realized by large-volume FASS [42, 3, 4, 104]. In this procedure, a sample zone of  $L_s \sim L_c$  is introduced and then removed from the column by reversing the electrode polarity to drive the running buffer away from the detector. Analytes are stacked while the sample zone is removed from the column. The polarity of the applied potential is then switched back, and the analytes are separated and eluted at the detector. This method is more complicated than simple FASS—polarity switching and/or electroosmotic flow modifiers are required—and all ions analyzed must be of the same sign. The greatest sensitivity enhancements by any ionic strength mediated stacking method have been demonstrated using field-amplified sample injection (also referred to as head-column FASS) [40, 41, 166, 167, 157, 158]. Stacking is attained by filling the column with running buffer and injecting the analytes from a reservoir of diluted buffer or even water [40]. In contrast to the other FASS methods that concentrate a sample limited by (at most) the volume of the separation column, with this procedure there is virtually no limit to the amount of sample that can be stacked. This approach appears to be very promising, particularly for cationic stacking. Stacking of both cations and anions requires a more complicated protocol involving carefully-timed polarity switching [41].

### 1.3 MICROFLUIDIC PROCESSES

“Microfluidic(s)” is a term that has been used to describe processes, devices, technologies, etc. that involve the manipulation of fluids on length scales  $\ll 1$  mm. One of the most exciting and promising applications of microfluidics is lab-on-a-chip technology, which is expected to revolutionize chemical analysis processes much like the integrated circuit revolutionized the microelectronics industry [63, 31, 97, 17, 61, 101]. With this rapidly emerging technology, the physical and chemical processes required of a chemical analysis are miniaturized, multiplexed, and integrated onto a microchip. Microfluidic chips are fabricated by etching or embossing reservoirs and microchannels of  $O(10 \mu\text{m})$  width in substrates such as glass, silicon, and various polymers, and electric potential gradients and/or microelectromechanical systems (MEMS) are used to control processes on the chip.

#### 1.3.1 ADVANTAGES

One of the primary advantages of lab-on-a-chip technology is high throughput. Improved heat dissipation in microfluidic systems permits higher electric field strengths, thereby reducing separation times. Shorter injection zones further reduce separation times, which are typically on the order of seconds or less, as compared to minutes to tens of minutes in standard capillary electrophoresis devices [31]. Jacobson et al. [90] recently accomplished a separation on a microchip in less than a millisecond. High throughput is achieved not only by faster separations, but more importantly by

**multiplexation and integration.** Several researchers have developed multiplexed electrophoresis devices, in which as many as 96 samples have been processed in parallel [160, 150, 138, 137]. Integration of the steps involved in an analysis—e.g. reagent dilution and mixing, amplification or intercalation reactions, separation, and detection—on a single chip allows the entire process to be automated. This not only speeds the analysis but also reduces the amount of laboratory space required and eliminates the potential for human error and/or contamination during handling between instruments. Some examples of complete analyses that have been realized on a microfluidic device are immunoassays [39], enzyme assays [72], and DNA analyses [37, 151]. Other potential advantages of lab-on-a-chip technology include reduced reagent consumption and waste streams, increased precision and accuracy, and disposability [63].

### 1.3.2 ELECTROKINETICS

A fundamental challenge in developing microfluidic systems is the precise control of fluid motion through networks of microchannels. Flows in these networks are typically on the order of nanoliters per second, and many microfluidic processes require flow control to picoliters per second accuracy [31]. While microscale mechanical pumps have failed in this to date, a pumping mechanism that has been demonstrated to be capable of this is electroosmosis [31], which arises naturally when an electric potential gradient is applied along an electrolyte-filled channel, capillary, or interstice. Electroosmotic fluid motion is produced by electrical stresses in the diffuse charge

layer near a charged interface; the applied electric field imparts motion to the ions, which transfer momentum to the bulk fluid through molecular interactions. Flow is manipulated by controlling the voltage at various points in the network [56, 91].

Electroosmotic pumping is also attractive because the potential gradients required must already be supplied to most systems to support electrophoretic separations, which are ubiquitously employed in microfluidic devices. Electrophoretic separations in microchannels etched in planar substrates were first demonstrated in 1992 by Harrison, Manz, and coworkers [74, 109]. Since then, such separations have been performed for a wide variety of species, including DNA fragments [54, 159], proteins [45], peptides [75, 81], and amino acids [86].

Although in uniform conductivity buffers, electroosmosis has the essential character of plug flow in fully-developed regions, many important applications involve nonuniform conductivities. For example, it has been demonstrated that samples can be transported without separation by high-ionic-strength electroosmotic pumping [31]. In this pumping method, electromigration is suppressed by dissolving the sample components in a high-ionic-strength (high-conductivity) electrolyte, relative to the running buffer. This is desirable to deliver a plug of controlled composition to a given process in a microfluidic device. As another example, electroosmosis occurs naturally and is commonly harnessed to mobilize the carrier fluid in electrophoretic separations (in capillaries as well as in microchips); most separation schemes, e.g. ITP, IEF, and FASS, employ nonuniform conductivity buffers. Electrically-driven flows in such buffer configurations are unsteady, spatially nonuniform, and nonlin-

early coupled to the ion transport.

## 1.4 SIMULATION OF MICROANALYSIS PROCESSES

Numerical simulations have the potential to play a vital role in the development of microfluidic and analytical separations processes by providing a tool to explore the effects of various operating parameters. Simulations also afford the opportunity to examine processes, such as the evolution of the concentration, fluid velocity, electric, and conductivity fields, which are not amenable to experimental investigation in microscale systems. The feasibility of accurate and efficient simulations is suggested by the well-behaved fluid motion on microfluidic length scales. Since Reynolds numbers  $Re$  in these microscale processes are essentially always  $\leq O(1)$ , fluid motion is laminar and thus can be described without invoking less-developed theories of turbulence. Moreover, typically  $Re \ll 1$ , and therefore most flows are quasi-steady.

Theories of electrokinetic motion began with the work of Helmholtz [76] and Smoluchowski [140], who developed formulae relating electrophoretic and electroosmotic velocities to the surface potential and applied electric field in the thin double-layer and low zeta potential limit [132]. More general theories have followed [132, 85], but until recently most of the effort was focused on linear theory [132, 133]. Analytical solutions elucidated much of the underlying physics and chemistry of electrophoresis and electroosmosis, but have limited utility in predicting the behavior of inherently nonlinear microfluidic processes. A general set of nonlinear balance

laws for electrophoretic separations was first introduced by Bier and coworkers [20] in the early 1980s. They later developed a 1-D simulation of the classical modes of electrophoretic separation [113, 134, 122], and since then many researchers have used similar 1-D simulations to advance our understanding of the dynamics of electrophoresis [64, 51, 59, 136, 135, 55, 108, 87].

Nevertheless, because they are one-dimensional, such investigations omit the effects, such as solute dispersion, of nonuniform electroosmotic fluid motion. It has been observed experimentally, for example, that analytes can only be stacked by up to a factor of about 10 with simple FASS [36, 92]. With a 1-D, analytical model, Burgi and Chien [36] demonstrated that stacking performance is limited by analyte dispersion resulting from nonuniform electroosmosis. Their analysis, however, neglects dispersion of the analytes during the stacking process, i.e. while they are transported through the heterogeneous buffer region. Although the model of Burgi and Chien [36] fits most of their data, for some configurations, their calculations err substantially. This results because, as will be shown, analyte dispersion during stacking is significant, and a comprehensive analysis requires consideration of the coupling of solutal transport to the unsteady 2-D fluid motion. A quantitative understanding of dispersion during stacking is also needed to explain the limitations of other FASS techniques such as large-volume and head-column FASS [42, 3, 4, 104, 40, 41, 166, 167, 157, 158]. With these methods, the buffer is homogeneous except while the analytes are stacking, and thus fluid motion in the nonuniform electrolyte is expected to dominate analyte dispersion.

Another microfluidic process in which dispersion in heterogeneous electrolytes is important, is high ionic strength electroosmotic pumping [31]. In this process, buffer nonuniformities are employed to suppress analyte separation at the expense of additional dispersion resulting from nonuniform electroosmosis. A tradeoff therefore exists between analyte dispersion and separation suppression. Simulations can aid in the development of electroosmotic pumping by exploring the tradeoff for various operating conditions. The resolution of separation processes such as ITP and IEF is also limited by analyte dispersion, which cannot be evaluated without consideration of electrically-driven fluid motion in heterogeneous buffer systems.

Previously-published simulations of electrophoretic separations suffer not only from 1-D model limitations, but also from numerical difficulties. To avoid spurious, spatiotemporal oscillations in the calculations, these simulations either used numerical diffusion to artificially spread sharp gradients [108, 87], or were limited to electric field strengths at least an order of magnitude lower than those typically used in practice ( $O(0.1 - 1)$  kV/cm) [113, 64, 51, 59, 136, 55]. An accurate computational representation of microfluidic systems and analytical separation schemes thus requires (i) numerical techniques that capture sharp gradients at electric field strengths  $\geq O(100)$  V/cm, and (ii) proper accounting of the unsteady fluid motion and multi-dimensional ion transport. No simulations of *any* electrically-driven transport processes, that include both of these capabilities, have been published.

#### 1.4.1 ELECTRIC FIELD STRENGTHS USED IN PRACTICE

The high-field deficiencies of the early numerical schemes [113, 64, 51] result from the accumulation of substantial discretization errors introduced in regions of sharp concentration gradients by higher-order (order 2 and above) finite difference approximations. These discretization errors accumulate to form artifactual peaks or valleys which spawn additional peaks and valleys, and perpetuate the growth of spurious oscillations. Ermakov et al. [55, 58] controlled the numerical oscillations by adding artificial dispersion terms to the discretized equations, and hence were able to simulate ZE and ITP at higher electric field strengths. This method, though a substantial improvement over previous numerical implementations, still failed to suppress oscillations in simulations with local field strengths of  $O(100 \text{ V/cm})$ . Martens et al. [108] evaluated the application of several implicit upwind numerical methods, including first and higher-order schemes, to the simulation of ZE and ITP separations. The higher-order schemes exhibited numerical oscillations and/or significant mass balance errors. The first-order upwind schemes suppressed all oscillations without significant mass balance errors, but included numerical diffusion that resulted in overprediction of zone boundary thicknesses. Ikuta and Hirokawa [87] simulated high-field ZE with an explicit first-order upwind method that proved to be numerically monotonic but also suffered from numerical diffusion. Application of these high-field methods to the simulation of isoelectric focusing (IEF) has not been reported.

Development of higher-order finite difference methods for solving advection prob-

lems involving sharp gradients began in the early 1970s with the use of flux limiters [143, 105, 27]. Van Leer [105] and Boris and Book [27] independently introduced the first flux limiter methods, and development of these and related methods has continued over the last three decades. The flux-corrected transport (FCT) method originated by Boris and Book was initially developed for hyperbolic conservation laws [27, 25, 28, 29, 26, 163, 30], and is an appealing method because it is both monotonic and second-order accurate. FCT algorithms are multi-step finite difference schemes in which numerical diffusion is included in a higher-order finite difference representation of the conservation law; this prevents spurious peak formation. The numerical diffusion is then removed in a subsequent “antidiffusion” step, except from regions where it is needed to offset the discretization error that would otherwise lead to spurious peak development. An antidiffusion-flux limiter is used to decide where and how much of the numerical diffusion should be removed. Successful implementations of FCT have been demonstrated for various higher-order schemes, numerical diffusion and antidiffusion coefficients, antidiffusion flux limiters, etc. [25, 28, 29, 26, 163, 30, 119, 67]. In the specific context of electrophoresis, Clifton [44] and Blanco et al. [23] respectively applied an FCT algorithm to a steady-state, continuous-flow (CFE) model and to high-field protein ZE.

### 1.4.2 ELECTRICALLY-DRIVEN FLOWS

Previous studies of multi-dimensional electrophoresis and electroosmosis have focused on the steady velocity fields that obtain in uniform electrolytes. The structure of these flows results from either of two factors: (1) non-uniform charge or  $\zeta$ -potential distributions on the rigid surfaces that bound the flow [8, 94, 126, 9, 106]; or (2), specialized geometries, such as those on MEMS devices [57, 56, 9, 123, 82, 48, 18, 11].

Anderson and Idol [8] obtained a general solution for the electrically-driven Stokes flow in a cylindrical capillary of axially nonuniform zeta potential, in the thin Debye layer and high aspect ratio limits. In a similar vein, Long et al. [106] have developed analytical formulae for the general case of arbitrary surface charge inhomogeneities in planar and cylindrical capillaries. The effects that such flows have on analyte transport have been studied by Keely et al. [94], who used the general solution of Anderson and Idol to construct a Taylor dispersion analysis for a cylindrical capillary with a piecewise-linear zeta potential, and Potoček et al. [126], who simulated the two-dimensional migration of an analyte through a cylindrical capillary with various  $\zeta$ -potential profiles. Others have investigated dispersion in channels with nonuniform electroosmosis by restricting the mathematical analysis to regions of fully-developed flow, far from the (axial) nonuniformities [36, 79, 98, 128].

A desire to understand flow in microfluidic devices has stimulated several fundamental studies of electroosmosis and analyte transport in specialized geometries. Andreev et al. [9] presented an analytical solution for steady 2-D fully-developed

flow in channels of rectangular cross-section and different zeta potential on each wall. For the same geometry, Arulanandam and Li [11] developed a numerical algorithm to conduct parametric studies of the cross-sectional velocity and electric potential profiles. Others have investigated electroosmotic flows and potential fields at cross elements and mixing tees [123, 82, 48, 18]; this work was initiated by Patankar and Hu [123], who simulated in three dimensions, the steady fluid motion and electric potential distribution at a cross element configured for electrokinetic focusing. In addition to solving for fluid velocities and potentials, Ermakov et al. [57, 56] included the transport of dilute analytes to simulate 2-D injection and mixing techniques on microfluidic devices.

## 1.5 PRESENT STUDY

The first step toward simulating microanalysis processes in heterogeneous buffers is to solve the numerical problems associated with the advection-dominant solute transport. The presentation of my dissertation research begins in Chapter 2 with a brief summary of my published work, presented in Appendices A and B, that explains how to solve these problems. The manuscript in Appendix A, published in the *Journal of Chromatography A*, describes an FCT algorithm that we applied to the solute mass balances in the transient, 1-D electrophoresis model. The FCT scheme is evaluated by simulating benchmark ZE, ITP, and IEF separations, and comparing the results to those generated by previously-published numerical schemes. The paper demon-

strates the general effectiveness of the FCT algorithm in simulations of high-field electrophoretic separations. Converged solutions for ZE and ITP are accomplished where the other schemes fail, and FCT captures IEF zones more accurately than any other published method.

Although techniques such as FCT and upwinding prevent numerical oscillations by employing numerical diffusion and/or antidiffusion, unless these artificial transport mechanisms are included in the charge balance, electrophoresis simulations can generate artifactual pH variations. The manuscript in Appendix B, published in *Electrophoresis*, elucidates the cause of the pH errors in the context of upwinding and presents two algorithms for mitigating them. The general principles set forth in the manuscript apply to FCT as well.

In Chapter 3, microanalysis processes are investigated by extending the electrophoresis model to two dimensions and incorporating fluid motion. Dynamic simulation results are presented for electroosmotic pumping and sample stacking, and the time evolution of the field variables are discussed in detail. The results indicate that analyte dispersion during simple FASS severely limits the level of preconcentration attainable on microfluidic length scales, and in some cases no stacking is achieved. The weaker flows in electroosmotic pumping have a less significant effect on analyte dispersion, but a stronger effect on dispersion of the sample zone, which reduces the suppression of analyte separation over time.

Approximate semianalytic solutions for  $\mathbf{v}$  and  $\mathbf{E}$  are then constructed in Chapter 4, and their utility and accuracy is demonstrated for conditions typical of microfluidic

and analytical separation processes. The approximations are shown to apply over a wide range of operational conditions for the prototype problem discussed in Chapter 3, and average fluid speed errors in conductivity transition zones are less than 1%. Moreover, the scaling arguments used to derive the approximate solutions reveal general information about about the fundamental physics of electrically-driven transport in microchannels. The analysis indicates, for example, that axially applied electric fields in straight microchannels are essentially unidirectional, even when the transverse component of the conductivity gradient meets or exceeds the axial component. The results also demonstrate that, at sufficiently high values of  $\mathbf{E}$ , nonlinear electrical stresses alter the structure of the flow in the zone boundary, producing more complicated flow patterns not hitherto observed.

Chapter 5 demonstrates that the semianalytic expressions for  $\mathbf{v}$  and  $\mathbf{E}$  permit accurate 2-D simulations of analyte concentration fields. Approximation errors averaged over the sample zone are less than 1% for all test cases.

The presentation of the research ends in Chapter 6 with a description of a macro-transport representation of the solute conservation, derived from the approximations for  $\mathbf{v}$  and  $\mathbf{E}$ . This reduces the mathematical problem to one dimension, thus providing information on cross-sectionally averaged values in orders of magnitude less simulation time than that required to solve the full problem. The effective 1-D simulation results are shown to match those from 2-D simulations. Because of the accuracy and simplicity of the method, it permits examination of analyte dispersion for electrolyte configurations that are impractical to simulate in two dimensions.

Finally, the dissertation is closed in Chapter 7 with some concluding remarks and implications of the research for future studies. The effective 1-D simulations developed in this work can be used to further examine solutal dispersion in electroosmotic pumping, and possibly other processes such as ITP, IEF, and other FASS schemes. 2-D flow fields in these more complicated systems might also be investigated if the semianalytic expressions for  $\mathbf{v}$  and  $\mathbf{E}$  presented in this dissertation are accompanied by a similar approximation for the pH.

## CHAPTER 2

# SUPPRESSION OF NUMERICAL OSCILLATIONS

The first step toward simulating microanalytical processes is to improve the numerical methods used to solve the general electrophoresis model for heterogeneous electrolytes. The numerical deficiencies result from the accumulation of substantial discretization errors in regions of sharp concentration gradients, at high electric Peclet numbers. For higher-order finite difference approximations, these errors perpetuate the growth of spurious oscillations. Previously-published schemes have failed to eliminate the oscillations for electric field strengths  $\geq O(100)$  V/cm, without introducing excessive numerical diffusion or mass balance errors [113, 64, 51, 55, 58, 108, 87]. The problem is solved in this dissertation by applying FCT to the solute mass balance laws. This work has already been published in two papers that are included in Appendices A and B. The discussion in this Chapter is merely a synopsis of the research detailed therein.

### 2.1 FLUX-CORRECTED TRANSPORT (FCT)

In Appendix A, FCT is discussed as a general high-field method to simulate the various modes of electrophoretic separation, and the technique is compared to more conventional approaches (i.e. no flux limiter). The Boris and Book approach is adapted to the parabolic conservation laws of the transient electrophoresis model and the es-

essential aspects of FCT are preserved, viz. spurious oscillations are suppressed and numerical diffusion is controlled. Although Clifton and coworkers [44, 23] simulated CFE and ZE with an FCT algorithm, the effectiveness of any numerical approach can vary dramatically with the physics of the problem, and ITP and IEF differ mechanistically from ZE and CFE. Moreover, the electric field strengths simulated by Clifton et al. for CFE were less than  $O(100)V/cm$ , and the ZE analytes were separated in a uniform background buffer. Thus, to evaluate the broad performance of the FCT algorithm, three benchmark electrophoretic separations—a ZE, an ITP, and an IEF separation—are simulated at realistic electric field strengths. The ZE and ITP benchmarks have been used previously by others to evaluate various numerical schemes [55, 108, 87]. For comparison, the separations are also simulated using two other common explicit finite difference methods: a first-order explicit upwind scheme and the second-order central difference scheme employed by Palusinski et al. [122]. The spatial discretization of the upwind scheme is equivalent to the Diffusion Implicit Migration Explicit (DIME) scheme described by Martens et al. [108] except the diffusion term is treated explicitly rather than implicitly.

The FCT solutions converged on significantly coarser grids than did the upwind and central difference solutions, and FCT provided substantially more accurate solutions to the electrophoresis model when compared on the same grid. For example, FCT simulations of IEF were non-oscillatory on spatial grids where the explicit upwind scheme exhibited significant mass balance errors, and where the central difference scheme was either oscillatory or unstable. In contrast to the numerical method

described by Ermakov et al. [55], the FCT simulations showed no spurious oscillations on any spatial grid, and sharp zone boundaries were captured more faithfully than by the first-order upwind schemes described by Martens et al. [108] and by Ikuta and Hirokawa [87]. As a result, FCT solutions provided information on the benchmark separations that could not be obtained by the previously-published simulations [55, 108, 87].

## 2.2 POORLY BUFFERED SYSTEMS

While artificial diffusion and antidiffusion are certainly acceptable means to control and avoid numerical instabilities, without proper accounting for artificial transport mechanisms, electrophoresis simulations can generate artifactual pH variations. For example, Reijenga and Kašička [130] used a first-order upwind scheme (DIME) to study poorly buffered ITP systems, and reported significant pH dips or peaks (1 to 2 units) at the steady-state zone boundaries. Reijenga and Kašička referred to these unusual pH variations as discontinuities because one would normally expect pH to vary monotonically between neighboring ITP zones. In Appendix B, it is demonstrated that the pH discontinuities uncovered by Reijenga and Kašička are, in fact, artificial and are inherently generated by schemes such as DIME. The pH artifacts are manifested in simulations of poorly buffered systems if upwinding, or other forms of diffusion or antidiffusion, are included in the solute balance laws, but not in the charge balance.

First it is shown that pH discontinuities, analogous to those reported by Reijenga and Kašička, arise when molecular diffusion is omitted from the charge balance. This is done without employing numerical diffusion and establishes the need for a consistent description of the solute and the charge transport mechanisms. It is then demonstrated that inclusion of a numerical diffusion current in the charge balance substantially reduces the pH artifacts generated by a standard upwind scheme. Finally, a modified central difference scheme is presented that completely eliminates pH artifacts by treating numerical diffusion in the species and charge balances in a self-consistent way.

Taken together, these results imply that accurate determination of pH requires consistent treatment of diffusion (numerical or molecular) in the charge and species balance laws, especially in poorly buffered systems. That is, pH artifacts can result from either of two errors—one numerical, the other conceptual. The conceptual error involves the mechanisms for charge transport. Electrolyte solutions are ionic conductors, so charge is transported by ohmic and Brownian processes. Omitting the molecular diffusion current from the charge balance, while retaining molecular diffusion in the component balances, can result in substantially flawed results for the local pH, irrespective of the numerical method. The numerical method spawns errors when discrete representations of the spatial gradients in the charge balance differ from those used for the component mass balances.

## CHAPTER 3

2-D ELECTRICALLY-DRIVEN TRANSPORT: PROTOTYPE  
PROBLEM

Electroosmosis is an important mode of fluid motion that arises naturally when an applied voltage gradient is used to drive solutal transport through electrolyte-filled channels, capillaries and interstices. In some cases, e.g. microfluidic and capillary electrophoresis systems, electroosmosis constitutes an integral part of the technology, often serving to elute solutions through pores and capillaries of low hydraulic conductivity. However, when the structure of the flow is not fully-developed in the streamwise direction, electroosmosis may also cause undesirable effects. This is particularly true for microfluidic and electrophoretic separation techniques, where spatial variations in two or three dimensions can cause dispersion of solutes, and thus diminish important process characteristics such as resolution and sensitivity.

It is well known that, unless the driving electric field is in some sense small [133], electrokinetic motion in non-uniform buffers is an inherently nonlinear problem. Thus there are few studies of electroosmotic motion that is fully-coupled to the attendant electric field and the resulting ion transport. Clifton and coworkers [44, 1, 2] simulated steady, 3-D continuous-flow electrophoresis, where ion transport alters the fluid motion through bulk electrohydrodynamic stresses and electroosmotic wall slip. Also, Jacobs and Probst [89] developed 2-D simulations of electrokinetic remediation in

porous media, accounting for variations of the electroosmotic and Darcy flows with local sediment and solution chemistry. In this chapter, the prototype problem depicted in Fig. 3.1 is considered. A uniform running buffer that fills a rectangular channel is interrupted by a sample zone of different composition and ionic strength. An electric field of  $O(100 \text{ V/cm})$  is applied along the channel, so the voltage gradient exceeds those studied by Clifton et al. [44, 1, 2] and by Jacobs and Probst [89]—in some cases by an order of magnitude or more. The electrolyte variations create an axially nonuniform electroosmotic flow that disturbs the structure of the initial distribution, forcing the electric potential, fluid velocity, and ion concentration fields to evolve in time. When the conductivity in the sample zone is lower than that of the running buffer, this configuration represents a typical field-amplified sample stacking (FASS) protocol [36, 147, 120, 104]. When the conductivity in the sample zone is higher than that of the running buffer, analyte electromigration and separation are inhibited by the reduced electric field in the high conductivity zone. This protocol has been used to transport samples without separation in microfluidic processes that use electroosmosis as a pumping mechanism [31]. More generally, a fundamental characteristic of electrophoretic separations processes is the resolution of components into discrete zones that often vary in conductivity, ionic strength, and pH, such as in ITP and IEF [113]; the prototype problem of Fig. 3.1 includes the basic element of such processes, viz. a transition between zones of significantly different composition and electrical conductivity.

In this chapter, the formulation for the prototype problem is developed in §3.1, and

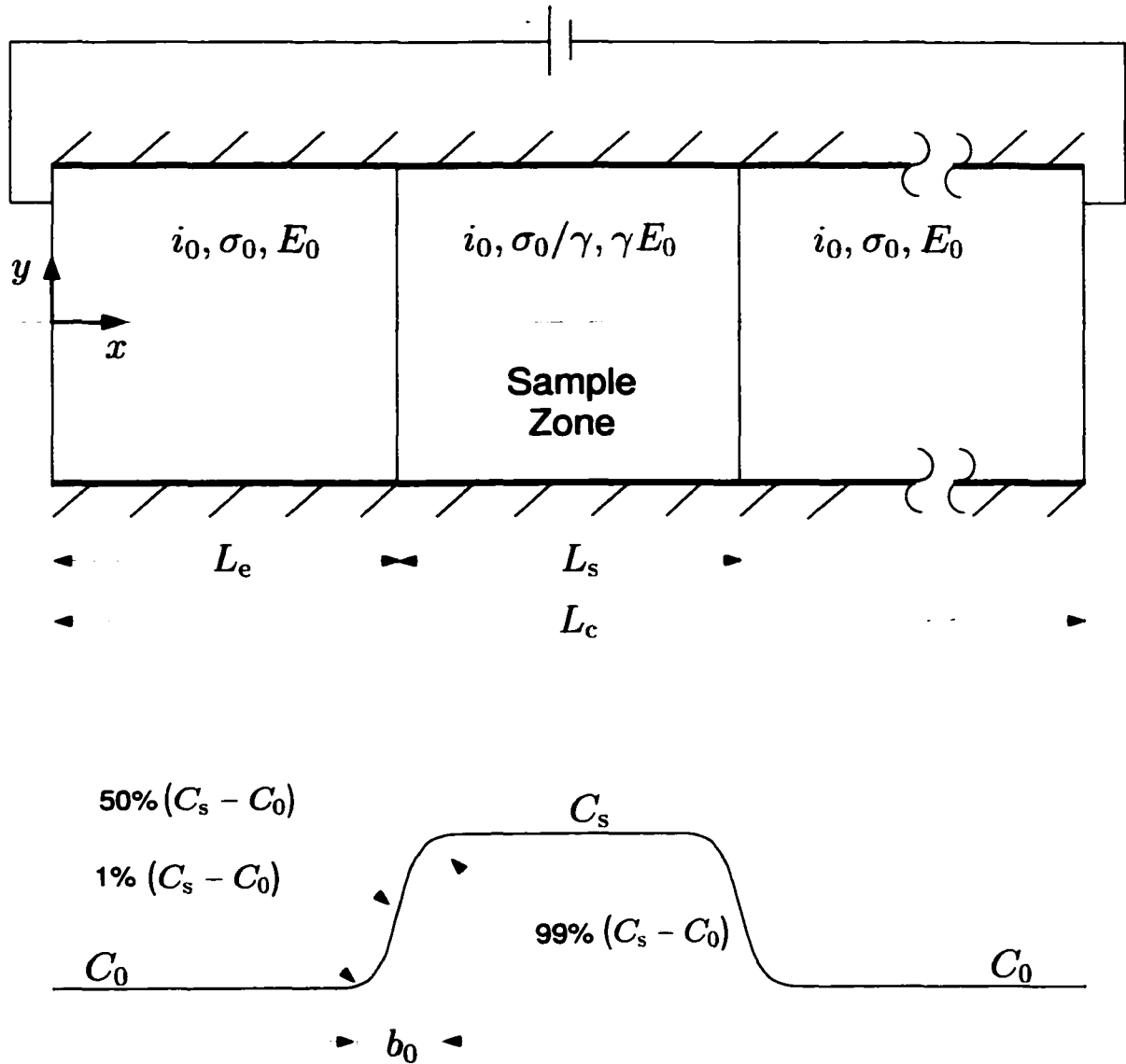


FIGURE 3.1. Sketch of system configuration and initial conditions. The concentration field shown applies to buffer and analyte components for  $\gamma < 1$ . For  $\gamma > 1$ ,  $C_s$  is less than  $C_0$  for buffer components.

the methods used to numerically solve the balance laws are described in §3.2. Dynamic simulation results are then presented for one electroosmotic pumping configuration (high conductivity sample zone) and one stacking configuration (low conductivity sample zone) in §3.3. The time evolution of the field variables are examined in detail, and some implications of the results are discussed in §3.4.

### 3.1 PROBLEM FORMULATION

#### 3.1.1 BALANCE LAWS

The balance laws for electrically-driven separations processes are well-known [113, 20, 134, 122], and the notation of the published papers in Appendices A and B is used here. Fluxes of ionic and neutral solutes are coupled locally through ionogenic reaction processes, motion of the solution, and the action of the electric field. Because dissociation–association reactions are fast compared to the mass transport, ion concentrations are constrained by mass-action equilibrium relations. For the protonation–deprotonation reactions of  $M$  solutal components, the (acidic) equilibrium constants  $K_k^z$  are

$$K_k^z \equiv \frac{[\text{H}^+]n_k^{z-1}}{n_k^z}, \quad \begin{cases} z = -N_k + 1, -N_k + 2, \dots, P_k \\ k = 1, 2, \dots, M, \end{cases} \quad (3.1)$$

where  $n_k^z$  is the concentration of the subspecies of the  $k$ th component with valence  $z$ , and  $P_k$  and  $N_k$  are, respectively, the number of cationic and anionic subspecies of the  $k$ th component. Electrostatic considerations (Debye screening) dictate that, to a good approximation, local electroneutrality prevails on length scales large compared

to  $\kappa^{-1}$ , the Debye screening length. Thus,

$$0 = \sum_{k=1}^M \bar{z}_k C_k + [\text{H}^+] - \frac{K_w}{[\text{H}^+]}, \quad (3.2)$$

if the dissociation constant for water is defined as  $K_w \equiv [\text{H}^+][\text{OH}^-]$ , and if the concentration and the effective valence of the  $k$ th component are, respectively, defined as

$$C_k \equiv \sum_{z=-N_k}^{P_k} n_k^z, \quad k = 1, 2, \dots, M, \quad (3.3)$$

and

$$\bar{z}_k \equiv \frac{\sum_{z=-N_k}^{P_k} z n_k^z}{C_k}, \quad k = 1, 2, \dots, M. \quad (3.4)$$

Conservation equations for the solutal components are of the form:

$$\frac{\partial C_k}{\partial t} = -\nabla \cdot \mathbf{f}_k = -\nabla \cdot [(\bar{\mu}_k^e \mathbf{E} + \mathbf{v}) C_k - D_k \nabla C_k], \quad k = 1, 2, \dots, M. \quad (3.5)$$

In Eq. (3.5),  $t$  denotes time,  $\mathbf{v}$  is the fluid velocity,  $\mathbf{E} = -\nabla\phi$  is the local electric field, and  $D_k = \omega_k k_B T$  is the diffusivity, where  $k_B T$  is the Boltzmann temperature and  $\phi$  is the electric potential;  $\mathbf{f}_k$ ,  $\omega_k$ , and  $\bar{\mu}_k^e$  are, respectively, the flux, the hydrodynamic mobility (taken here to be independent of component sub-speciation), and the effective electrophoretic mobility of component  $k$ . If  $M_p$  denotes the number of protein species,

$$\bar{\mu}_k^e = \begin{cases} [f(\kappa a_k)/(1 + \kappa a_k)] e \bar{z}_k \omega_k, & k = 1, 2, \dots, M_p \\ e \bar{z}_k \omega_k, & k = M_p + 1, M_p + 2, \dots, M, \end{cases} \quad (3.6)$$

where  $e$  is the charge on a proton ( $1.6 \times 10^{-19}$  C), and  $a_k$  is the (Stokes) radius of protein  $k$ ;  $f(\kappa a_k)$  is Henry's  $f$ -function [78].

The motion of the aqueous electrolyte is governed by the Navier-Stokes equations for incompressible flow, i.e.

$$\rho \left[ \frac{\partial \mathbf{v}}{\partial t} + \mathbf{v} \cdot \nabla \mathbf{v} \right] = -\nabla p + \mu \nabla^2 \mathbf{v} + \nabla \cdot \epsilon_0 \epsilon \left[ \mathbf{E} \mathbf{E} - \frac{1}{2} (\mathbf{E} \cdot \mathbf{E}) \mathbf{I} \right], \quad (3.7)$$

$$\nabla \cdot \mathbf{v} = 0, \quad (3.8)$$

where  $\rho$ ,  $\mu$ , and  $\epsilon$  are the fluid density, viscosity, and relative permittivity, respectively;  $p$  is the pressure,  $\epsilon_0$  is the permittivity of free space, and  $\mathbf{I}$  is the unit tensor. The last term on the RHS of Eq. (3.7) accounts for the electrical (Maxwell) stresses.

Since charge must be conserved, the governing equations are closed by combining the ion balances to obtain an equation for  $\phi$ , viz.

$$\begin{aligned} \nabla \cdot (\sigma \nabla \phi) &= -ek_B T \nabla \cdot \left( \sum_{k=1}^M \omega_k \nabla \bar{z}_k C_k + \omega_H \nabla [\text{H}^+] - \omega_{\text{OH}} K_w \nabla [\text{H}^+]^{-1} \right) \\ &= -\nabla \cdot \mathbf{i}^D, \end{aligned} \quad (3.9)$$

where

$$\sigma = e^2 \left[ \sum_{k=1}^{M_p} \frac{f(\kappa a_k)}{1 + \kappa a_k} \bar{z}_k^2 \omega_k C_k + \sum_{k=M_p+1}^M \bar{z}_k^2 \omega_k C_k + \omega_H [\text{H}^+] + \omega_{\text{OH}} \frac{K_w}{[\text{H}^+]} \right] \quad (3.10)$$

is the local electrical conductivity and  $\mathbf{i}^D$  is the diffusion current density;  $\bar{z}_k^2$  is the mean square valence of the  $k$ th component, i.e.

$$\bar{z}_k^2 \equiv \frac{\sum_{z=-N_k}^{+P_k} z^2 n_k^z}{C_k}, \quad k = 1, 2, \dots, M. \quad (3.11)$$

Note, for components that may undergo many protonation or deprotonation reactions (e.g. proteins), dissociation-association equilibrium constants are not necessarily

available. In such cases, subspecies concentrations are not calculated and, in place of Eqs. (3.4) and (3.11), effective and mean square valences are determined from titration data [113].

### 3.1.2 INITIAL AND BOUNDARY CONDITIONS

The prototype problem considered is sketched in Fig. 3.1. In a rectangular separation channel of length  $L_c$  and width  $2h$ , solutes (analytes) of concentration  $C_s$  are introduced to a sample zone of length  $L_s$  located at a distance  $L_e$  from the anodic end of the channel; note:  $L_c \gg L_e, L_s \gg h$ . The remainder of the channel is filled with a uniform running buffer of conductivity  $\sigma_0$  that extends into buffer reservoirs at the column ends. The initial conductivity of the buffer in the sample zone is  $\sigma_0/\gamma$ ; so if the field in the running buffer is  $E_0$ , the electric field in the sample zone is (initially)  $\gamma E_0$ . Thus  $\gamma$  is the field enhancement factor defined by Burgi and Chien [36] in the context of analyte stacking.

Because  $\kappa h \gg 1$ , the fluid motion in the diffuse layer is approximated by a slip condition along the length of the channel wall. If  $v_x(x, y, t)$  and  $v_y(x, y, t)$  respectively denote the  $x$  (axial) and  $y$  (transverse) components of  $\mathbf{v}(\mathbf{x}, t)$ , then at  $y = \pm h$

$$v_x(x, \pm h, t) \equiv v^{\text{eo}}(x, t) = \mu^{\text{eo}}(x, t)E_x(x, h, t), \quad v_y(x, \pm h, t) = 0. \quad (3.12)$$

The electroosmotic mobility for the channel wall,  $\mu^{\text{eo}}$ , is implicitly defined in Eq. (3.12);  $\mu^{\text{eo}}$  is a function of the local electrolyte composition and, so, varies with respect to  $x$  and  $t$ . For the calculations described later, we employ model IIIb of Thormann et

al. [147] to correlate  $\mu^{\text{eo}}$  with ionic strength  $I$ , buffer cation concentration  $[M^+]$ , and pH, viz.

$$\mu^{\text{eo}} = [\mu_{\text{a}}^{\text{eo}}\alpha + \mu_{\text{c}}^{\text{eo}}(1 - \alpha)] \sqrt{\frac{I_0}{I}} \frac{1 + K_{\text{wall}}[M^+]_0}{1 + K_{\text{wall}}[M^+]} \frac{1 + d_0 K' \sqrt{I}}{1 + d_0 K' \sqrt{I_0}} \beta. \quad (3.13)$$

In Eq. (3.13),

$$\alpha = \frac{10^{(\text{pH} - \text{p}K_{\text{s}})}}{1 + 10^{(\text{pH} - \text{p}K_{\text{s}})}} \quad (3.14)$$

is the degree of ionization of the wall,  $\beta$  is a temperature correction (0.813 for  $T = 25^\circ \text{C}$ ), and  $K_{\text{wall}}$ ,  $K'$ , and  $d_0$  are empirically determined parameters equal to  $0.004 \text{ mM}^{-1}$ ,  $3.2 \times 10^9 \text{ m}^{-1} \text{M}^{-0.5}$ , and  $3.0 \times 10^{-8} \text{ m}$ , respectively;  $\mu_{\text{a}}^{\text{eo}} = 6.75 \times 10^{-8} \text{ m}^2/\text{V}\cdot\text{s}$  and  $\mu_{\text{c}}^{\text{eo}} = 0.92 \times 10^{-8} \text{ m}^2/\text{V}\cdot\text{s}$  are absolute and correcting mobilities, respectively, for  $I = I_0 = 66.1 \text{ mM}$ ,  $[M^+] = [M^+]_0 = 60 \text{ mM}$ , and  $T = 35^\circ \text{C}$ . The ionization constant for silanol groups  $\text{p}K_{\text{s}} = 5.1$  in Eq. (3.14). Of the models investigated by Thormann et al., IIIb best captured the experimentally observed dependence of electroosmosis on pH and ionic strength for fused-silica capillaries.

When  $L_{\text{e}} \gg h$ , the uniform buffer at  $x = 0$ ,  $L_{\text{c}}$  is undisturbed by variations near the sample zone. Accordingly, there is unidirectional Poiseuille flow at  $x = 0, L_{\text{c}}$ , i.e.

$$v_x(0, y, t) = v_x(L_{\text{c}}, y, t) = \frac{3}{2} [v_0^{\text{eo}} - V(t)] \left[ \left( \frac{y}{h} \right)^2 - 1 \right] + v_0^{\text{eo}}, \quad (3.15)$$

and

$$v_y(0, y, t) = v_y(L_{\text{c}}, y, t) = 0, \quad (3.16)$$

where  $v_0^{\text{eo}}$  is the (constant) electroosmotic velocity in the the running buffer, and  $V(t)$

is the mean axial velocity, given by [8]

$$V(t) = \frac{1}{L_c} \int_0^{L_c} v^{\text{eo}}(x, t) \partial x. \quad (3.17)$$

Also at  $x = 0$  and  $L_c$ ,  $p$  is set to an arbitrary constant (zero), as there is no imposed pressure gradient.

The boundary conditions on the potential are

$$\begin{aligned} \sigma \nabla \phi \cdot \mathbf{n} &= \begin{cases} -i_0, & x = 0 \\ \mathbf{i}^{\text{D}} \cdot \mathbf{n}, & y = \pm h, \end{cases} \\ \phi &= 0, & x = L_c \end{aligned} \quad (3.18)$$

where  $i_0$  is the (constant) axial current density prescribed in the uniform buffer, and  $\mathbf{n}$  is the unit normal directed outward from the electrically insulating channel walls. The concentrations  $C_k$ ,  $k = 1, 2, \dots, M$ , are fixed at their running buffer values at  $x = 0, L_c$ . Adjustments in the surface charge density on the channel wall are considered to contribute negligibly to the species balances, and so:

$$\mathbf{f}_k \cdot \mathbf{n} = 0 \quad \text{at } y = \pm h, \quad k = 1, 2, \dots, M. \quad (3.19)$$

## 3.2 GENERAL 2-D SIMULATION METHOD

### 3.2.1 STOKES FLOW

The characteristic transverse channel dimension  $h$  is  $O(10 \mu\text{m})$  for microfluidic and analytical separations processes. Since  $|\mathbf{E}| \sim 100 \text{ V/cm}$ ,  $v_0^{\text{eo}} \sim 10^{-2} - 10^{-1} \text{ cm/s}$  and  $\mu/\rho \sim 10^{-2} \text{ cm}^2/\text{s}$ , the Reynolds number  $Re \equiv \rho v_0^{\text{eo}} h/\mu \ll 1$ , and to leading order Eq. (3.7) reduces to:

$$\mu \nabla^2 \mathbf{v} + \epsilon_0 \epsilon \mathbf{E} \nabla \cdot \mathbf{E} = \nabla p. \quad (3.20)$$

The quasi-steady velocity field is calculated at any given time by solving the biharmonic equation for the stream function, with a forcing function resulting from the electrical stresses, viz.

$$\nabla^4 \psi = -\frac{\epsilon_0 \epsilon}{\mu} \left[ \frac{\partial \phi}{\partial x} \frac{\partial (\nabla^2 \phi)}{\partial y} - \frac{\partial \phi}{\partial y} \frac{\partial (\nabla^2 \phi)}{\partial x} \right], \quad (3.21)$$

where

$$v_x = \frac{\partial \psi}{\partial y}, \quad v_y = -\frac{\partial \psi}{\partial x}. \quad (3.22)$$

Neumann boundary conditions on  $\psi$  are, from Eqs. (3.12) and (3.22),

$$\frac{\partial \psi}{\partial y} = v^{\text{eo}} \quad \text{at } y = \pm h, \quad (3.23)$$

and because  $v_y$  is zero on all boundaries,

$$\frac{\partial \psi}{\partial x} = 0 \quad \text{at } x = 0, L_c. \quad (3.24)$$

Dirichlet boundary conditions on  $\psi$  are derived by combining Eqs. (3.15) and (3.22), and integrating to obtain

$$\psi = \frac{3}{2} h (v_0^{\text{eo}} - V) \left[ \frac{1}{3} \left( \frac{y}{h} \right)^3 - \left( \frac{y}{h} \right) \right] + v_0^{\text{eo}} y \quad \text{at } x = 0, L_c. \quad (3.25)$$

Owing to symmetry,  $\psi$  has been arbitrarily set to zero at  $y = 0$ . Also, for impermeable channel walls, Eq. (3.25) yields

$$\psi = \pm V h \quad \text{at } y = \pm h. \quad (3.26)$$

### 3.2.2 NUMERICAL APPROACH

To save computation time, the simulation domain was restricted to a small region encompassing the nonuniform buffer and analyte zones, and the balance laws were solved numerically in a reference frame that translates with the mean velocity of the axial flow. If  $x'$  denotes the axial coordinate in the moving frame, i.e.  $x' = x - \int_0^t V(\xi)d\xi$ , then the boundaries  $x' = 0$  and  $x' = L_d$  were set back a distance of  $O(10h)$  from the sample zone and positioned to include all migrating analyte. At this distance, the running buffer remains undisturbed by the nonuniformities near the sample zone. Accordingly, the boundary conditions on  $\phi$  and the  $C_k$ ,  $k = 1, 2, \dots, M$ , at  $x = 0, L_c$  are applicable at  $x' = 0, L_d$ . The fluid velocity and stream function in the moving reference frame are

$$\mathbf{v}' = (v_x - V) \mathbf{e}_x + v_y \mathbf{e}_y, \quad (3.27)$$

and

$$\psi' = \psi - Vy, \quad (3.28)$$

where  $\mathbf{e}_x$  and  $\mathbf{e}_y$  are the unit vectors in the axial and transverse directions, respectively. Boundary conditions for  $\psi'$  and  $\mathbf{v}'$  follow straightforwardly from Eqs. (3.12), (3.15), and (3.23)–(3.28).

The mathematical model described above is comprised of a coupled set of nonlinear algebraic and partial differential equations (PDE's), including two elliptic PDE's (Eqs. (3.9) and (3.21)) and a parabolic PDE for each of the  $M$  components (Eq. (3.5)).

The parabolic equations were solved explicitly using a second-order 1-D FCT algorithm (Appendix A), and a Strang-type operator split to incorporate 2-D transport [66, 27]; the strong flux limiter of Boris and Book [27] was used. At each Runge-Kutta and operator-splitting step in this explicit scheme, the set of nonlinear algebraic equations (Eqs. (3.1)–(3.4)) was solved iteratively using an initial guess for the pH based on the previous step. Also at each step, the elliptic equations were solved by incorporating publicly available subroutines into the main code. A multigrid cycling algorithm with smoothing by incomplete line lu-decomposition was used to solve Eq. (3.9) [165], and a conjugate gradient algorithm using fourier transforms was used to solve Eq. (3.21) [21].  $\mathbf{v}'$  was calculated using central difference approximations of the stream function derivatives, and the integral in Eq. (3.17) was calculated using the trapezoidal rule.

### 3.3 RESULTS AND DISCUSSION

#### 3.3.1 ELECTROOSMOTIC PUMPING

Electroosmotic pumping of analytes in a high ionic strength sample zone was first simulated by setting  $1/\gamma = 5$  for the prototype problem of Fig. 3.1. The running buffer consisted of 100 mM Tris base and 200 mM cacodylic acid (pH = 6.2,  $\sigma_0 = 0.452$  S/m). Two amino acids (1  $\mu$ M histidine (HIS) and arginine (ARG)) and two proteins (1  $\mu$ M hemoglobin (HEM) and ferritin (FER)) were included in the sample zone to represent analytes that might be transported by electroosmotic pumping.

Although wall adsorption is not considered here, the proteins have been included to illustrate the effect of order of magnitude differences in analyte diffusivity. Component properties are provided in Tables 3.1 and 3.2. The geometric lengths of the system were  $L_e = L_s = 1$  mm,  $h = 20$   $\mu$ m, and  $L_c = 5$  cm. A constant current was maintained by requiring  $i_0 = 8000$  A/m<sup>2</sup> in the running buffer, corresponding to  $E_0 = 180$  V/cm.

TABLE 3.1. Buffer, amino acid, and solvent ion properties [113]

Component	pK <sub>1</sub>	pK <sub>2</sub>	$e\omega_k$ (10 <sup>-4</sup> cm <sup>2</sup> /V·s)	$D_k$ (10 <sup>-5</sup> cm <sup>2</sup> /s)
Cacodylic acid	6.21		2.31	0.59
Tris	8.30		2.41	0.62
Histidine	6.04	9.17	2.85	0.73
Arginine	9.04	12.48	2.26	0.58
Glutamic Acid	2.16	4.29	2.97	0.76
H <sup>+</sup>			36.27	9.32
OH <sup>-</sup>			19.87	5.11

Well defined initial conditions for the zone boundaries require simulation of the injection process, which is beyond the scope of this dissertation. Therefore, sigmoidal zone boundaries—such as expected from diffusion of a square sample plug—were initialized with a width  $b$  (defined here as the length over which the concentration changes from 1% to 99% of the concentration difference between one zone and another) equal to 12% of  $L_s$ . A zone boundary of approximately this length scale would result within 7 seconds given only diffusion as a dispersion mechanism.

Streamlines for the electroosmotic pumping problem are shown in Fig. 3.2, in the moving reference frame, at three different times. The nondimensional variable

TABLE 3.2. Protein properties<sup>†</sup>

pH	Net charge	
	HEM	FER
2.0		18.8
2.5		13.2
3.0	68.5	8.5
3.5	43.5	5.0
4.0		2.0
4.5	25.5	0.0
5.0		-2.0
5.5		-3.5
6.0	10.3	-5.5
6.5		-6.8
7.0	0.0	-8.5
7.5		-10.0
8.0	-10.3	-11.5
8.5		-13.0
9.0	-20.5	-17.0
9.5		-19.5
10.0	-30.8	-23.0
11.0	-50.0	
$D_k$ ( $10^{-7}$ cm <sup>2</sup> /s)	6.8	3.25

<sup>†</sup> HEM data from [113] and  
FER data from [146]

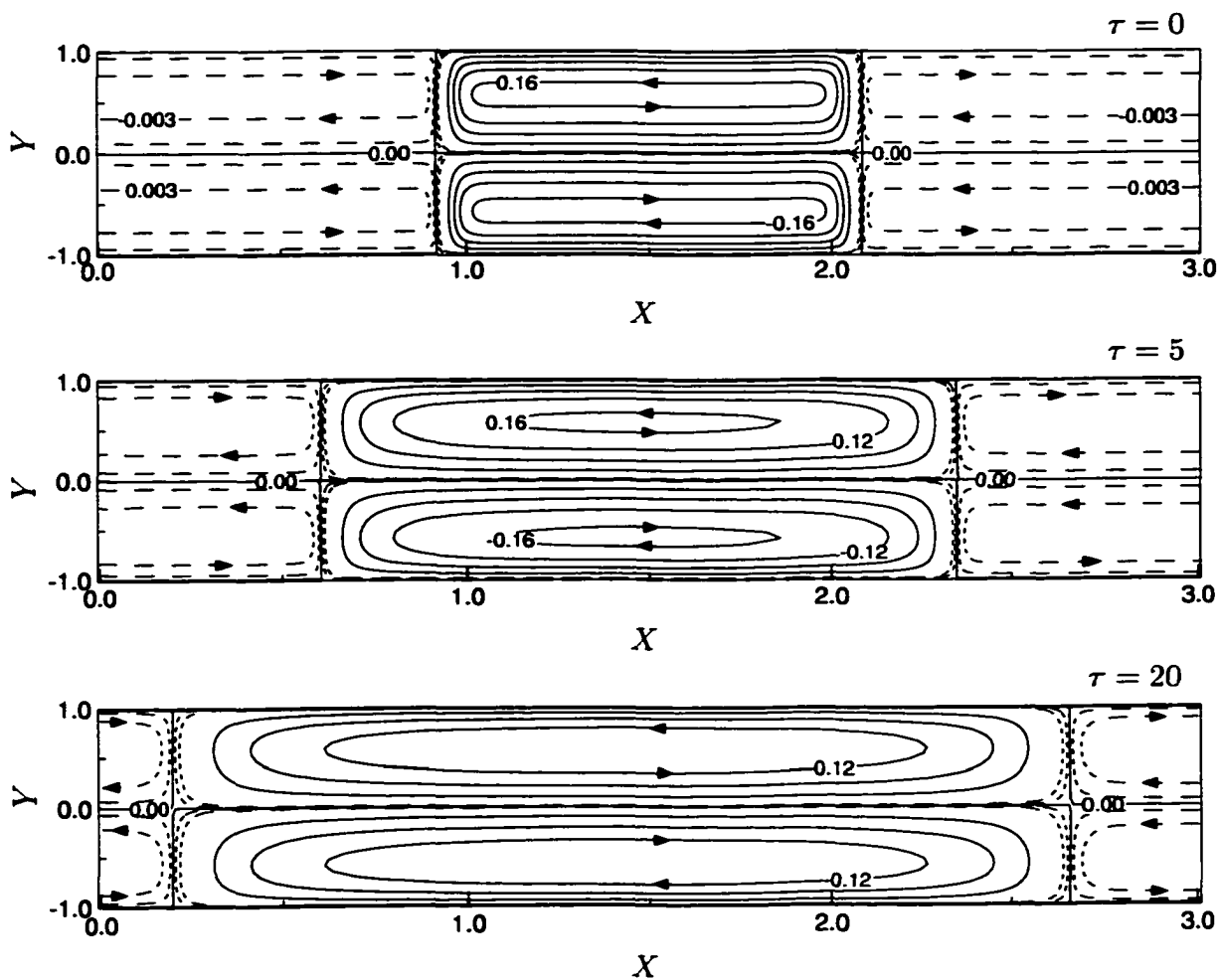


FIGURE 3.2. Streamlines for  $\gamma = 1/5$  at  $\tau = 0, 5,$  and  $20$ . Solid lines represent contours of constant  $\Psi \equiv \psi' / (h v_0^{eo})$  from  $-0.16$  to  $0.16$  at intervals of  $0.04$ ; dashed lines represent contours of constant  $\Psi$  from  $-0.003$  to  $0.003$  at intervals of  $0.002$ . Running buffer:  $200$  mM cacodylic acid,  $100$  mM Tris;  $\sigma_0 = 0.452$  S/m;  $E_0 = 180$  V/cm;  $i_0 = 8$  kA/m<sup>2</sup>;  $v_0^{eo} = 0.802$  mm/s; pH = 6.2.  $L_s = 1$  mm,  $L_c = 5$  cm,  $h = 20$   $\mu$ m. Anode/cathode at  $X \equiv x'/L_s = 0/50$  ( $\tau = 0$ ),  $-4.9/45.1$  ( $\tau = 5$ ), and  $-19.5/30.5$  ( $\tau = 20$ ).  $Y \equiv y/h$ .

$\tau \equiv tv_0^{\text{eo}}/L_s$  indicates approximately the number of (initial) sample zone lengths that the variable conductivity zone has translated. In the sample zone, the electroosmotic slip velocity is less than 80% of that in the running buffer, so a strong pressure-driven flow is induced to satisfy continuity (cf. [8]). Thus, relative to the mean flow, the fluid circulates in the sample zone at high velocities. The flow is much weaker in the running buffer because it comprises 98% of the channel length, and therefore the electroosmotic slip velocity is close to the mean flow rate (see Eq. (3.17)). The fluid velocity variations in the sample zone boundaries disperse the buffer ions, as well as the analytes, causing the high conductivity (and low electric field) zone to spread. The buffer concentration and electric fields evolve, and the electroosmotic slip velocity changes—nevertheless the basic eddy pattern persists. As the sample zone disperses, the velocity gradients diminish in the zone boundary, as evident in Fig. 3.3, which shows streamlines and normalized fluid speed  $|\hat{\mathbf{v}}| \equiv |\mathbf{v}'|/v_0^{\text{eo}}$  in the upstream transition region. Since the fluid motion spreads the sample zone, this (unsteady) dispersion mechanism decays with time, but will completely vanish only when there are no axial conductivity gradients.

Figure 3.4 shows the time evolution of the conductivity field. Although the initial conductivity field is cross-sectionally uniform, unsteady, 2-D conductivity variations are produced by the fluid motion. In the aft (or upstream) zone boundary, the positive  $v'_x$  at the channel center (Fig. 3.2) brings low  $\sigma$  buffer forward (or downstream), while the negative  $v'_x$  at the walls carries high  $\sigma$  fluid upstream. Transverse conductivity gradients generated by this convective transport process are limited by transverse

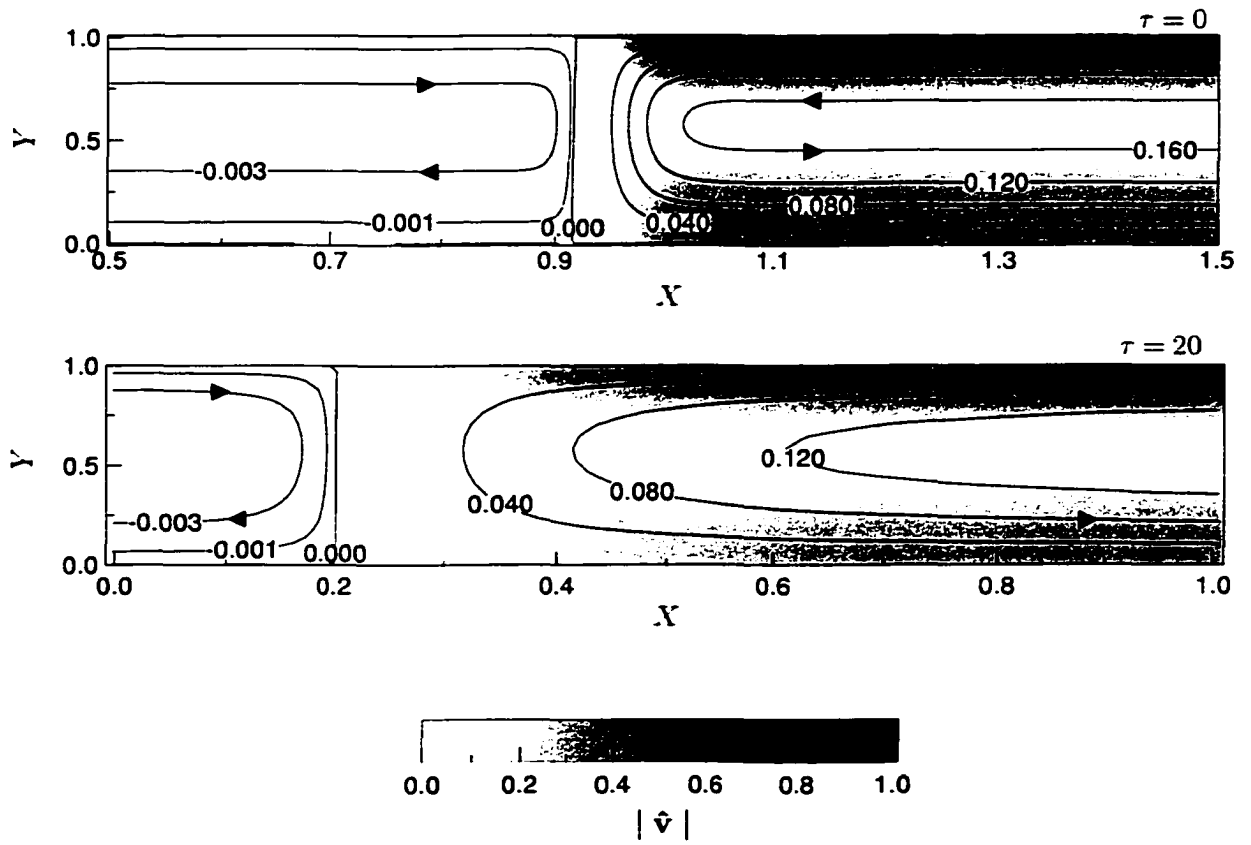


FIGURE 3.3. Streamlines and  $|\hat{v}|$  in upstream zone boundary at  $\tau = 0$  and 20. Values of  $\Psi$  are given for each countour. Simulation conditions are as for Fig. 3.2.

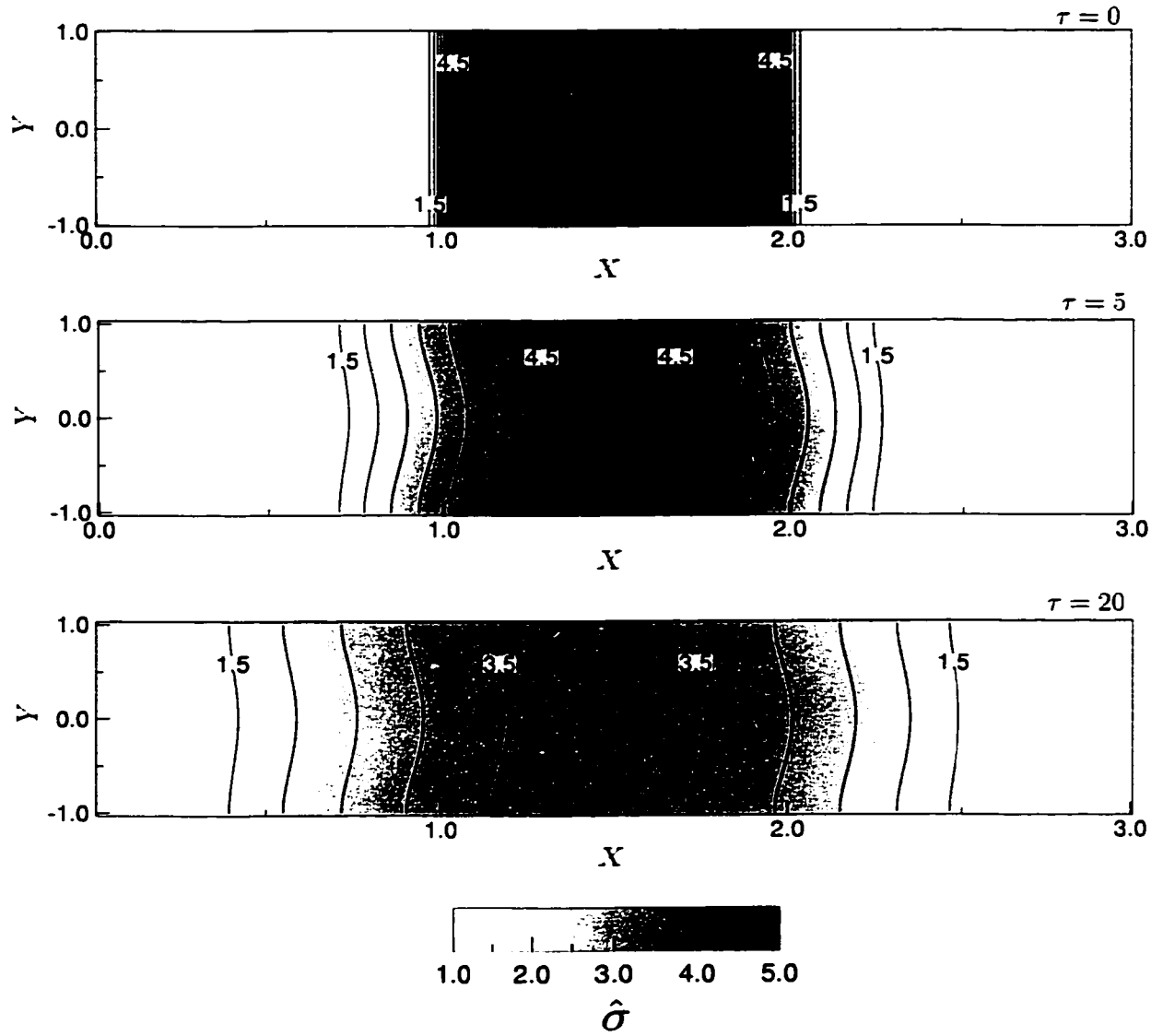


FIGURE 3.4. Conductivity field at  $\tau = 0, 5$ , and 20. Contours of constant  $\hat{\sigma} \equiv \sigma/\sigma_0$  from 1.5 to 4.5 at intervals of 0.5 are shown. Simulation conditions are as for Fig. 3.2.

diffusion, leading to the characteristic shape of the conductivity contours seen in Fig. 3.4. Since  $|\mathbf{v}'|$  increases with  $\sigma$ , higher velocities toward the center of the sample zone generate greater transverse  $\sigma$  variations than in the lower  $\sigma$  regions. Also, after developing from naught, the transverse conductivity variations eventually decrease as the fluid circulation weakens. Coupled to the weakening flow is also a decrease in the maximum conductivity, clearly seen by the lighter shade of the high  $\sigma$  zone at  $\tau = 20$ . The peak  $\sigma$  decreases by 26% from  $\tau = 0$  to 20.

Despite modest transverse conductivity variations at  $\tau = 5$ , the electric field, as shown in Fig. 3.5, is remarkably unidirectional (and remains so throughout the pump-

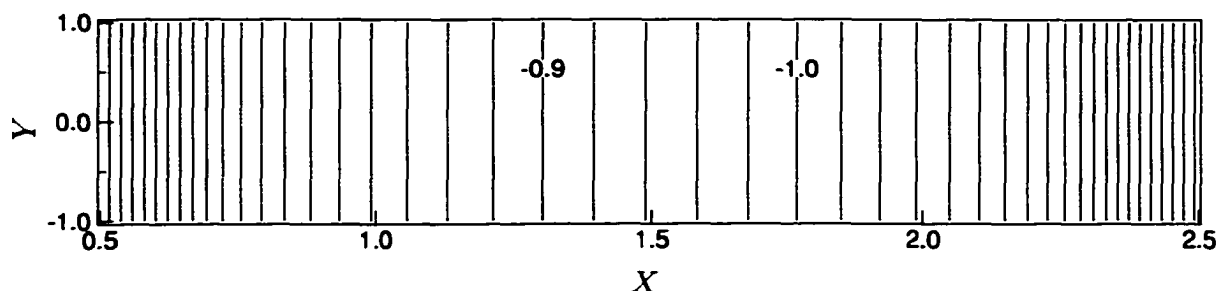


FIGURE 3.5. Contours of constant  $\Phi \equiv [\phi - \phi(x' = 0)]/(E_0 L_s)$  (from  $-1.4$  to  $-0.5$  at intervals of  $0.02$ ) at  $\tau = 5$ . Simulation conditions are as for Fig. 3.2.

ing process). The electric field is applied axially and is constrained to be essentially axial at the nonconducting channel walls and at the channel centerline; since conductivity changes between  $0$  and  $h$  are less than  $O(1)$ , the electric field is essentially unidirectional.  $\hat{E} \equiv |\mathbf{E}|/E_0$  is plotted in Fig. 3.6 at selected values of  $\tau$ . The width of the low field zone grows, and the field increases (35% at the center of the sample zone at  $\tau = 20$ ) with time. This degrades the effectiveness of the pumping

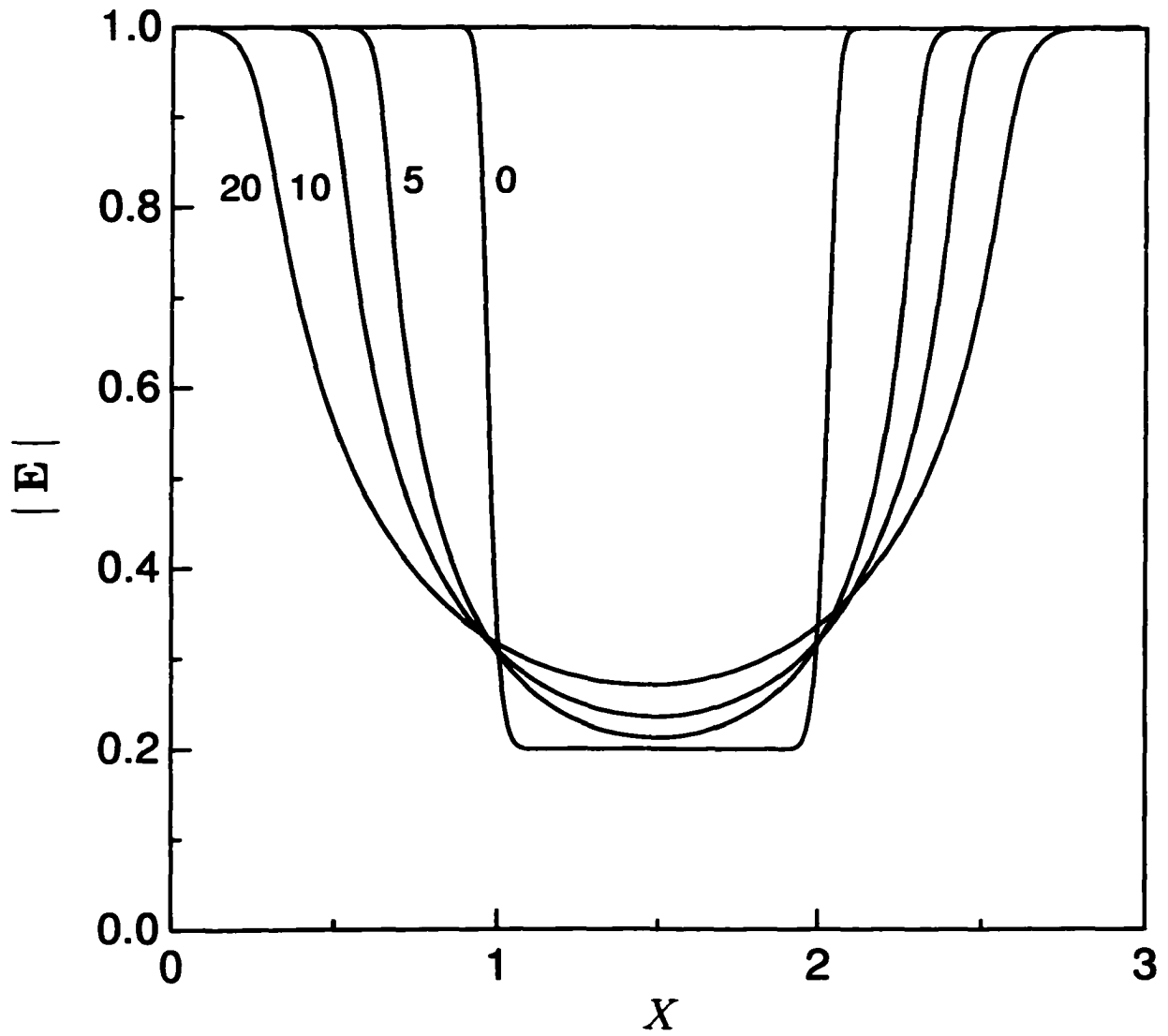


FIGURE 3.6. Electric field at selected values of  $\tau$ . Simulation conditions are as for Fig. 2.

process, which seeks to minimize the electric field in the sample zone in order to minimize analyte electromigration and separation. Two analytes in the same electric field separate at a rate  $\sim \Delta\bar{\mu}^e \mathbf{E}$ , where  $\Delta\bar{\mu}^e$  is the difference between the effective electrophoretic mobilities of the analytes. The separation rate of any two analytes has therefore increased about 35% by  $\tau = 20$ .

Figure 3.7 shows concentration fields at  $\tau = 2.2$ , of HIS, HEM, and FER. (ARG is not shown because results are similar to HIS.) A low concentration of HIS emerges from the initial sample zone; as the HIS migrates out of the sample zone, the concentration is reduced by the factor  $1/\gamma$  because the electromigrational velocity of HIS in the running buffer is a factor of  $1/\gamma$  greater than in the sample zone. Transverse concentration variations are not noticeable in the region that has migrated out of the sample zone because there the fluid velocity is everywhere close to the mean (Fig. 3.3). The HIS contours are similar to those of the conductivity because the amino acids and buffer constituents have comparable diffusivities (Table 3.1). The protein concentration fields, on the other hand, have an entirely different character. HEM and FER have more than an order of magnitude lower diffusivity and electrophoretic mobility than HIS (Tables 3.1 and 3.2). The electrophoretic mobility of FER is too low to permit FER to escape the sample zone by  $\tau = 2.2$ . Because of the lower diffusivity, transverse diffusion is not sufficient to prevent significant distortion of the FER zone by the electrolyte motion. Sharp axial transitions in concentration are formed near the centerline and the wall at the forward and aft sample zone boundaries, respectively, because there  $v'_x$  decreases in the direction of motion. The opposite occurs

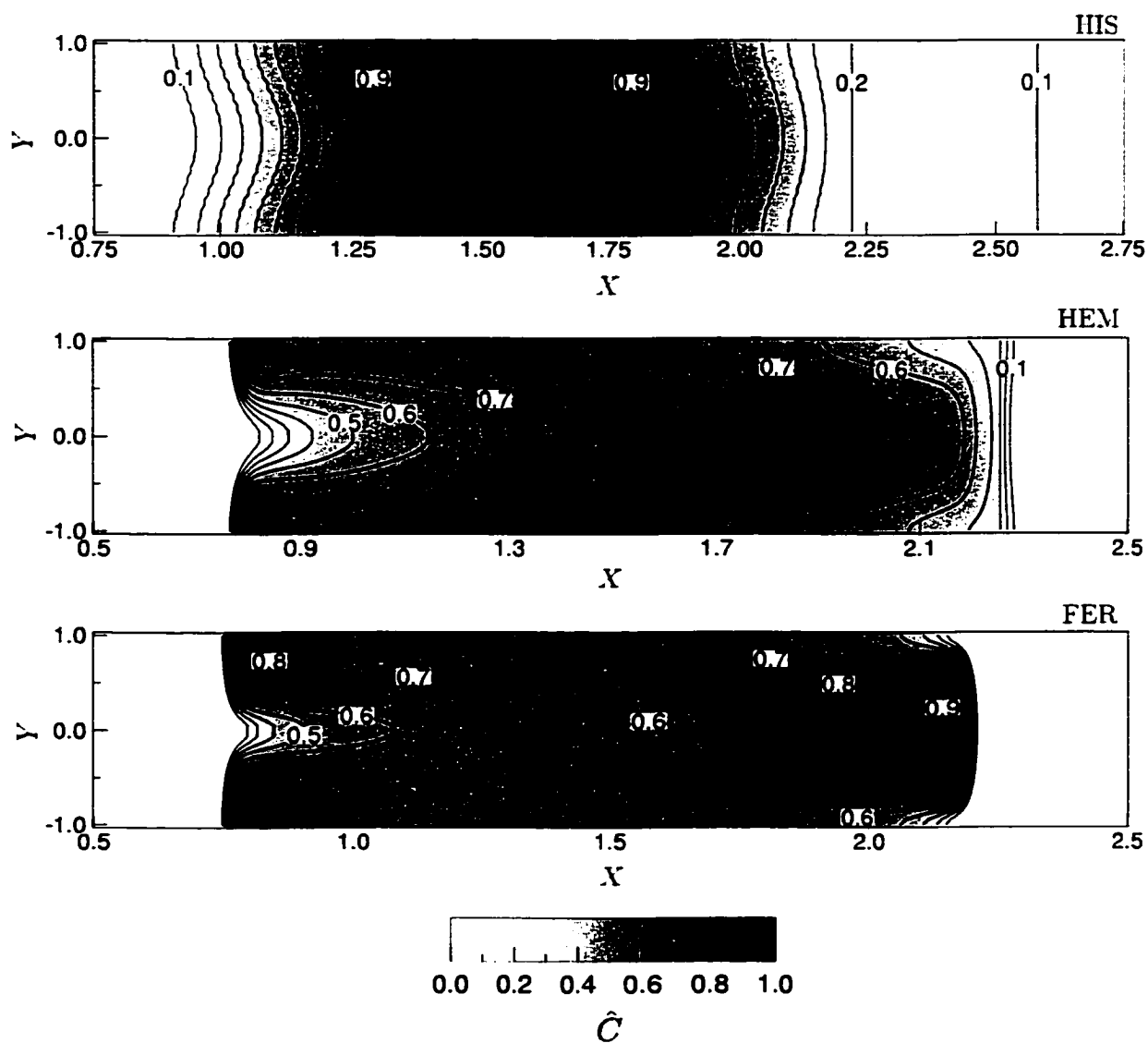


FIGURE 3.7. Analyte concentration fields at  $\tau = 2.2$ . Contours of constant  $\hat{C} \equiv C/C_s$  from 0.1 to 0.9 (HIS) and 0.1 to 0.7 (HEM and FER) at intervals of 0.1 are shown. Anode/cathode at  $X = -2.1/47.9$ . Simulation conditions are as for Fig. 3.2.

near the wall and centerline, respectively, of the forward and aft sample zone boundaries because there  $v'_x$  increases in the direction of motion. The HEM concentration field evolves similarly, but because it has a higher diffusivity than FER, concentration variations are less dramatic. Also,  $\bar{\mu}^e$  of HEM is high enough that it begins to leak out of the high  $\sigma$  zone, as evidenced by the contours on the downstream end of the sample zone; these contours bend slightly upstream at the center of the channel, following the weak flow in the running buffer.

The concentration fields of HIS, HEM, and FER at  $\tau = 5$  are shown in Fig. 3.8. Diffusion has smoothed out some of the FER variations seen in Fig. 3.7. Because axial  $\mathbf{v}'$  variations occur over a longer length scale at  $\tau = 5$  (Fig. 3.2), diffusion has time to erode some of the concentration variations that tend to form from the electrolyte motion. While all the analyte zones have spread, the peak concentrations of the proteins are approximately 30% lower than the peak HIS concentration, as the slower diffusing species disperse hydrodynamically throughout the variable conductivity zone.

The time evolution of the normalized cross-sectionally-averaged concentrations  $\langle \hat{C} \rangle \equiv (1/h) \int_0^h \hat{C}(x, y, t) \partial y$  of the amino acids (panel (a)) and the proteins (panel (b)) are shown in Fig. 3.9. The amino acids begin to escape the high  $\sigma$  zone by  $\tau = 2$ . Analyte molecules entrained in the high  $\sigma$  zone are dispersed by the persistent eddy pattern, which broadens with time (Fig. 3.2). By  $\tau = 20$ , essentially all of the ARG has migrated out of the sample zone, and a tail has formed from the dispersion of ARG in the high conductivity zone. FER, on the other hand, remains entirely in the sample zone;  $\bar{\mu}^e$  of FER is sufficiently low that the high  $\sigma$  zone spreads faster

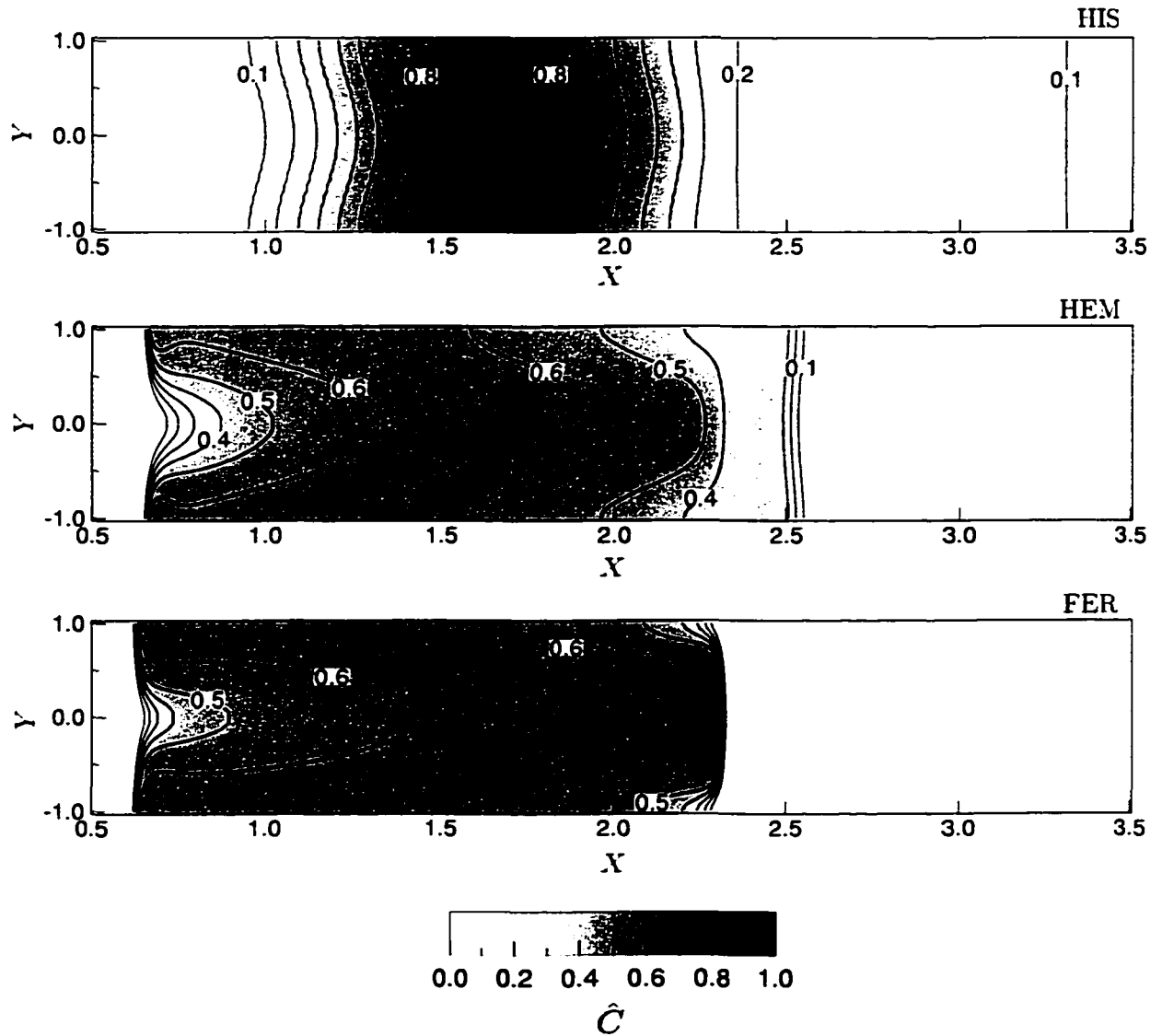


FIGURE 3.8. Analyte concentration fields at  $\tau = 5$ . Contours of constant  $\hat{C}$  from 0.1 to 0.8 (HIS) and 0.1 to 0.6 (HEM and FER) at intervals of 0.1 are shown. Simulation conditions are as for Fig. 3.2.

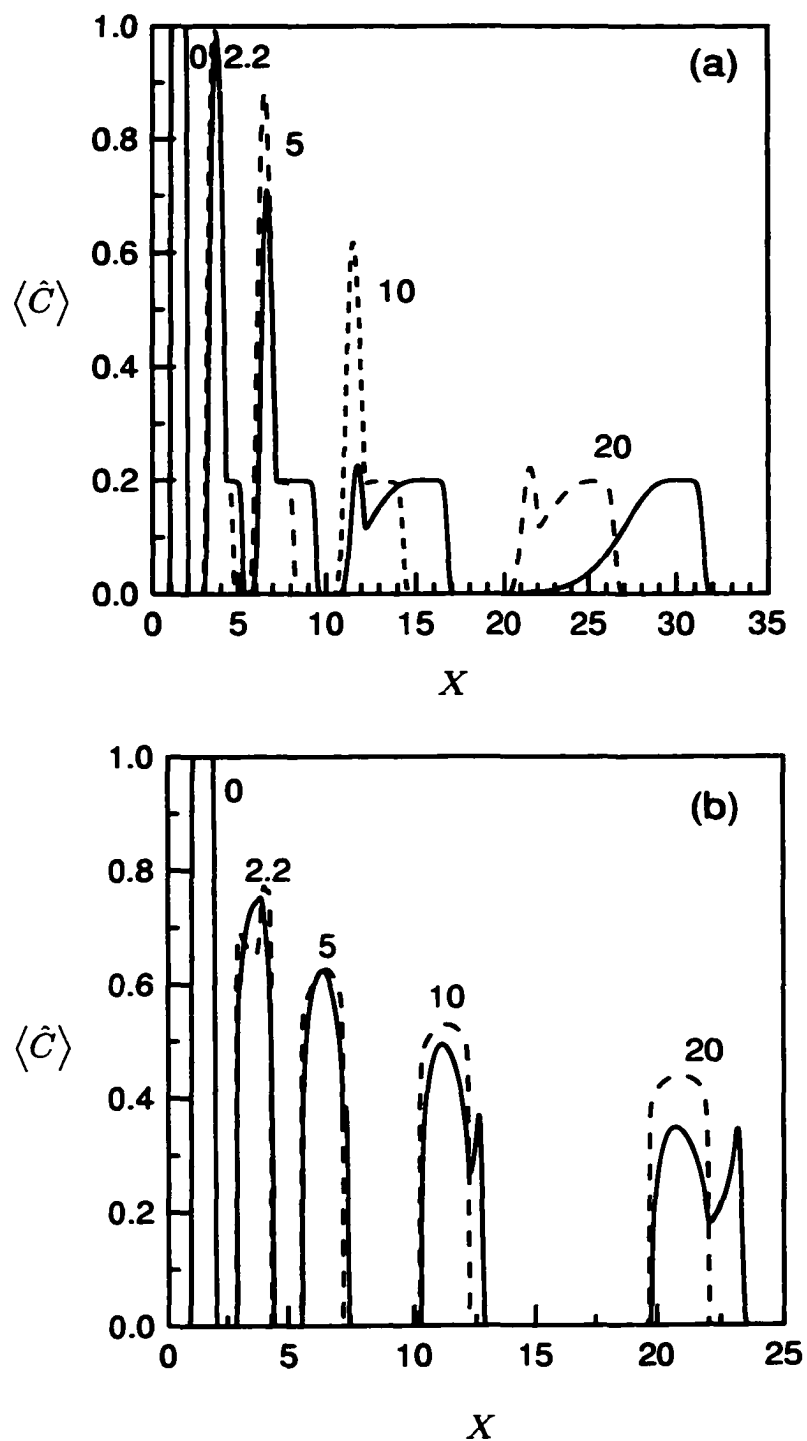


FIGURE 3.9. Cross-sectionally averaged analyte concentrations at selected values of  $\tau$ . (a) ARG (solid) and HIS (dashed), (b) HEM (solid) and FER (dashed). Dotted line is the initial condition for all analytes. Simulation conditions are as for Fig. 3.2.

than the FER electromigrates. HEM electromigrates out of the sample zone, but, owing to the 2-D structure of the HEM concentration field (Figs. 3.7 and 3.8), the (cross-sectionally-averaged) concentration of HEM leaking into the running buffer is not  $1/5$  the concentration in the sample zone.

To ensure effective electroosmotic pumping, analytes clearly must not escape the high conductivity (low field) sample zone. For most analytes that requires a low field zone that is longer than the sample plug. A more general pumping configuration is depicted in Fig. 3.10. Two operational variables that dramatically affect process

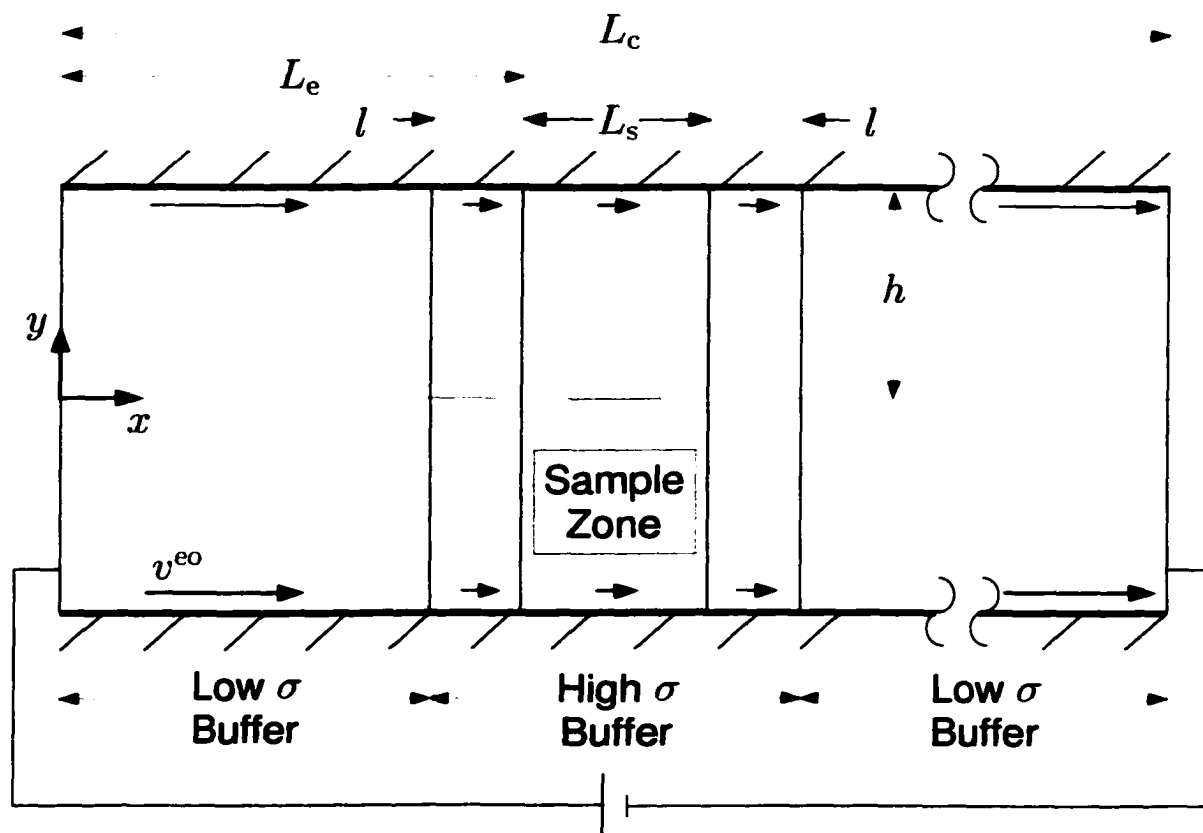


FIGURE 3.10. Sketch of more general electroosmotic pumping configuration. The high conductivity buffer zone is longer than the analyte zone.

performance, are  $\gamma$  and the initial length  $l$  between the analyte and low field zone boundaries. It is desirable to set  $1/\gamma$  as high as possible to prevent analyte separation and migration out of the low field zone. However,  $|\hat{v}|$ , and hence convective solutal dispersion, increases with  $1/\gamma$ . Increasing  $l$  prevents analyte from escaping the low field zone, but the length required varies with  $\gamma$ . A tradeoff, controlled by  $\gamma$  and  $l$ , therefore exists between inhibition of analyte migration and dispersion.

To evaluate this tradeoff for the amino acids, histidine and arginine zone variances and relative median positions are plotted versus  $1/\gamma$  in Figure 3.11, for  $l$  equal to 0 and  $L_s/2^*$ . Panel (a) shows the difference between the median positions of the histidine and arginine zones  $\Delta x_m$  normalized by the initial sample zone length  $L_s$ . At  $1/\gamma = 2$ , the electric field is not low enough to prevent complete separation of the analytes—even with  $l = L_s/2$ —after ten seconds of pumping. For  $l = 0$ , increasing  $1/\gamma$  to 5 reduces the median separation by a fourth, but further increase to 10 and 20 reduces it by another 80% and 90%, respectively. With  $l = L_s/2$ , separation is more effectively suppressed, particularly for  $\gamma = 5$  because  $l$  is long enough to contain most of the analyte in the low field zone.

Panel (b) shows the analyte variances  $S^2$  normalized by their initial variances  $S_0^2$ , after 10 seconds of pumping. Most of the variance functionality can be explained in terms of electromigration dispersion. For  $l = 0$ , both analyte variances increase dramatically as  $1/\gamma$  is increased to 5 because of increased electromigration dispersion

---

\*The results in Figures 3.11 and 3.12 were obtained using Model I of Thormann et al. [147] (rather than Model IIIa as described in §3.1) to calculate  $\mu^{eo}$ . This model does not account for the effects of  $I$  and  $[M^+]$ .

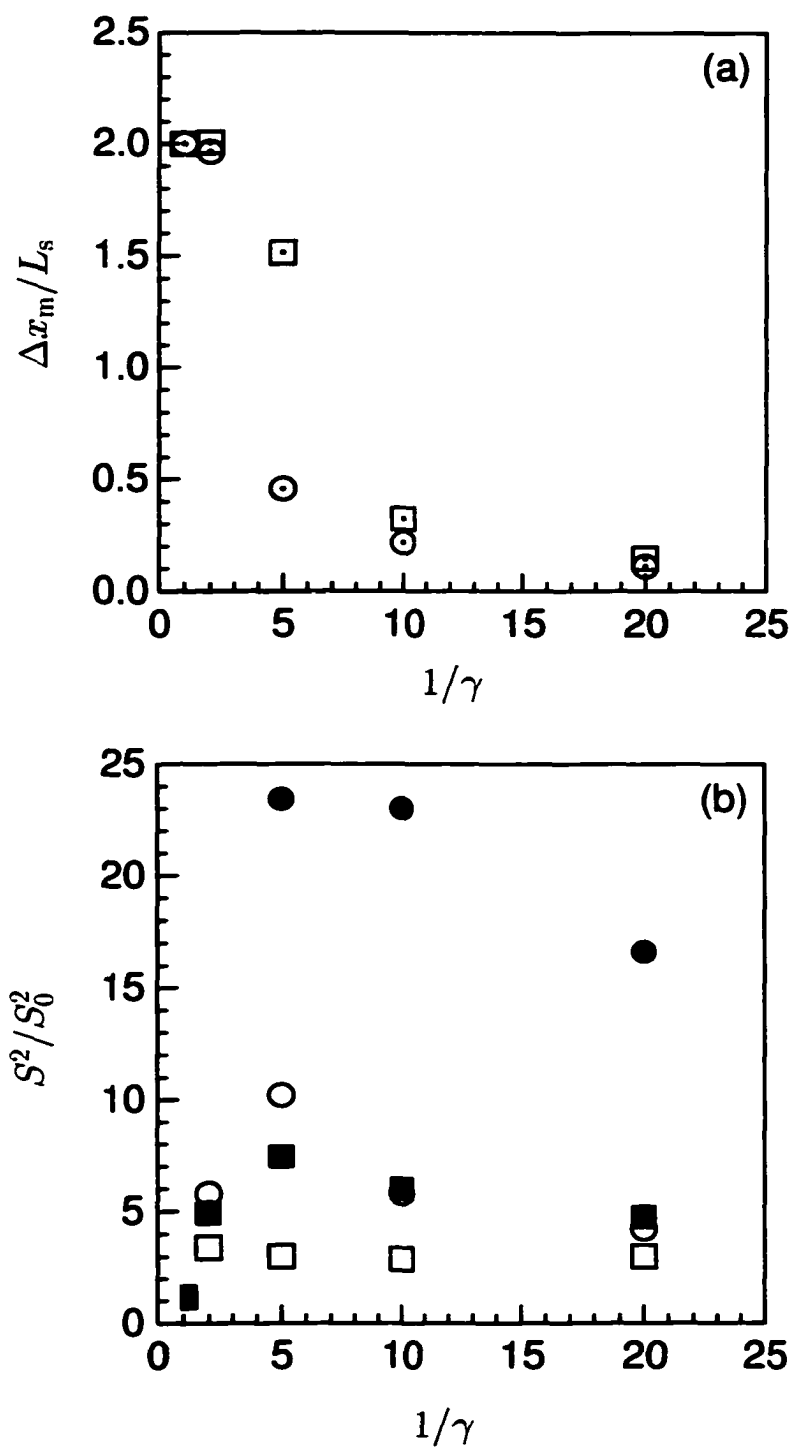


FIGURE 3.11. Peak (a) relative median position and (b) variance in electroosmotic pumping at  $\tau = 10.6$ .  $\square$ ,  $l = 0$ ;  $\odot$ ,  $l = L_s/2$ ;  $\blacksquare$ , histidine at  $l = 0$ ;  $\square$ , histidine at  $l = L_s/2$ ;  $\bullet$ , arginine at  $l = 0$ ;  $\circ$ , arginine at  $l = L_s/2$ . Simulation conditions are as for Fig. 3.2.

associated with analyte escaping the low field zone. As  $1/\gamma$  is increased above 5, the variances decrease because the electric field is reduced sufficiently to prevent as much analyte from escaping. This indicates that, if  $l = 0$ , no trade off exists between minimizing sample separation and dispersion, for  $1/\gamma$  up to 20; to prevent essentially complete separation,  $1/\gamma$  must be at least 5, and increasing  $1/\gamma$  above 5 reduces both analyte dispersion and separation. The results are similar for  $l = L_s/2$ , but the peak variances are reduced by as much as 74% relative to  $l = 0$ . Also, histidine dispersion peaks at  $1/\gamma = 2$ , but reaches a minimum at  $1/\gamma = 10$ .  $l$  is long enough at  $L_s/2$  to essentially eliminate any histidine leakage for  $1/\gamma \geq 10$ , so dispersion is controlled by convective transport, which increases with  $1/\gamma$ .

Figure 3.12 shows peak variances for  $1/\gamma = 10$  at three values of  $l$ . In addition to histidine and arginine, the amino acid glutamine is included among the analytes because it has a hydrodynamic mobility (or diffusivity) similar to histidine, but, like arginine, is fully dissociated at pH=6.2. When  $l$  is equal to  $L_s/2$ , the ordering of the analyte peak variances correlates with the ordering of effective electrophoretic mobilities because dispersion is dominated by electromigration effects. When  $l = 2L_s$ , the peak variances increase with decreasing analyte diffusivity, indicating that dispersion is controlled by convective dispersion; the high conductivity buffer zone is long enough to contain the analytes while they are transported a distance of 10 initial sample zones. Setting  $l = L_s$  is sufficient to eliminate most of the electromigrational dispersion, particularly for histidine and arginine. Enough glutamine escapes to disperse that analyte more than histidine.

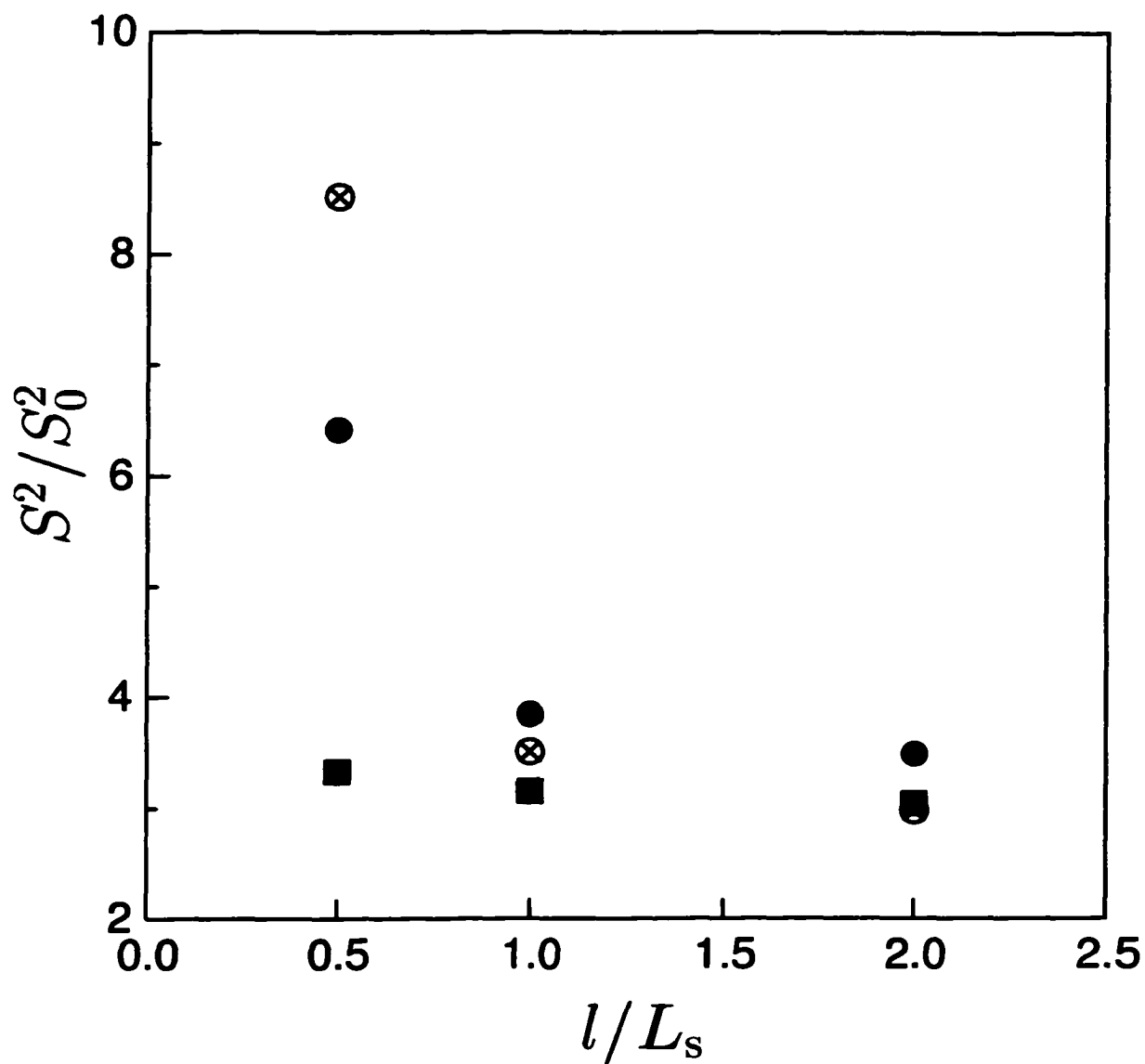


FIGURE 3.12. Peak variance at values of  $l$  for  $1/\gamma = 10$  and  $\tau = 10.6$ .  $\blacksquare$ , histidine;  $\bullet$ , arginine;  $\otimes$ , glutamic acid. Simulation conditions are as for Fig. 3.2.

### 3.3.2 ANALYTE STACKING

The buffer described above for electroosmotic pumping was also used to simulate FASS of the two amino acids (1  $\mu M$  HIS and ARG) and proteins (1  $\mu M$  HEM and FER). Stacking occurs in the configuration depicted in Fig. 3.1 when the buffer is diluted in the sample zone, i.e. for  $\gamma > 1$ . Under such conditions, the electric field is higher in the sample zone than in the running buffer, causing the analytes to accumulate into narrower zones as they migrate out of the diluted buffer. The stacking process was simulated for  $\gamma = 2$ , until both amino acids and HEM emerged from the diluted buffer zone. The diluted buffer zone is here defined as the region in which the conductivity is less than 99% of that of the running buffer, and the analytes were considered out of this zone when 99% of their mass was outside this region. All other simulation conditions were the same as those used for electroosmotic pumping.

Streamlines and  $|\hat{v}|$  in the upstream sample zone boundary are shown in Fig. 3.13. They are qualitatively similar to those obtained for electroosmotic pumping—the essential difference being the direction of fluid circulation. For  $\gamma > 1$ , the electric field is higher and the ionic strength is lower in the sample zone than in the running buffer. As such the slip velocity in the sample zone is greater than the mean flow, so  $v'_x$  is positive near the channel walls, rather than negative as was the case for  $\gamma < 1$ . At  $\tau = 3.68$ , when both amino acids have just escaped the low  $\sigma$  zone, the maximum  $|\hat{v}|$  ( $|\hat{v}|_{\max}$ ), has diminished by 12%; at  $\tau = 30.2$ , when HEM escapes, it is about half the initial value. The strength of the eddy pattern generated during stacking

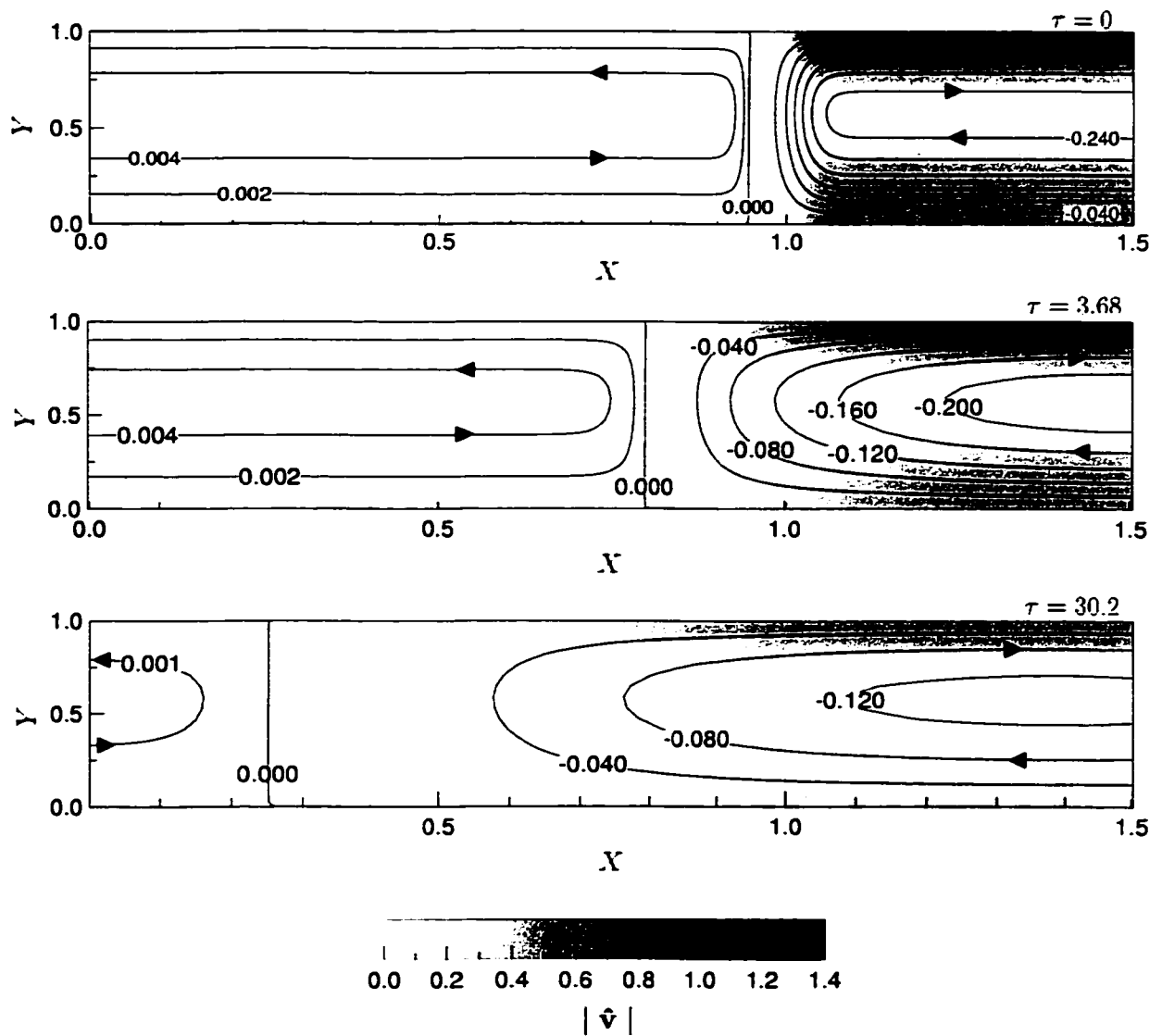


FIGURE 3.13. Streamlines and  $|\hat{\psi}|$  in upstream zone boundary for  $\gamma = 2$  at  $\tau = 0, 3.68,$  and  $30.2$ . Unlabeled streamlines in the top panel are shown for  $\Psi$  from  $-0.20$  to  $-0.08$  at intervals of  $0.04$ ; values of  $\Psi$  are given for all other contours. Anode/cathode at  $X = 0/50$  ( $\tau = 0$ ),  $-3.8/46.2$  ( $\tau = 3.68$ ), and  $-30.8/19.2$  ( $\tau = 30.2$ ). All other simulation conditions are as for Fig. 3.2.

( $\gamma = 2$ ) decays much faster than that produced by pumping ( $\gamma = 1/5$ ), as reflected by Fig. 3.14. This occurs for two reasons. First, as one can show,  $|\hat{v}|_{\max}$  is on

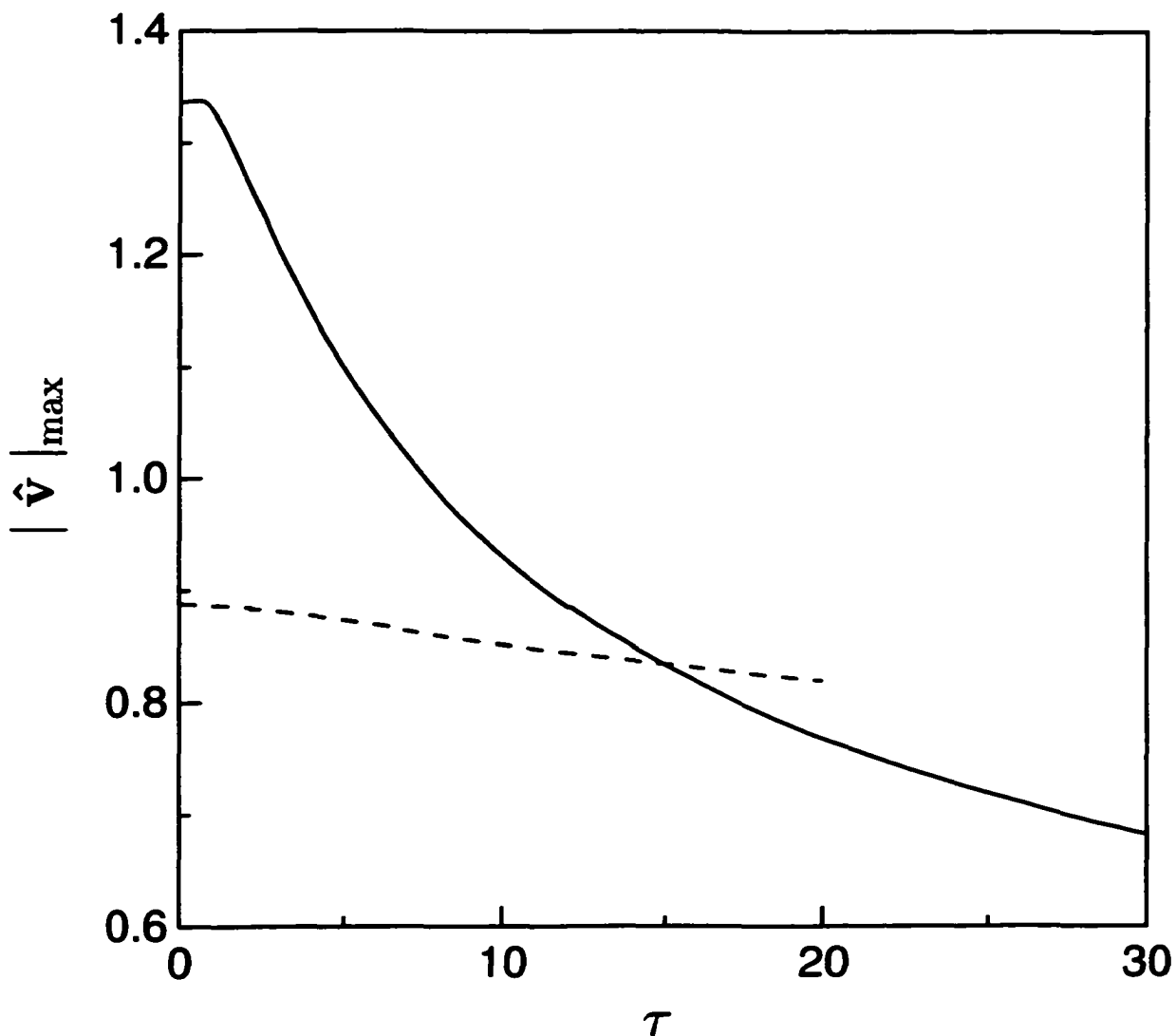


FIGURE 3.14. Maximum fluid speed for  $\gamma = 2$  (solid) and  $1/5$  (dashed). Simulation conditions are as for Fig. 3.2.

the order of  $|\hat{E} - 1|_{\max}$ , and at the outset,  $|\hat{E} - 1|_{\max}$  is  $|\gamma - 1|$ . Consequently the stacking eddy is initially stronger than the pumping eddy. Ionic solutes and the conductivity field are thus more vigorously dispersed, at least until  $\tau = 15$ . When

$\tau > 15$ ,  $|\hat{\mathbf{v}}|_{\max}$  is less for  $\gamma = 2$  than it is for  $\gamma = 1/5$ , but the strength of the eddy pattern continues to decay more rapidly for the stacking problem ( $\gamma = 2$ ). This results from a greater sensitivity of the electric field to changes in ion concentrations at low conductivities. Since  $|\hat{\mathbf{v}}|_{\max} \sim |\hat{E} - 1|_{\max}$ , then  $\delta |\hat{\mathbf{v}}|_{\max} \sim \delta |\hat{E} - 1|_{\max}$ , where  $\delta$  denotes a variation in the parameter. It follows that

$$\delta |\hat{\mathbf{v}}|_{\max} \sim \begin{cases} \delta \hat{E}_{\max}, & \gamma > 1 \\ -\delta \hat{E}_{\min}, & \gamma < 1. \end{cases} \quad (3.29)$$

Since  $\hat{E} \sim 1/\hat{\sigma}$ ,  $\delta \hat{E} \sim -(1/\hat{\sigma}^2)\delta\hat{\sigma}$ , and thus

$$\delta |\hat{\mathbf{v}}|_{\max} \sim \begin{cases} -\delta\hat{\sigma}_{\min}/\hat{\sigma}_{\min}^2, & \gamma > 1 \\ \delta\hat{\sigma}_{\max}/\hat{\sigma}_{\max}^2, & \gamma < 1. \end{cases} \quad (3.30)$$

The conductivity variations are controlled primarily by axial dispersion of the buffer ions in the sample zone, which is dominated by convective transport. Therefore, given similar fluid velocity fields,  $\delta |\hat{\mathbf{v}}|_{\max}$  will be greater for stacking, where  $\hat{\sigma}$  is low in the sample zone, than for pumping, where  $\hat{\sigma}$  is high in the sample zone.

Conductivity fields for the stacking process are presented in Fig. 3.15. Again the results are qualitatively similar to those obtained for  $\gamma = 1/5$ , but the conductivity here is low in the sample zone and the contours bend in the opposite direction because of the sense of the circulation. Also, the reduction in  $|\mathbf{v}'|$  between  $\tau = 3.68$  and  $\tau = 30.2$  is reflected in the reduction in curvature of the contours. Figure 3.16 shows the electric field at selected values of  $\tau$ . The peak  $\hat{E}$  is reduced by 7% and 24%, respectively, at  $\tau = 3.68$  and  $\tau = 30.2$ . Comparison of Figs. 3.16 and 3.6 clearly shows that the electric field changes faster during stacking than electroosmotic pumping, as expected from the scale arguments above.

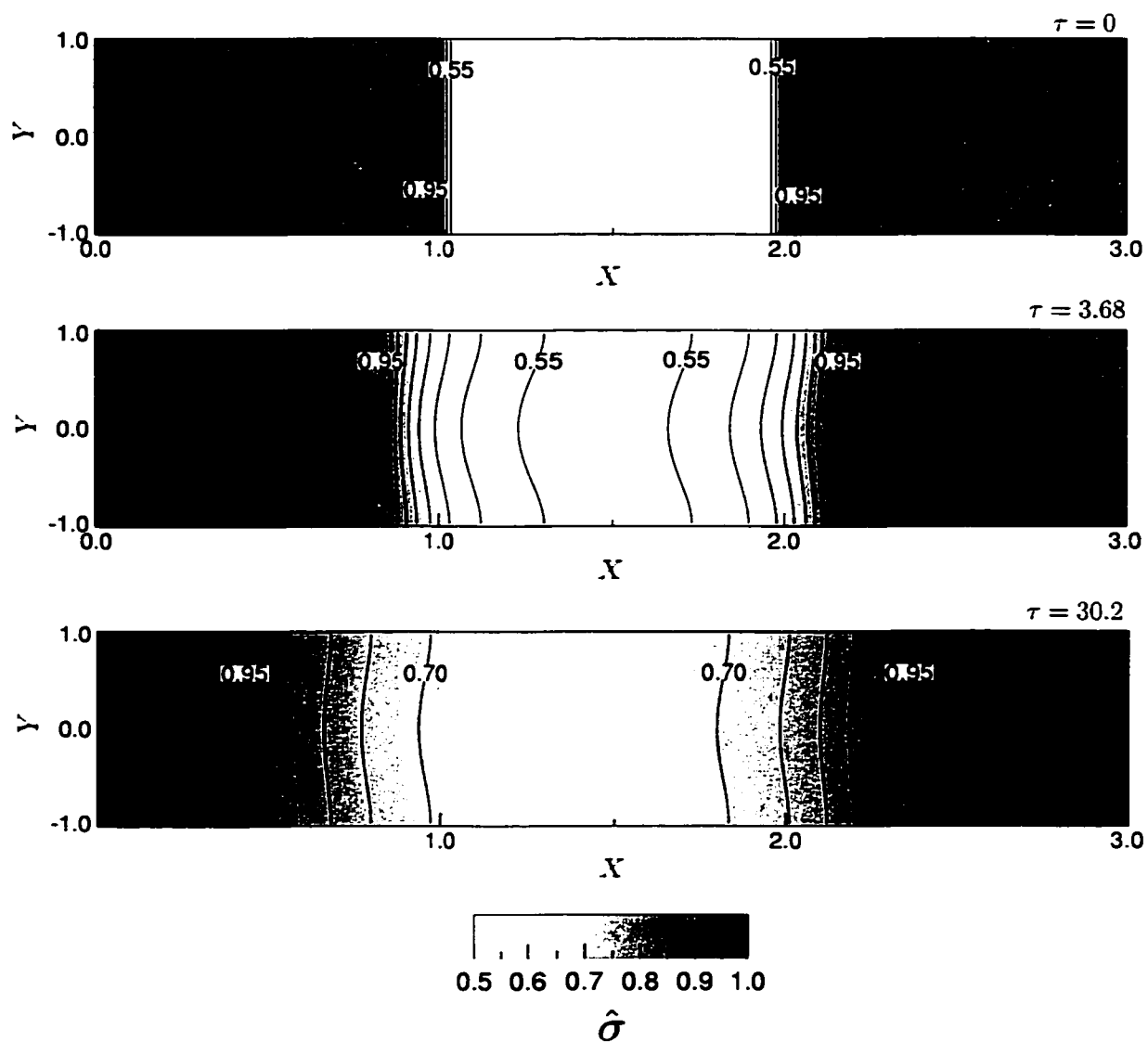


FIGURE 3.15. Conductivity field at  $\tau = 0, 3.68$ , and  $30.2$ . Contours of constant  $\hat{\sigma}$  from 0.55 to 0.95 at intervals of 0.05 are shown. Simulation conditions are as for Fig. 3.13.

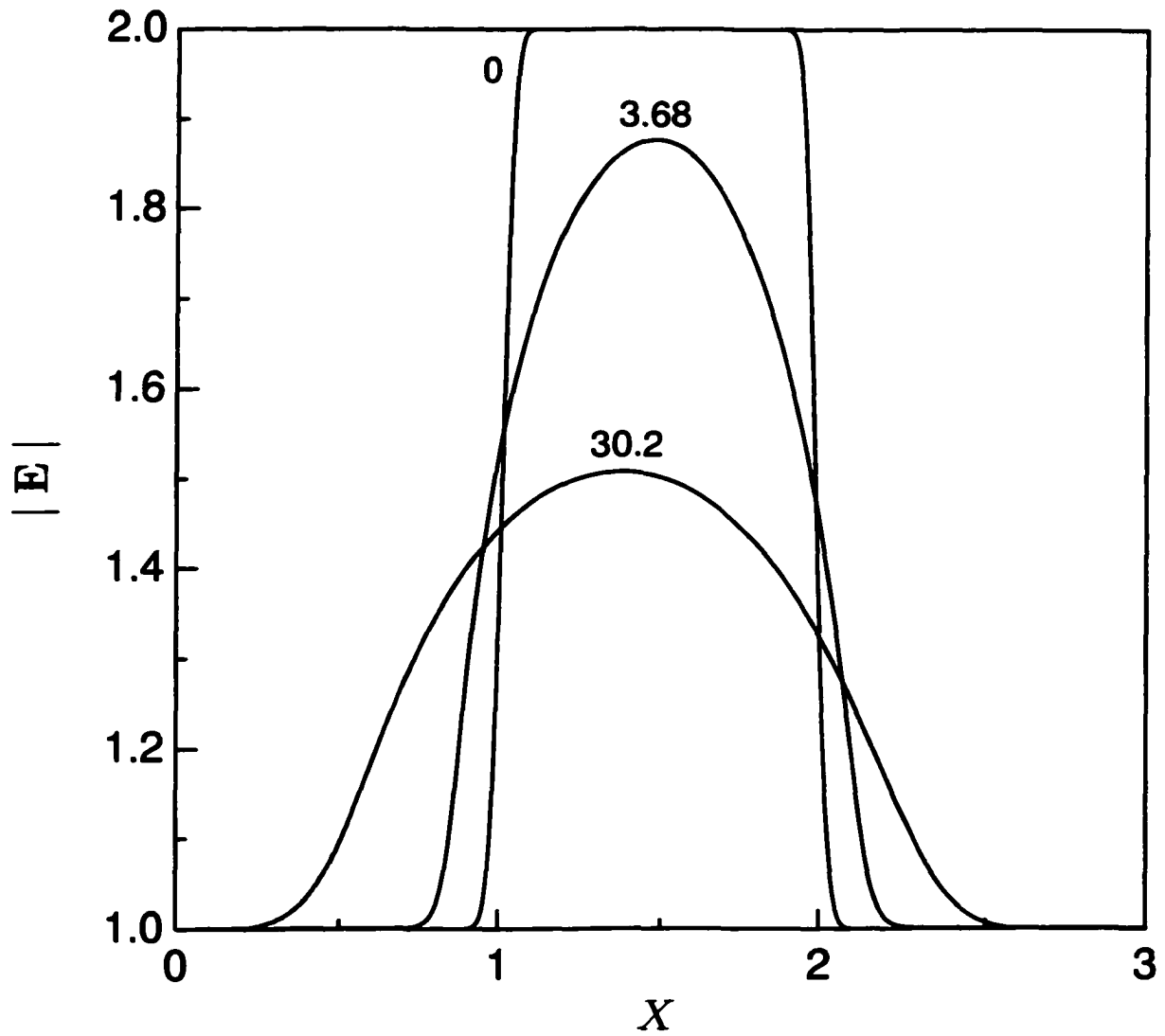


FIGURE 3.16. Electric field at selected values of  $\tau$ . Simulation conditions are as for Fig. 3.13.

Figure 3.17 shows the time evolution of  $\langle \hat{C} \rangle$  for the amino acids (panel (a)) and the proteins (panel (b)) during the stacking process. As the amino acids migrate electrophoretically out of the initial sample zone, they accumulate and emerge from the zone as distinct peaks, concentrated by approximately the factor  $\gamma$ . Although the ARG ions have a lower  $\mu^e$  than the HIS ions, ARG electromigrates faster because it is fully-ionized, whereas HIS is not; the buffer pH is near  $\text{pK}_1$  of HIS, so  $\bar{\mu}^e$  of HIS is about half  $\mu^e$ . Dispersion of the analyte zones during stacking prevents them from emerging as a plug, as assumed in the analysis of Burgi and Chien [36]. Also, because the upstream boundary of the analyte zones spend more time in the initial sample zone, the peaks are slightly skewed with a sharper transition downstream. This is evident in the HEM peak (panel (b)), which is characterized by a long tail after emerging from the low  $\sigma$  zone. Neither of the proteins stack to near the ideal  $\langle \hat{C} \rangle$  of 2. In fact, FER does not stack at all, and  $\langle \hat{C} \rangle_{\text{FER}}$  is everywhere reduced from the initial value. The electrophoretic mobility is insufficient to stack the analyte faster than it is dispersed by the fluid motion, and it remains trapped in the low  $\sigma$  zone. The electrolyte circulation has a greater impact on the protein stacking because (1) they have lower electrophoretic mobilities and therefore remain in the sample zone longer, and (2) they have lower diffusivities and are therefore dispersed more while in the sample zone.

Analyte stacking performance is enhanced by increasing  $\gamma$ , but dispersion limits the maximum level of preconcentration. The stacking limit can be anticipated with

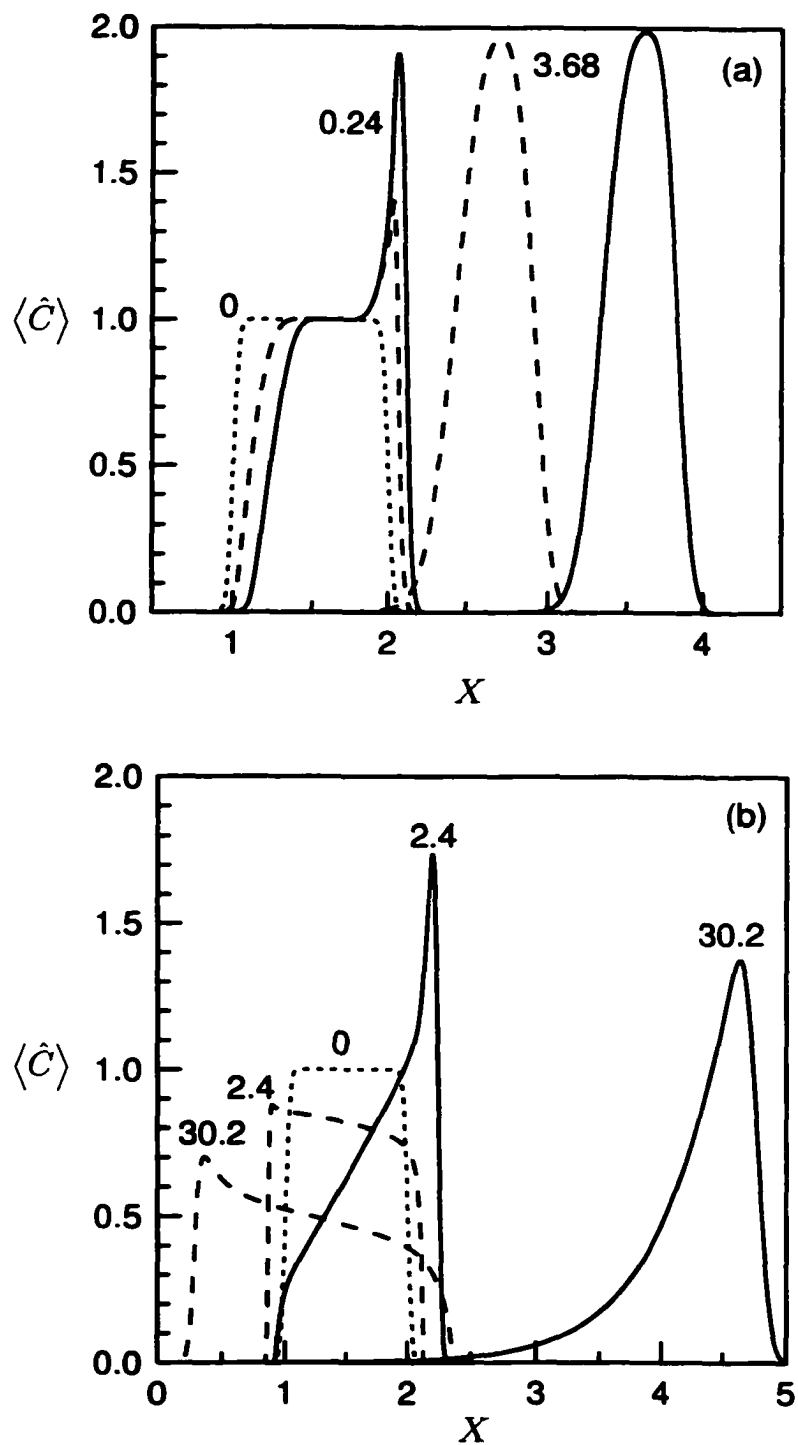


FIGURE 3.17. Cross-sectionally-averaged analyte concentrations at selected values of  $\tau$ . (a) ARG (solid) and HIS (dashed), (b) HEM (solid) and FER (dashed). Dotted line is the initial condition for all analytes. Simulation conditions are as for Fig. 3.13.

some simple scale arguments. The value of  $\gamma$  at which significant diminishing returns is expected to begin ( $\gamma_{\max}$ ), is estimated by balancing the relevant dispersion and electrophoretic time scales, viz. a transition from ideal stacking to  $\gamma$ -independent stacking is expected to occur when the time required for dispersion to affect the concentration of the center of the diluted buffer zone is equal to the time required for an analyte to migrate electrophoretically out of this zone. When these time scales match, both the analyte and injection zones are substantially dispersed during the time the trailing analyte zone boundary migrates through the the initial sample zone. The time required for an analyte to escape the initial sample zone is then protracted, both by the dispersion of the trailing boundary of the analyte zone, and by the forward migration of the leading boundary of the diluted buffer region. Also, since dispersion is increasing the conductivity of the diluted buffer zone during the extended stacking time, the electric field is decreasing in this zone, thus reducing the stacking factor during stacking.

The electromigration time scale for the analytes  $t_e$  is

$$t_e \sim \frac{L_s}{\alpha_a \omega_a e \gamma E_0}, \quad (3.31)$$

where  $\omega_a$  and  $\alpha_a$  are a characteristic hydrodynamic mobility and degree of ionization, respectively, of the analytes. The dispersion time scale for the high field zone  $t_D$  is

$$t_D \sim \frac{(L_s/2)^2}{2D_b^c} \sim \frac{25L_s^2 \omega_b k_B T}{4(\gamma \mu_0^{\text{eo}} E_0)^2 h^2}, \quad (3.32)$$

where  $D_b^c$  and  $\omega_b$  are a characteristic dispersion coefficient and hydrodynamic mobil-

ity, respectively, of the buffer ions. Setting  $t_e$  equal to  $t_D$  and rearranging yields

$$\gamma_{\max} \sim \frac{25ek_B T L_s \alpha_a \omega_a \omega_b}{4E_0 (h\mu_0^{\text{eo}})^2}. \quad (3.33)$$

For the conditions of this study,

$$\gamma_{\max} \sim \begin{cases} 4, & \text{histidine} \\ 6, & \text{arginine,} \end{cases} \quad (3.34)$$

which suggests that stacking of histidine and arginine in this configuration is limited to less than an order of magnitude increase in concentration.

Figure 3.18 shows histidine and arginine peak height and variance after stacking for  $\gamma$  up to 50<sup>†</sup>. The values provided in the figure are determined at the time each analyte emerges from the injection zone. In close agreement with the scale analysis, analyte stacking is limited to a factor of 3 and 5 (panel (b)), respectively, for histidine and arginine. Arginine is stacked slightly more effectively than histidine because it has a higher electrophoretic mobility, and thus escapes the low conductivity zone faster. The minimum peak variances (panel (a)) are more than an order of magnitude higher than those obtained in the absence of fluid motion or if the electroosmotic flow is approximated as plug flow (cf. [147]).

### 3.4 CONCLUDING REMARKS

Electrically-driven flows in channels filled with axially nonuniform electrolytes are inherently unsteady, and gradients in the field variables are dispersed by fluid eddies.

---

<sup>†</sup>Electrical stresses are neglected in these calculations so that converged solutions can be presented. Although electrical stresses alter the structure of the flow, at least transiently, in sharp conductivity transition regions, the effect on solute dispersion may be insignificant, as demonstrated in Chapter 4 for  $\gamma = 5$ .

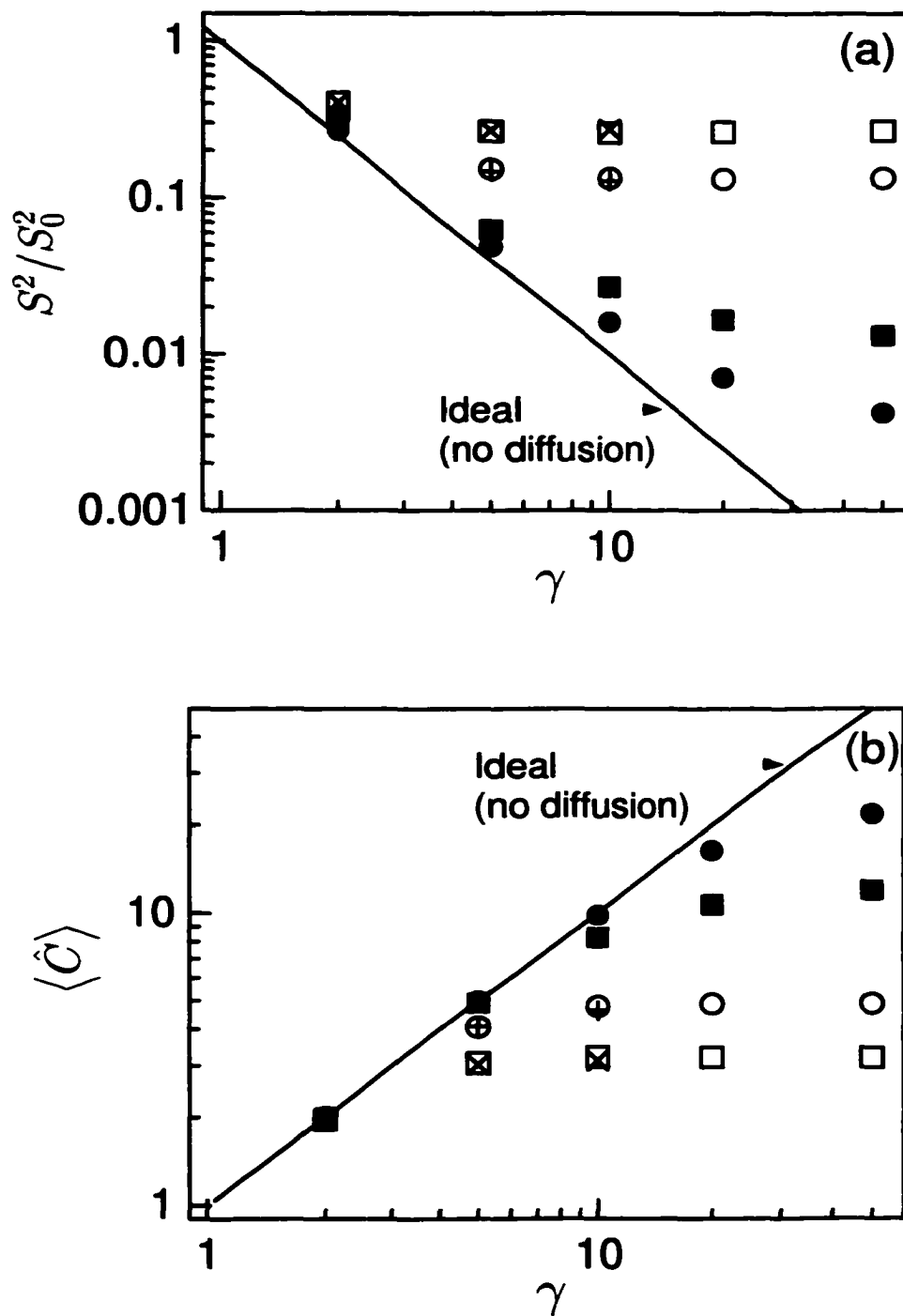


FIGURE 3.18. Peak (a) variance and (b) height in FASS after each analyte emerges from sample zone. ■, histidine in plug flow; ●, arginine in plug flow; ×, histidine in 2-D flow; +, arginine in 2-D flow; □, histidine in 2-D flow, calculated with macro-transport representation (see Chapter 6); arginine in 2-D flow, calculated with macro-transport representation.

In electroosmotic pumping, the tradeoff between analyte separation and dispersion, and the effect of the zone length scales, depends on the properties of the analytes and the distance they must be transported. When analytes are stacked from a low conductivity zone, the enhancement is partially offset by electroosmotic dispersion, even for  $\gamma = 2$ . At higher values of  $\gamma$ , dispersion during stacking increases and ultimately limits the level of sample preconcentration.

More generally, the dispersion of the nonuniform conductivity zone in this prototype problem implies that other separation and microfluidic systems with inherent axial conductivity gradients, such as ITP and IEF, will be affected by similar unsteady electrolyte circulation patterns. It is expected that ITP zone boundaries and IEF peaks will not be as sharp in the presence of electroosmosis. Finally, the essentially unidirectional electric field and modest transverse concentration gradients obtained for the prototype configuration, suggest that it may be possible to construct effective 1-D representations of the transport problem. We report on this in Chapters 4–6.

## CHAPTER 4

# LUBRICATION APPROXIMATIONS

Unsteady simulations of electrokinetic motion in multiple dimensions, using the method described in Chapter 3, are computationally intensive, and, in some cases, impractical. The simulations require (at least once) at every time step, a numerical solution to: (i) a set of nonlinear parabolic PDE's for the solutal component concentrations; (ii) a set of nonlinear algebraic equations for the individual ion concentrations; (iii) a second-order elliptic PDE for  $\phi$ ; and (iv) the Navier-Stokes or Stokes equations for  $\mathbf{v}$ . Most of the computational expense is devoted to tasks (ii)–(iv). Each of these three computations consumes roughly a third of the total simulation time. (Actual distribution among the three steps varies with simulation conditions and numerical methods.) For an important class of microanalysis processes, however, scaling arguments suggest that approximate, semianalytic solutions for  $\mathbf{v}$  and  $\mathbf{E}$  are possible, introducing the possibility of eliminating about 2/3 of the computational effort.

In this chapter, an approximate theory is developed for the electrohydrodynamic motion in the configuration depicted in Fig. 4.1. A rectangular, microfluidic-scale channel of width  $h$  and infinite extent perpendicular to the  $x$ - $y$  plane, contains an electrolyte with an axial  $\sigma$  transition of length  $b$ . For electroosmotic flow in straight channels, changes in  $\mathbf{v}$  and  $\mathbf{E}$  are driven by changes in  $\sigma$ , so  $b$  characterizes the length for axial variations in  $\mathbf{v}$  and  $\mathbf{E}$ . Solutal dispersion mechanisms dictate that

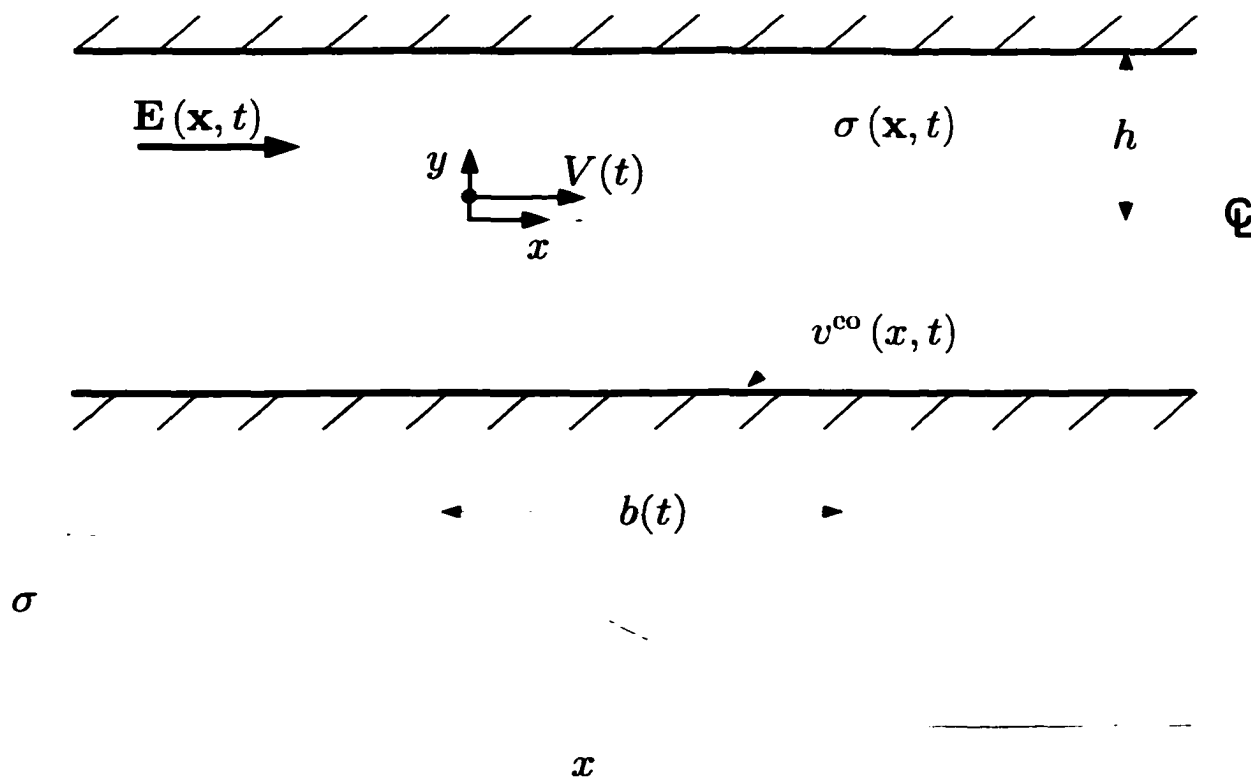


FIGURE 4.1. Definition sketch for approximate theory. A rectangular channel of infinite extent perpendicular to the  $x$ - $y$  plane, filled with a spatiotemporally-variable electrolyte, and subject to an applied electric field in the  $x$ -direction.  $\kappa h \gg 1$ ,  $(h/b)^2 \ll 1$ ,  $(h/b)^3 Pe \ll 1$ ,  $(h/b) Re \ll 1$ .

$b$  is, in many cases, large relative to  $h$ . Also, on microfluidic length scales,  $\mathbf{v}$  and  $\mathbf{E}$  are often quasi-steady, viz. the fluid motion and electric field adjust to changing ion distributions on time scales that are small relative to the time scales for ion transport. In such instances, if the Peclet number  $Pe$  is not too large (specifically if  $(h/b)^3 Pe \ll 1$ ), the classical lubrication approximation  $(h/b)^2 \ll 1$  simplifies the problem formulation, and explicit semianalytic expressions for  $\mathbf{v}$  and  $\mathbf{E}$  are obtained in terms of the ion distributions at any given time. The expressions are semianalytic because the balance laws governing the ion distributions are nonlinear and must be solved numerically.

As Long et al. [106] had done in the context of electroosmotic flow in the vicinity of a surface defect, a lubrication approximation is used to calculate  $\mathbf{v}$ . The theory presented here differs markedly from theirs, however, because the 2-D fluid motion stems from nonuniformities in the electrolyte rather than the surface properties. Consequently, electrical stresses acting within the fluid volume must be considered, and  $\mathbf{E}$  must be calculated not only to evaluate the electrical stresses but also the nonuniform electroosmotic slip velocity. Furthermore, in this configuration,  $\mathbf{v}$  and  $\mathbf{E}$  are coupled to the nonlinear ion transport, and therefore evolve in time.

After developing the approximations, they are evaluated by comparison to simulations of the prototype problem discussed in Chapter 3, and are shown to produce accurate representations of the fluid motion, ion transport, and electric field. In some cases, approximation error is introduced to a narrow region within a zone boundary during an initial transient. The error is highly localized, diminishes rapidly, and does

not significantly affect the solution at later times. For all configurations examined, the average fluid speed approximation error in the conductivity transition zones is less than 1% at all times, and 0.2% after two characteristic times for convection across the sample zone.

Although numerical simulation is still required to calculate the unsteady ion distributions, the approximate solutions for  $\mathbf{v}$  and  $\mathbf{E}$  essentially eliminate the computation time devoted to solving the charge balance and the Navier-Stokes equations, reducing total simulation times by 50% to 80%. The approximations also lay the foundation for additional approximations that will reduce simulation times even more, and possibly permit simulation of more complicated electrolyte systems such as IEF and ITP. For example, the approximations for  $\mathbf{v}$  and  $\mathbf{E}$  have inspired Taylor-Aris macrotransport approximations [33] for the solute conservation, that have led to an effective 1-D representation of the problem in terms of cross-sectionally averaged values. Effective 1-D simulations predict solutal migration and dispersion in orders of magnitude less simulation time, and can therefore be used to investigate a wide variety of processes and conditions. Also, a similar approximation to that developed in this chapter for  $\mathbf{v}$  and  $\mathbf{E}$ , may be possible for the pH, the calculation of which consumes most of the remaining simulation time. This would reduce 2-D simulation times by at least an order of magnitude over that required to solve the full problem, and would provide details of the fluid motion and ion transport in electrolyte systems that remain intractable.

The approximate theory presented in this chapter has significance beyond improving computational efficiency. The scaling of the balance laws and explicit expressions

obtained for  $\mathbf{v}$  and  $\mathbf{E}$  also provide important insights into the dominant physics of electrically-driven transport processes in microchannels. The analysis indicates that applied electric fields in straight microchannels are essentially unidirectional, even when the transverse component of the conductivity gradient meets or exceeds the axial component. The small transverse component of  $\mathbf{E}$ , though orders of magnitude smaller than the axial component, can nevertheless have a significant effect on the fluid motion. Moreover, at sufficiently high values of  $\mathbf{E}$ , the results demonstrate that the electrical stresses alter the structure of the flow in the zone boundary, producing more complicated flow patterns not hitherto demonstrated.

The presentation in this chapter begins with a scale analysis in §4.1. From the scaling arguments, approximate solutions for  $\mathbf{E}$  are developed in §4.2, and for  $\mathbf{v}$  in §4.3. In §4.4, the approximations are evaluated by comparing simulation results to those generated by numerical solutions to the full problem described in Chapter 3. The Chapter is then concluded in §4.5, with some remarks on the implications of the results.

## 4.1 SCALE ANALYSIS

An axial conductivity transition, or a zone boundary, in a microchannel or capillary is a basic element of most electrophoretic separation processes, e.g. ITP, IEF, and sample stacking [13, 113], as well as other microfluidic processes such as high ionic strength electroosmotic pumping [31]. In these protocols, multiple zones of differ-

ent composition and conductivity are partitioned along the separation axis. In this section, the system of PDE's (Eqs. (3.5),(3.7),(3.8), and (3.9)) describing electrically-driven transport processes are scaled for a general zone boundary of length  $b$  in a rectangular channel to provide order of magnitude estimates of the terms. Scaling arguments are first presented for the variables in the charge balance (Eq. (3.9)). This produces characteristic scales for  $E_x \equiv \mathbf{E} \cdot \mathbf{e}_x \equiv -\partial\phi/\partial x$  and  $E_y \equiv \mathbf{E} \cdot \mathbf{e}_y \equiv -\partial\phi/\partial y$ , which are required to scale the electrical stresses in the momentum balance (Eq. (3.7)). Then, the characteristic scales derived from the scaling of Eqs. (3.7), (3.8), and (3.9) are applied to scale the component mass balances (Eq. (3.5)).

#### 4.1.1 CHARGE BALANCE

Construction of approximate solutions for  $\mathbf{v}(\mathbf{x}, t)$  and  $\mathbf{E}(\mathbf{x}, t)$  begins with a scaling of the charge balance (Eq. (3.9)), which is written for the 2-D Cartesian coordinate system\* shown in Fig. 4.1 as

$$\frac{\partial}{\partial x} (\sigma E_x) + \frac{\partial}{\partial y} (\sigma E_y) = -\frac{\partial i_x^D}{\partial x} - \frac{\partial i_y^D}{\partial y}, \quad (4.1)$$

where  $i_x^D \equiv \mathbf{i}^D \cdot \mathbf{e}_x$  and  $i_y^D \equiv \mathbf{i}^D \cdot \mathbf{e}_y$ . Characteristic scales for some of the variables in this equation are not obvious from the geometry and initial conditions, but can be deduced through physical arguments and simplified expressions. Concentration, conductivity, and electric field changes in the axial direction occur over the length scale  $b$ . This

---

\*For the remainder of this dissertation, all variables will be calculated in the coordinate system moving at the velocity of the mean flow, and hence the “ $\prime$ ” superscripts used in Chapter 3 will be dropped from  $x$ ,  $v_x$ ,  $\mathbf{v}$ , and  $\psi$ .

characteristic length is initially dictated by the injection process, but changes as the zone boundaries evolve in time. Characteristic scales for the components of the diffusion current follow from their definition (Eq. (3.9)), viz.

$$\mathbf{i}^D \sim ek_B T \sum_{k=1}^M \omega_k \nabla (\bar{z}_k C_k). \quad (4.2)$$

So for components of  $O(1)$  valence,

$$i_x^D \sim ek_B T \Delta\omega_c \frac{\delta C_B}{\delta x}, \quad (4.3)$$

where  $C_B$  is a characteristic buffer concentration and  $\Delta\omega_c$  is a characteristic mobility difference of the buffer ions.  $\Delta\omega_c$  is  $O(\omega_c)$ , where  $\omega_c$  is a characteristic mobility, unless all buffer ions have mobilities that differ by less than  $O(\omega_c)$ . We will keep track of it as  $\Delta\omega_c$  to allow for this special case. By inspection of Eq. (3.10), we can relate  $C_B$  to  $\sigma$  by  $\sigma \sim e^2 \omega_c C_B$ , which yields

$$i_x^D \sim \frac{\Delta\omega_c}{\omega_c} \left( \frac{k_B T}{e} \right) \frac{|\gamma - 1| \sigma_0}{\gamma b} \quad (4.4)$$

for a characteristic conductivity change of  $\sigma_0 |\gamma - 1| / \gamma$  over the length scale  $b$ .

Similarly,

$$i_y^D \sim \frac{\Delta\omega_c}{\omega_c} \left( \frac{k_B T}{e} \right) \frac{\delta\sigma}{\delta y}. \quad (4.5)$$

The proper scaling for  $\delta\sigma/\delta y$  follows from the observation that concentration and conductivity changes in the transverse direction, even if initially zero, develop from the fluid motion (cf. Chapter 3). Let  $\sigma' \equiv \sigma - \langle\sigma\rangle$  and  $C'_k \equiv C_k - \langle C_k \rangle$ , where the angle brackets imply a cross-sectional-average, viz.

$$\langle\sigma\rangle \equiv \frac{1}{h} \int_0^h \sigma \partial y \quad \text{and} \quad \langle C_k \rangle \equiv \frac{1}{h} \int_0^h C_k \partial y. \quad (4.6)$$

The scale for  $\sigma'$  is estimated by arguing that axial convection, driven by the electroosmotic slip velocity, tends to generate transverse concentration gradients that are limited by transverse diffusion, once the components have had time to sample the cross-section (Taylor's approximation [144]). That is, for  $t \gg h^2/\omega_k k_B T$ ,

$$\omega_k k_B T \frac{\partial^2 C'_k}{\partial y^2} \sim v_x \frac{\partial C_k}{\partial x}, \quad k = 1, 2, \dots, M. \quad (4.7)$$

Now transverse concentration gradients are only produced when the slip velocity deviates from the mean axial velocity, so the fluid velocity in Eq. (4.7) is evaluated in a reference frame that moves with the mean velocity of the flow. For a zone boundary separating a region of conductivity  $\sigma_0$  from one of  $\sigma_0/\gamma$ ,

$$V \sim F \gamma v_0^{\text{eo}} + (1 - F) v_0^{\text{eo}}, \quad (4.8)$$

where  $F$  is the fraction of the channel initially occupied by the region of conductivity  $\sigma_0/\gamma$ . The characteristic value for  $v_x \sim \gamma v_0^{\text{eo}} - V$  is

$$v_x \sim |\gamma - 1| v_0^{\text{eo}}, \quad (4.9)$$

if  $F \ll 1$ . The appropriate axial and transverse length scales are  $b$  and  $h$ , respectively, and the scale factor for  $C_k$  is  $C_0 |\gamma - 1| / \gamma$ . To balance terms in Eq. (4.7), it must be that

$$C'_k \sim \left(\frac{h}{b}\right) Pe_k \frac{|\gamma - 1|}{\gamma} C_0, \quad k = 1, 2, \dots, M, \quad (4.10)$$

where

$$Pe_k \equiv \frac{|\gamma - 1| v_0^{\text{eo}} h}{\omega_k k_B T}. \quad (4.11)$$

Moreover

$$\sigma' \sim \left(\frac{h}{b}\right) Pe \frac{|\gamma - 1|}{\gamma} \sigma_0, \quad (4.12)$$

where  $Pe = Pe_k$  for a characteristic buffer component. According to Eq. (4.5), the characteristic value for  $i_y^D$  is therefore

$$i_y^D \sim \left(\frac{\Delta\omega_c}{\omega_c}\right) \left(\frac{k_B T}{e}\right) \frac{|\gamma - 1| Pe \sigma_0}{\gamma b} \sim Pe i_x^D. \quad (4.13)$$

Because the electric field is applied axially,  $E_y$  is initially zero if the initial ion concentration fields are cross-sectionally uniform.  $E_y$  however is induced by the developing transverse conductivity gradients and the attendant transverse diffusion current. Thus  $\sigma E_y \sim i_y^D$ , or

$$E_y \sim \left(\frac{\Delta\omega_c}{\omega_c}\right) \left(\frac{k_B T}{e}\right) \frac{Pe}{b}. \quad (4.14)$$

With the characteristic scales derived above, the charge balance (Eq. 4.1) is cast in nondimensional form. If the scaled variables

$$X \equiv \frac{x}{b}, \quad Y \equiv \frac{y}{h} \quad (4.15)$$

$$\langle \varsigma \rangle \equiv \frac{\langle \sigma \rangle}{\frac{|\gamma - 1|}{\gamma} \sigma_0}, \quad \varsigma' \equiv \frac{\sigma'}{\left(\frac{h}{b}\right) Pe \frac{|\gamma - 1|}{\gamma} \sigma_0}, \quad (4.16)$$

$$E_a \equiv \frac{E_x}{|\gamma - 1| E_0}, \quad E_t \equiv \frac{E_y b}{\left(\frac{\Delta\omega_c}{\omega_c}\right) \left(\frac{k_B T}{e}\right) Pe}, \quad (4.17)$$

$$i^D \equiv \frac{i_x^D b}{\left(\frac{\Delta\omega_c}{\omega_c}\right) \left(\frac{k_B T}{e}\right) \frac{|\gamma - 1|}{\gamma} \sigma_0}, \quad j^D \equiv \frac{i_y^D b}{\left(\frac{\Delta\omega_c}{\omega_c}\right) \left(\frac{k_B T}{e}\right) \frac{|\gamma - 1|}{\gamma} \sigma_0 Pe} \quad (4.18)$$

are introduced, then after substituting  $\langle\sigma\rangle + \sigma'$  for  $\sigma$  in Eq. (4.1), it reads

$$\begin{aligned} \frac{\partial}{\partial X} \left[ \langle\varsigma\rangle E_a + \left(\frac{h}{b}\right) Pe\varsigma' E_a \right] + \Gamma \left[ \langle\varsigma\rangle \frac{\partial E_t}{\partial Y} + \left(\frac{h}{b}\right) Pe \frac{\partial}{\partial Y} (\varsigma' E_t) \right] \\ = -\Lambda \frac{\partial i^D}{\partial X} - \Gamma \frac{\partial j^D}{\partial Y}. \end{aligned} \quad (4.19)$$

In Eq. (4.1),

$$\Gamma \equiv \left( \frac{\Delta\omega_c}{\omega_c} \right) \left( \frac{\mu_0^{\text{eo}}}{\omega_c e} \right) \quad (4.20)$$

and

$$\Lambda \equiv \left( \frac{\Delta\omega_c}{\omega_c} \right) \left( \frac{(k_B T/e)}{|\gamma - 1| E_0 b} \right) \quad (4.21)$$

are nondimensional groups that include the normalized characteristic hydrodynamic mobility variation of the buffer ions  $\Delta\omega_c/\omega_c$ , the ratio of the electroosmotic to a characteristic electrophoretic mobility in the running buffer  $\mu_0^{\text{eo}}/\omega_c e$ , and  $(k_B T/e) / |\gamma - 1| E_0 b$ , the ratio of the Boltzmann potential to the characteristic potential difference across the length scale  $b$ .

#### 4.1.2 NAVIER-STOKES EQUATIONS

If Eq. (3.8) is written for the coordinate system shown in Fig. 4.1 and scaled, it reads

$$\frac{\partial u}{\partial X} + \frac{\partial v}{\partial Y} = 0, \quad (4.22)$$

where

$$u \equiv \frac{v_x}{|\gamma - 1| v_0^{\text{eo}}}, \quad v \equiv \frac{v_y b}{|\gamma - 1| v_0^{\text{eo}} h}. \quad (4.23)$$

The scale for  $v_y$  is chosen to satisfy continuity for a 2-D flow. Eq. (3.7) is written for the coordinate system of Fig. 4.1 and scaled by eliminating  $v_y$ ,  $v_x$ ,  $E_x$ ,  $E_y$ ,  $x$ , and  $y$  in favor of  $u$ ,  $v$ ,  $E_a$ ,  $E_t$ ,  $X$ , and  $Y$ , and introducing the scaled variables

$$\tau \equiv \frac{t |\gamma - 1| v_0^{\text{eo}}}{b}, \quad P \equiv \frac{ph^2}{\mu |\gamma - 1| v_0^{\text{eo}} b}, \quad U \equiv \frac{V}{v_0^{\text{eo}}}, \quad (4.24)$$

to yield

$$\begin{aligned} \left(\frac{h}{b}\right) Re \left[ \frac{\partial u}{\partial \tau} + \frac{1}{|\gamma - 1|} \frac{\partial U}{\partial \tau} + u \frac{\partial u}{\partial X} + v \frac{\partial u}{\partial Y} \right] &= -\frac{\partial P}{\partial X} + \left(\frac{h}{b}\right)^2 \frac{\partial^2 u}{\partial X^2} \\ &+ \frac{\partial^2 u}{\partial Y^2} + \left(\frac{h}{b}\right) \lambda E_a \left[ \frac{\partial E_a}{\partial X} + \Gamma \frac{\partial E_t}{\partial Y} \right] \end{aligned} \quad (4.25)$$

and

$$\begin{aligned} Re \left(\frac{h}{b}\right)^3 \left[ \frac{\partial v}{\partial \tau} + u \frac{\partial v}{\partial X} + v \frac{\partial v}{\partial Y} \right] &= -\frac{\partial P}{\partial Y} + \left(\frac{h}{b}\right)^2 \left[ \left(\frac{h}{b}\right)^2 \frac{\partial^2 v}{\partial X^2} + \frac{\partial^2 v}{\partial Y^2} \right] \\ &+ \left(\frac{h}{b}\right)^3 \lambda \Gamma E_t \left[ \frac{\partial E_a}{\partial X} + \Gamma \frac{\partial E_t}{\partial Y} \right], \end{aligned} \quad (4.26)$$

where

$$\lambda \equiv \frac{\epsilon \epsilon_0 |\gamma - 1| E_0 h}{\mu \mu_0^{\text{eo}}} \quad (4.27)$$

is the ratio of the characteristic electrical stress to the characteristic viscous stress,

and

$$Re \equiv \frac{\rho |\gamma - 1| v_0^{\text{eo}} h}{\mu} \quad (4.28)$$

is the Reynolds number.

### 4.1.3 COMPONENT MASS BALANCES

If the scaled variables

$$\Theta_k \equiv \frac{C_k \gamma}{C_0 |\gamma - 1|}, \quad \Theta'_k \equiv \frac{C'_k \gamma}{(h/b) Pe_k |\gamma - 1| C_0}, \quad (4.29)$$

and

$$M_k^e \equiv \frac{\bar{\mu}_k^e}{\omega_c e} \quad (4.30)$$

are defined, then the scaled component mass balances (Eq. (3.5)) are written as

$$\begin{aligned} \frac{\partial \Theta_k}{\partial \tau} = & - \left( \frac{\omega_c e}{\mu_0^{e0}} \right) \frac{\partial (M_k^e E_a \Theta_k)}{\partial X} - \left( \frac{\Delta \omega_c}{\omega_c} \right) \frac{\partial (M_k^e E_t \Theta_k)}{\partial Y} - u \frac{\partial \Theta_k}{\partial X} - \left( \frac{h}{b} \right) Pe_k v \frac{\partial \Theta'_k}{\partial Y} \\ & + \left( \frac{h}{b} \right) \frac{1}{Pe_k} \frac{\partial^2 \Theta_k}{\partial X^2} + \frac{\partial^2 \Theta'_k}{\partial Y^2}, \quad k = 1, 2, \dots, M. \end{aligned} \quad (4.31)$$

## 4.2 APPROXIMATION FOR $\mathbf{E}(\mathbf{x}, t)$

Unless  $\Gamma \ll 1$ , i.e.  $\Delta \omega_c / \omega_c \ll \omega_c e / \mu_0^{e0}$ , a condition that is not generally satisfied, the scaling in Eq. (4.19) does not immediately suggest an approximate solution for  $\mathbf{E}(\mathbf{x}, t)$ .

However, the scaling will show that for most microanalysis applications in straight microchannels and capillaries,  $E_x \approx \langle E_x \rangle$ , which leads to approximate solutions for  $E_x$  and  $E_y$ . Since  $\mathbf{E}$  is conservative,

$$\frac{\partial E_x}{\partial y} = \frac{\partial E_y}{\partial x}. \quad (4.32)$$

$E_x$  has been scaled on  $|\gamma - 1| E_0$ , which characterizes the change in  $E_x$  over the axial length scale  $b$ . But transverse variations in  $E_x$  are small relative to  $|\gamma - 1| E_0$ ,

so  $\partial E_a / \partial Y$  is not  $O(1)$ . As was done for the conductivity in §4.1, a new dependent variable  $E'_x \equiv E_x - \langle E_x \rangle$  is introduced that changes by  $O(E'_x)$  over the transverse length scale  $h$ . Eq. (4.32) then reads

$$\frac{\partial E'_x}{\partial y} = \frac{\partial E_y}{\partial x}. \quad (4.33)$$

A characteristic value for  $E'_x$  is derived by scaling Eq. (4.33) such that both terms are  $O(1)$  and hence the equality of the two terms is satisfied, viz.

$$\frac{\partial E'_a}{\partial Y} = \frac{\partial E_t}{\partial X} \quad (4.34)$$

requires  $E'_a \equiv E'_x / \left(\frac{h}{b}\right)^2 \Gamma \mid \gamma - 1 \mid E_0$ . Accordingly,

$$E_a = \langle E_a \rangle + \left(\frac{h}{b}\right)^2 \Gamma E'_a. \quad (4.35)$$

Since typically  $\Gamma \leq O(1)$ ,  $E_a \approx \langle E_a \rangle$  for  $\left(\frac{h}{b}\right)^2 \ll 1$ , which is the same requirement that leads to the lubrication approximation for  $\mathbf{v}(\mathbf{x}, t)$  in the Navier-Stokes equations.

#### 4.2.1 APPROXIMATION FOR $E_a$ ( $(h/b)^2 \Gamma \ll 1$ , $(h/b)^3 Pe \Gamma \ll 1$ )

By applying the Divergence Theorem to Eq. (4.19), it follows that

$$\left\langle \langle \varsigma \rangle E_a + \left(\frac{h}{b}\right) Pe \varsigma' E_a + \Lambda i^D \right\rangle = j_0, \quad (4.36)$$

where  $j_0 \equiv i_0 \gamma / [(\gamma - 1)^2 \sigma_0 E_0]$ . Combining Eqs. (4.35) and (4.36), leads to

$$\begin{aligned} \langle \langle \varsigma \rangle \langle E_a \rangle \rangle + \left\langle \left(\frac{h}{b}\right)^2 \Gamma \langle \varsigma \rangle E'_a \right\rangle + \left\langle \left(\frac{h}{b}\right) Pe \varsigma' \langle E_a \rangle \right\rangle + \\ \left\langle \left(\frac{h}{b}\right)^3 Pe \Gamma \varsigma' E'_a \right\rangle + \langle \Lambda i^D \rangle = j_0. \end{aligned} \quad (4.37)$$

Since  $\langle E'_a \rangle = \langle \zeta' \rangle = 0$ , Eq. (4.37) reduces to

$$\langle E_a \rangle = \frac{j_0 - \Lambda \langle i^D \rangle - \left(\frac{h}{b}\right)^3 Pe\Gamma \langle \zeta' E'_a \rangle}{\langle \zeta \rangle}, \quad (4.38)$$

after rearrangement. Upon substitution of Eq. (4.38) into Eq. (4.35) we have

$$E_a = \frac{j_0 - \Lambda \langle i^D \rangle - \left(\frac{h}{b}\right)^3 Pe\Gamma \langle \zeta' E'_a \rangle}{\langle \zeta \rangle} + \left(\frac{h}{b}\right)^2 \Gamma E'_a. \quad (4.39)$$

For  $\left(\frac{h}{b}\right)^2 \Gamma \ll 1$  and  $\left(\frac{h}{b}\right)^3 Pe\Gamma \ll 1$ , this yields a simple leading order solution  $E_a^{(0)}$  for  $E_a$ , viz.

$$E_a^{(0)} = \frac{j_0 - \Lambda \langle i^D \rangle}{\langle \zeta \rangle}, \quad (4.40)$$

which, if  $\langle i^D \rangle$  and  $\langle \zeta \rangle$  are replaced by  $i^D$  and  $\zeta$ , is equivalent to the explicit expression that is obtained for  $E_a$  when  $\partial i_y / \partial y$  is identically zero [113]. Also note that typically  $\Lambda \ll 1$ , but since it is a trivial matter to calculate the average diffusion current,  $\langle i^D \rangle$  is retained here.

#### 4.2.2 APPROXIMATION FOR $E_t$ ( $(h/b)^2 \Gamma \ll 1$ , $(h/b)^3 Pe\Gamma \ll 1$ )

Although  $\mathbf{E}$  is nearly unidirectional for  $\left(\frac{h}{b}\right)^2 \Gamma \ll 1$ , the “small”  $E_y$  often has an important effect on the ion transport and fluid motion. The scaled component mass balances (Eq. (4.31)) suggest that for  $\Delta\omega_c/\omega_c \sim O(1)$ , transverse electromigration cannot be neglected, and the scaled  $x$ -momentum equation (Eq. (4.25)) suggests that for  $\left(\frac{h}{b}\right) \lambda\Gamma \geq O(1)$ ,  $E_t$  is required to calculate the electrical stresses. Fortunately, the approximation  $E_a \approx E_a^{(0)} \approx \langle E_a \rangle$  permits an approximate solution for  $E_t$  also.

By rearranging Eq. (4.19) and substituting  $\langle \varsigma \rangle = \varsigma - \left(\frac{h}{b}\right) Pe\zeta'$ , the charge balance is written

$$\frac{\partial}{\partial Y} (\varsigma E_t + j^D) = -\frac{1}{\Gamma} \frac{\partial}{\partial X} (\varsigma E_a + \Lambda i^D). \quad (4.41)$$

Integrating Eq. (4.41) from zero to an arbitrary position  $Y$ , combining with Eqs. (4.39) and (4.40), and rearranging produces an explicit expression for  $E_t$ , viz.

$$E_t = -\frac{1}{\varsigma} \left\{ j^D + \frac{1}{\Gamma} \int_0^Y \frac{\partial}{\partial X} \left[ \varsigma E_a^{(0)} - \left(\frac{h}{b}\right)^3 Pe\Gamma\varsigma \frac{\langle \zeta' E_a' \rangle}{\langle \varsigma \rangle} + \left(\frac{h}{b}\right)^2 \Gamma\varsigma E_a' + \Lambda i^D \right] \partial \xi \right\}. \quad (4.42)$$

Thus, the requirements  $\left(\frac{h}{b}\right)^2 \Gamma \ll 1$  and  $\left(\frac{h}{b}\right)^3 Pe\Gamma \ll 1$  also permit a leading order solution  $E_t^{(0)}$  for  $E_t$ , viz.

$$E_t^{(0)} = -\frac{1}{\varsigma} \left\{ j^D + \frac{1}{\Gamma} \int_0^Y \frac{\partial}{\partial X} [\varsigma E_a^{(0)} + \Lambda i^D] \partial \xi \right\}. \quad (4.43)$$

If  $\Lambda \ll 1$ , this simplifies to

$$E_t^{(0)} = -\frac{1}{\varsigma} \left[ j^D + \frac{1}{\Gamma} \frac{\partial}{\partial X} \left( E_a^{(0)} \int_0^Y \zeta' \partial \xi \right) \right] \quad (\Lambda \ll 1). \quad (4.44)$$

Furthermore, if  $\Gamma \gg 1$ , then a much simpler expression for  $E_t^{(0)}$  results, viz.

$$E_t^{(0)} = -\frac{j^D}{\varsigma} \quad (\Lambda \ll 1, \Gamma \gg 1). \quad (4.45)$$

Finally, if  $\Delta\omega_c/\omega_c \ll 1$  and  $\left(\frac{h}{b}\right) \lambda\Gamma \ll 1$ , then  $E_t$  is small enough to be neglected in the species mass balances (Eq. (4.31)) and the Navier-Stokes equations (Eqs. (4.22)–(4.26)), and  $\mathbf{E}$  can be calculated as  $E_a^{(0)}(x, t)\mathbf{e}_x$ .

### 4.3 APPROXIMATION FOR $v(X, t)$

If  $\left(\frac{h}{b}\right) Re \ll 1$ , the classical lubrication approximation,  $\left(\frac{h}{b}\right)^2 \ll 1$ , leads to explicit expressions for  $u(X, Y, \tau)$  and  $v(X, Y, \tau)$ .

#### 4.3.1 APPROXIMATION FOR $u$ ( $(h/b)^2 \ll 1$ , $(h/b)Re \ll 1$ )

If  $\left(\frac{h}{b}\right)^2 \ll 1$  and  $\left(\frac{h}{b}\right) Re \ll 1$ , Eqs. (4.25) and (4.26) are to leading order

$$\frac{\partial^2 u^{(0)}}{\partial Y^2} = \frac{\partial P^{(0)}}{\partial X} - \left(\frac{h}{b}\right) \lambda E_a \left[ \frac{\partial E_a}{\partial X} + \Gamma \frac{\partial E_t}{\partial Y} \right] \quad (4.46)$$

and

$$\frac{\partial P^{(0)}}{\partial Y} = \left(\frac{h}{b}\right)^3 \lambda E_t \left[ \Gamma \frac{\partial E_a}{\partial X} + \Gamma^2 \frac{\partial E_t}{\partial Y} \right]. \quad (4.47)$$

Integrating Eq. (4.47) from 0 to an arbitrary position  $Y$  yields an expression for the pressure, viz.

$$P^{(0)} = \left(\frac{h}{b}\right)^3 \lambda \Gamma \left[ \int_0^Y E_t(X, Z, \tau) \frac{\partial E_a(X, Z, \tau)}{\partial X} \partial Z + \frac{1}{2} \Gamma E_t^2 - P_0(X, \tau) \right], \quad (4.48)$$

where  $P_0(X, \tau) \equiv P^{(0)}(X, 0, \tau)$  is an unknown parameter to be evaluated later. Substituting Eq. (4.48) into Eq. (4.46), integrating from 0 to  $Y$ , and then from 1 to  $Y$  yields, for  $(h/b)^2 \ll 1$ ,

$$u^{(0)} = u^{eo} - \frac{1}{2} \frac{\partial P_0(X, \tau)}{\partial X} [Y^2 - 1] + \left(\frac{h}{b}\right) \lambda \Gamma \int_1^Y \int_0^\zeta G(X, \xi, \tau) \partial \xi \partial \zeta, \quad (4.49)$$

where

$$u^{eo}(X, \tau) \equiv \frac{v^{eo} - V}{v_0^{eo} |\gamma - 1|}, \quad (4.50)$$

and

$$G(X, \xi, \tau) \equiv \frac{\partial}{\partial X} \left[ \frac{1}{2} \left( \frac{h}{b} \right)^2 \Gamma E_t^2(X, \xi, \tau) - \frac{1}{2\Gamma} E_a^2(X, \xi, \tau) \right] - E_a(X, \xi, \tau) \frac{\partial E_t(X, \xi, \tau)}{\partial \xi}. \quad (4.51)$$

$\partial P_0 / \partial X$  is evaluated by recognizing that  $\langle u \rangle = 0$ . Integrating Eq. (4.49) over  $Y$  from 0 to 1 and setting the LHS equal to zero gives

$$\frac{\partial P_0}{\partial X} = 3 \left\{ u^{e0} + \left( \frac{h}{b} \right) \lambda \Gamma \int_0^1 \int_1^Y \int_0^\zeta G(X, \xi, \tau) \partial \xi \partial \zeta \partial Y \right\}. \quad (4.52)$$

Upon substitution of Eq. (4.52) into Eq. (4.49), an explicit expression for  $u^{(0)}$  is obtained, viz.

$$u^{(0)} = u^{e0} + \frac{3}{2} \left\{ u^{e0} + \left( \frac{h}{b} \right) \lambda \Gamma \int_0^1 \int_1^Y \int_0^\zeta G(X, \xi, \tau) \partial \xi \partial \zeta \partial Y \right\} [Y^2 - 1] + \int_1^Y \int_0^\zeta G(X, \xi, \tau) \partial \xi \partial \zeta, \quad (4.53)$$

where  $u^{e0}$  and the integrand  $G$  depend on the electric field. To leading order, then, the axial velocity distribution can be calculated directly, if the electric field is known.

#### 4.3.2 APPROXIMATION FOR $v$ AND $\Psi$ ( $(h/b)^2 \ll 1$ , $(h/b)Re \ll 1$ )

The transverse velocity component follows from continuity, viz.

$$v = - \int_0^Y \frac{\partial u(X, \xi, \tau)}{\partial X} \partial \xi. \quad (4.54)$$

Substituting  $u^{(0)}$  from Eq. (4.49) for  $u$  in Eq. (4.54), and carrying out the integration yields a leading order expression for  $v$ , viz.

$$v^{(0)} = \frac{1}{2} \frac{\partial u^{\text{eo}}}{\partial X} (Y - Y^3) - \frac{1}{2} \left( \frac{h}{b} \right) \lambda \Gamma (Y^3 - 3Y) \int_0^1 \int_1^Y \int_0^\zeta \frac{\partial G}{\partial X}(X, \xi, \tau) \partial \xi \partial \zeta \partial Y - \left( \frac{h}{b} \right) \lambda \Gamma \int_1^Y \int_0^\zeta \frac{\partial G}{\partial X}(X, \xi, \tau) \partial \xi \partial \zeta. \quad (4.55)$$

The scaled stream function is calculated similarly as

$$\Psi \equiv \psi / v_0^{\text{eo}} | \gamma - 1 | h = \int_0^Y u(X, \xi, \tau) \partial \xi. \quad (4.56)$$

To leading order

$$\Psi^{(0)} = \frac{1}{2} \left\{ u^{\text{eo}} + \int_0^1 \left( \frac{h}{b} \right) \lambda \beta \int_1^Y \int_0^\zeta \frac{\partial G}{\partial X}(X, \xi, \tau) \partial \xi \partial \zeta \partial Y \right\} [Y^3 - 3Y] + u^{\text{eo}} Y + \int_0^Y \left( \frac{h}{b} \right) \lambda \beta \int_1^Y \int_0^\zeta \frac{\partial G}{\partial X}(X, \xi, \tau) \partial \xi \partial \zeta \partial Y. \quad (4.57)$$

### 4.3.3 FURTHER SIMPLIFICATION ( $(h/b)^2 \Gamma \ll 1$ , $(h/b) Re \ll 1$ )

Simpler expressions for  $u^{(0)}$ ,  $v^{(0)}$ , and  $\Psi^{(0)}$  follow from approximations that are often reasonable for microanalysis processes in straight microchannels. Usually  $\Gamma \sim O(1)$ , so if  $(h/b)^2 \ll 1$ ,  $G$  typically reduces to

$$G = -E_a \frac{\partial E_t}{\partial Y} - \frac{1}{2\Gamma} \frac{\partial E_a^2}{\partial X}. \quad (4.58)$$

Also, it was shown in §4.2 that if  $(\frac{h}{b})^2 \Gamma \ll 1$ ,  $E_a \approx E_a(X, \tau)$ , and with these approximations, Eq. (4.49) reduces to

$$\begin{aligned} u^{(0)} = & u^{e0} + \frac{3}{2} \left[ u^{e0} - \left( \frac{h}{b} \right) \lambda \Gamma E_a \int_0^1 \int_1^Y E_t(X, \xi, \tau) \partial \xi \partial Y \right] (Y^2 - 1) \\ & - \left( \frac{h}{b} \right) \lambda \Gamma E_a \int_1^Y E_t(X, \xi, \tau) \partial \xi. \end{aligned} \quad (4.59)$$

$v^{(0)}$  and  $\Psi^{(0)}$  are then calculated, respectively, as

$$\begin{aligned} v^{(0)} = & \frac{1}{2} (Y - Y^3) \frac{\partial u^{e0}}{\partial X} + \frac{1}{2} (Y^3 - 3Y) \left( \frac{h}{b} \right) \lambda \Gamma \frac{\partial}{\partial X} \left[ E_a \int_0^1 \int_1^Y E_t \partial \xi \partial Y \right] \\ & + \left( \frac{h}{b} \right) \lambda \Gamma \frac{\partial}{\partial X} \left[ E_a \int_0^Y \int_1^Y E_t \partial \xi \partial Y \right] \end{aligned} \quad (4.60)$$

and

$$\begin{aligned} \Psi^{(0)} = & \frac{1}{2} (Y^3 - Y) u^{e0} - \frac{1}{2} (Y^3 - 3Y) \left( \frac{h}{b} \right) \lambda \Gamma E_a \int_0^1 \int_1^Y E_t \partial \xi \partial Y \\ & - \left( \frac{h}{b} \right) \lambda \Gamma E_a \int_0^Y \int_1^Y E_t \partial \xi \partial Y. \end{aligned} \quad (4.61)$$

Finally, if  $(h/b)\lambda\Gamma \ll 1$ , the electrical stresses are negligible, and  $u^{(0)}$ ,  $v^{(0)}$ , and  $\Psi^{(0)}$  are calculated, respectively, as

$$u^{(0)} = u^{e0} + \frac{3}{2} u^{e0} (Y^2 - 1) \quad ((h/b)\lambda\Gamma \ll 1), \quad (4.62)$$

$$v^{(0)} = \frac{1}{2} (Y - Y^3) \frac{\partial u^{e0}}{\partial X} \quad ((h/b)\lambda\Gamma \ll 1), \quad (4.63)$$

and

$$\Psi^{(0)} = \frac{1}{2} (Y^3 - Y) u^{e0} \quad ((h/b)\lambda\Gamma \ll 1). \quad (4.64)$$

## 4.4 RESULTS AND DISCUSSION

To evaluate the approximations, the prototype nonuniform buffer configuration examined in Chapter 3 and described in Fig. 3.1, is simulated with the numerical solution presented in Chapter 3 and compared with the results obtained using the semianalytic expressions derived for  $\mathbf{E}$  and  $\mathbf{v}$  in §4.2 and §4.3. For simulations with buffer B, the numerical scheme used to solve the component mass balances is slightly modified to increase computational efficiency. Since diffusion dominates the ion transport in the transverse direction, the transverse finite difference equation (resulting from the operator split) is solved implicitly; the time derivative is discretized with a first-order backward difference approximation, and FCT is not implemented. Since all numerical results presented in this dissertation are converged, this does not affect any of the comparisons.

In all test cases, the initial concentration fields are cross-sectionally uniform, and sigmoidal zone boundaries are initialized with a width  $b_0$ . The evaluation begins in §4.4.1 with a simulation of the electroosmotic pumping problem discussed in §3.4.1, but with  $\gamma = 1/10$ . Because  $\Delta\omega_c/\omega_c \ll 1$  for this buffer,  $E_t$  is not calculated. The initial fluid velocity field is first examined in detail, and shown to be accurately captured using the approximations. It is then demonstrated that during transport of the high-conductivity zone, significant errors are temporarily introduced over a small part of the zone boundary, because of a transient sharpening of the conductivity gradient in that region. The error is short-lived and affects only a small section of

the transition region. The pumping configuration is modified in §4.4.2 by reducing the initial zone boundary length such that  $h/b_0 = 2$ . It is shown that although the lubrication approximation for  $\mathbf{v}$  yields a poor representation of the initial velocity field, dispersion rapidly reduces  $h/b_0$ , and the approximation error quickly decays to that for  $h/b_0 = 2$ . The approximations are shown to accurately predict the field variables at  $\tau_s \equiv t \mid \gamma - 1 \mid v_0^{\text{eo}}/L_s = 2$ .

In §4.4.3, electroosmotic pumping is simulated with another buffer for which  $\Delta\omega_c/\omega_c \sim O(1)$ . It is first shown that, if  $E_t$  is not calculated, ion transport is not captured as well for this buffer. Approximations for  $E_t$  from Eqs. (4.43) and (4.45) are then compared, and their inclusion in the problem formulation is shown to improve solutions for  $\sigma$  and  $\mathbf{v}$  at  $\gamma = 1/10$ . Results are also compared for  $\gamma = 1/50$ , and it is shown that approximation errors are insignificant and decay after a transient growth. The more general formula for  $E_t$  (Eq. (4.43)) is shown to reduce approximation errors substantially for  $\gamma = 1/10$  and  $1/50$ .

The semianalytic expressions for  $\mathbf{v}$  and  $\mathbf{E}$  are evaluated for analyte stacking ( $\gamma > 1$ ) in §4.4.4. Approximation errors are shown to be small for  $\gamma = 2$ , particularly if  $E_t$  is computed using Eq. (4.43). For  $\gamma = 5$ , it is shown that the electrical stresses alter the character of the flow, but only transiently, and the simple approximations that neglect these stresses (Eqs. (4.62)–(4.64)) are effective after the transient. Higher values of  $\gamma$  are not simulated because converged solutions of the full problem are impractical on a uniform grid. A final evaluation is then made for a dynamic flow that is significantly affected by the electrical stresses, and can be characterized using

Eqs. (4.53), (4.55), and (4.57). The fidelity of these approximations are demonstrated by increasing the electric field by a factor of four, and simulating stacking at  $\gamma = 2$ .

Values of the non-dimensional groups for each set of initial buffer conditions are provided in Table 4.1. The zone boundary length  $b$  changes with time, so  $b$  only

TABLE 4.1. Dimensionless groups for 2-D simulations

$E_0$ (V/cm)	Buffer	$\gamma$	$Re$	$Pe$	$\lambda$	$\Gamma$	$\Lambda$
180	A	1/10	0.014	24	5.0	0.08	$10^{-4}$
		1/10	0.022	21	3.3	0.82	$10^{-3}$
	B	1/50	0.024	23	3.6	0.82	$10^{-3}$
		2	0.025	23	3.6	0.82	$10^{-3}$
		5	0.099	93	14.6	0.82	$10^{-4}$
720	B	2	0.099	93	14.6	0.82	$10^{-4}$

$h/L_s = 0.02$  for all simulations

equals  $b_0$  at the outset, when all fields are cross-sectionally uniform. Recall that the scaling arguments in the charge balance only apply for  $t > h^2/\omega_c k_B T$ , at which time simulation results have shown that  $b$  has spread to  $O(L_s)$ . As a result,  $\Lambda$  and  $h/b$  are presented in Table 4.1 with  $b = L_s$ ; all other dimensionless groups are independent of  $b$ . For all buffer configurations in this Chapter,  $E_a$  is calculated from Eq. (4.40).

#### 4.4.1 $\gamma < 1$ , BUFFER A ( $\Delta\omega_c/\omega_c \ll 1$ ), $(h/b_0)^2 \ll 1$

The approximations are first tested by simulating electroosmotic pumping at  $\gamma = 1/10$ , using the buffer studied in Chapter 3, which will henceforth be referred to as buffer A. The running buffer consists of 100 mM Tris base and 200 mM cacodylic

acid (pH = 6.2,  $\sigma_0 = 0.452$  S/m). The geometric lengths of the system are  $L_e = L_s = 1$  mm,  $h = 20$   $\mu\text{m}$ , and  $L_c = 5$  cm. A constant current is maintained by requiring  $i_0 = 8000$  A/m<sup>2</sup> in the running buffer, corresponding to  $E_0 = 180$  V/cm.  $b_0/L_s = 0.12$ , so  $h/b_0 = 1/6$ .

For the approximate solutions, Eqs. (4.62)–(4.64) are used to calculate  $u$ ,  $v$ , and  $\Psi$ . Because the Tris base and cacodylic acid have approximately the same mobility,  $\Delta\omega_c/\omega_c \ll 1$ , and so  $E_t$  is not calculated.

Initial streamlines in the moving reference frame are shown in Fig. 4.2. Since the initial electric field is identically unidirectional, initial approximation errors re-

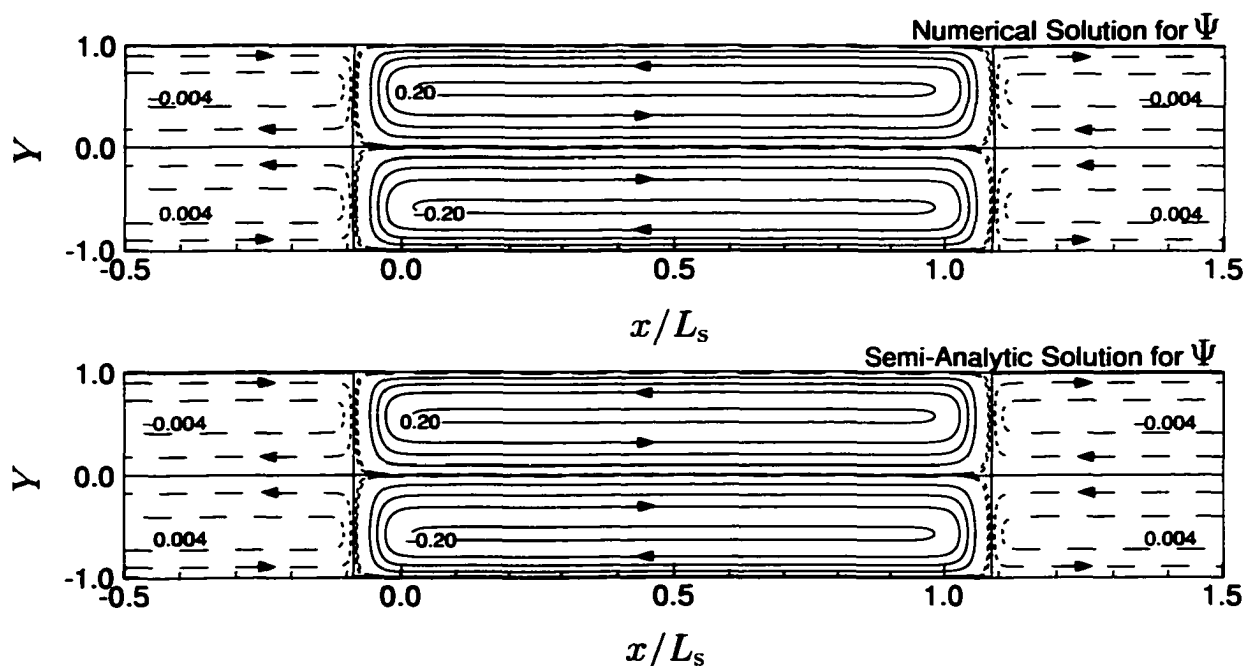


FIGURE 4.2. Initial streamlines for buffer A,  $\gamma = 1/10$ . Solid lines represent contours of constant  $\Psi$  from  $-0.2$  to  $0.2$  at intervals of  $0.05$ ; dashed lines represent contours of constant  $\Psi$  from  $-0.004$  to  $0.004$  at intervals of  $0.002$ .  $h/b_0 = 1/6$ . Running buffer:  $200$  mM cacodylic acid,  $100$  mM Tris;  $\sigma_0 = 0.45$  S/m,  $E_0 = 180$  V/cm,  $i_0 = 8$  kA/m<sup>2</sup>,  $v_0^{\text{eo}} = 0.8$  mm/s, pH = 6.2.  $L_s = 1$  mm,  $L_c = 5$  cm,  $h = 20$   $\mu\text{m}$ .

sult only from the lubrication approximation used to calculate  $\mathbf{v}$ . The streamlines obtained using the approximations are indistinguishable, on the sample zone length scale, from those obtained with the complete numerical solution. Figure 4.3 focuses on the streamlines in the upstream zone boundary. The approximate streamlines

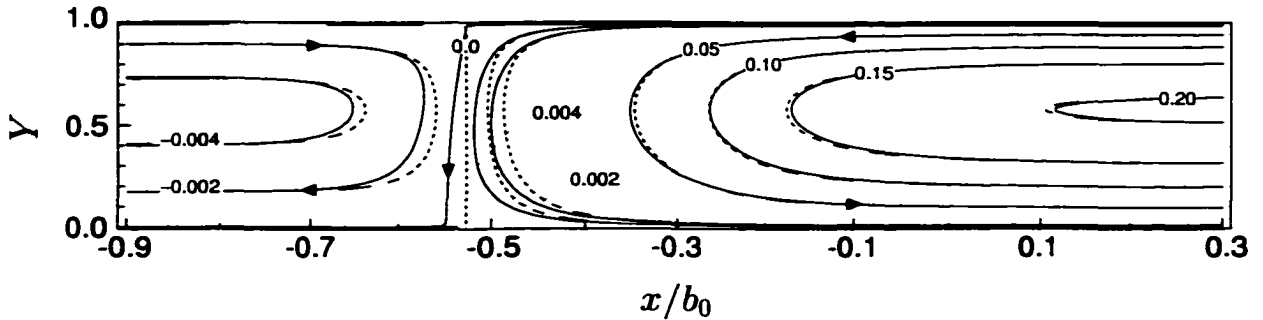


FIGURE 4.3. Initial streamlines in upstream zone boundary calculated by complete numerical solution (solid) and approximate solution (dashed). Values of  $\Psi$  are given for each contour. Simulation conditions are as for Fig. 4.2.

(dashed) deviate slightly from those calculated numerically (solid), primarily near the stagnation streamline. The lubrication approximation is least accurate in this region because  $u$  changes over a smaller length scale than  $b$ . This results from the nonlinear relationship between  $E_x$  and  $\sigma$ , viz.

$$E_x \sim \frac{i_0}{\sigma} \Rightarrow \frac{\delta E_x}{\delta \sigma} \sim \frac{i_0}{\sigma^2}, \quad (4.65)$$

which implies that  $b$  (the characteristic axial length scale for  $\sigma$ ) is not necessarily the characteristic axial length scale for  $E_x$ , and consequently for  $v_x$ . A more general axial length scale  $b^*$  for variations of  $E_x$  and  $v_x$  is derived as follows:

Since  $\delta E_x/\delta x \sim |\gamma - 1| E_0/b^*$  implies

$$b^* \sim \frac{|\gamma - 1| E_0}{\delta E_x/\delta \sigma \delta \sigma/\delta x}, \quad (4.66)$$

and  $\delta \sigma/\delta x \sim |\gamma - 1| \sigma_0/b\gamma$ , then

$$b^* \sim \gamma \left( \frac{\sigma}{\sigma_0} \right)^2 b. \quad (4.67)$$

So as  $\sigma$  ranges from  $\sigma_0$  to  $\sigma_0/\gamma$  in the transition from running buffer to sample zone,  $b^*$  ranges from  $\gamma b$  to  $b/\gamma$ , respectively, i.e.

$$b^* = b/\alpha, \quad \alpha \equiv \begin{cases} \gamma, & \text{Inner Region } (\sigma \sim \sigma_0/\gamma) \\ 1/\gamma, & \text{Outer Region } (\sigma \sim \sigma_0). \end{cases} \quad (4.68)$$

Thus  $b^* \sim b$  throughout the boundary zone only for  $\gamma = O(1)$ . For  $\gamma \gg 1$  or  $\gamma \ll 1$ , the scaling in §4.1 applies to the region of the zone boundary where  $b^* \sim b$ , i.e. where  $\sigma/\sigma_0 \sim 1/\sqrt{\gamma}$ . Near the stagnation streamline,  $\sigma \sim \sigma_0$ , so  $\alpha = 1/\gamma$ , and  $b^* = \gamma b = b/10$ .

It is important to note that the  $\Psi$  contours are shown in increments of 0.002 where the most significant errors are observed; increments of 0.05 are shown in the region where better agreement is obtained. Since the fluid velocity components are given by spatial derivatives of  $\Psi$ , the relative error in the velocity field is only significant where the fluid velocity approaches zero. Fig. 4.4 shows initial axial velocity profiles in the upstream zone boundary. The profiles have a parabolic form throughout the zone boundary, and are essentially equivalent to those given by the lubrication approximation.

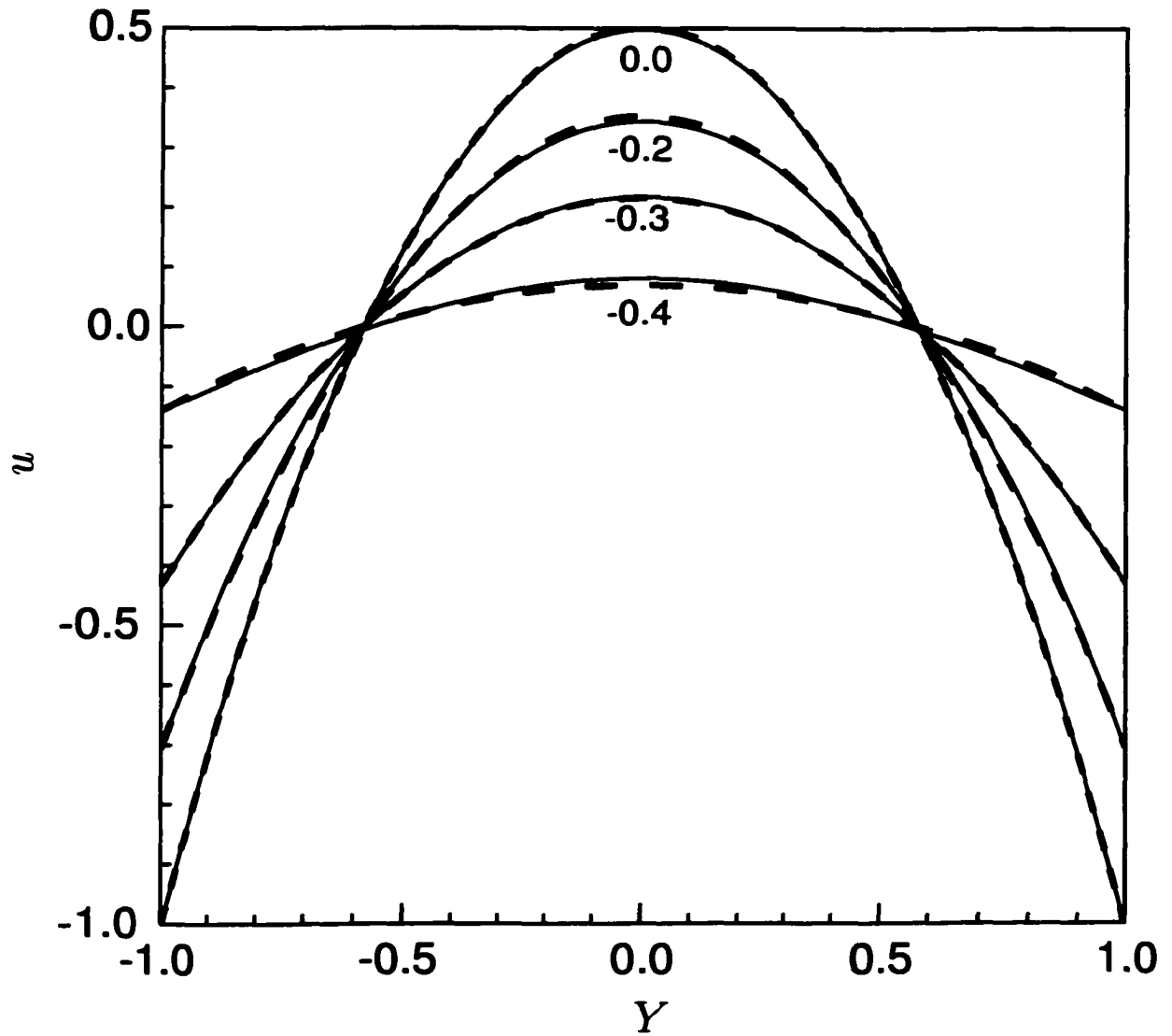


FIGURE 4.4. Initial axial velocity profiles in upstream zone boundary, at selected values of  $x/b_0$ . Complete numerical solution (solid); approximate solution (dashed). Simulation conditions are as for Fig. 4.2.

The zone boundaries are ultimately distorted by the fluid motion and electrodiffusional transport, causing the conductivity, electric, fluid velocity, and component concentration fields to evolve in time. Fig. 4.5 shows the absolute value of the error in the fluid speed  $\varepsilon \equiv || \mathbf{v}^{(0)} || - || \mathbf{v} ||$  after 0, 0.4, and 2 characteristic times for convection across the sample zone. The approximation error increases substantially over a small part of the zone boundary (see Fig. 4.6) by  $\tau_s \equiv t | \gamma - 1 | v_0^{eo} / L_s = 0.4$ , but then decreases by  $\tau_s = 2$ . The error develops because the conductivity gradient in the zone boundary initially increases over part of the channel cross-section; this occurs where  $|u|$  decreases in the direction of  $u$ , i.e. where  $\partial u / \partial X < 0$ . Fig. 4.6 shows that when  $\tau_s = 0.4$ , the conductivity gradient near the wall, in the low conductivity region of the zone boundary, is greater than at  $\tau_s = 0$ . The sharper conductivity gradient decreases the local transition length for the electric field and thus the electroosmotic slip velocity, as shown in Figure 4.7. The characteristic length for velocity changes approaches  $h$  in this region where  $|\partial u_{eo} / \partial X|$  is the greatest, and there the lubrication approximations fail. This process affects but a short segment along the wall, and has the most impact where the flow is weakest. Also, diffusion eventually reduces the conductivity and velocity gradients (Figs. 4.6 and 4.7), and the error diminishes (Fig. 4.5) by  $\tau_s = 2$ . Thus the flow in the lubrication approximation is both short-lived and confined to a small portion of the domain.

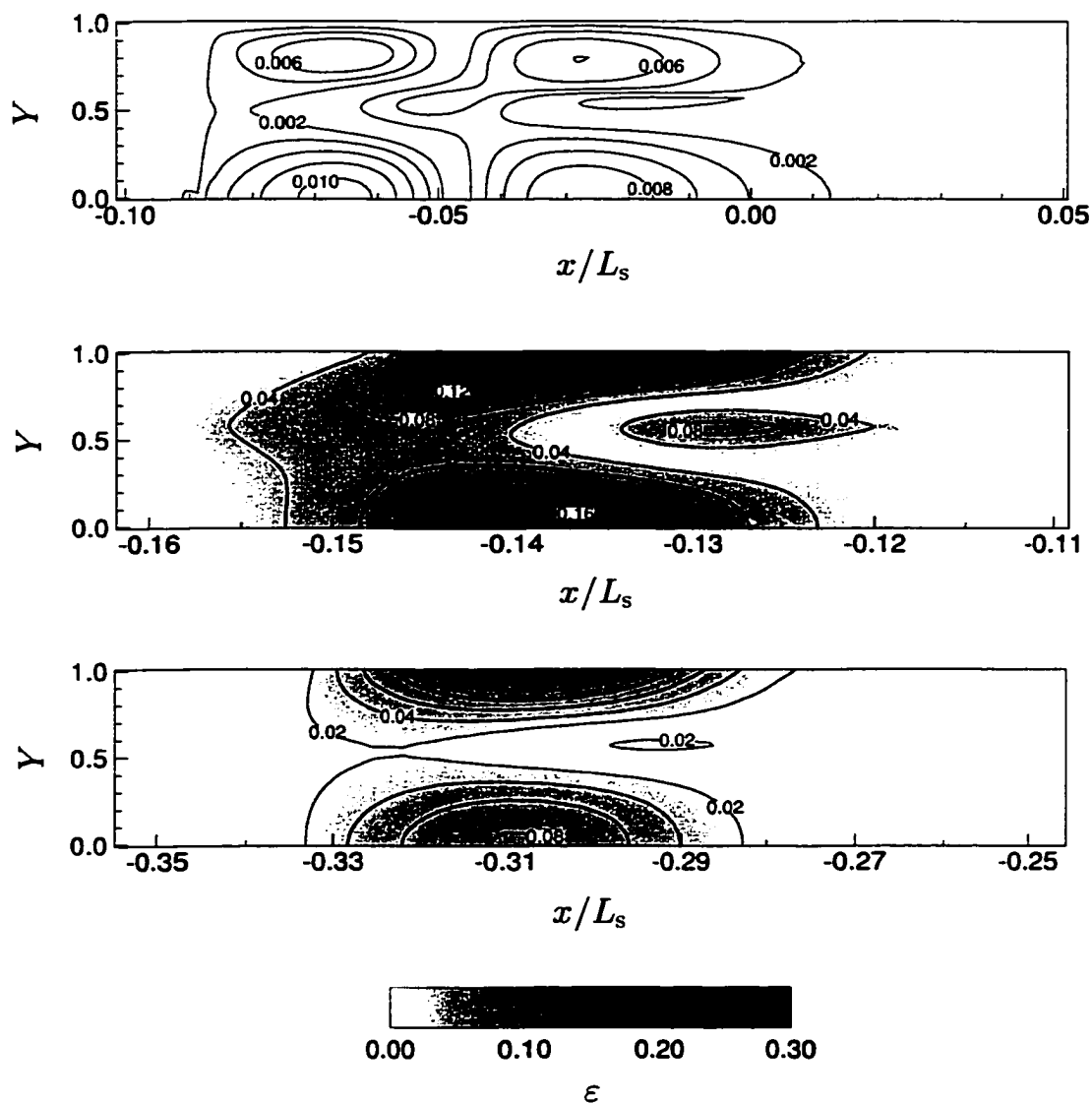


FIGURE 4.5. Fluid speed approximation error  $\varepsilon$  in upstream zone boundary, at  $\tau_s = 0$ , 0.4, and 2. Solid lines represent contours of constant  $\varepsilon$  from 0.002 to 0.01 at intervals of 0.002 ( $\tau_s = 0$ ), from 0.04 to 0.28 at intervals of 0.04 ( $\tau_s = 0.4$ ), and from 0.02 to 0.14 at intervals of 0.02 ( $\tau_s = 2$ ). Simulation conditions are as for Fig. 4.2.

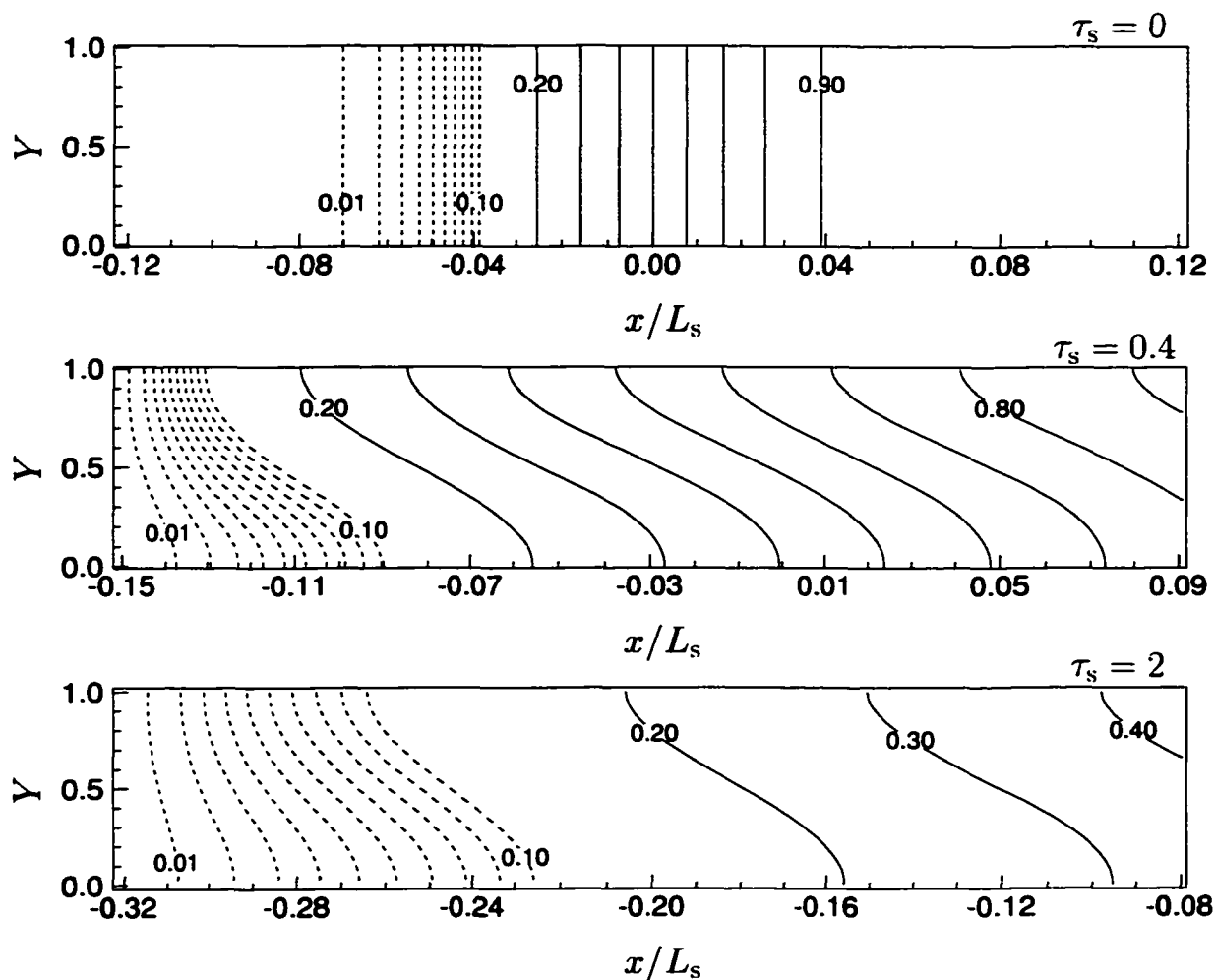


FIGURE 4.6. Conductivity field in upstream zone boundary calculated by complete numerical solution. Solid lines represent contours of constant  $\gamma(\hat{\sigma} - 1)/(1 - \gamma)$  from 0.2 to 0.9 at intervals of 0.1; dashed lines represent contours of constant  $\gamma(\hat{\sigma} - 1)/(1 - \gamma)$  from 0.01 to 0.1 at intervals of 0.01. Simulation conditions are as for Fig. 4.2.

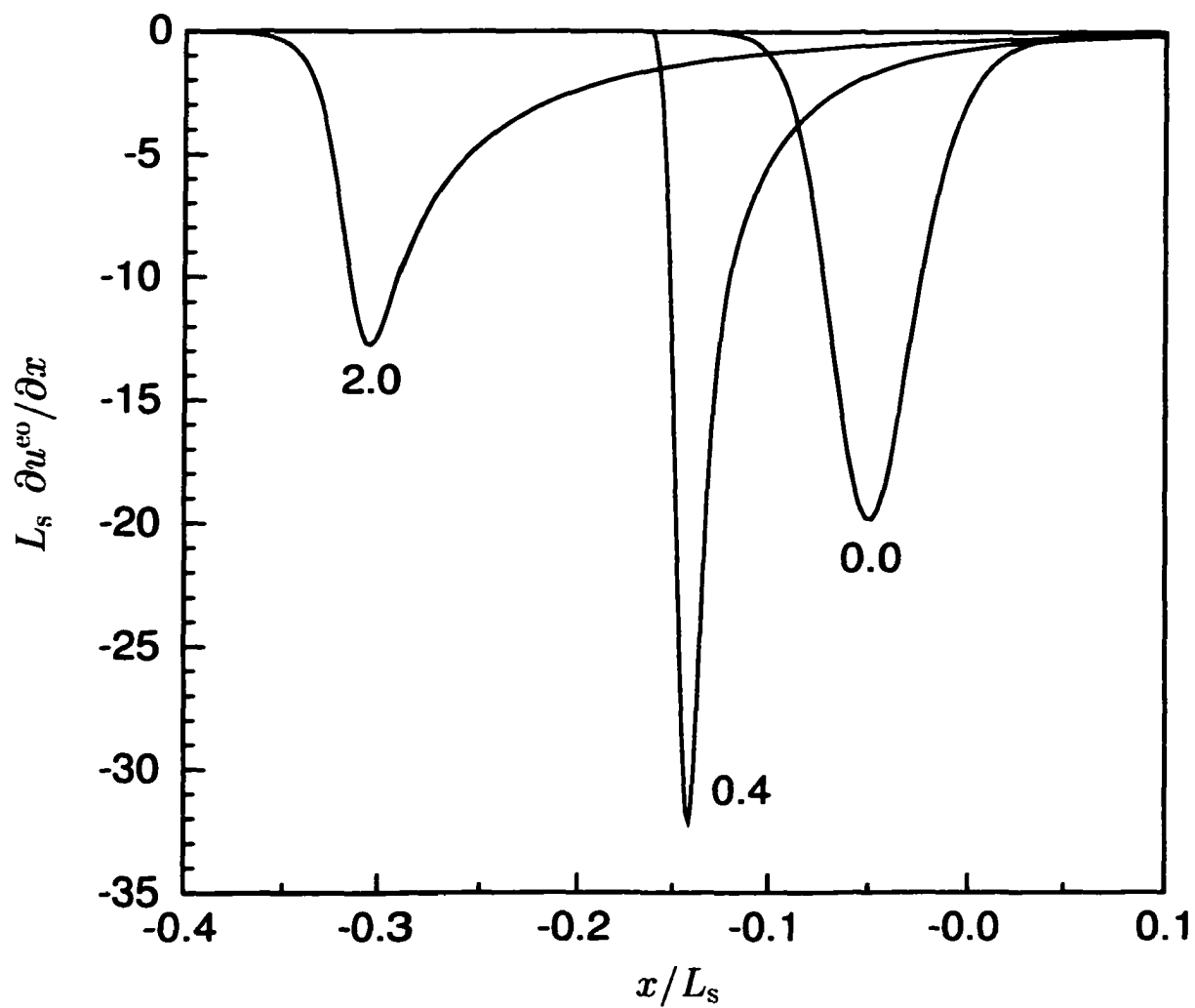


FIGURE 4.7. Axial derivative of slip velocity in upstream zone boundary calculated by complete numerical solution, at selected values of  $\tau_s$ . Simulation conditions are as for Fig. 4.2.

#### 4.4.2 $\gamma < 1$ , BUFFER A ( $\Delta\omega_c/\omega_c \ll 1$ ), $h/b_0 = O(1)$

Since the zone boundary length in the previous configuration is initialized somewhat arbitrarily, the simulation is repeated with  $h/b_0 = 2$ . A zone boundary of approximately this length would result within 0.05 seconds given only diffusion as a dispersion mechanism. Initial streamlines and axial velocity profiles near the upstream zone boundary are shown in Figs. 4.8 and 4.9, respectively. Clearly the lubrication

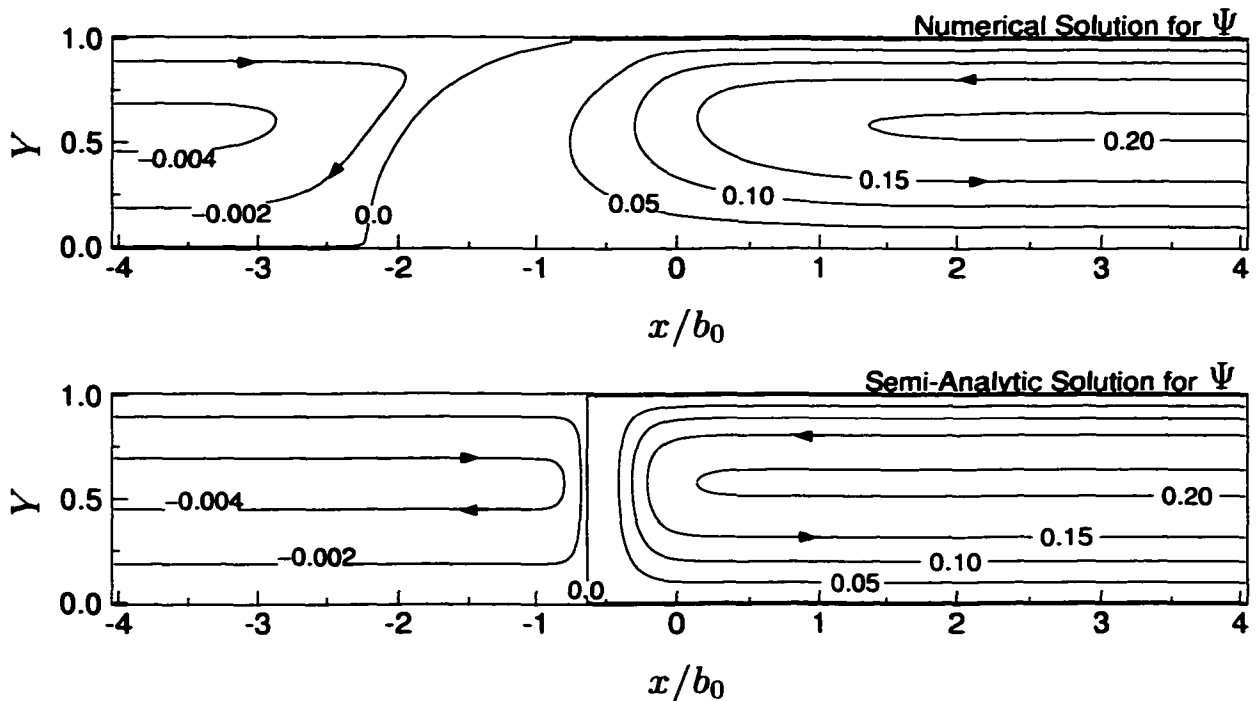


FIGURE 4.8. Initial streamlines in upstream zone boundary. Values of  $\Psi$  are given for each contour.  $h/b_0 = 2$ ; all other simulation conditions are as for Fig. 4.2.

approximation does not accurately capture the initial fluid velocity field. The axial velocity profiles are not parabolic in the zone boundary as predicted by the lubrication approximation, and the region of 2-D fluid motion extends well beyond the

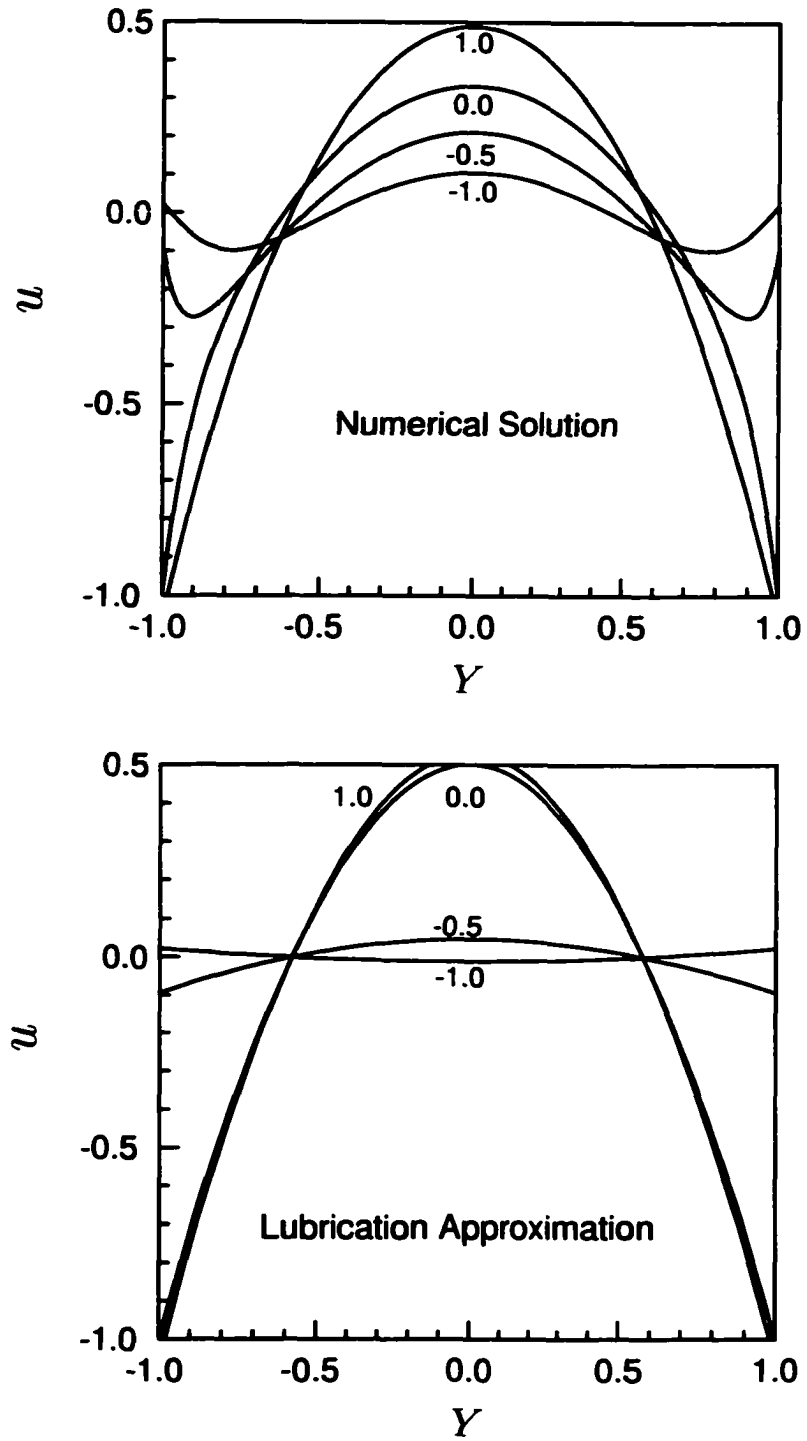


FIGURE 4.9. Initial axial velocity profiles in upstream zone boundary, at selected values of  $x/b_0$ . Simulation conditions are as for Fig. 4.8.

zone boundary. However, the zone boundary rapidly spreads such that  $(h/b)^2 \ll 1$  within fractions of a second ( $\tau_s < 1$ ). Figure 4.10 shows the maximum and average  $\varepsilon$  ( $\varepsilon_{\max}$  and  $\varepsilon_{\text{avg}}$ ) in the zone boundaries for  $h/b_0 = 2$  and  $h/b_0 = 1/6$ . As discussed previously, for  $h/b_0 = 1/6$  the error increases initially, and then decays as the zone boundaries spread. For  $h/b_0 = 2$ ,  $\varepsilon$  is initially as high as 0.8, but decays immediately, and ultimately follows a course nearly identical to that for  $h/b_0 = 1/6$ . This occurs because for  $\tau_s > 0.5$ ,  $\sigma$ ,  $\mathbf{v}$ , and  $\mathbf{E}$  are approximately the same for any  $h/b_0 \geq 1/6$ ; i.e. the system is insensitive to the initial zone boundary length at least up to  $h/b_0 = 1/6$ .

Streamlines, and contours of constant conductivity and electric potential in both zone boundaries are shown in Fig. 4.11 at  $\tau_s = 2$ . The approximate and numerical solutions are in substantial agreement over most of the transition from running buffer to sample zone. The modest transverse conductivity gradients are caused by the electrolyte motion, and despite this, the potential contours show the electric field is virtually unidirectional. Such results are consistent with the scaling arguments (cf. Eqs. (4.12) and (4.35)), which suggest that transverse variations in  $\varsigma$  and  $E_a$  should be  $O[(h/b)Pe] \sim O[(h/L_s)Pe] \sim O(10^{-1})$ , and  $O[(h/b)^2\Gamma] \sim O[(h/L_s)^2\Gamma] \sim O(10^{-5})$ , respectively.

#### 4.4.3 $\gamma < 1$ , BUFFER B ( $\Delta\omega_c/\omega_c \sim 1$ )

Electroosmotic pumping at  $\gamma = 1/10$  is simulated with another buffer (buffer B) to demonstrate that the approximations are not limited to a parameter space with

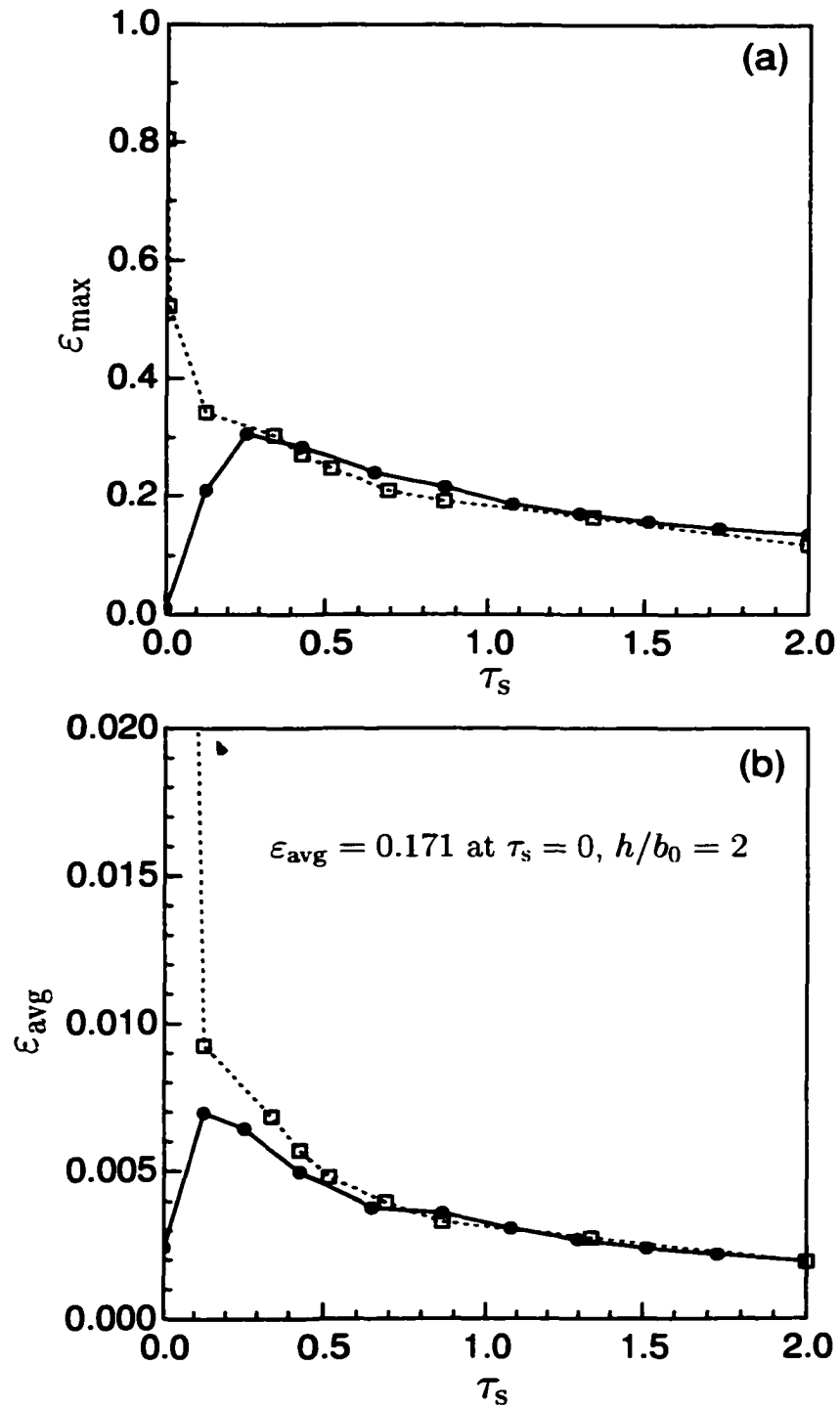


FIGURE 4.10. Time dependence of fluid speed approximation error for  $h/b_0 = 1/6$  (solid) and 2 (dotted). Simulation conditions are as for Fig. 4.2.

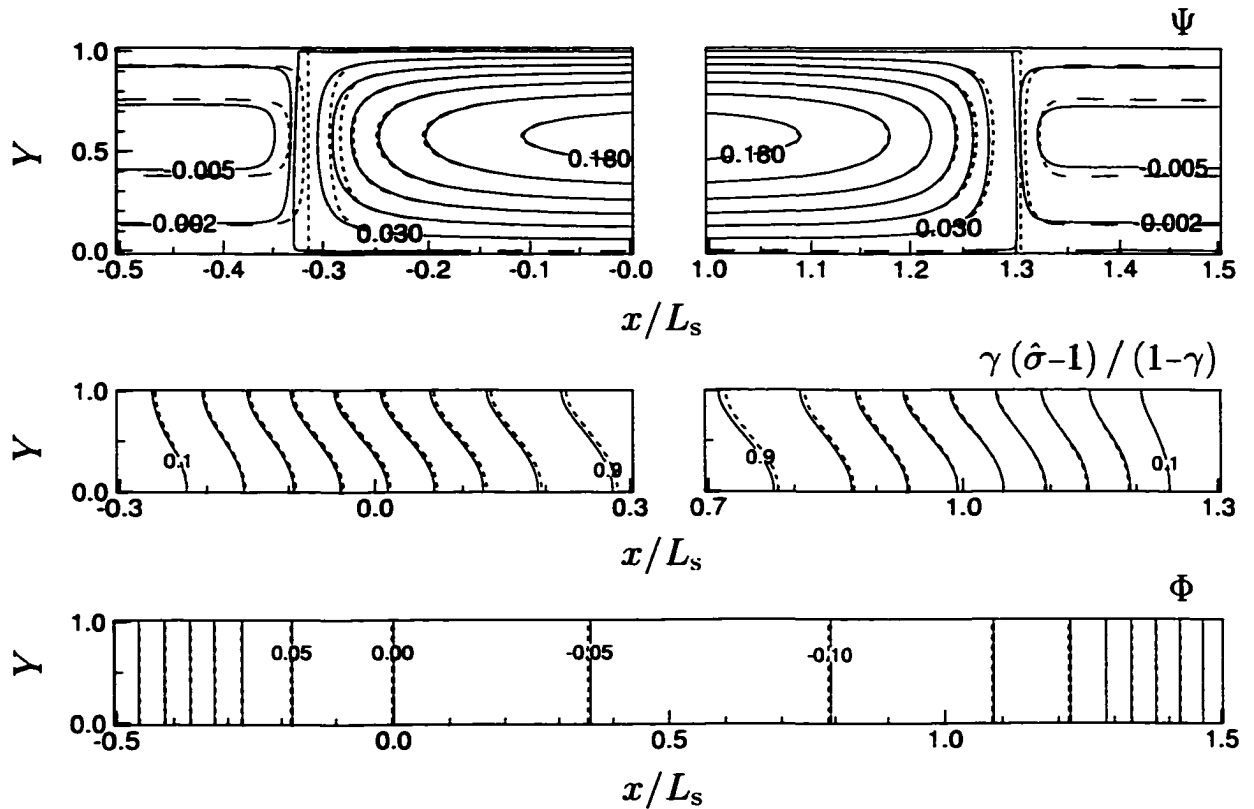


FIGURE 4.11. Streamlines, and conductivity and potential contours at  $\tau_s = 2$ . Complete numerical solution (solid); approximate solution (dashed). Unlabeled streamlines in top panel are shown for  $\Psi$  from 0.06 to 0.15 at intervals of 0.03; values of  $\Psi$  are given for all other streamlines. Conductivity contours are shown for  $\gamma(\hat{\sigma} - 1) / (1 - \gamma)$  from 0.1 to 0.9 at intervals of 0.1; Potential contours are shown for  $\Phi \equiv [\phi - \phi(x = 0)] / (E_0 |\gamma - 1| L_s)$  from -0.45 to 0.30 at intervals of 0.05. Simulation conditions are as for Fig. 4.8.

$\Delta\omega_c/\omega_c \ll 1$ . The running buffer consists of 20 mM ACES and 9 mM NaOH (pH = 6.2,  $\sigma_0 = 0.0723$  S/m) [147]. All other simulation conditions are equivalent to those in §4.4.1. If  $E_t$  is not calculated, the ion transport is not predicted as accurately as for buffer A, as can be seen in the conductivity contours shown of Fig. 4.12, Panel (a).  $E_t$  is more important for buffer B because  $\Delta\omega_c/\omega_c \sim 1$ . This is clear

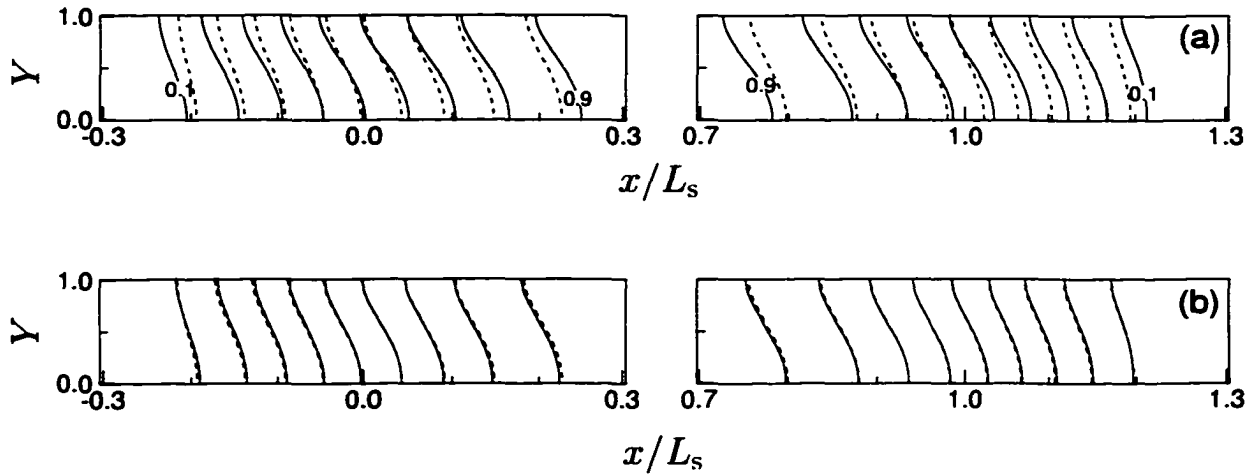


FIGURE 4.12. Conductivity contours at  $\tau_s = 2$  for  $\gamma = 1/10$ , calculated by complete numerical solution (solid) and approximate solution (dashed). (a) buffer B; (b) buffer B with  $\omega_{\text{ACES}}$  set equal to  $\omega_{\text{Na}^+}$ . Contours are shown for  $\gamma(\bar{\sigma} - 1)/(1 - \gamma)$  from 0.1 to 0.9 at intervals of 0.1. Running buffer: 20 mM ACES, 9 mM NaOH;  $\sigma_0 = 0.072$  S/m,  $E_0 = 180$  V/cm,  $i_0 = 1.3$  kA/m<sup>2</sup>,  $v_0^{\text{eo}} = 1.2$  mm/s, pH = 6.2.  $L_s = 1$  mm,  $L_c = 5$  cm,  $h = 20$   $\mu\text{m}$ .

from Panel (b), which shows that the approximate conductivity contours match the complete numerical solution at least as well as for buffer A when the mobility of ACES is changed to equal that of NaOH.

The approximation can be improved significantly for buffer B by calculating  $E_t$  using Eq. (4.43), or even the simple expression in Eq. (4.45). Figure 4.13 compares approximate  $E_t$  contours calculated by Eqs. (4.43) and Eq. (4.45) with those computed

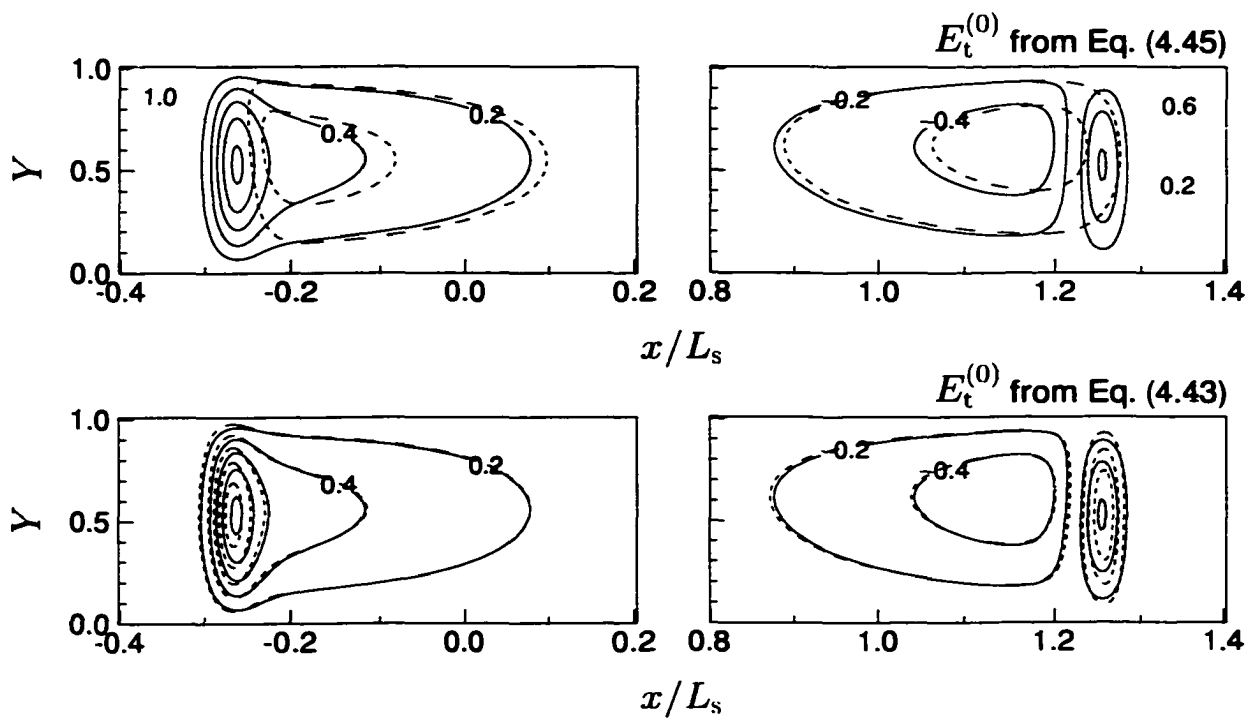


FIGURE 4.13.  $E_t$  contours for buffer B,  $\gamma = 1/10$  at  $\tau_s = 2$ , calculated by complete numerical solution (solid) and approximate solutions (dashed). Contours are shown for  $E_t$  from  $-0.4$  to  $1.0$  at intervals of  $0.2$ . Simulation conditions are as for Fig. 4.12.

by the complete numerical solution. Although  $\Gamma \sim 1$ , Eq. (4.45) provides a reasonable approximation of  $E_t$  in the inner region of the zone boundary, but fails in the outer region where the integral in Eq. (4.43) becomes important. The slightly more complicated expression in Eq. (4.43) greatly improves the estimate of  $E_t$  throughout both zone boundaries and has an insignificant effect on simulation time.

To understand why Eq. (4.45) produces a good approximation for  $E_t$  in the inner region, the deviations from the scaling in §4.1 must be considered. Since  $E_a$  changes by  $O(1)$  over the length scale  $b/\alpha$ , Eq. (4.43) is written more generally if  $X$  is rescaled on  $b/\alpha$ , whence it reads

$$E_t^{(0)} = -\frac{1}{\zeta} \left[ j^D + \frac{\alpha}{\Gamma} \frac{\partial}{\partial X^*} \left( E_a^{(0)} \int_0^Y \zeta' \partial \xi \right) \right], \quad (4.69)$$

where  $X^* \equiv x\alpha/b$ . Thus the integral in Eq. (4.69) is approximately an order of magnitude less than  $j^D$  in the inner region ( $\alpha = \gamma = 1/10$ ), which extends from  $\sigma = \sigma_0/\gamma$  to  $\sigma_0/\sqrt{\gamma}$ , and does not significantly affect the calculation of  $E_t$  over approximately 2/3 of the zone boundary. In the outer region where  $\alpha = 1/\gamma = 10$ , the integral is important, and the calculation of  $E_t$  from Eq. (4.45) is a poor approximation.

Figures 4.14 and 4.15 show the conductivity contours and streamlines, respectively, at  $\tau_s = 2$ , calculated using all three approximations for  $E_t$ . Eqs. (4.43) and (4.45) substantially improve the approximations. Eq. (4.43) only slightly improves the approximation of the streamlines in the outer region over that provided by Eq. (4.45) because much of the residual error in this region results from the lubrication approx-

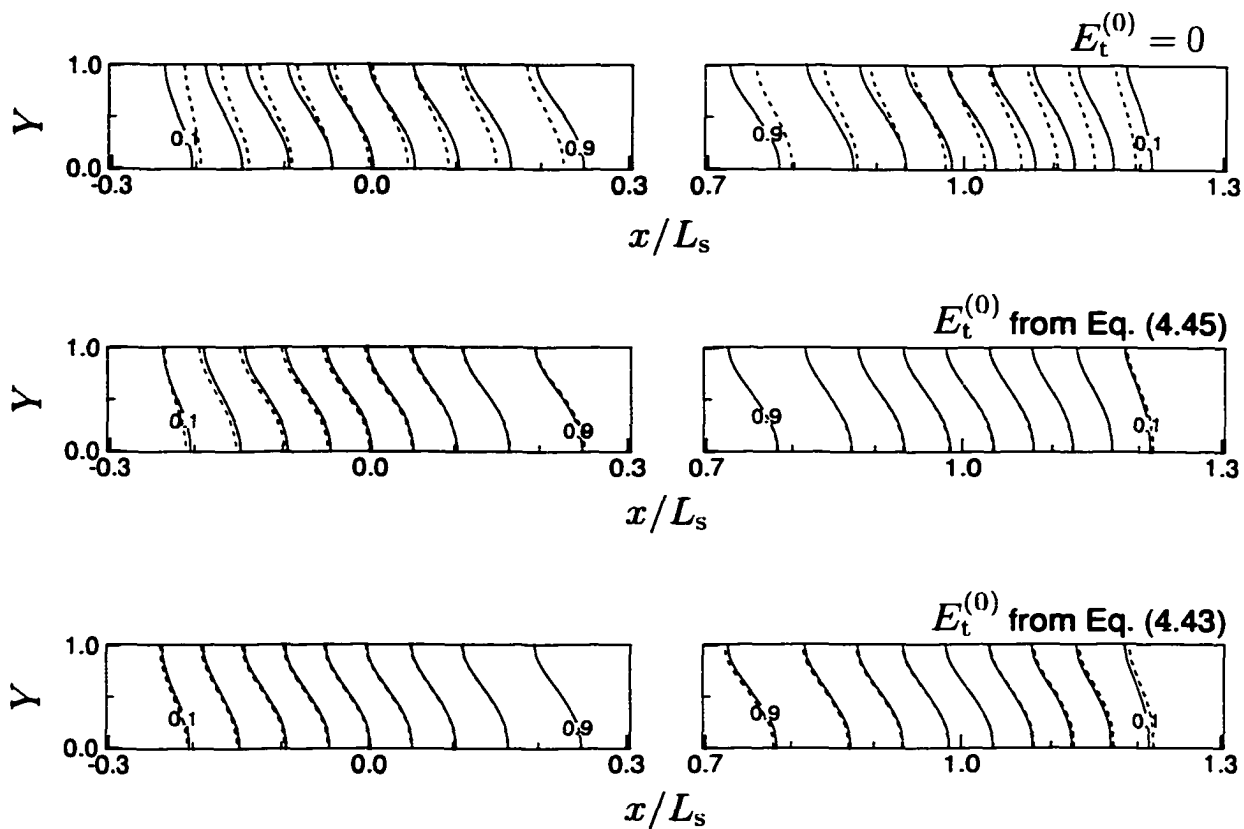


FIGURE 4.14. Conductivity contours for buffer B,  $\gamma = 1/10$  at  $\tau_s = 2$ , calculated by complete numerical solution (solid) and approximate solutions (dashed). Contours are shown for  $\gamma(\hat{\sigma} - 1)/(1 - \gamma)$  from 0.1 to 0.9 at intervals of 0.1. Simulation conditions are as for Fig. 4.12.

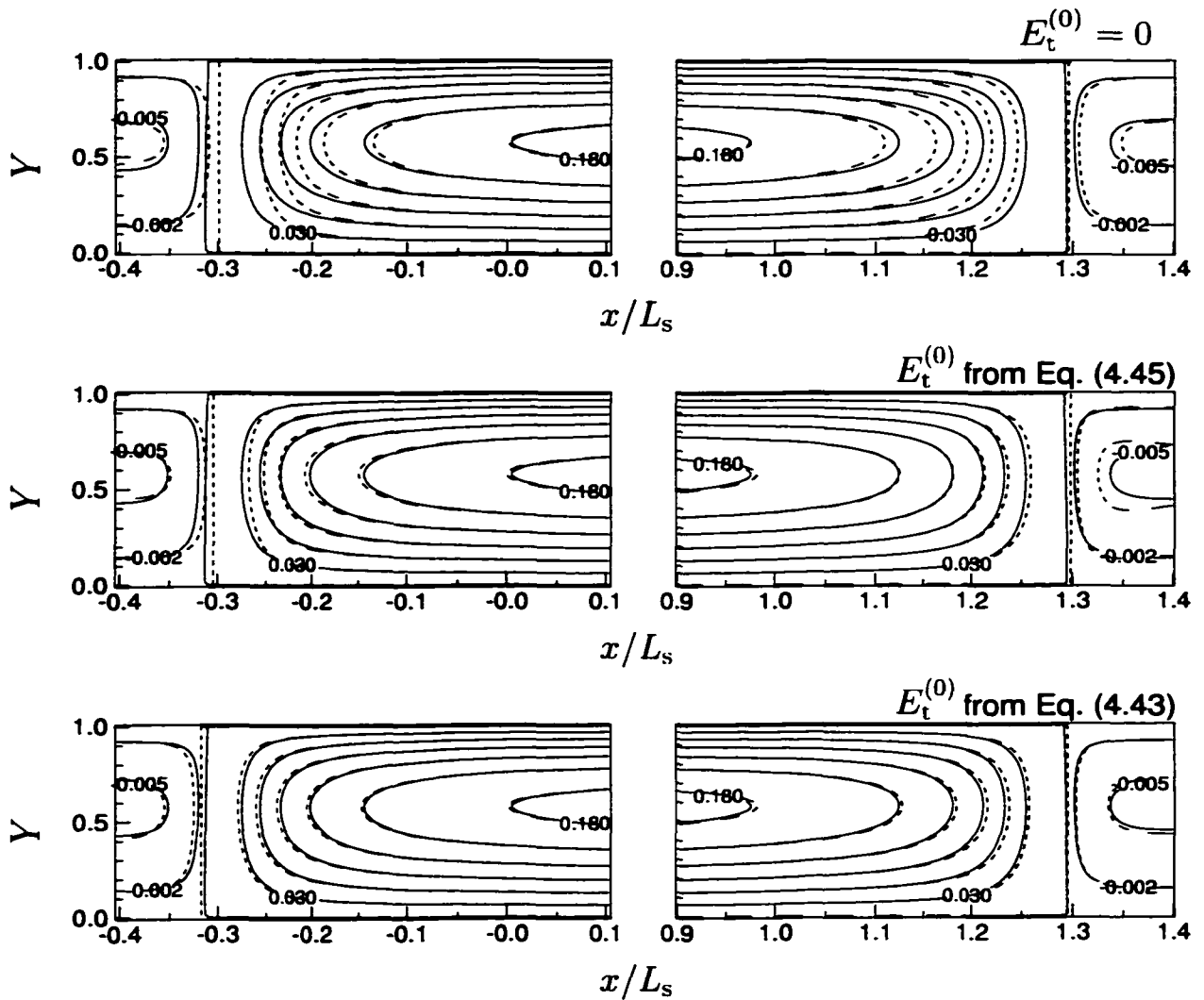


FIGURE 4.15. Streamlines for buffer B,  $\gamma = 1/10$  at  $\tau_s = 2$ , calculated by complete numerical solution (solid) and approximate solutions (dashed). Unlabeled streamlines are shown for  $\Psi$  from 0.06 to 0.15 at intervals of 0.03. Simulation conditions are as for Fig. 4.12.

imation.

Similar results are obtained for  $\gamma = 1/50$ , as shown in Figs. 4.16 and 4.17. The more accurate approximation of  $E_t$  in the outer region provided by Eq. (4.43) has a

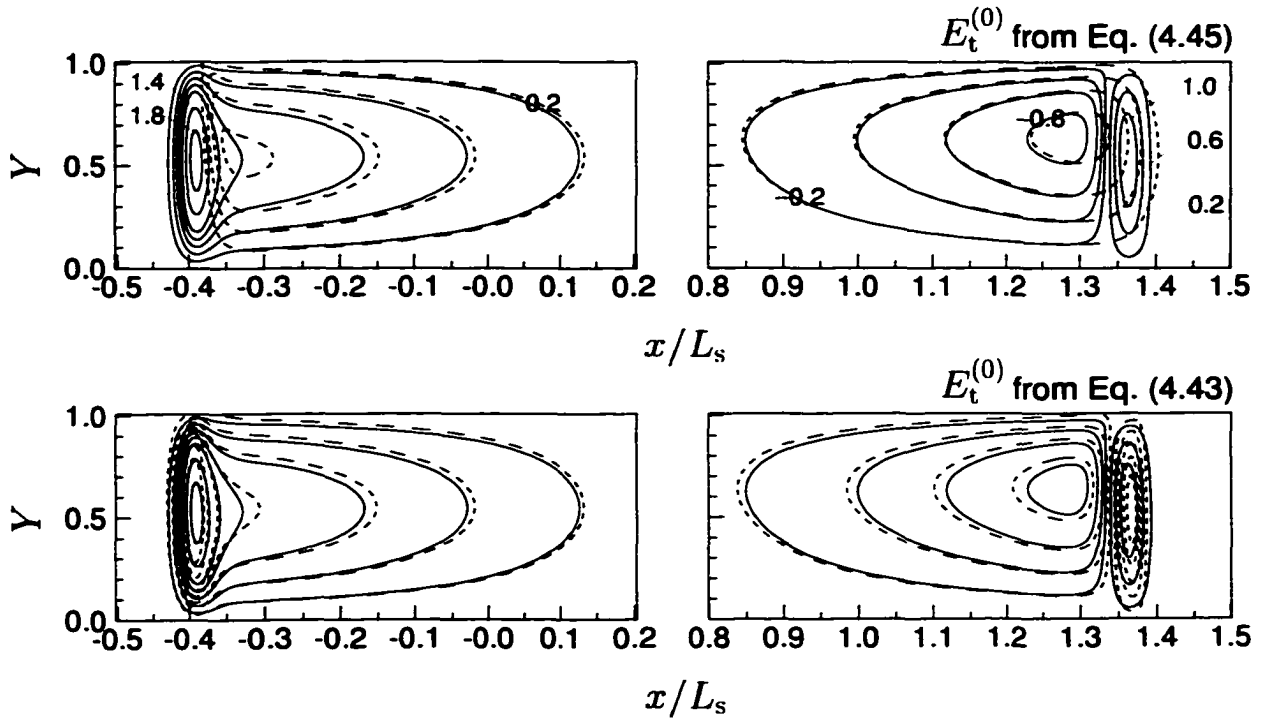


FIGURE 4.16.  $E_t$  contours for buffer B,  $\gamma = 1/50$  at  $\tau_s = 2$ , calculated by complete numerical solution (solid) and approximate solutions (dashed). All other simulation conditions are as for Fig. 4.12. Contours are shown for  $E_t$  in upstream boundary from 0.2 to 1.0 at intervals of 0.2; 1.4, 1.8. In downstream boundary from -0.2 to -0.8 at intervals of 0.2, and from 0.2 to 1.0 at intervals of 0.4.

more important effect on the streamlines at  $\gamma = 1/50$  because  $\alpha$  is a factor of 5 larger. The accuracy of the approximations for the electroosmotic pumping configuration with buffer B is summarized by Fig. 4.18, which presents  $\varepsilon_{\max}$  and  $\varepsilon_{\text{avg}}$  as a function of time. As for buffer A, the errors peak before  $\tau_s = 0.5$  and then decay. Eq. (4.43) reduces  $\varepsilon_{\max}$  and  $\varepsilon_{\text{avg}}$  by as much as 2/3 from those resulting from Eq. (4.45). By

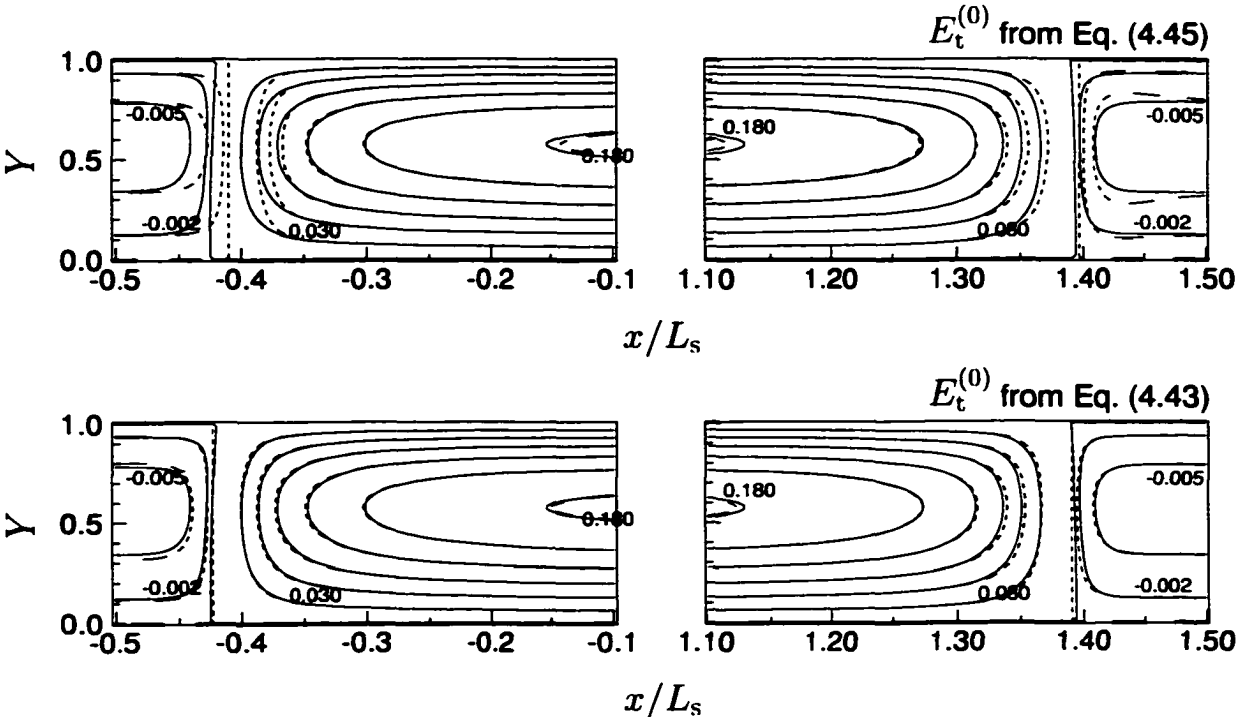


FIGURE 4.17. Streamlines for buffer B,  $\gamma = 1/50$  at  $\tau_s = 2$ , calculated by complete numerical solution (solid) and approximate solutions (dashed). All other simulation conditions are as for Fig. 4.12. Unlabeled streamlines are shown for  $\Psi$  from 0.06 to 0.15 at intervals of 0.03.

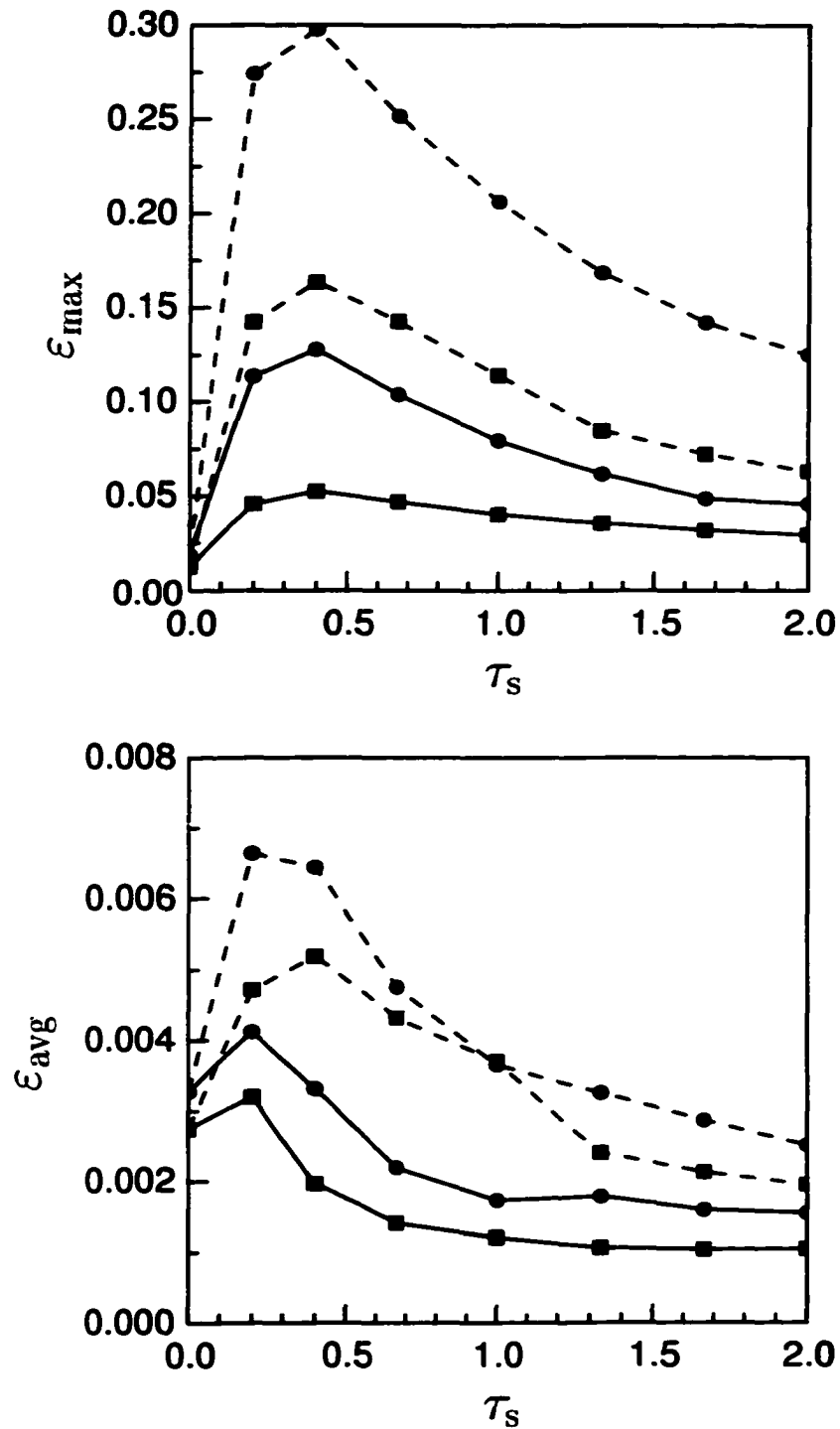


FIGURE 4.18. Time dependence of fluid speed approximation error for buffer B,  $\gamma < 1$ .  $E_t$  calculated by Eq. (4.43) (solid) and Eq. (4.45) (dashed);  $\blacksquare$ ,  $\gamma = 1/10$ ;  $\bullet$ ,  $\gamma = 1/50$ . All other simulation conditions are as for Fig. 4.12.

$\tau_s = 2$ ,  $\varepsilon_{\text{avg}} < 0.003$  for all cases.

#### 4.4.4 $\gamma > 1$ , BUFFER B

Sample stacking is simulated first for  $\gamma = 2$  with buffer B. All other simulation conditions are as described in §4.4.1. Since  $\gamma = O(1)$  ( $\alpha = O(1)$ ), the integral in Eq. (4.69) is important, and Eq. (4.45) yields a poor approximation for  $E_t$  throughout the zone boundaries. Figure 4.19 shows  $\varepsilon_{\text{max}}$  and  $\varepsilon_{\text{avg}}$  vs.  $\tau_s$ . The calculation of  $E_t$  by Eq. (4.43) rather than from Eq. (4.45) reduces  $\varepsilon_{\text{max}}$  and  $\varepsilon_{\text{avg}}$  by approximately an order of magnitude, and  $\varepsilon_{\text{max}}$  never exceeds 0.03.

The maximum error peaks at a lower value than for  $\gamma = 1/10$  and  $\gamma = 1/50$  because  $E_a$  and  $u$  change over the length scale  $b$  for  $\gamma = 2$  since  $\gamma = O(1)$ ; for  $\gamma \ll 1$ , on the other hand, most of the electric field and velocity change occurs over a narrow region near the uniform buffer.

At  $\gamma = 5$ , the electrical stresses begin to affect the fluid motion, but only slightly and ephemerally. As shown in Fig. 4.20, a small secondary circulation pattern develops in the downstream zone boundary, and the streamlines are slightly distorted at  $\tau_s = 0.1$ . As the zone boundary spreads, however, the electrical stresses quickly diminish and do not have a lasting effect. By  $\tau_s = 1$ , the structure of the flow begins to resemble that obtained for  $\gamma < 5$ . The electrical stresses do not significantly impact the fluid motion and ion transport after the initial transient, and so Eqs. (4.43) and (4.62)–(4.64) still provide good approximations at  $\tau_s = 2$  (Fig. 4.21).

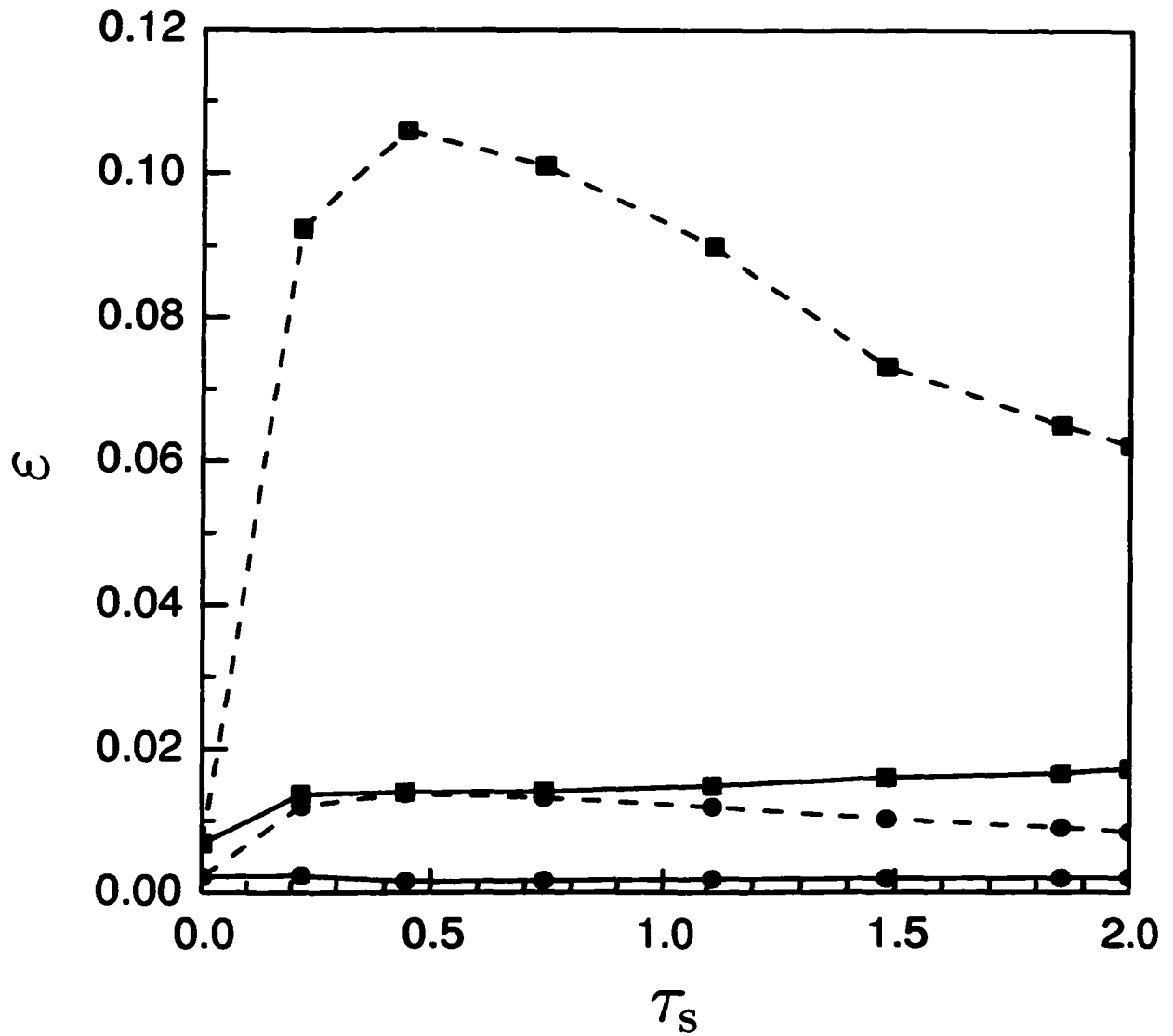


FIGURE 4.19. Time dependence of fluid speed approximation error for buffer B,  $\gamma = 2$ . All other simulation conditions are as for Fig. 4.12.  $E_t$  calculated by Eq. (4.43) (solid) and Eq. (4.45) (dashed);  $\blacksquare$ ,  $\epsilon_{\max}$ ;  $\bullet$ ,  $\epsilon_{\text{avg}}$ .

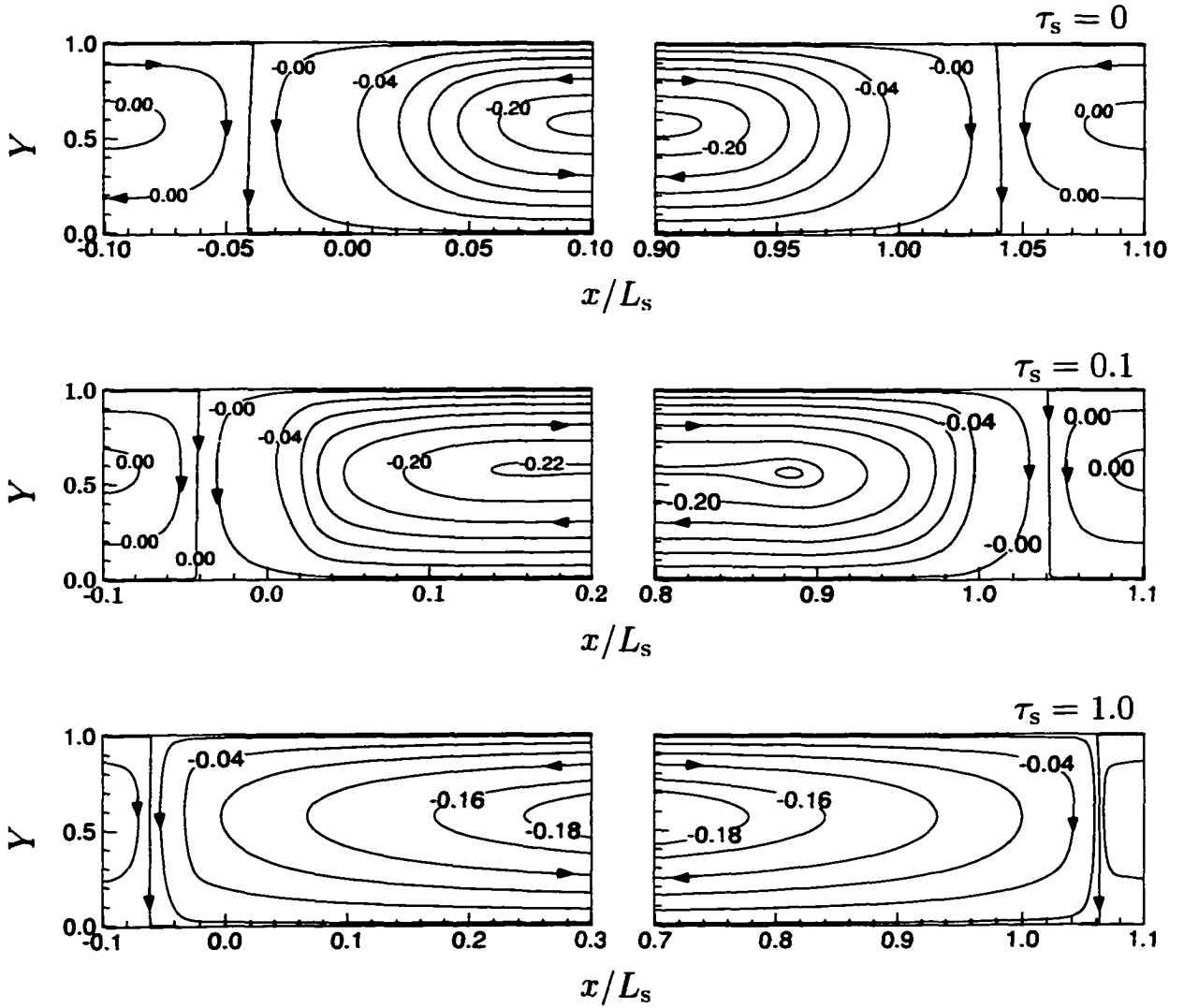


FIGURE 4.20. Time evolution of streamlines for buffer B,  $\gamma = 5$ , calculated by complete numerical solution. All other simulation conditions are as for Fig. 4.12. Unlabeled streamlines are shown for  $\Psi$  from  $-0.16$  to  $-0.08$  at intervals of  $0.04$ .

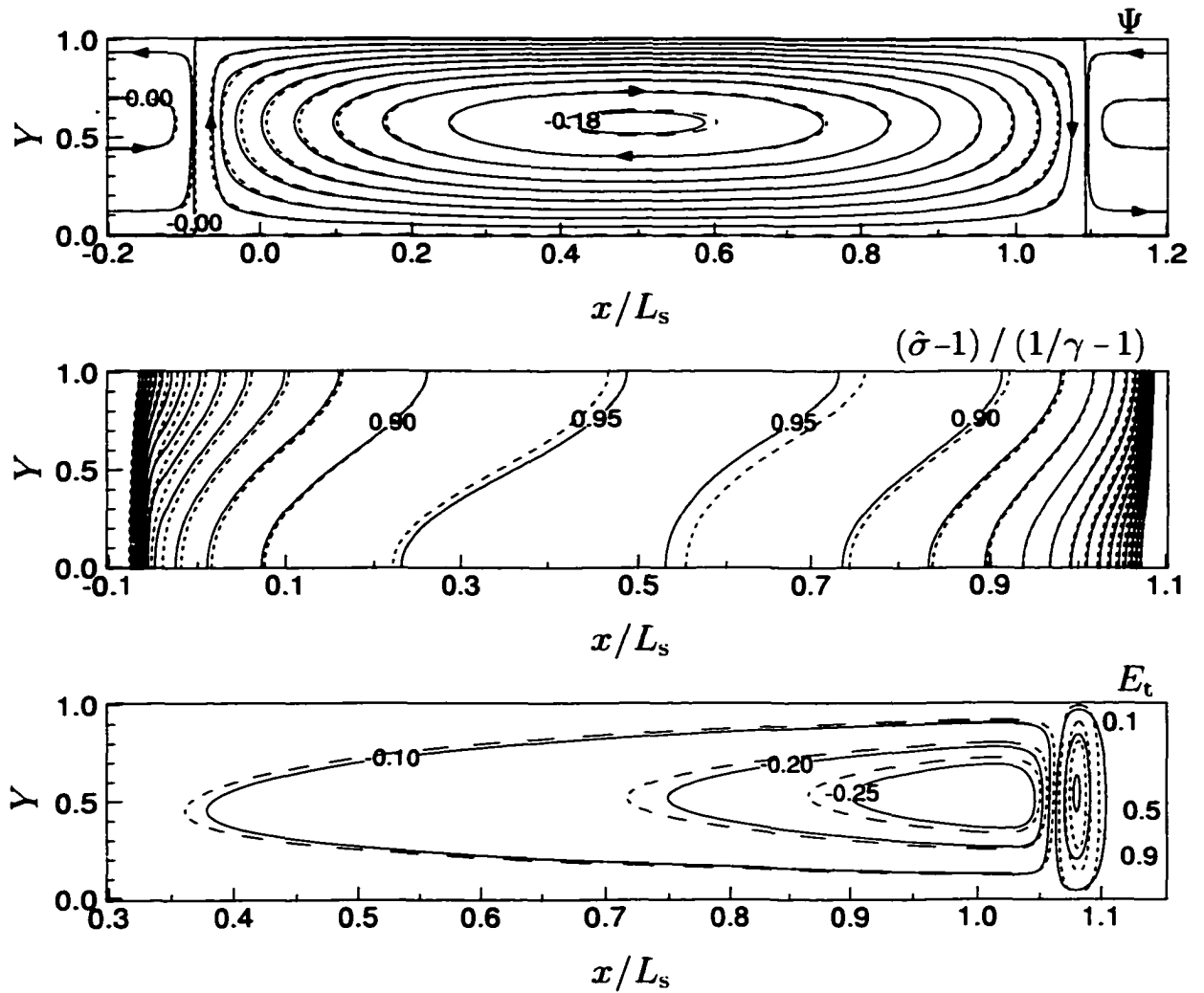


FIGURE 4.21. Streamlines, and conductivity and  $E_t$  contours for buffer B,  $\gamma = 5$  at  $\tau_s = 2$ . All other simulation conditions are as for Fig. 4.12. Complete numerical solution (solid); approximate solution (dashed). Unlabeled streamlines in top panel are shown for  $\Psi$  from  $-0.16$  to  $-0.02$  at intervals of  $0.02$ ; Conductivity contours are shown for  $\gamma(\hat{\sigma} - 1) / (1 - \gamma)$  from  $0.25$  to  $0.95$  at intervals of  $0.05$

At  $\gamma = 10$ , the effects of the electrical stresses are more profound but difficult to converge upon numerically. The electrical stresses also have a significant effect on the flow for  $\gamma = O(1)$  at higher values of  $E_0$ . Figure 4.22 shows streamlines for  $\gamma = 2$  and  $E_0 = 720$  V/cm. The electrical stresses have more influence on the flow

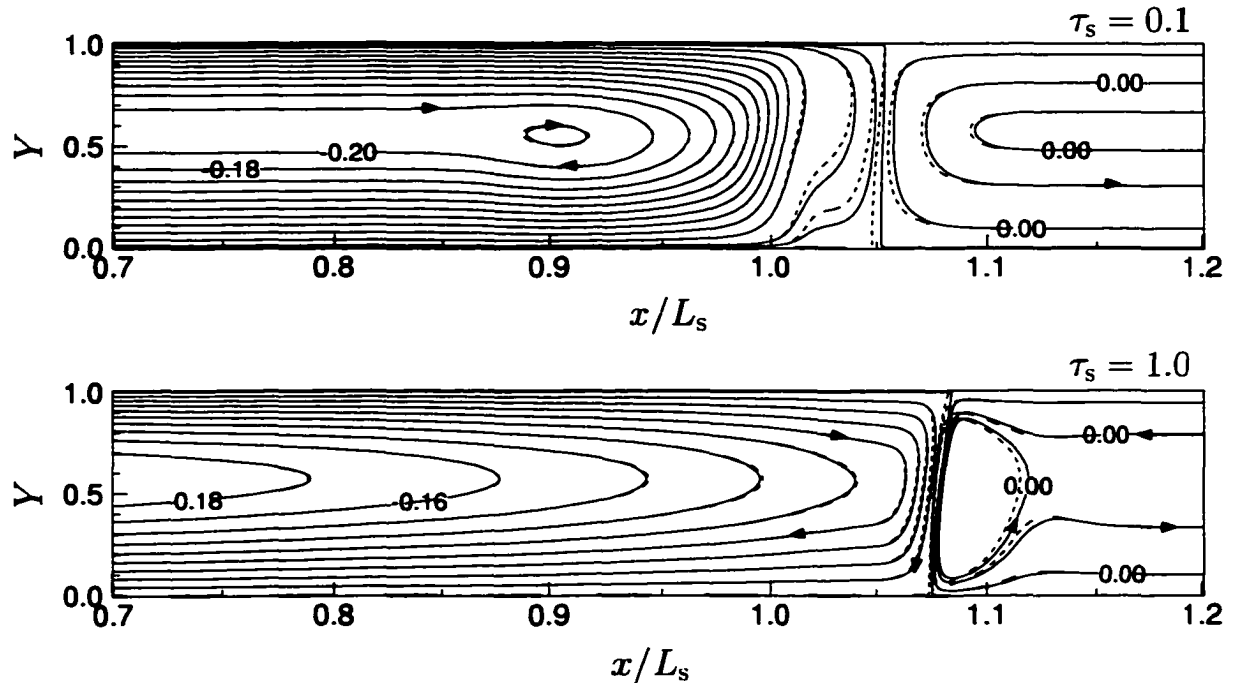


FIGURE 4.22. Streamlines for buffer B,  $\gamma = 2$ ,  $E_0 = 720$  V/cm at  $\tau_s = 0.1$  and  $\tau_s = 1.0$ . Unlabeled streamlines are shown for  $\Psi$  from  $-0.02$  to  $-0.16$  at intervals of  $0.02$ .  $i_0 = 5.2$  kA/m<sup>2</sup>,  $v_0^{eo} = 4.8$  mm/s. All other simulation conditions are as for Fig. 4.12.

at this condition than at  $\gamma = 5$  and  $E_0 = 180$  V/cm, and the effects last longer. Calculating these streamlines with a semianalytic solution requires inclusion of the electrical stresses in the lubrication approximation for  $\mathbf{v}$ . Unfortunately, Eq. (4.43) does not yield a solution for  $E_t$  that is accurate enough to approximate the electrical stresses in Eqs. (4.59)–(4.61). However, if  $\mathbf{E}$  is calculated numerically by the method

described in Chapter 3, Eqs. (4.59), (4.60), and (4.61) yield good approximations for  $u$ ,  $v$ , and  $\Psi$ . The streamlines are compared in Fig. 4.22 at  $\tau_s = 0.1$  and 1.

#### 4.5 CONCLUDING REMARKS

This analysis shows that for conditions typical of many microfluidic processes in straight channels,  $\mathbf{v}$  and  $\mathbf{E}$  can be calculated explicitly at any given time if the ion distributions are known. The semianalytic expressions for  $\mathbf{v}$  and  $\mathbf{E}$  reduce dynamic simulation times by about 3/4, and comparisons to complete numerical solutions of the prototype problem described in Chapter 3 show remarkable agreement for various electrolyte conditions. The scaling arguments indicate that the approximate solutions are reasonable for a fairly liberal parameter space delineated by  $(\frac{h}{b})^2 \ll 1$ ,  $(\frac{h}{b})^3 Pe \ll 1$ , and  $(\frac{h}{b}) Re \ll 1$ . Simulation results imply, however, that the approximation for  $E_t$  is not sufficiently accurate to calculate the nonlinear electrical stresses when they begin to change the character of the flow ( $(h/b)\lambda \geq O(1)$ ). Even with this limitation, the semianalytic expression for  $\mathbf{E}$  is useful for local field strengths at least up to 1 kV/cm. No such restriction is imposed on the approximation for  $\mathbf{v}$ , which can be used for  $(h/b)\lambda \geq O(1)$ , if the elliptic equation for  $\phi$  is solved numerically.

In microanalysis processes, solute distributions inherently evolve in time, so conductivity transition lengths  $b$  are generally not constant. The potential therefore exists for the approximations, although initially accurate, to fail during a transient sharpening of a zone boundary. Conversely, the approximations may fail initially,

but accurately represent the remainder of the system behavior (as in § 4.4.2) due to spreading of the zone boundaries. Fortunately, the 2-D electrically-driven fluid motion that creates the need to evaluate  $\mathbf{v}$  and  $\mathbf{E}$  in two dimensions, also disperses the electrolyte zones—usually enough to maintain  $(\frac{h}{b})^2 \ll 1$ , except during brief transients that have little effect on the solutions.

The analysis in this chapter also provides general information on the physical behavior of electrokinetic processes in capillaries. Applied electric fields in straight microchannels are essentially unidirectional, even when the transverse component of  $\nabla\sigma$  meets or exceeds the axial component. The transverse component of the electric field  $E_y$ , however, although orders of magnitude smaller than  $E_x$ , has an important effect on solutal transport when electrolyte ion mobilities are not approximately identical. Through the coupling of the ion balances to the electroosmotic velocity, this also affects the fluid motion.  $E_y$  impacts the flow even more dramatically when  $(h/b)\Gamma \geq O(1)$ , and the electrical stresses generate additional circulation patterns in conductivity transition regions. When the electrical stresses are not significant and  $(\frac{h}{b})^2$ ,  $(\frac{h}{b})^3 Pe$ , and  $(\frac{h}{b}) Re \ll 1$ , the axial fluid velocity profile has a simple parabolic form.

## CHAPTER 5

2-D ANALYTE TRANSPORT USING LUBRICATION  
APPROXIMATIONS FOR  $\mathbf{v}$  AND  $\mathbf{E}$ 

Microanalysis processes entail the manipulation of analytes and other solutal components in two and three dimensional geometries, for the purpose of determining mixture compositions. Describing multi-dimensional analyte transport is therefore fundamental to understanding microanalytical systems. Since the dominant transport mechanisms are electromigration, convection, and diffusion, faithful representations of the electric field and fluid motion are critical to a proper description of analyte motion. In Chapter 4, the classical lubrication approximation was enlisted to derive explicit semianalytic expressions for  $\mathbf{E}$  and  $\mathbf{v}$ , and their fidelity was demonstrated for buffer configurations used in FASS and high ionic strength electroosmotic pumping. By eliminating the need to numerically solve the two elliptic PDE's (Eqs. (3.9) and (3.22)) in the problem formulation (§3.1), the time evolution of 2-D unsteady electrically-driven flows and electric fields were predicted in about 1/4 the simulation time.

It is the purpose of this chapter to demonstrate that analyte concentrations are also accurately predicted in simulations employing the approximations developed in Chapter 4 for  $\mathbf{E}$  and  $\mathbf{v}$ . The simplified simulation scheme is useful in rectangular channels\*, when axial conductivity transition lengths  $b$  are long relative to the chan-

---

\*Similar approximations can be derived for cylindrical capillaries

nel half-width  $h$ . More specifically, the parameter space is limited to  $(h/b)^2 \ll 1$ ,  $(h/b)^3 Pe \ll 1$ , and  $(h/b)Re \ll 1$ , which, fortunately, is characteristic of many important microanalysis processes. Dynamic simulations of up to 6 component concentrations are accomplished, with insignificant approximation error, in less than half the time required to solve the full problem. With the approximations in Chapter 4, the simulation time is devoted almost entirely to solving the set of nonlinear algebraic equations for the pH and component speciation (Eqs. (3.1)–(3.4)), and therefore increases with the number of analytes. pH variations are often “small”, however, particularly in FASS and high-ionic-strength electroosmotic pumping, and thus additional approximations have the potential to improve the efficiency of this algorithm even more; because it is now the rate-limiting step, reducing the time required to calculate the pH will reduce the simulation time commensurately.

The presentation in this chapter begins in §5.1 with a summary of the approximate formulae and numerical approach used to calculate the time evolution of the analyte concentrations. The results are then evaluated in §5.2 by comparing approximate solutions to those produced by solving the full problem as described in Chapter 3. The chapter is concluded with some closing comments in §5.3.

## 5.1 APPROXIMATE FORMULATION

In Chapter 3, a general theory for multidimensional ion transport was presented with simulation methodology and initial and boundary conditions appropriate for

electrophoretic separations and related processes (§3.1 and §3.2). The theory was simplified in Chapter 4 by developing approximate solutions for  $\mathbf{v}$  and  $\mathbf{E}$  (§4.1–§4.3). In this section, the simplified problem formulation for electrically-driven ion transport in microchannels is summarized. This approximate method is used in §5.2 to compute unsteady analyte concentrations, which are compared with those obtained by the general method of Chapter 3.

The unsteady transport of analytes, as well as buffer components, is governed by conservation equations of the form:

$$\frac{\partial C_k}{\partial t} = -\nabla \cdot \mathbf{f}_k = -\nabla \cdot [(\bar{\mu}_k^e \mathbf{E} + \mathbf{v}) C_k - D_k \nabla C_k], \quad k = 1, 2, \dots, M. \quad (5.1)$$

In Eq. (5.1),  $t$  denotes time,  $\mathbf{v}$  is the fluid velocity,  $\mathbf{E}$  is the local electric field, and  $k_B T$  is the Boltzmann temperature;  $\omega_k$  and  $\bar{\mu}_k^e$  are, respectively, the hydrodynamic and effective electrophoretic mobility of component  $k$ . The component concentration is defined as

$$C_k \equiv \sum_{z=-N_k}^{P_k} n_k^z, \quad k = 1, 2, \dots, M, \quad (5.2)$$

where  $n_k^z$  is the concentration of the subspecies of the  $k$ th component with valence  $z$ .

The subspecies concentrations  $n_k^z$  are determined by mass-action and electroneutrality. For the protonation-deprotonation reactions of  $M$  solutal components, the mass-action equilibrium relations are

$$K_k^z \equiv \frac{[\text{H}^+] n_k^{z-1}}{n_k^z}, \quad \begin{cases} z = -N_k + 1, -N_k + 2, \dots, P_k \\ k = 1, 2, \dots, M, \end{cases} \quad (5.3)$$

where  $K_k^z$  is the equilibrium constant for the dissociation of the subspecies of the  $k$ th

component with valence  $z$ , and  $P_k$  and  $N_k$  are, respectively, the number of cationic and anionic subspecies of the  $k$ th component. Electroneutrality prevails on length scales large compared to the Debye screening length  $\kappa^{-1}$ , and thus

$$0 = \sum_{k=1}^M \bar{z}_k C_k + [\text{H}^+] - \frac{K_w}{[\text{H}^+]}, \quad (5.4)$$

if  $K_w \equiv [\text{H}^+][\text{OH}^-]$ , and

$$\bar{z}_k \equiv \frac{\sum_{z=-N_k}^{P_k} z n_k^z}{C_k}, \quad k = 1, 2, \dots, M. \quad (5.5)$$

To solve Eq. (5.1) for the component concentrations, expressions are required for  $\bar{\mu}_k^e$ ,  $\mathbf{E}$ , and  $\mathbf{v}$ . If  $M_p$  denotes the number of protein species,

$$\bar{\mu}_k^e = \begin{cases} [f(\kappa a_k)/(1 + \kappa a_k)] e \bar{z}_k \omega_k, & k = 1, 2, \dots, M_p \\ e \bar{z}_k \omega_k, & k = M_p + 1, M_p + 2, \dots, M, \end{cases} \quad (5.6)$$

where  $e$  is the charge on a proton ( $1.6 \times 10^{-19}$  C), and  $a_k$  is the (Stokes) radius of protein  $k$ ;  $f(\kappa a_k)$  is Henry's  $f$ -function [78]. For the configuration of Fig. 4.1,  $\mathbf{E}$  is given by

$$\mathbf{E}(\mathbf{x}, t) = E_x(x, t)\mathbf{e}_x + E_y(x, y, t)\mathbf{e}_y, \quad (5.7)$$

with orthogonal components approximated by

$$E_x(x, t) = \frac{i_0 - \langle i_x^D \rangle}{\langle \sigma \rangle} \quad (5.8)$$

and

$$E_y(x, y, t) = -\frac{1}{\sigma} \left\{ i_y^D + \int_0^y \frac{\partial}{\partial x} [\sigma E_x + i_x^D] \partial \xi \right\}, \quad (5.9)$$

if  $(h/b)^2\Gamma \ll 1$  and  $(h/b)^3Pe\Gamma \ll 1$ . In Eqs. (5.8) and (5.9),  $i_x^D \equiv \mathbf{i}^D \cdot \mathbf{e}_x$  and  $i_y^D \equiv \mathbf{i}^D \cdot \mathbf{e}_y$ , where

$$\mathbf{i}^D = ek_B T \left( \sum_{k=1}^M \omega_k \nabla \bar{z}_k C_k + \omega_H \nabla [\text{H}^+] - \omega_{\text{OH}} K_w \nabla [\text{H}^+]^{-1} \right) \quad (5.10)$$

is the diffusion current density;

$$\sigma = e^2 \left[ \sum_{k=1}^{M_p} \frac{f(\kappa a_k)}{1 + \kappa a_k} \bar{z}_k^2 \omega_k C_k + \sum_{k=M_p+1}^M \bar{z}_k^2 \omega_k C_k + \omega_H [\text{H}^+] + \omega_{\text{OH}} \frac{K_w}{[\text{H}^+]} \right] \quad (5.11)$$

is the local electrical conductivity, and  $\langle(\cdot)\rangle$  denotes a cross-sectional average of  $(\cdot)$ , viz.

$$\langle(\cdot)\rangle = \frac{1}{h} \int_0^h (\cdot) \partial y. \quad (5.12)$$

The nondimensional group

$$\Gamma \equiv \left( \frac{\Delta\omega_c}{\omega_c} \right) \left( \frac{\mu_0^{\text{eo}}}{\omega_c e} \right) \quad (5.13)$$

is typically less than or equal to  $O(1)$ .

If the local fluid velocity is written as

$$\mathbf{v}(\mathbf{x}, t) = v_x(x, y, t)\mathbf{e}_x + v_y(x, y, t)\mathbf{e}_y, \quad (5.14)$$

then, for  $(h/b)^2\Gamma \ll 1$ ,  $(h/b)Re \ll 1$ , and  $(h/b)\lambda\Gamma \ll 1$ ,

$$v_x(x, y, t) = \frac{1}{2} (v^{\text{eo}}(x, t) - V(t)) \left[ 3 \left( \frac{y}{h} \right)^2 - 1 \right] \quad (5.15)$$

and

$$v_y(x, y, t) = \frac{h}{2} \left[ \left( \frac{y}{h} \right) - \left( \frac{y}{h} \right)^3 \right] \frac{\partial v^{\text{eo}}(x, t)}{\partial x}. \quad (5.16)$$

In Eqs. (5.15) and (5.16),  $V(t)$  is the mean axial velocity, given by [8]

$$V(t) = \frac{1}{L_c} \int_0^{L_c} v^{\text{eo}}(x, t) \partial x, \quad (5.17)$$

and

$$v^{\text{eo}}(x, t) = \mu^{\text{eo}}(x, t) E_x(x, h, t) \quad (5.18)$$

is the electroosmotic slip velocity at the channel wall; the electroosmotic mobility  $\mu^{\text{eo}}$  is calculated as a function of electrolyte composition according to Eq. (3.13) (cf. §3.1.2 and [147]). The nondimensional group

$$\lambda \equiv \frac{\epsilon \epsilon_0 |\gamma - 1| E_0 h}{\mu \mu_0^{\text{eo}}} \quad (5.19)$$

is the ratio of the characteristic electrical stress to the characteristic viscous stress.

The problem is closed with the following boundary conditions on  $C_k$ :

$$\left. \begin{array}{l} C_k = C_k^{\text{a}} \quad \text{at } x = 0 \\ C_k = C_k^{\text{c}} \quad \text{at } x = L_c \\ \mathbf{f}_k \cdot \mathbf{n} = 0 \quad \text{at } y = \pm h \end{array} \right\}, \quad k = 1, 2, \dots, M, \quad (5.20)$$

where  $C_k^{\text{a}}$  and  $C_k^{\text{c}}$  are the constant running buffer concentrations at the anode and cathode, respectively.

The only differential equations in this simplified problem formulation are the coupled set of parabolic PDE's (Eq. (5.1)) for the component concentrations. These are solved numerically using 1-D finite difference algorithms and a Strang-type operator split [66, 27]. For buffer A, the transverse differential equation is solved using a second-order FCT algorithm (Appendix A), while for buffer B, the spatial derivatives are discretized with second-order central differences and the time derivative with a

first-order backward difference. For all simulations, the FCT algorithm is used to solve the axial problem. At each Runge-Kutta and operator-splitting step, the set of nonlinear algebraic equations (Eqs. (5.2)–(5.5)) governing the ionic speciation, is solved iteratively using an initial guess for the pH based on the previous step.

## 5.2 RESULTS AND DISCUSSION

To evaluate the approximate solutions, electroosmotic pumping of analytes in a high ionic strength sample zone is first simulated by setting  $1/\gamma = 10$  for buffer A in the prototype configuration of Fig. 3.1. An amino acid (1  $\mu M$  histidine (HIS)) and two proteins (1  $\mu M$  hemoglobin (HEM) and ferritin (FER)) are included in the sample zone. These analytes have been chosen because they span a broad range of diffusivities ( $O(10^{-7} - 10^{-5})$  cm<sup>2</sup>/s), a parameter that has an important effect on the character of the concentration fields. Although wall adsorption is not considered here, the proteins have been included because they have diffusivities on the order of  $10^{-7}$  to  $10^{-6}$  cm<sup>2</sup>/s. Component properties are provided in Tables 3.1 and 3.2. As in the last two chapters, the geometric lengths of the system are  $L_e = L_s = 1$  mm,  $h = 20$   $\mu m$ , and  $L_c = 5$  cm. A constant current is maintained by requiring  $i_0 = 8000$  A/m<sup>2</sup> in the running buffer, corresponding to  $E_0 = 180$  V/cm. The approximate simulation results are calculated by the method described in §5.1, except  $E_y$  is neglected.

The analyte concentrations in the sample zone at  $\tau_s = 2$  are shown in Figure 5.1 for  $h/b_0=1/6$ . The approximate concentration contours (dashed) are essentially in-

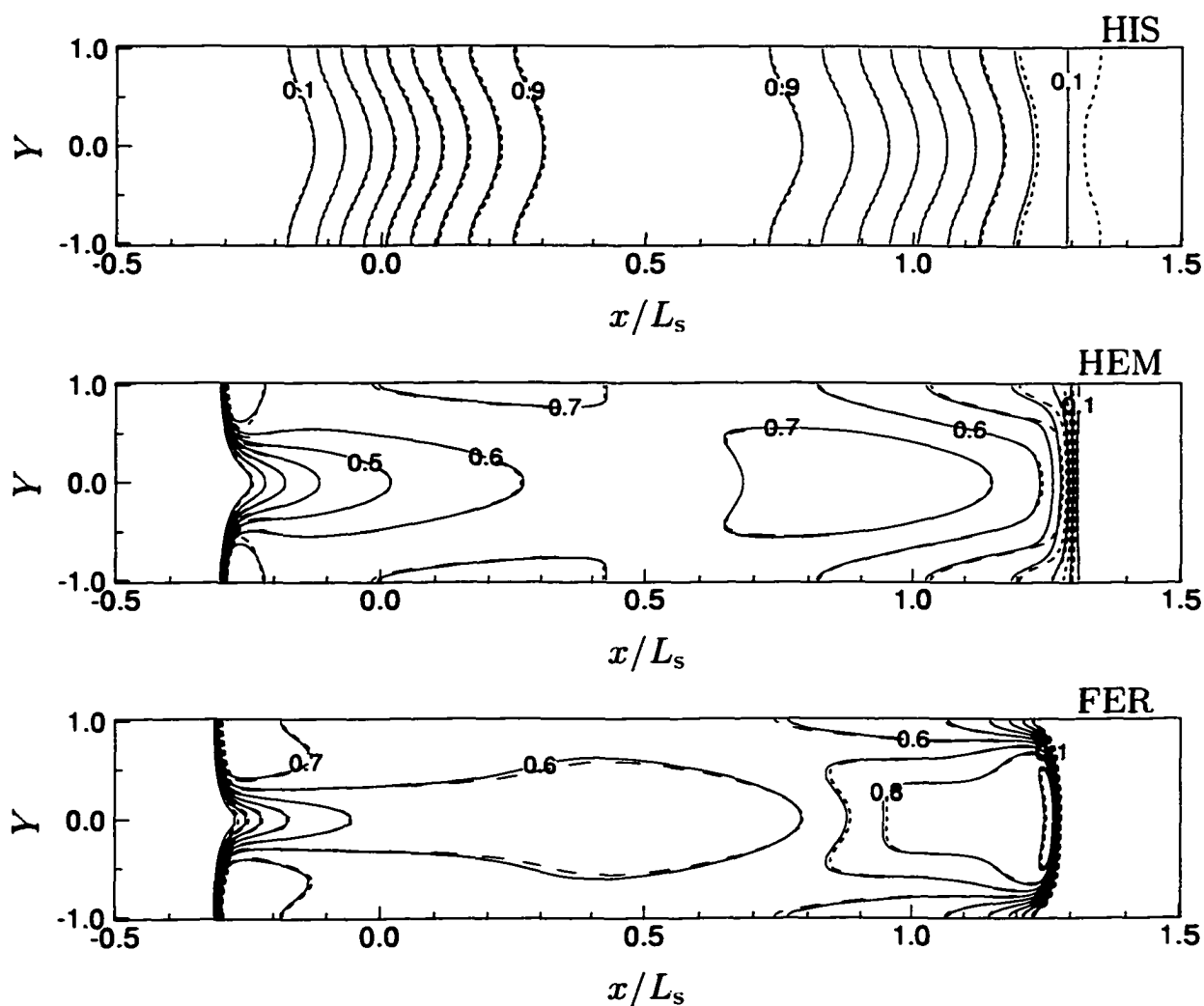


FIGURE 5.1. Analyte concentration contours for electroosmotic pumping with buffer A calculated by complete numerical solution (solid) and approximate solution (dashed).  $h/b_0 = 1/6$ ;  $\tau_s = 2$ ;  $1/\gamma = 10$ . Running buffer: 200 mM cacodylic acid, 100 mM Tris;  $\sigma_0 = 0.452$  S/m;  $E_0 = 180$  V/cm;  $i_0 = 8$  kA/m<sup>2</sup>;  $v_0^{eo} = 0.802$  mm/s; pH = 6.2.  $L_s = 1$  mm,  $L_c = 5$  cm,  $h = 20$   $\mu$ m. Contours are shown for  $\hat{C}$  from 0.1 to 0.9.

distinguishable from those generated by solving the full problem (solid), over most of the analyte domains. The only significant deviation is in the downstream region of the histidine zone where  $\hat{C} \equiv C/C_0=0.1$ . The contour for  $\hat{C}=0.1$  should have no observable curvature because in this region the histidine has migrated out of the high conductivity zone into the uniform buffer region where the flow is very weak (cf. Chapter 3). The curvature of the approximate contour for  $\hat{C}=0.1$  reflects an overprediction of the fluid velocity in this region. Figure 5.2 shows the results of this simulation with  $h/b_0=2$  instead of  $1/6$ . Although the approximations for  $\mathbf{v}$  and  $\mathbf{E}$  fail for  $(h/b)^2 \geq O(1)$ , the approximate analyte concentration fields match those produced by the solution of the full problem about as well as for  $h/b_0=1/6$ . The approximations work because  $(h/b)^2$  is  $O(1)$  for but a short interval; the zone boundaries are rapidly dispersed by the fluid circulation, and little error is introduced during the transient. It should be noted, by comparison of Figs. 5.1 and 5.2, that the analyte concentration fields at  $\tau_s = 2$  are insensitive to the initial zone boundary length up to at least  $h/b_0 = 1/6$ .

In Chapter 4, it was shown that computation of  $E_y$  significantly improved the accuracy of  $\mathbf{v}$  and  $\sigma$  in simulations with buffer B. This comes at an insignificant computational cost because an explicit expression for  $E_y$  (Eq. (5.9)) follows from the same approximations used to derive the leading order solution for  $E_x$  (Eq. (5.8)). To evaluate the accuracy of the approximations in simulations of analyte transport with a different buffer, electroosmotic pumping at  $1/\gamma = 50$  and analyte stacking at  $\gamma = 2$  is simulated with buffer B.  $h/b_0$  is set to  $1/6$ , and all other simulation conditions are the

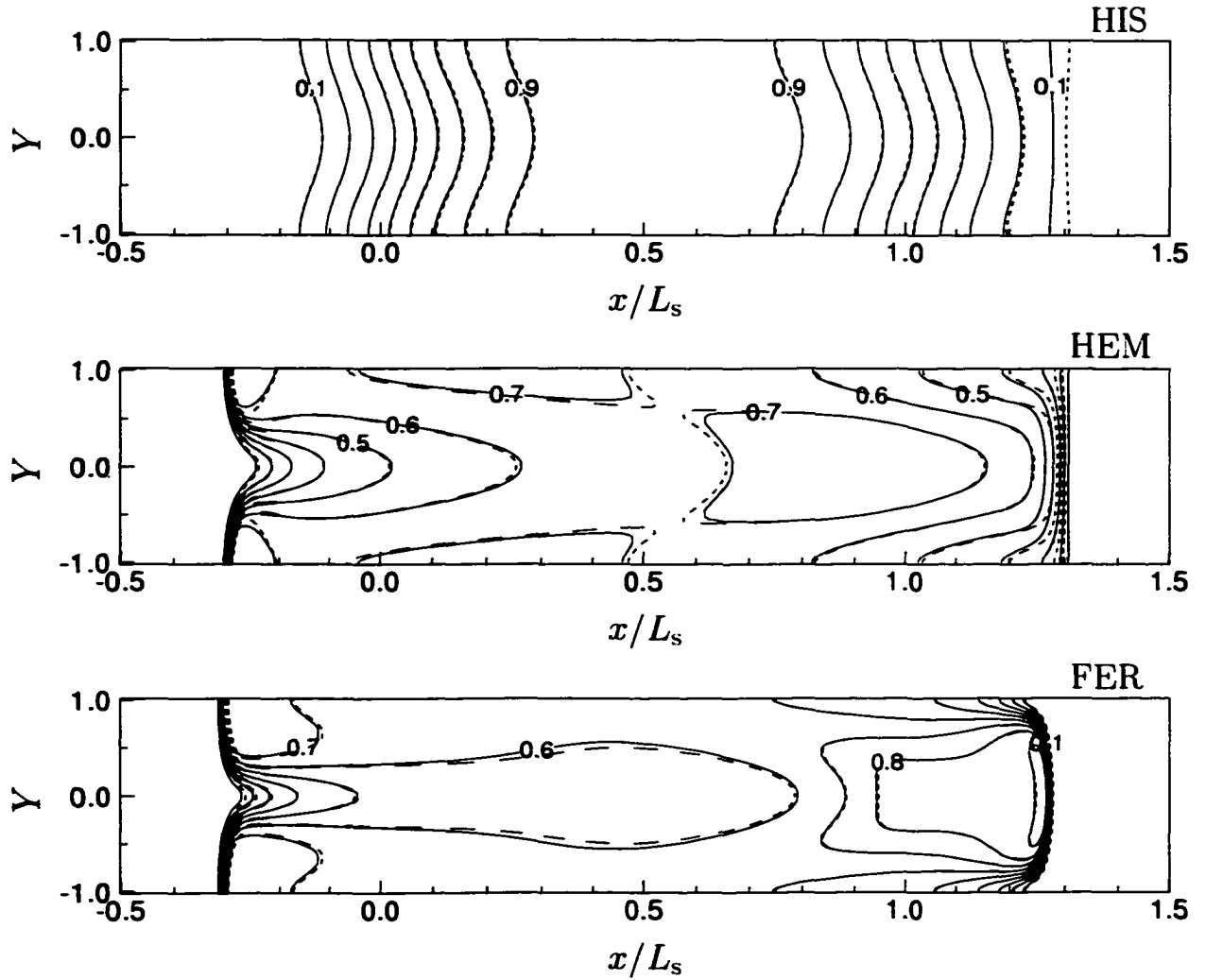


FIGURE 5.2. Analyte concentration contours for electroosmotic pumping with buffer A calculated by complete numerical solution (solid) and approximate solution (dashed).  $h/b_0 = 2$ . All other simulation conditions are as for Fig. 5.1. Contours are shown for  $\hat{C}$  from 0.1 to 0.9.

same as for the simulations with buffer A. The formulation in §5.1, including Eq. (5.9) for  $E_y$ , is used for the approximate simulation method. Figures 5.3 and 5.4 show that the approximate analyte concentration fields are essentially indistinguishable from those obtained by solving the full problem.

The results of this evaluation are summarized in Table 5.1, which presents the

TABLE 5.1. Approximation errors for analyte concentrations

Buffer	$\gamma$	$h/b_0$	$\varepsilon_{av}^c \times 10^3$		
			HIS	HEM	FER
A	1/10	1/6	3.73	6.07	8.91
		2	3.22	7.48	8.77
B	1/50	1/6	0.31	2.29	2.94
		2	3.91	5.98	3.81

approximation error  $\varepsilon^c \equiv | \text{Approximate } \hat{C} - \text{Numerical } \hat{C} |$  averaged over the analyte zone  $\varepsilon_{av}^c$ . The analyte zone is defined as the region where the cross-sectionally averaged analyte concentration is greater than or equal to 1% of  $C_0$ . The errors are slightly higher for the proteins, which exhibit more cross-sectional variation than arginine, but  $\varepsilon_{av}^c$  is less than 0.01 for all the simulations. It is important to note that although the comparisons in this chapter were made at  $\tau_s = 2$ , the results of Chapter 4 indicate that the error in  $v$  drops off sharply for  $\tau_s > 0.5$  because of the spreading of the sample zone boundaries. Thus, it is anticipated that the accuracy of the approximate analyte zones will not diminish for  $\tau_s > 2$ .

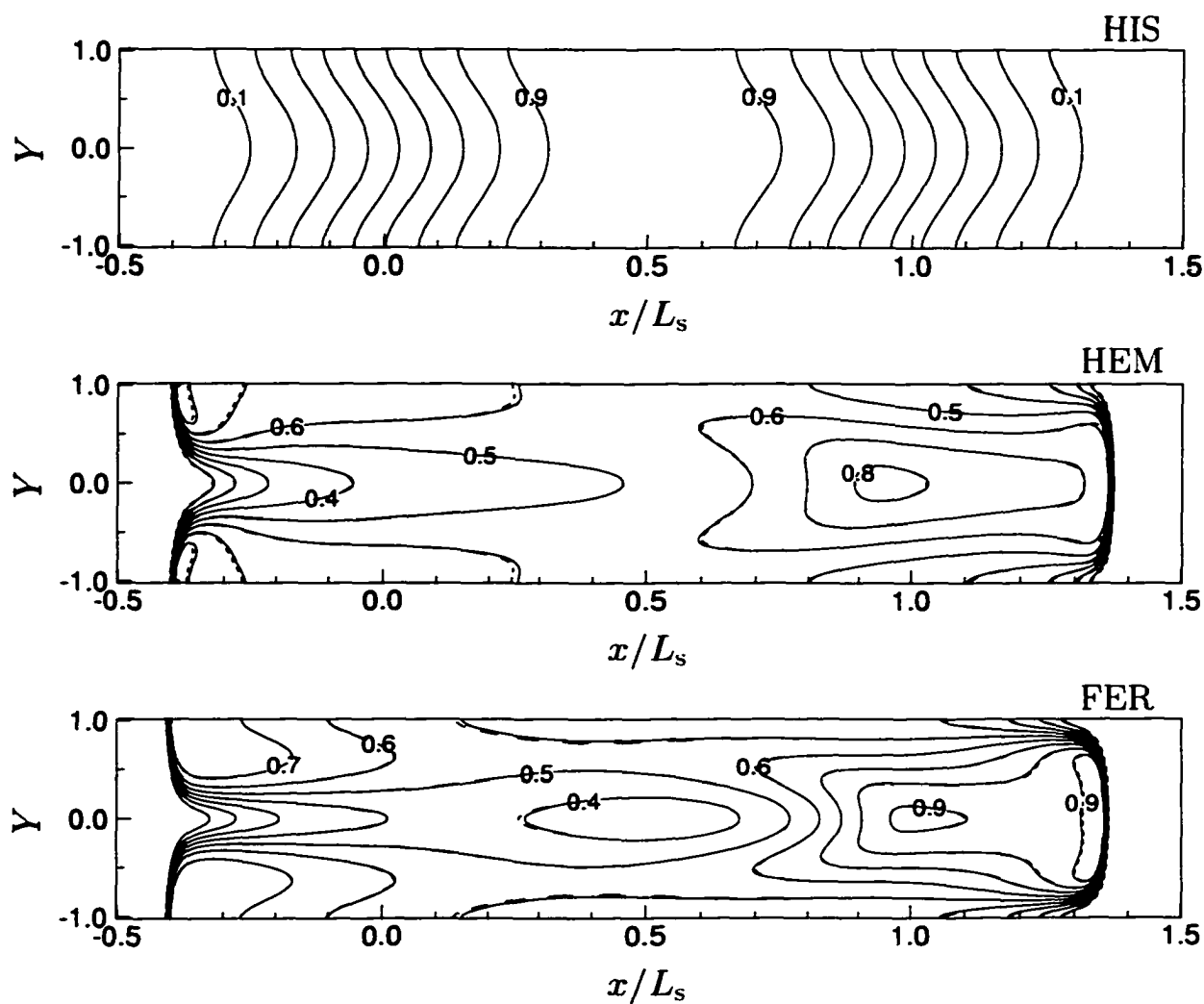


FIGURE 5.3. Analyte concentration contours for electroosmotic pumping with buffer B calculated by complete numerical solution (solid) and approximate solution (dashed).  $h/b_0 = 1/6$ ;  $\tau_s = 2$ ;  $1/\gamma = 50$ . Running buffer: 20 mM ACES, 9 mM NaOH;  $\sigma_0 = 0.072$  S/m;  $E_0 = 180$  V/cm;  $i_0 = 1.3$  kA/m<sup>2</sup>;  $v_0^{eo} = 1.2$  mm/s; pH = 6.2.  $L_s = 1$  mm,  $L_c = 5$  cm,  $h = 20$   $\mu$ m. Contours are shown for  $\hat{C}$  from 0.1 to 0.9.

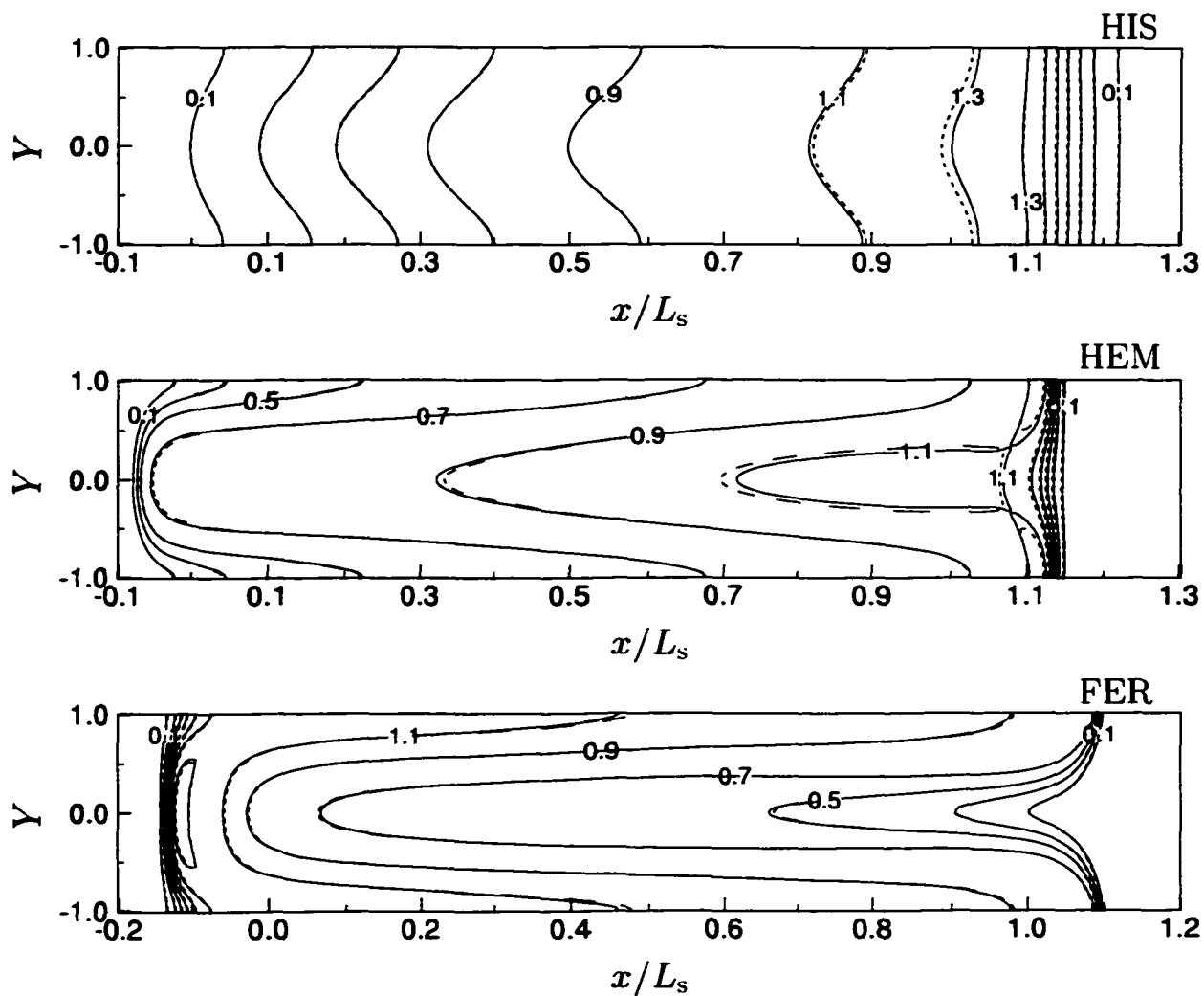


FIGURE 5.4. Analyte concentration contours for sample stacking with buffer B calculated by complete numerical solution (solid) and approximate solution (dashed).  $h/b_0 = 1/6$ ;  $\tau_s = 2$ ;  $\gamma = 2$ . All other simulation conditions are as for Fig. 5.3. Contours are shown for  $\hat{C}$  from 0.1 to 0.9.

### 5.3 CONCLUDING REMARKS

Two-dimensional analyte concentration profiles in discontinuous buffers are accurately approximated using seminanalytic expressions for the local fluid velocity and electric field. The simplified problem formulation applies to electrokinetic motion in rectangular channels where  $(h/b)^2 \ll 1$ ,  $(h/b)^3 Pe \ll 1$ , and  $(h/b)Re \ll 1$ , and similar formulae can be derived for cylindrical capillaries. The results indicate that transient deviations from this parameter space may have an insignificant effect on the accuracy of the approximations, as, for example, when initially sharp conductivity gradients are dispersed by electrically-driven flow. With the model described in §5.1, numerical solutions are realized in less than half the simulation time. If pH variations can be neglected, simulation times can be reduced by another factor of 3. When pH dynamics are important, solving a large set of nonlinear algebraic equations becomes the rate-limiting step, and computational improvement is limited by this calculation. However, the algorithm used here to solve for the pH is not sophisticated; computational optimization and/or approximations similar to those developed for  $\mathbf{v}$  and  $\mathbf{E}$  are likely to reduce simulation times substantially more.

## CHAPTER 6

1-D MACROTRANSPORT REPRESENTATION OF SOLUTE  
CONSERVATION

In the past two decades, 1-D simulations have provided much insight into the fundamental physics and chemistry of electrophoretic separations [64, 51, 55, 136, 135, 108, 87, 113]. Unfortunately, these studies omit important effects of 2-D fluid motion, such as solute dispersion in regions of nonuniform electrolyte. The 2-D simulation methods described in Chapters 3–5 of this dissertation provide quantitative information on component dispersion, as well as detailed descriptions of the spatio-temporal evolution of the field variables, but require more computational expense and lack the simplicity of the 1-D representations of electrophoretic separations. Macrotransport representations that incorporate the effects of fluid motion into a 1-D formulation of solute transport have been demonstrated, however, for many physical processes. This began with the classical work of Taylor [144] and Aris [10]. Taylor used cross-sectional averaging and order-of-magnitude scaling arguments to derive a dispersion coefficient for late-time solute transport in unidirectional Poiseuille flow; Aris more rigorously developed the same result by introducing the method of moments. Since then, their work has been extended to a variety of more complicated systems, including, e.g., microfluidic geometries [12, 68, 69], rivers and streams [118, 161, 168], branched channels [139, 60], oscillatory flows [103, 139, 152], and fractured and porous

media [33, 38, 49, 53].

In Chapter 4, it was shown that applied electric fields and electrically-driven flows in straight channels are quasi-steady and quasi-developed if  $(\frac{h}{b})^2 \ll 1$ ,  $(\frac{h}{b}) Re \ll 1$ , and  $(\frac{h}{b})^3 Pe \ll 1$ . The simple form of the semianalytic solutions thus obtained for  $\mathbf{E}$  and  $\mathbf{v}$  suggest that solute transport in microanalysis processes might be amenable to a macrotransport analysis similar to those presented by other researchers for 2-D flows [35, 47, 83, 94, 142]. As in those configurations, and in contrast to the classical problem of Taylor [144], electrokinetic flows in heterogeneous buffers vary in the streamwise direction, and so dispersion is non-Gaussian. The solute transport described here also includes electromigration and is nonlinearly coupled to the fluid motion, which is therefore unsteady.

It is the purpose of this chapter to construct a 1-D representation, in terms of cross-sectionally averaged field variables, of electrokinetic transport in heterogeneous buffer systems. Such macrotransport simulations do not provide information about the spatial details of the fluid motion or solute transport, but in the context of chemical analysis, cross-sectionally averaged values are the most important output; average analyte concentrations are measured at the detector, and from these data, mixture compositions are deduced. Thus 1-D macrotransport simulations can potentially be used to rapidly explore the impact of operational variables on separation or other process efficacy. The 1-D representations reduce simulation times by an order of magnitude or more relative to their 2-D counterparts, and consequently permit analysis of problems that are impractical to solve in two dimensions, such as FASS for

$\gamma \gg 1$ .

In the spirit of Stone and Brenner's [142] derivation of a spatially-variable dispersion coefficient for radial flow between parallel plates, the development here follows the intuitive approach of Taylor [144]. Our analysis differs from theirs in that an electromigrational flux must be handled, and that the form of the fluid velocity field is slightly different. The essential result is a convective dispersion coefficient of the same form as those of Taylor and Stone and Brenner, but because the flow in this system is unsteady as well as two-dimensional, the dispersion coefficient varies spatiotemporally. Moreover, the solution here for the cross-sectionally averaged solute concentration fields requires a different method. The effective 1-D mass balances developed in this chapter are nonlinear and fully-coupled, and so must be solved numerically, as in previous 1-D studies of electrophoretic separations [64, 51, 55, 136, 135, 108, 87, 113].

In addition to developing the formulation, the simple 1-D model is evaluated with comparisons to solutions of the full problem, and then applied to explain previously-published experimental FASS data [36]. It is first shown that the 1-D simulations accurately capture cross-sectionally averaged concentrations, conductivities, and electric fields for several buffer configurations of the prototype problem first discussed in Chapter 3. The FASS experiments published by Burgi and Chien [36] are then revisited to explain a lack of agreement between their data for  $\gamma = 100$  and their closed-form analyte dispersion model. Scaling arguments indicate that the integrity of high field sample plugs shorter than about 14 cm is not preserved for the conditions of their experiments when  $\gamma \gg 1$ . Simulation results clearly demonstrate that

the non-Gaussian dispersion of this plug, not accounted for in their model, has an important effect on analyte dispersion for  $\gamma > 10$ .

In the presentation that follows, the approximate 1-D formulation is developed in §6.1, followed by the evaluation in §6.2. The approximate method is then used in §6.3 to explain the experimental FASS data presented by Burgi and Chien [36]. The chapter is closed in §6.4 with some concluding remarks.

## 6.1 MACROTRANSPORT APPROXIMATION

In this section, an effective 1-D representation of the solute balances is developed. This is initiated by cross-sectionally averaging Eq. (3.5), which is written in the coordinate system of Fig. 4.1 as

$$\frac{\partial C_k}{\partial t} = -\frac{\partial f_{x,k}}{\partial x} - \frac{\partial f_{y,k}}{\partial y}, \quad k = 1, 2, \dots, M, \quad (6.1)$$

where  $f_{x,k}$  and  $f_{y,k}$  are  $\mathbf{f}_k \cdot \mathbf{e}_x$  and  $\mathbf{f}_k \cdot \mathbf{e}_y$ , respectively. Integrating over  $y$  from 0 to  $h$  and dividing by  $h$  yields\*

$$\frac{\partial \langle C_k \rangle}{\partial t} = -\frac{\partial \langle f_{x,k} \rangle}{\partial x} = -\frac{\partial}{\partial x} \langle \bar{\mu}_k^e E_x C_k \rangle - \frac{\partial}{\partial x} \langle v_x C_k \rangle + \omega_k k_B T \frac{\partial^2 \langle C_k \rangle}{\partial x^2}, \quad (6.2)$$

where the integral of  $\partial f_{y,k} / \partial y$  vanishes because  $f_{y,k}$  vanishes at 0 and  $h$ . In terms of scaled variables, Eq. (6.2) reads

$$\frac{\partial \langle \Theta_k \rangle}{\partial \tau} = -\frac{\omega_c e}{\mu_0^e} \frac{\partial}{\partial X} \langle M_k^e E_a \Theta_k \rangle + \left( \frac{h}{b} \right) \frac{1}{Pe_k} \frac{\partial^2 \langle \Theta_k \rangle}{\partial X^2} - \frac{\partial}{\partial X} \langle u \Theta_k \rangle. \quad (6.3)$$

---

\*For the remainder of this Chapter, it will be assumed that equations with variables that are subscripted with the index  $k$ , are written for  $k = 1, 2, \dots, M$ , and hereafter this statement will be dropped.

This equation is in 1-D form, but to be useful, it must be transformed such that the dependent variable  $\Theta_k$  is eliminated in favor of  $\langle \Theta_k \rangle$ .

The electromigration term is arranged in the proper form by using scaling arguments to show that  $E_a$  and  $M_k^e$  are, to leading order, independent of  $Y$ . As demonstrated in Chapter 4,  $E_a \approx \langle E_a \rangle \approx E_a^{(0)}(X, \tau)$  (given by Eq. (4.40)) if  $(h/b)^2 \ll 1$ ,  $(h/b)Re \ll 1$ , and  $(h/b)^3 Pe \ll 1$ .  $M_k^e$  varies locally with the pH and (for macroions, such as proteins) the ionic strength. Since

$$M_k^e = F(a\kappa) \bar{z}_k \omega_k / \omega_c, \quad (6.4)$$

where  $F(a\kappa) \equiv f(a\kappa) / (1 + a\kappa)$  (see Eq. (3.6)), then

$$\delta M_k^e \sim \omega_k / \omega_c [F(a\kappa) \delta \bar{z}_k + \bar{z}_k \delta F(a\kappa)]. \quad (6.5)$$

The ionic strength dependence is manifested in  $F(a\kappa)$ , where  $\kappa$  scales on  $\sqrt{I}$ . Cross-sectional ionic strength variations scale on cross-sectional ion concentration variations, which are  $O[(h/b)Pe]$ . For  $a\kappa \leq O(1)$ , the dependence of  $F(a\kappa)$  on ionic strength is weak (viz.  $\delta F(a\kappa) \ll \delta I$ ). So for  $(h/b)Pe \leq O(1)$ , we anticipate little cross-sectional variation in  $F(a\kappa)$ .

The mean valence  $\bar{z}_k$  is a function of pH, and the sensitivity varies dramatically with component properties (pK's) and the system pH. The sensitivity of the pH to the component concentrations varies dramatically with the buffer composition. It is therefore problematic to quantify  $\delta \bar{z}_k$  in terms of the system characteristic scales. In general, we anticipate insignificant cross-sectional pH variations for many microanalysis processes, since, due in part to buffering, even the axial pH often varies by only

$O(10^{-1})$ . In such instances,  $M_k^e \approx \langle M_k^e \rangle$ , and Eq. (6.3) reads

$$\frac{\partial \langle \Theta_k \rangle}{\partial \tau} = -\frac{\omega_c e}{\mu_0^{\text{eo}}} \frac{\partial}{\partial X} [\langle M_k^e \rangle E_a^{(0)} \langle \Theta_k \rangle] + \left(\frac{h}{b}\right) \frac{1}{Pe_k} \frac{\partial^2 \langle \Theta_k \rangle}{\partial X^2} - \frac{\partial}{\partial X} \langle u \Theta_k \rangle. \quad (6.6)$$

To derive an expression for the average convective flux

$$\langle u \Theta_k \rangle = \left(\frac{h}{b}\right) Pe_k \langle u \Theta'_k \rangle = \frac{1}{2} \left(\frac{h}{b}\right) Pe_k u^{\text{eo}}(X, \tau) \int_0^1 (3Y^2 - 1) \Theta_k \partial Y \quad (6.7)$$

in terms of  $\langle \Theta_k \rangle$ , we follow the intuitive approach introduced by Taylor [144], and also used by Stone and Brenner [142] for a 2-D flow. Because of the similarity to those works, we only point out the major steps and justify the approximations for the configuration considered here. Integrating Eq. (6.7) by parts yields

$$\langle u \Theta'_k \rangle = -\frac{1}{2} u^{\text{eo}} \int_0^1 [Y^3 - Y] \frac{\partial \Theta'_k}{\partial Y} \partial Y. \quad (6.8)$$

An approximate expression for  $\partial \Theta'_k / \partial Y$  is constructed with a scale analysis of the full 2-D solute mass balances. By substituting  $\Theta_k = \langle \Theta_k \rangle + \left(\frac{h}{b}\right) Pe_k \Theta'_k$  into Eq. (4.31) and subtracting Eq. (6.6), it can be shown that<sup>†</sup>

$$u \frac{\partial \langle \Theta_k \rangle}{\partial X} \approx \frac{\partial^2 \Theta'_k}{\partial Y^2} \quad (6.9)$$

if  $(h/b)Pe_k \ll 1$ ,  $(h/b)Pe_k(\omega_c e / \mu_0^{\text{eo}}) \ll 1$ , and  $\Delta\omega_c / \omega_c \ll 1$ . It follows then that

$$\frac{\partial \Theta'_k}{\partial Y} \approx u^{\text{eo}} (Y^3 - Y) \frac{\partial \langle \Theta_k \rangle}{\partial X}, \quad (6.10)$$

<sup>†</sup>In this scaling,  $t$  is scaled on the characteristic time for convection across the zone boundary. We also need to consider concentration changes resulting from the unsteady fluid motion. This is characterized by the time scale for dispersion of the zone boundaries, given by  $50Db^2/(\gamma - 1)^2(u_0^{\text{eo}})^2h^2$ . If  $t$  is rescaled on this characteristic time, the time-dependent term in Eq. (4.31) is negligible for  $(1/50)(h/b)^2Pe_k^2 \ll 1$ , which is always true for  $(h/b)Pe_k \ll 1$ . Thus no additional constraints on the parameter space are required to ensure that the time scale for cross-sectional diffusion is small relative to the time-scale for changes in the fluid velocity.

and after substituting Eq. (6.10) into Eq. (6.8) and integrating, that

$$\langle u\Theta'_k \rangle = -\frac{2}{105} (u^{\text{eo}})^2 \frac{\partial \langle \Theta_k \rangle}{\partial X}. \quad (6.11)$$

Conservation equations in terms of the cross-sectionally averaged component concentrations are thus obtained, viz.

$$\begin{aligned} \frac{\partial \langle \Theta_k \rangle}{\partial \tau} &= -\frac{\omega_c e}{\mu_0^{\text{eo}}} \frac{\partial}{\partial X} [\langle M_k^e \rangle E_a^{(0)} \langle \Theta_k \rangle] + \left(\frac{h}{b}\right) \frac{1}{Pe_k} \frac{\partial^2 \langle \Theta_k \rangle}{\partial X^2} \\ &+ \left(\frac{h}{b}\right) \frac{\partial}{\partial X} \left[ \frac{1}{Pe_k^c(X, \tau)} \frac{\partial \langle \Theta_k \rangle}{\partial X} \right]. \end{aligned} \quad (6.12)$$

In Eq. (6.12),

$$Pe_k^c(X, \tau) \equiv \frac{|\gamma - 1| E_0 \mu_0^{\text{eo}} b}{D_k^c(X, \tau)}, \quad (6.13)$$

where the dispersion coefficient

$$D_k^c(X, \tau) \equiv \frac{2h^2}{105D_k} [v^{\text{eo}}(X, \tau) - V(\tau)]^2 \quad (6.14)$$

is nearly identical to that for Pousieulle flow in rectangular geometry [33]. The important distinction is that the constant mean Pousieulle flow velocity is here replaced by  $v^{\text{eo}} - V$ , which is a function of  $X$  and  $\tau$  through its dependence on  $\mathbf{E}$ ,  $I$ ,  $[M^+]$ , and pH. Thus the coupling of the fluid motion to the solute macrotransport is manifested in this dispersion coefficient. For a cylindrical capillary, the dispersion coefficient is calculated similarly as

$$D_k^c(X, \tau) \equiv \frac{h^2}{48D_k} [v^{\text{eo}}(X, \tau) - V(\tau)]^2 \quad (\text{cylindrical capillary}) \quad (6.15)$$

The dispersion coefficients in Eqs. (6.14) and (6.15) obviate the need to calculate the fluid velocity in order to compute the cross-sectionally averaged solute concentrations. Eqs. (6.12) are solved here numerically using the explicit FCT algorithm<sup>‡</sup> described in Appendix A. The cross-sectionally averaged conductivity is calculated as

$$\begin{aligned} \langle \sigma \rangle = e^2 & \left[ \sum_{k=1}^{M_p} F(\kappa a_k) \langle \overline{z_k^2} \rangle \omega_k \langle C_k \rangle + \sum_{k=M_p+1}^M \langle \overline{z_k^2} \rangle \omega_k \langle C_k \rangle + \omega_H \langle [H^+] \rangle \right. \\ & \left. + \omega_{OH} \frac{K_w}{\langle [H^+] \rangle} \right] \end{aligned} \quad (6.16)$$

which permits  $E_a^{(0)}$  to be calculated from Eq. (4.40).  $\langle M_k^e \rangle$ ,  $\langle \overline{z_k^2} \rangle$ , and  $F(\kappa a_k)$  are calculated by computing  $I$  and pH as a function of cross-sectionally averaged concentrations, and  $u^{e0}$  is calculated from Eq. (3.12) to incorporate the effects of the fluid motion into the dispersion coefficient. The remainder of the simulation scheme follows that described in Appendix A, with all cross-sectionally nonuniform variables replaced with cross-sectionally averaged values.

---

<sup>‡</sup>With convective dispersion included in the macrotransport representation of the solute transport, the component balances are often parabolic, rather than hyperbolic, at electric field strengths typically used in practice. Consequently, FCT is sometimes unnecessary, and simpler numerical schemes can be used. When dispersion dominates the transport, an implicit method can easily be implemented to prevent severe restrictions on the time step.

## 6.2 EVALUATION

### 6.2.1 BUFFER A

The accuracy of the macrotransport representation described above is examined by comparing effective 1-D simulation results to those obtained by solving the full problem as in Chapter 3. Electroosmotic pumping is first simulated by setting  $1/\gamma = 5$  for buffer A in the prototype configuration of Fig. 3.1. The concentrations of two analytes are examined. ARG and FER, initialized at  $1 \mu M$ , represent, respectively, analytes with relatively high ( $5.8 \times 10^{-6} \text{ cm}^2/\text{s}$ ) and low ( $3.2 \times 10^{-7} \text{ cm}^2/\text{s}$ ) diffusivities. The geometric lengths of the system are  $L_e = L_s = 1 \text{ mm}$ ,  $h = 20 \mu\text{m}$ , and  $L_c = 5 \text{ cm}$ . The electric field in the running buffer is fixed at  $E_0 = 180 \text{ V/cm}$  by maintaining a constant current of  $i_0 = 8000 \text{ A/m}^2$ .

The time evolution of the analyte concentrations is presented in Fig. 6.1. The approximate ARG concentrations (panel a) are essentially indistinguishable from those calculated by solving the full problem. FER concentrations (panel b) are initially not predicted as well using the macrotransport representation, but the accuracy increases with  $\tau_s$ , and the error is insignificant for  $\tau_s \geq 5$ . At short times, the macrotransport representation is inaccurate because FER, the slower diffusing species, requires more time to sample the cross-section than ARG, which has more than an order of magnitude higher diffusivity. The relevant time scale ratios for all the configurations discussed in this chapter, are provided in Tables 6.1 and 6.2. As in Chapter 4, the axial length scale is taken to be  $L_s$  although it is initially  $b_0$ ; the axial transition

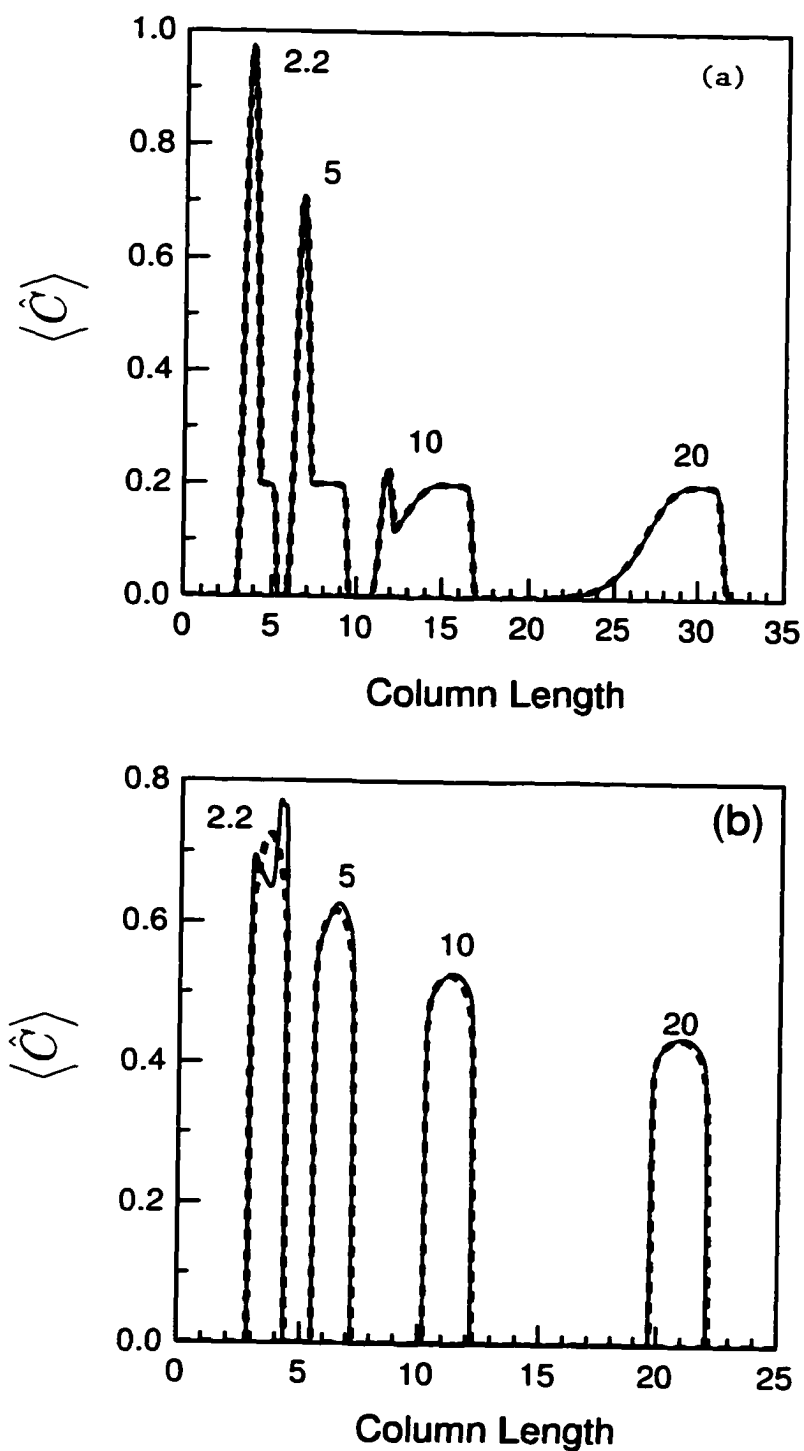


FIGURE 6.1. Cross-sectionally-averaged analyte concentrations for electroosmotic pumping at selected values of  $\tau_s$ . (a) ARG, (b) FER. Complete solution (solid); macrotransport representation (dashed).  $h/b_0 = 1/6$ ;  $1/\gamma = 5$ ; Running buffer A (200 mM cacodylic acid, 100 mM Tris);  $\sigma_0 = 0.452$  S/m;  $E_0 = 180$  V/cm;  $i_0 = 8$  kA/m<sup>2</sup>;  $v_0^{\text{eo}} = 0.802$  mm/s; pH = 6.2.  $L_s = 1$  mm,  $L_c = 5$  cm,  $h = 20$   $\mu$ m.

length is only transiently  $b_0$ , as it is quickly dispersed by the fluid motion to  $O(L_s)$ . Even though, for ARG,  $(h/L_s)Pe_k$  is only slightly less than one, the approximate concentrations agree with the full solution.  $(h/L_s)Pe_k \gg 1$  for FER which explains the poor agreement at  $\tau_s = 2.2$ . FER does not have time to sufficiently sample the channel cross-section as it is transported axially by convection and electromigration. As  $\tau_s$  increases, however, the zone boundary apparently spreads to a sufficiently large length scale for FER to be approximated by the 1-D representation.

TABLE 6.1. Dimensionless groups for 1-D simulations

Buffer	$\gamma$	$Re$	$Pe$	$\lambda$	$\Gamma$	$h/L_s$	$\Delta\omega_c/\omega_c$
A	1/5	0.012	21	4	0.080	0.020	0.04
	5	0.060	100	2	0.080	0.020	0.04
B	1/50	0.024	23	4	0.820	0.020	0.40
	5	0.099	93	15	0.820	0.020	0.40
C	2	0.011	15	41	0.006	0.005	0.02
	4	0.033	45	120	0.006	0.005	0.02
	8	0.074	100	280	0.006	0.005	0.02
	100	0.620	860	2600	0.006	0.005	0.02

TABLE 6.2. The critical dimensionless group for solutes in 1-D simulations

Buffer	$\gamma$	ARG	HIS	FER	CAC	Tris	Na <sup>+</sup>	ACES	MES
A	1/5	0.4		8	0.4	0.4			
	5	2	2		2	2			
B	1/50	0.8		14			0.3	0.6	
	5	3	3				1	2	
C	2	0.09	0.07						0.07
	4	0.3	0.2						0.2
	8	0.6	0.5						0.5
	100	5	4						4

Figure 6.1 also shows the non-Gaussian dispersion of the analytes. ARG is dispersed primarily by electromigrational velocity variations, accounting for the distorted peak shape. FER, on the other hand, is contained in the low-field zone and thus electromigrational dispersion is insignificant. The non-Gaussian shape results from the spatially variable dispersion coefficient, which is highest in the center of the sample zone and orders of magnitude smaller towards the edges. Thus, the FER concentration gradient remains sharp on the edges and disperses almost like a square sample plug growing in width.

Figure 6.2 shows the time evolution of the conductivity. The effective 1-D results approximate the 2-D solution well at all times. The error increases when  $\tau_s$  increases from 2.2 to 20, but remains marginal. This error develops primarily from a gradual shift in the approximate zone position relative to that calculated by solving the full 2-D system. Similar results are obtained for the electric field as shown in Fig. 6.3.

Figures 6.2 and 6.3 also show that  $b$  is  $O(L_s)$  for  $\tau_s$  up to 20. The macrotransport representation of FER works for  $\tau_s > 5$  despite the fact that  $(h/L_s)Pe_k$  is  $O(10)$ . Perhaps this is because FER is only dispersed significantly in the center of the sample zone where the fluid velocity is highest, but velocity gradients are lowest. As evident from Fig. 6.3,  $\hat{E}$ , and accordingly  $u^{eo}$ , changes very little over much of the sample zone and then drops sharply. The fluid velocity transition is therefore highly nonlinear, and  $L_s$  underestimates the characteristic length scale for an  $O(1)$  change in  $u$  over most of the sample zone (where  $Pe_k$  is highest). The sharp portion of the transition, on the other hand, owes its existence to a much smaller local  $Pe_k$  than the characteristic  $Pe_k$

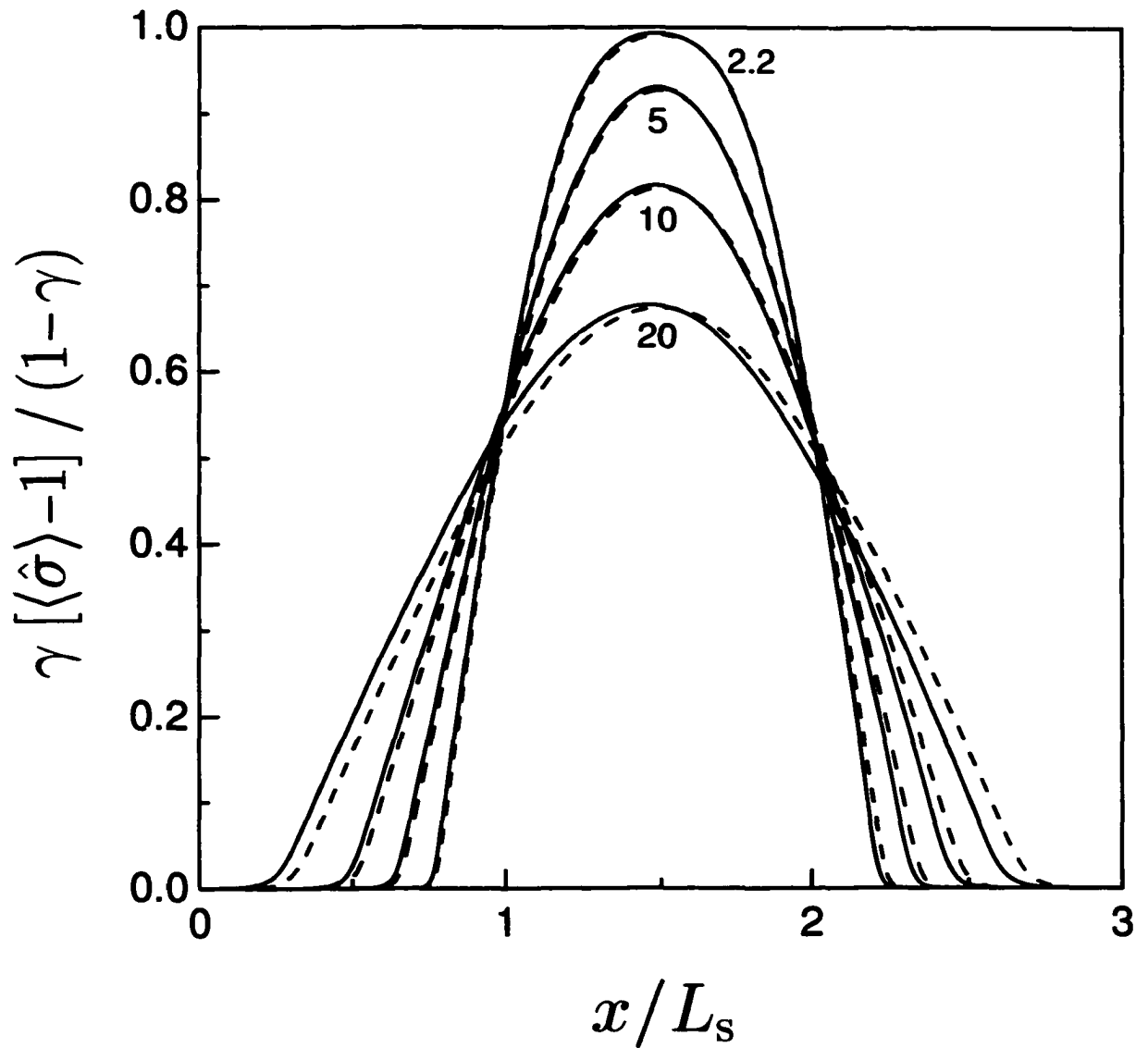


FIGURE 6.2. Cross-sectionally averaged conductivity (scaled) for electroosmotic pumping at selected values of  $\tau_s$ . Complete solution (solid); macrotransport representation (dashed). Simulation conditions are as for Fig. 6.1.

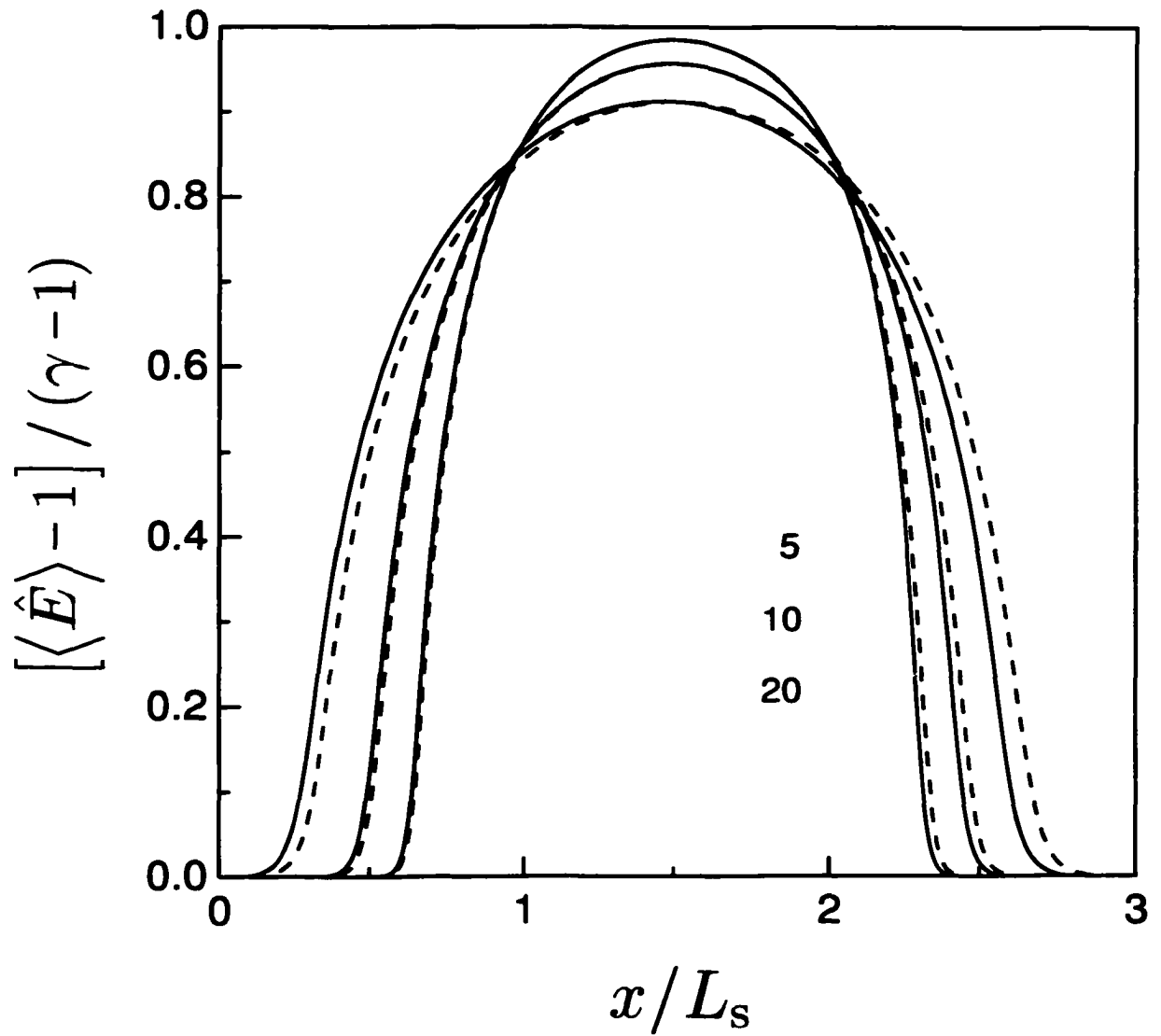


FIGURE 6.3. Cross-sectionally averaged electric field (scaled) for electroosmotic pumping at selected values of  $\tau_s$ . Complete solution (solid); macrotransport representation (dashed). Simulation conditions are as for Fig. 6.1.

used to estimate  $(h/L_s)Pe_k$ . There the fluid motion is much weaker, and convective dispersion less significant.

The macrotransport representation is also evaluated for simple FASS in buffer A. It was demonstrated in §3.3.2 that proteins do not stack in this configuration, so FER is replaced by HIS. The cross-sectionally averaged conductivity, electric field, and concentrations of HIS and ARG are presented in Fig. 6.4, for  $\gamma = 5$  and  $\tau_s = 14.1$  (when HIS emerges from the sample zone). The approximations are equally as effective for evaluating dispersion in FASS at  $\gamma = 5$  as in electroosmotic pumping. Also as for pumping of FER, and for the same reason, the approximations work even though  $(h/L_s)Pe_k > 1$ . The higher rate of convective solutal transport is accompanied by a higher rate of dispersion, and therefore a longer local characteristic transition length.

### 6.2.2 BUFFER B

To show that the utility of the effective 1-D simulation method is not limited to a buffer with  $\Delta\omega_c/\omega_c \ll 1$ , it is tested here using buffer B. Electroosmotic pumping and sample stacking are simulated by setting  $1/\gamma = 50$  and  $5$ , respectively, for buffer B in the prototype configuration of Fig. 3.1. As for buffer A, ARG and FER are included in the sample zone for pumping, and ARG and HIS for stacking, initialized at  $1 \mu M$ . The geometric lengths of the system are  $L_e = L_s = 1 \text{ mm}$ ,  $h = 20 \mu m$ , and  $L_c = 5 \text{ cm}$ . The electric field in the running buffer is fixed at  $E_0 = 180 \text{ V/cm}$  by

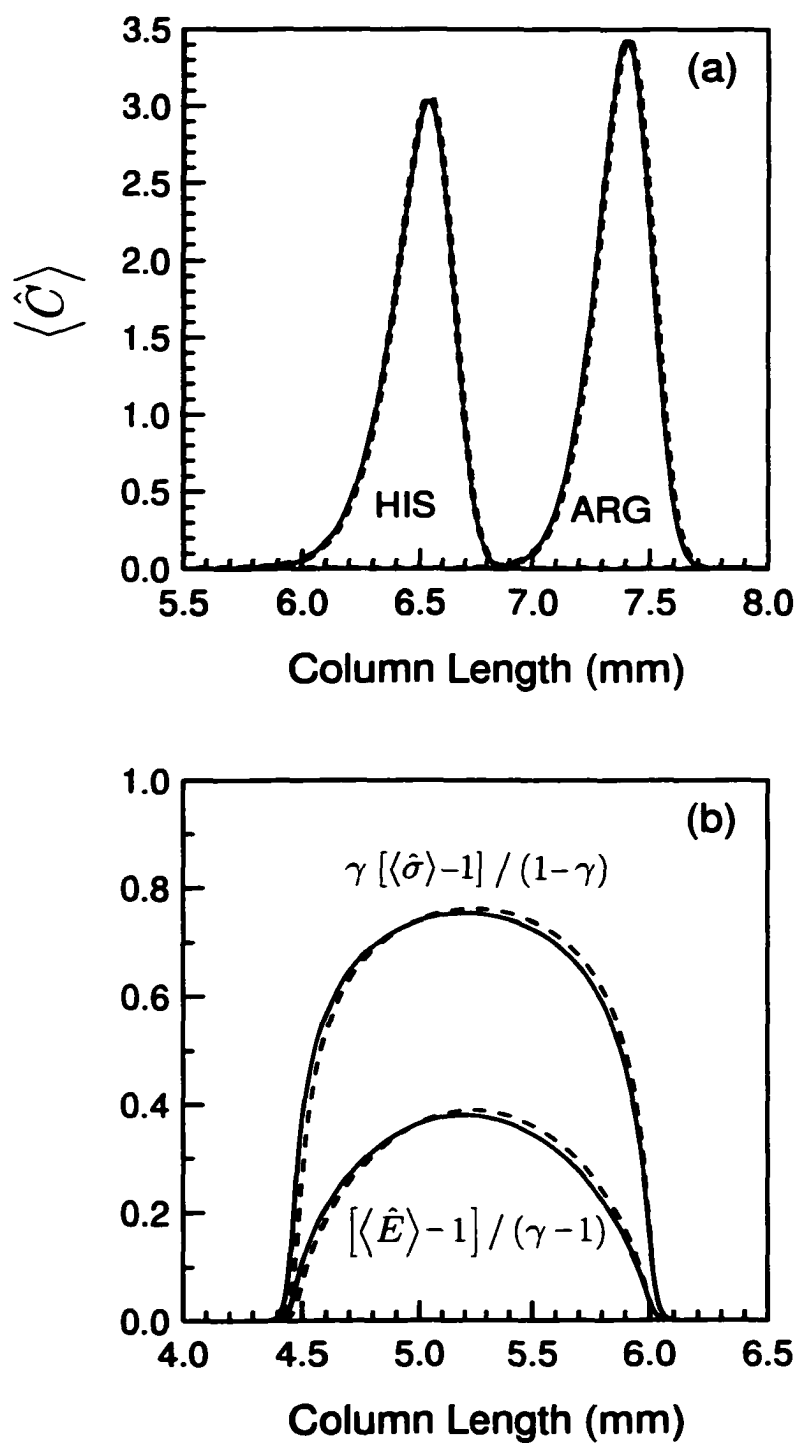


FIGURE 6.4. Cross-sectionally-averaged (a) analyte concentrations and (b) conductivity and electric field for analyte stacking.  $\gamma = 5$ ;  $\tau_s = 14.1$ . Complete solution (solid); macrotransport representation (dashed). All other simulation conditions are as for Fig. 6.1.

maintaining a constant current of  $i_0 = 1300 \text{ A/m}^2$ .

In Figure 6.5, the macrotransport solution for  $\gamma = 1/50$  at  $\tau_s = 20$  is compared to the solution of the full problem. The cross-sectionally averaged conductivity, electric field, and analyte concentrations are reasonably approximated by the 1-D simulations, though not quite as well as for buffer A at  $\gamma = 1/10$ . Comparisons for analyte stacking at  $\gamma = 5$  are made at  $\tau_s = 10.1$  (when ARG emerges from the sample zone) in Fig. 6.6. For this configuration, the agreement is about as good as for buffer A.

Comparing panel (b) of Fig. 6.5 with that of Fig. 6.6 reveals that the character of the injection plug dispersion is substantially different for pumping than for stacking. This stems from a greater sensitivity of  $\langle \hat{E} \rangle$  to changes in the ion concentrations at lower values of  $\langle \hat{\sigma} \rangle$  (cf. §3.3.2), viz.  $\delta \langle \hat{E} \rangle \sim -i_0 / \delta \langle \hat{\sigma}^2 \rangle$ . Thus in high-ionic-strength electroosmotic pumping, a 40% reduction in the peak value of  $\langle \hat{\sigma} \rangle - 1$  changes the peak value of  $\langle \hat{E} \rangle - 1$  by only a couple percent. Conversely, in stacking, a 20% reduction in  $\langle \hat{\sigma} \rangle - 1$  reduces the peak  $\langle \hat{E} \rangle - 1$  by about 60%. The shape of the dispersed plugs are also different for the same reason. Spatial variations in  $\langle \hat{E} \rangle$  are greater than spatial variations in  $\langle \hat{\sigma} \rangle$  at lower conductivities, and vice versa at higher conductivities. Because the conductivity, in the pumping configuration, is initially a factor of 50 larger in the sample zone than in the running buffer, the electric field is nearly zero and insensitive to dispersion of the buffer components. The field and flow remain nearly uniform over most of the sample plug, and thus the buffer conductivity dispersion is nearly Gaussian. This result is not obtained for stacking because the electric field in the low-conductivity plug is more sensitive to the dispersion of the

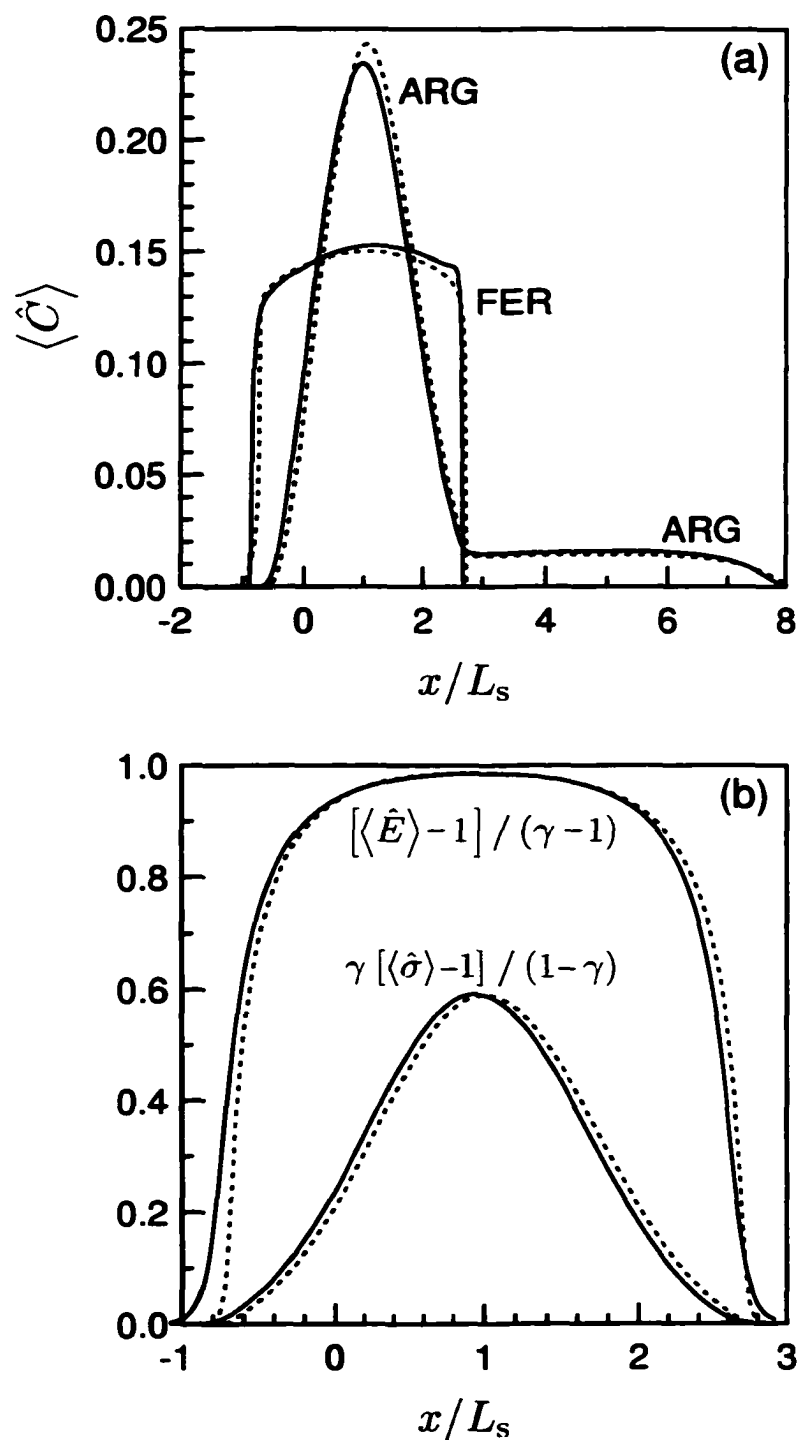


FIGURE 6.5. Cross-sectionally-averaged (a) analyte concentrations and (b) conductivity and electric field for analyte stacking.  $\gamma = 1/50$ ;  $\tau_s = 20$ . Complete solution (solid); macrotransport representation (dotted). Running buffer B (20 mM ACES, 9 mM NaOH);  $\sigma_0 = 0.072$  S/m;  $E_0 = 180$  V/cm;  $i_0 = 1.3$  kA/m<sup>2</sup>;  $v_0^{\text{eo}} = 1.2$  mm/s; pH = 6.2. All other simulation conditions are as for Fig. 6.1.

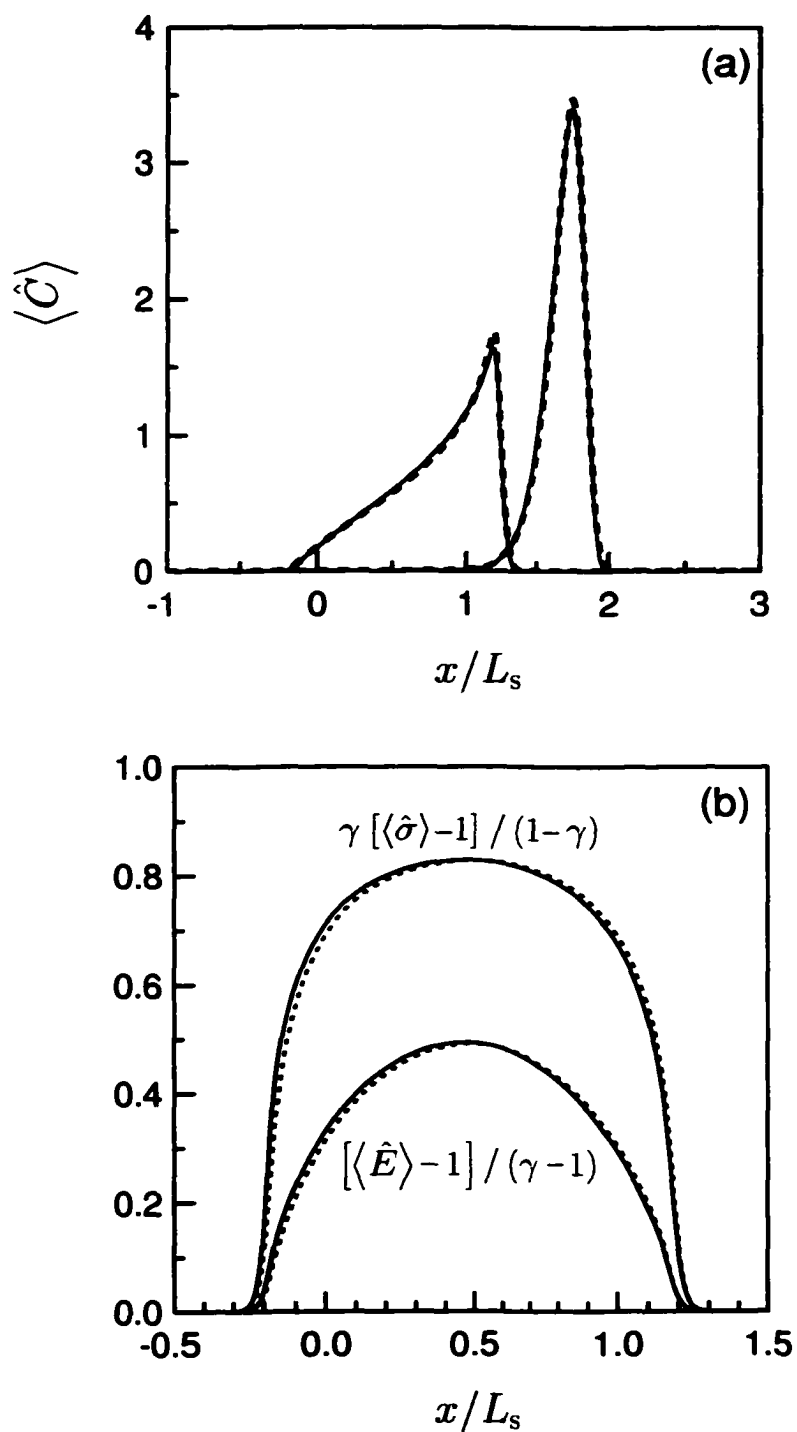


FIGURE 6.6. Cross-sectionally-averaged (a) analyte concentrations and (b) conductivity and electric field for analyte stacking.  $\gamma = 5$ ;  $\tau_s = 10.1$ . Complete solution (solid); macrotransport representation (dotted). All other simulation conditions are as for Fig. 6.5.

buffer ions.

### 6.3 DISPERSION IN SIMPLE FASS EXPERIMENTS

In this section, the FASS study of Burgi and Chien [36] is revisited to explain the disagreement between their model and experimental data at  $\gamma = 100$ . Figure 6.7 compares their measured and calculated PTH-Arginine (PTH-Arg) peak variances as a function of  $\gamma$  for various injection lengths. Although the data agree well up to  $\gamma = 8$ , for higher values, the observed peak variances for the smaller sample zones do not increase with  $\gamma$ , as predicted by their model. To explain this, the experiments for the 2-minute injection are simulated with the 1-D macrotransport method. Properties for PTH-Arg are not readily available nor provided in [36]. An approximate diffusivity that is about the same as ARG, however, can be extracted from the data in their paper. So, lacking any other data on PTH-Arg, properties for ARG are used in the simulations and in their model. The running buffer is composed of 100 mM each of MES and Histidine, and a constant 30 kV is applied across a 1 m long capillary of 75  $\mu\text{m}$  i.d. From Figures 1 and 6 of [36], the injection plug length is calculated as 0.8 cm. Because electroosmotic mobilities are very specific to capillary materials and buffer constituents, the mobility model of Thormann et al. [147] (cf. §3.1.2) was calibrated to match the ARG migration time in the uniform buffer experiment shown in Fig. 6 of [36]. The buffer and analyte properties used here are provided in Table 6.3.

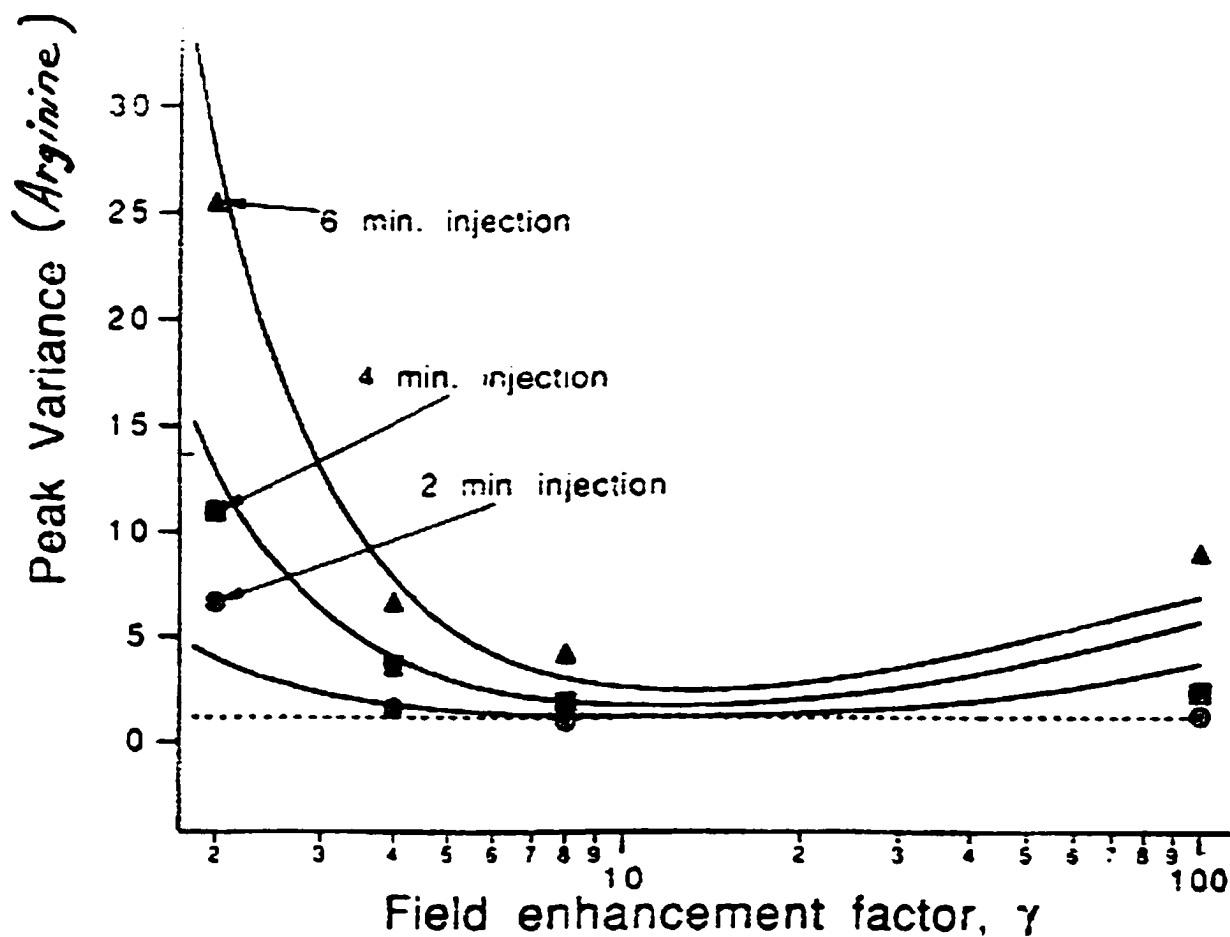


FIGURE 6.7. Burgi and Chien's [36] plot comparing their measured (symbols) and calculated (solid lines) peak variances of PTH-Arg vs.  $\gamma$  for three injection times. Circles, squares, and triangles are for 2-, 4-, and 6-min. injections, respectively. Dotted line is 10% greater than the diffusion-limited variance. Running buffer: 100 mM MES, 100 mM Histidine; pH = 6.13.  $L_c = 1$  m,  $a = 37.5$   $\mu$ m. Anode at constant 30 kV relative to the cathode.

TABLE 6.3. Buffer, analyte, and solvent ion properties<sup>†</sup>

Component	pK <sub>1</sub>	pK <sub>2</sub>	$e\omega_k$ (10 <sup>-4</sup> cm <sup>2</sup> /V·s)	$D_k$ (10 <sup>-5</sup> cm <sup>2</sup> /s)
MES	6.10		2.80	0.72
Histidine	6.04	9.17	2.85	0.73
Arginine	9.04	12.48	2.26	0.58
H <sup>+</sup>			36.27	9.32
OH <sup>-</sup>			19.87	5.11

<sup>†</sup> MES data from [80]. All other data from [113]

The model of Burgi and Chien [36] disagrees with their data for the 2- and 4-minute injections at  $\gamma > 10$  because it neglects the dispersion of the injection plug, which is most important for smaller injections. Peak variances are calculated as the sum of three variances that represent the contribution from diffusion, an ideally-stacked injection zone, and dispersion from the weak flow in the uniform running buffer; the flow in the running buffer is calculated, assuming that the injection plug is fixed at its initial condition. In the notation of this dissertation, this is

$$S^2 = 2Dt + \frac{F^2 L_c^2}{12\gamma^2} + \left[ \frac{F(\gamma\mu_s^{\text{eo}}E_s - \mu_0^{\text{eo}}E_0)}{\gamma F + (1 - F)} \right]^2 \frac{a^2 t}{24D}, \quad (6.17)$$

where  $\mu_s^{\text{eo}}$  and  $E_s$  are the initial electroosmotic mobility and unidirectional electric field in the sample zone. Figure 6.8 shows simulation results for the cross-sectionally averaged electric field and ARG concentration at  $\gamma = 8$ . The injection zone is substantially dispersed (panel (a)) during the migration of ARG (panel (b)) to the detector. This causes the electric field, and concomitantly  $D^c$  in the running buffer, to decrease with time, as shown in Fig. 6.9. For  $\gamma \leq 8$ , however,  $D^c$  is more than an order

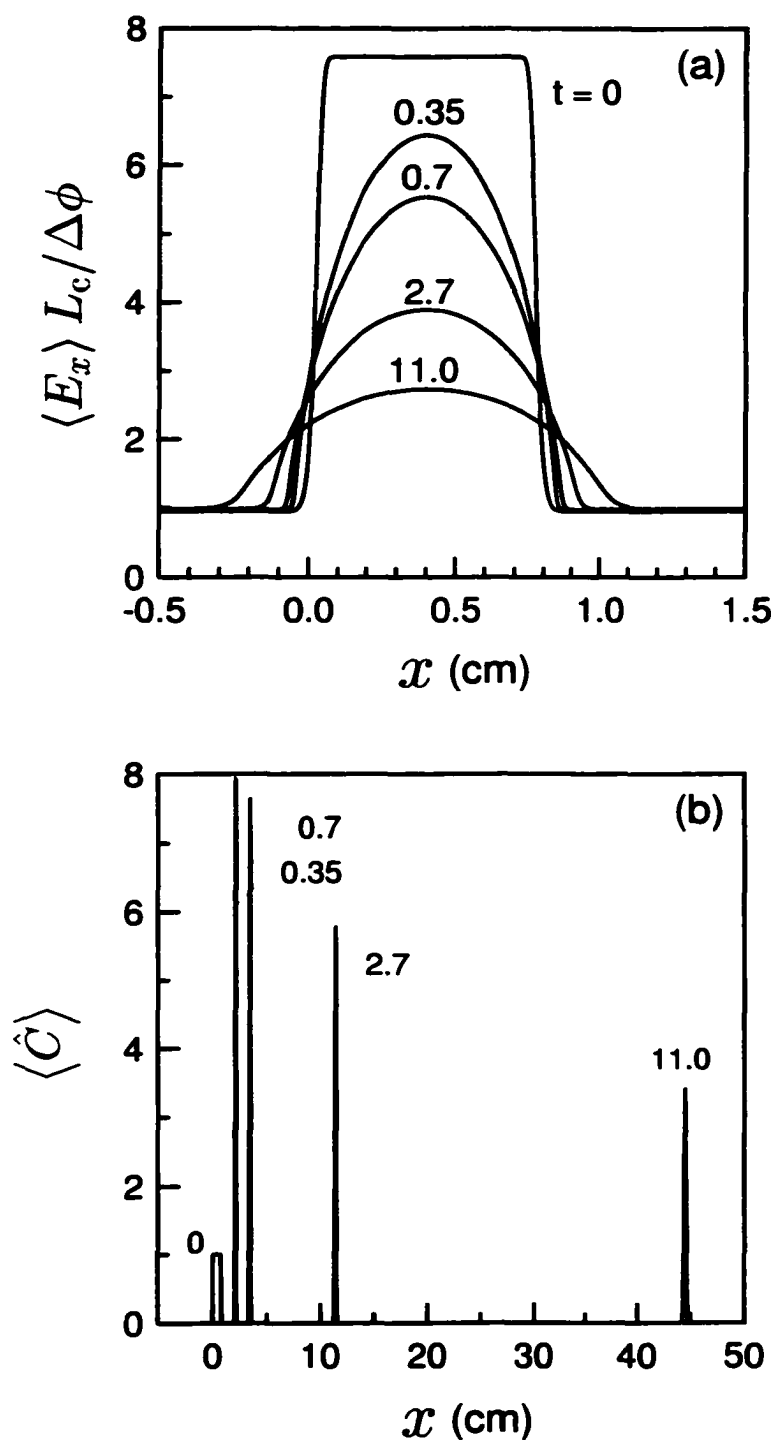


FIGURE 6.8. Simulated dispersion of ARG and high-field zone for buffer C,  $\gamma = 8$ . Cross-sectionally-averaged (a)  $E_x$  and (b) ARG concentration at selected values of  $t$  in minutes.  $h/b_0 = 0.046$ ; Running buffer C (100 mM MES, 100 mM Histidine);  $\sigma_0 = 0.261$  S/m;  $L_s = 0.8$  cm,  $L_c = 1$  m,  $a = 37.5$   $\mu\text{m}$ . Anode to the left at constant 30 kV relative to the cathode ( $\Delta\phi = 30$  kV);  $i_0$  ranges from 7.44 to 7.70 kA/m<sup>2</sup>.

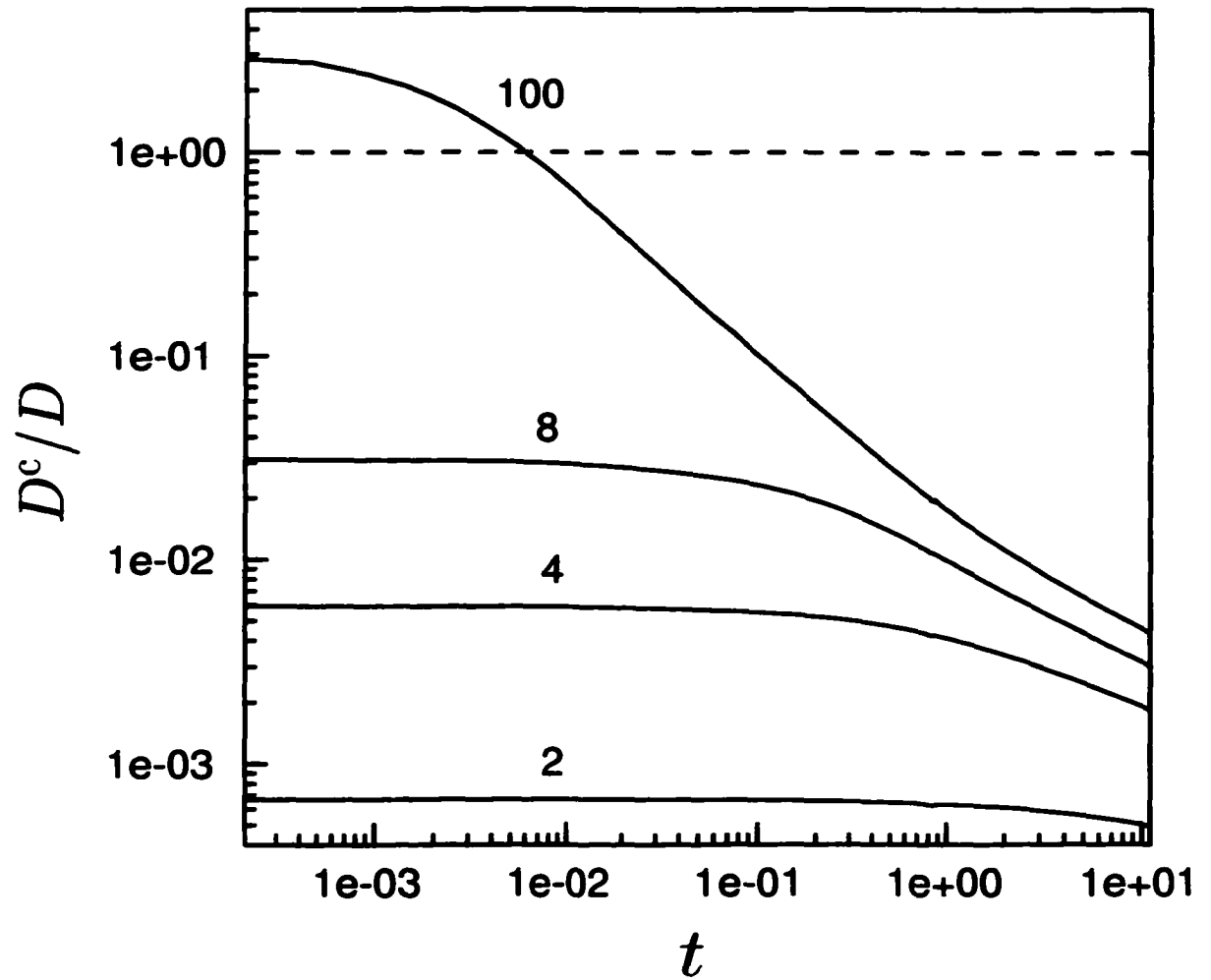


FIGURE 6.9. Dispersion coefficient  $D^c$  in the running buffer vs.  $t$ , at selected values of  $\gamma$ .  $D^c$  is normalized by  $D$ . Simulation conditions are as for Fig. 6.8.

of magnitude less than the diffusion coefficient, and therefore does not significantly affect the ARG variance. Their model fits the data for  $\gamma \leq 8$  because the fluid motion is irrelevant. For  $\gamma = 100$ , the fluid motion initially dominates the dispersion, but within a second, becomes less important than diffusion. ARG dispersion from the fluid motion becomes insignificant long before the analyte reaches the detector (11 minutes). Consequently, the flow has much less effect on the ARG variance at  $\gamma = 100$  than predicted by the model of Burgi and Chien [36], as shown in Fig. 6.10. Comparing Fig. 6.10 to Fig. 6.7 shows that the simulation results for the 2-minute injection closely approximates the experimental data over the entire range of measured  $\gamma$ .

#### 6.4 CONCLUDING REMARKS

A 1-D macrotransport representation of the solute mass balances has been constructed for electrokinetic motion in heterogeneous electrolytes. The simplified formulation applies where  $(\frac{h}{b})^2 \ll 1$ ,  $(\frac{h}{b}) Re \ll 1$ , and  $(\frac{h}{b})^3 Pe \ll 1$ , and when the characteristic time for cross-sectional diffusion is small relative to that for convection, electromigration, and the evolving unsteady flow. The method has been demonstrated, with several examples, to provide an accurate representation of non-Gaussian dispersion processes in high-ionic-strength electroosmotic pumping and FASS. Cross-sectionally averaged solute concentrations, conductivity, and electric field are predicted in orders of magnitude less simulation time, which has permitted the simulation of processes

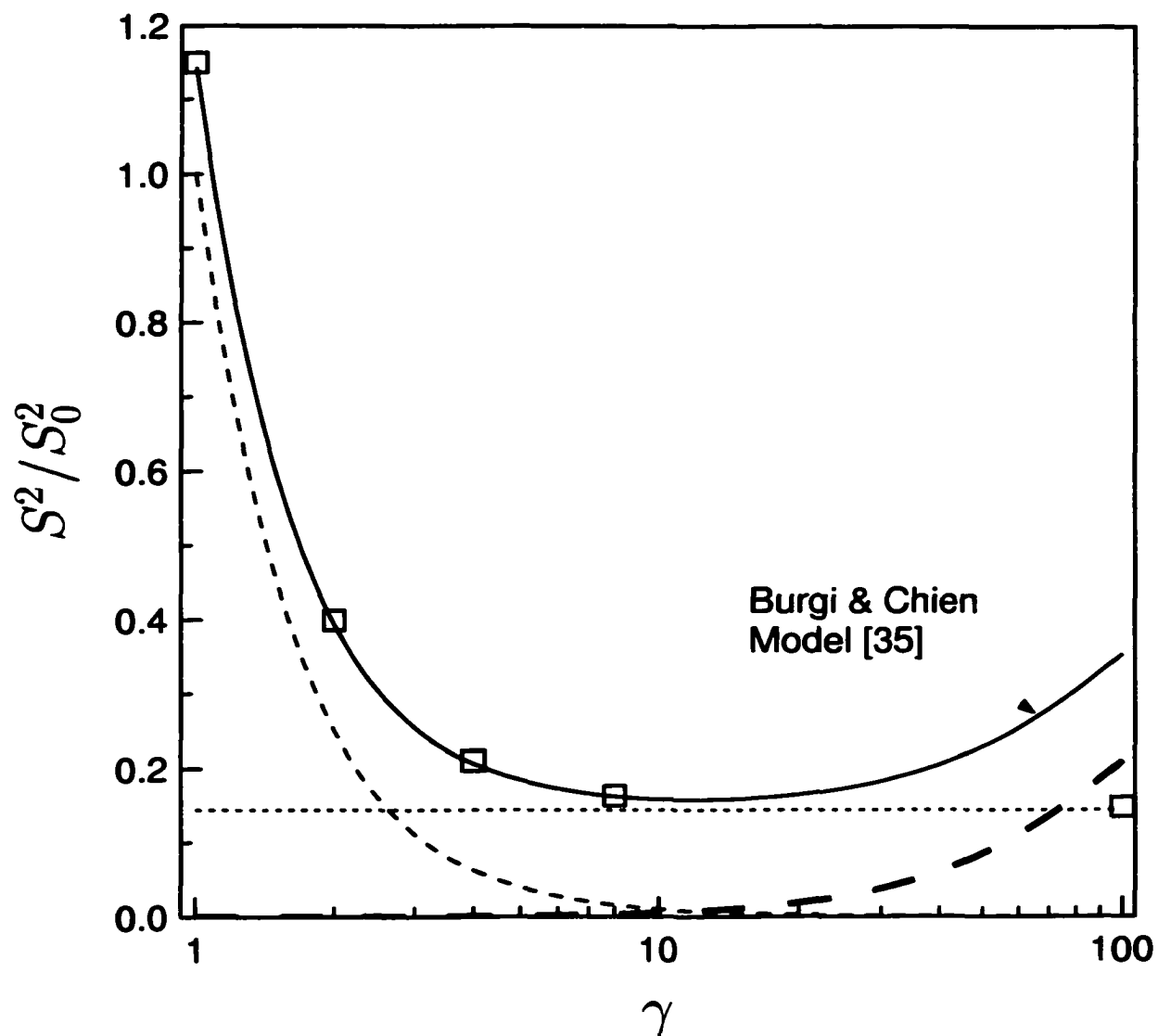


FIGURE 6.10. Simulated ARG peak variances (squares) vs.  $\gamma$  compared to Burgi and Chien [36] model (solid line). Variances are calculated when the peak concentration reaches detector, located 0.65 m from the anode ( $t = 11$  min.). Dotted line is the diffusion-limited variance; light dashed line is the variance of an ideally stacked injection zone; heavy dashed line is the variance resulting from fluid motion, according to the Burgi and Chien model. Simulation conditions are as for Fig. 6.8.

that are difficult to solve on a 2-D computational domain. For example, simulations of FASS experiments published by Burgi and Chien [36], have shown that dispersion of the high-field injection plug is substantial, and has a significant effect on analyte resolution for  $\gamma > 10$ . An quantitative representation of processes in heterogeneous buffers thus requires proper accounting of the coupling between the ion transport and electrically-driven fluid motion.

## CHAPTER 7

## SUMMARY AND FUTURE STUDIES

Electrophoretic separations and other electrokinetic processes are playing an increasingly important role in analytical chemistry, particularly with the rapid development of microfluidics. This powerful technology has numerous economic and other advantages over current methods, and is thus expected to revolutionize chemical analysis procedures. An integral component of lab-on-a-chip technology is the use of electrokinetic motion to control processes such as mixing, dilution, sample transport and injection, as well as separations. Many such processes inherently involve spatiotemporal conductivity gradients that result in unsteady, nonuniform electroosmotic flows and electric fields.

It is clear from the dearth of research on these processes that they are not well understood. In fact, prior to the work presented here, no 2-D simulations of nonlinearly coupled electrokinetic processes in analytical and microfluidic systems had been reported. It is the purpose of this dissertation to increase our understanding of electrokinetic motion by developing theory and simulations of nonlinearly coupled microfluidic and analytical separation processes. I have applied a flux-limiter technique to the electrophoretic separation model, and demonstrated that it yields monotonic solutions for benchmark simulations of all three of the extant modes of separation—ZE, ITP, and IEF. I have also shown that the method outperforms all

other published schemes on the benchmark simulations. I have further illustrated some numerical errors that can result when, as in flux-limiter and upwind techniques, artificial transport mechanisms are added to the mass balances or if the diffusion current is neglected (Appendix B). I have definitively explained the cause of such errors and the measures required to eliminate them. This research completes a critical first step toward simulation of microfluidic processes, viz. demonstrating the ability to capture sharp gradients at field strengths commonly employed in microscale devices.

After improving the numerical methods used to simulate electrophoretic separations, I extended the model to include the coupling of the solute balances to fluid motion. I have simulated a prototype 2-D problem with streamwise variations in the electrical conductivity (Chapter 3). The problem was simulated under conditions for which it represents a sample stacking and an electroosmotic pumping protocol, both of which are important microfluidic processes. The results illustrate the complicated process by which electrolytes are dispersed, causing the fluid velocity, concentration, and electric fields to evolve in time. The results further suggest that approximate solutions might simplify the simulation procedure and therefore reduce simulation times for an important class of problems. I have constructed these approximations and demonstrated their effectiveness. The approximations not only reduce simulation times, but have also provided valuable insight into the structure of the flow, electric potential, and ion transport in conductivity transition regions. Finally, I have shown that electrical stresses begin to significantly affect the flow in the transition regions for electric fields on the order of several hundred V/cm.

The work of this dissertation has done much to elucidate the fundamental physics and chemistry of electrically-driven microscale processes involving spatial gradients of the electrical conductivity. And although some restrictive numerical limitations have been eliminated, and approximations have been applied to improve simulation efficiency, further development is required to permit examination of more complicated processes.

An important parameter that affects electroosmotic flows in channels with stream-wise gradients of the electrical conductivity is the field enhancement factor  $\gamma$  defined as the ratio of the electric field in the sample zone to that in the running buffer [36]. 2-D simulations in this dissertation were restricted to  $\gamma \leq 5$  (except when neglecting electrical stresses, where analyte zones could be resolved for  $\gamma \leq 20$ ). At higher values of  $\gamma$ , analytes stack into sharper zones, requiring a finer mesh to resolve them. Also more nodes are required in the conductivity transition regions to converge on  $\mathbf{E}$  and  $\mathbf{v}$ . As a result, localized zones of the simulation domain require orders of magnitude more nodes than the rest, so simulation of higher values of  $\gamma$  requires a nonuniform grid. This restriction is inconsequential for electroosmotic pumping problems, for which  $\gamma < 1$ . However, for analyte stacking problems,  $\gamma$  is typically at least 5, and can be as high as 100 or more.

One reason to simulate stacking for  $\gamma \gg 1$  is to examine the structure of the flow in the buffer zone boundaries as the electrical stresses become more dominant. In Chapter 4, it was shown that, for  $\gamma = 5$ , the electrical stresses briefly alter the character of the fluid motion in a sharp conductivity transition. Scaling arguments

suggest that at higher values of  $\gamma$  these effects become more important. With a nonuniform grid, the fluid physics in the zone boundaries can also be revealed for  $\gamma \geq O(10)$ , and for  $\gamma \sim 1$  and  $|\mathbf{E}| \geq O(10^3)$  V/cm. Other reasons to simulate stacking in two dimensions for  $\gamma \gg 1$  are to check the effective 1-D simulation results presented in Chapter 6, and to quantify dispersion in Head-Column and Large-Volume FASS; because of the longer sample zones, these processes might not be accurately described using the macrotransport method of Chapter 6.

A fixed nonuniform grid may be sufficient to simulate FASS at  $\gamma \gg 1$  because the conductivity transitions are essentially stationary in a reference frame moving with the velocity of the mean flow, and the analytes stack into sharp peaks in these stationary transition regions. However, in most microanalysis processes analyte and/or buffer transitions are not stationary and often translate at different speeds. A fixed nonuniform grid will therefore be of limited utility, and an adaptive meshing algorithm will need to be employed. Although adaptive meshing and grid optimization routines have been developed for many applications, applying these algorithms to the model discussed here is particularly challenging because of the many dependent variables to which the grid must adapt. An adaptive grid should permit simulation of ITP and IEF, for which  $\gamma$  is typically  $O(1)$ , but requires a much larger simulation domain to encompass all electrolyte variations in the separation column. Such simulations could be used, for example, to investigate the effect of the applied voltage on the self-sharpening analyte zone boundaries. In the absence of fluid motion, the boundaries sharpen with increasing  $|\mathbf{E}|$ . At sufficiently high  $|\mathbf{E}|$ , however, electrically-driven

fluid motion in the zone boundary will oppose the self-sharpening mechanisms and may limit the benefit of increasing the applied potential.

Although adaptive and fixed nonuniform grids will increase computational efficiency substantially, there is another numerical limitation that may render many problems of interest impractical to simulate. As the mesh is refined locally to resolve a sharp transition in one of the dependent variables, the time step must be reduced in direct proportion to the reduction of the grid spacing. In some cases this may require a prohibitively small time step. Other numerical techniques may need to be employed then to further improve the computational efficiency. The simplest improvement may be to introduce column segmentation, and reduce the timestep as needed in each section. As such, only the nodes in the fine mesh regions would need to be advanced by the smaller time steps. Further improvement can be realized by using more advanced flux limiter techniques. The stability limit for the FCT algorithm used in this dissertation requires that  $Co \leq 0.5$ . Other algorithms have been developed that permit  $Co$  at least as high as 1 [119]. Also, higher order implicit Total Variation Diminishing (TVD) schemes have been developed that, because they are implicit, are unconditionally stable. For these schemes, the time step is only limited by convergence requirements.

Dispersion in some processes can be studied without a nonuniform grid by employing the 1-D macrotransport model presented in Chapter 6. Effective 1-D simulations of high ionic strength electroosmotic pumping could be used to optimize this protocol for various mixtures and pumping distances. Also, the aforementioned ITP and

IEF zone boundary studies might be amenable to this kind of treatment under some conditions.

In addition to separations and electroosmotic pumping, which are implemented in straight channels, there are other important microfluidic processes that involve nonuniform electrolytes and more complicated geometries. For example, solutions are often mixed at tee intersections on microfluidic chips. Processes such as this could be investigated and optimized by extending the simulator to accommodate geometries commonly employed in microfluidic devices.

Another important extension of the simulator would be to eliminate the electroneutrality approximation, and solve a more general set of balance laws including Gauss' Law and an unsteady charge balance. To solve this model, an iterative process is used to determine the initial charge density  $\rho_e$ , and then  $\phi$  is computed from Gauss' Law, viz.

$$\nabla^2 \phi = \frac{-\rho_e}{\epsilon \epsilon_0}. \quad (7.1)$$

At each time step,  $\rho_e$  is advanced by numerically solving the unsteady charge balance, viz.

$$\frac{\partial \rho_e}{\partial t} = \nabla \cdot [\sigma \nabla \phi - \mathbf{i}^D] \quad (7.2)$$

with an explicit scheme such as Runge-Kutta-Fehlberg. The solute concentrations and fluid velocity are calculated as in the scheme described in this dissertation, and

$[\text{H}^+]$  is calculated similarly from

$$\rho_e = \sum_{k=1}^M \bar{z}_k C_k + [\text{H}^+] - \frac{K_w}{[\text{H}^+]}. \quad (7.3)$$

With this more general model, unsteady ion transport processes that occur on length scales of the same order as the Debye length could be investigated. This would include, e.g., ion transport in sub-micron pores in membranes or nanotubes, or in pores of the length scale examined here, but at lower ionic strengths ( $\leq O(10^{-5})\text{mM}$ ).

Application of the electrophoresis model discussed in this dissertation is not limited to electrophoretic separations and microfluidic processes. With minor modifications, such as to boundary conditions and geometry, other technologies that involve electric fields can be examined. For example, in electrodecantation, suspensions are purified by a buoyancy-driven flow that is coupled to ion transport, which is driven by an applied electric field. By changing some of the boundary conditions and including the effects of gravity on  $\mathbf{v}$  with the Boussinesq approximation [15], the rate of clarification can be calculated using the electrophoresis model. Jacobs and Probst [89] used a model similar to that described in this dissertation to simulate electroremediation in porous media at electric field strengths of  $O(1)$  V/cm. With the high-field numerical methods developed in this dissertation, this technology could be explored at orders of magnitude higher field strengths. Other technologies to which the model could be applied include electrofiltration, electrodeionization, semiconductor wafer rinsing, and generally any ion transport process that occurs on a continuum length scale.

## APPENDIX A

**SIMULATION OF ELECTROPHORETIC SEPARATIONS BY  
THE FLUX-CORRECTED TRANSPORT METHOD**

This manuscript has been published in *Journal of Chromatography A* (890. 321-336, 2000) and is reproduced here with kind permission from Elsevier Science.



## Simulation of electrophoretic separations by the flux-corrected transport method

T.L. Sounart, J.C. Baygents\*

*Department of Chemical and Environmental Engineering, The University of Arizona, Tucson, AZ 85721, USA*

Received 5 January 2000; received in revised form 30 March 2000; accepted 18 April 2000

### Abstract

Electrophoretic separations at typical experimental electric field strengths have been simulated by applying the flux-corrected transport (FCT) finite difference method to the transient, one-dimensional electrophoresis model. The performance of FCT on simulations of zone electrophoresis (ZE), isotachopheresis (ITP), and isoelectric focusing (IEF) has been evaluated. An FCT algorithm, with a three-point, central spatial discretization, yields numerical solutions without numerical oscillations or spurious peaks, which have plagued previously-published second-order solutions to benchmark ZE and ITP problems. Moreover, the FCT technique captures sharp zone boundaries and IEF peaks more accurately than previously-published, first-order upwind schemes. © 2000 Elsevier Science B.V. All rights reserved.

**Keywords:** Flux-corrected transport; Computer simulation; Electric field strength

### 1. Introduction

Electrophoretic separations encompass a variety of well-established techniques for fractionating mixtures of ionic solutes for analytical and preparative applications. The desire to enhance separation efficiencies, resolution, and sensitivity continues to spur the development of new and improved methods. For example, lab-on-a-chip technology has introduced a new approach to electrophoretic separations, and underscored the need for a more refined understanding of electromigrational transport processes [1]. Computer simulations have the potential to play a vital role in the development of new separations by providing a tool to explore the effects of various

operating parameters. Simulations also afford the opportunity to examine processes, such as the evolution of the concentration, fluid velocity, electric, and conductivity fields, which are not amenable to experimental investigation in microscale systems. However, the potential utility of numerical simulations has not been completely realized inasmuch as many problems of interest are not yet tractable.

A general set of balance laws for electrophoretic separations was first introduced by Bier and co-workers [2], who developed a computer simulation of the classical modes of electrophoretic separation [3–5]. Dose and Guiochon [6] subsequently reduced computation times by introducing column segmentation to eliminate repetitious calculations in regions where the first and second spatial derivatives of all components vanished. Schafer-Nielsen [7] recognized that for separations involving weak electrolytes, most of the computation time was devoted

\*Corresponding author. Tel.: +1-520-621-6043; fax: +1-520-621-6048.

E-mail address: jcb@maxwell.che.arizona.edu (J.C. Baygents).

to solving the nonlinear set of algebraic equations required to evaluate the pH and ionic speciation; computation efficiency was improved by eliminating this calculation where and when all component concentrations remained constant. These early and other similar schemes [8] were suited to nominal electric field strengths approximately two orders of magnitude lower than those now typically used in practice (50–500 V/cm). Their high-field deficiencies result from the accumulation of substantial discretization errors introduced in regions of sharp concentration gradients by higher-order (order 2 and above) finite difference approximations. These discretization errors accumulate to form artifactual peaks or valleys which spawn additional peaks and valleys, and perpetuate the growth of spurious oscillations.

Ermakov et al. [9,10] controlled the numerical oscillations by adding artificial dispersion terms to the discretized equations, and hence were able to simulate zone electrophoresis (ZE) and isotachopheresis (ITP) at higher electric field strengths. This method, though a substantial improvement over previous numerical implementations, still failed to suppress oscillations in simulations with local field strengths of  $O(100 \text{ V/cm})$ . Martens et al. [11] evaluated the application of several implicit upwind numerical methods, including first and higher-order schemes, to the simulation of ZE and ITP separations. The higher-order schemes exhibited numerical oscillations and/or significant mass balance errors. The first-order upwind schemes suppressed all oscillations without significant mass balance errors, but included numerical diffusion that resulted in overprediction of zone boundary thicknesses. Ikuta and Hirokawa [12] simulated high-field ZE with an explicit first-order upwind method that proved to be numerically monotonic but also suffered from numerical diffusion. Application of these high-field methods to the simulation of isoelectric focusing (IEF) has not been reported.

Development of higher-order finite difference methods for solving advection problems involving sharp gradients began in the early 1970s with the use of flux limiters [13–15]. Van Leer [14] and Boris and Book [15] independently introduced the first flux limiter methods, and development of these and related methods has continued over the last three

decades. The flux-corrected transport (FCT) method originated by Boris and Book was initially developed for hyperbolic conservation laws [15–21], and is an appealing method because it is both monotonic and second-order accurate. FCT algorithms are multi-step finite difference schemes in which numerical diffusion is included in a higher-order finite difference representation of the conservation law; this prevents spurious peak formation. The numerical diffusion is then removed in a subsequent 'antidiffusion' step, except from regions where it is needed to offset the discretization error that would otherwise lead to spurious peak development. An antidiffusion-flux limiter is used to decide where and how much of the numerical diffusion should be removed. Successful implementations of FCT have been demonstrated for various higher-order schemes, numerical diffusion and antidiffusion coefficients, antidiffusion flux limiters, etc. [16–23]. In the specific context of electrophoresis, Clifton [24] and Blanco et al. [25] respectively applied an FCT algorithm to a steady-state, continuous-flow (CFE) model and to high-field protein ZE.

In this paper we examine FCT as a general high-field method to simulate the various modes of electrophoretic separation, and compare the technique to more conventional approaches (i.e. no flux limiter). We adapt the Boris and Book approach to the parabolic conservation laws of the transient electrophoresis model and preserve the essential aspects of FCT, viz., spurious oscillations are suppressed and numerical diffusion is controlled. The effectiveness of any numerical approach can vary dramatically with the physics of the problem, and ITP and IEF differ mechanistically from ZE and CFE. Thus, to evaluate the broad performance of the FCT algorithm, we simulate three benchmark electrophoretic separations—a ZE, an ITP, and an IEF separation—at realistic electric field strengths. The ZE and ITP benchmarks have been used previously by others to evaluate various numerical schemes [10–12]. For comparison, the separations are also simulated using two other common explicit finite difference methods: a first-order explicit upwind scheme and the second-order central difference scheme employed by Palusinski et al. [4]. The spatial discretization of the upwind scheme is equivalent to the Diffusion Implicit Migration Explicit (DIME)

scheme described by Martens et al. [11], except the diffusion term is treated explicitly rather than implicitly. The FCT solutions converged on significantly coarser grids than did the upwind and central difference solutions, and FCT provided substantially more accurate solutions to the electrophoresis model when compared on the same grid. For example, FCT simulations of IEF were non-oscillatory on spatial grids where the explicit upwind scheme exhibited significant mass balance errors, and where the central difference scheme was either oscillatory or unstable. In contrast to the numerical method described by Ermakov et al. [10], the FCT simulations showed no spurious oscillations on any spatial grid, and sharp zone boundaries were captured more faithfully than by the first-order upwind schemes described by Martens et al. [11] and by Ikuta and Hirokawa [12]. As a result, FCT solutions provided information on the benchmark separations that could not be obtained by the previously-published simulations [10–12].

## 2. Balance laws for electrophoretic separations

A general set of balance laws, governing the transport of ionic and neutral compounds in isothermal electrophoretic separations, was developed in the 1980s [2–4], and later detailed in a monograph by Mosher et al. [5]. This coupled set of nonlinear partial differential and algebraic equations includes an unsteady electromigration–diffusion equation for each solutal component, a charge balance, the electroneutrality approximation, expressions for ionogenic dissociation–association equilibria, and a model for calculating protein mobilities as a function of pH and ionic strength. The balance laws are summarized here in a form suited to FCT simulations. A notation similar to that introduced by Clifton [25] is used.

Ion concentrations, pH, and effective valences are determined by a coupled set of mass–action relations. These include the dissociation of water, viz.

$$K_w \equiv [H^+][OH^-] = 10^{-14} M^2 \quad (1)$$

and the ion dissociation–association equilibria for  $M$  solutal components. If the neutral form of the  $k$ th component  $A_k^0$  is protonated or deprotonated to form

$P_k$  cationic and  $N_k$  anionic species, then the mass action relations for ions of valence  $z$  are

$$A_k^z \equiv H^+ + A_k^{z-1}, \\ \begin{cases} z = -N_k + 1, -N_k + 2, \dots, +P_k \\ k = 1, 2, \dots, M, \end{cases}$$

which are characterized by the equilibrium constants

$$K_k^z \equiv \frac{[H^+][n_k^{z-1}]}{n_k^z}, \\ \begin{cases} z = -N_k + 1, -N_k + 2, \dots, +P_k \\ k = 1, 2, \dots, M, \end{cases} \quad (2)$$

where  $n_k^z$  is the concentration of subspecies  $A_k^z$ . It follows from the electroneutrality approximation that

$$0 = \sum_{k=1}^M \bar{z}_k C_k + [H^+] - \frac{K_w}{[H^+]}, \quad (3)$$

where  $C_k$  is the concentration and  $\bar{z}_k$  is the effective valence of the  $k$ th component, i.e.

$$C_k \equiv \sum_{z=-N_k}^{+P_k} n_k^z, \quad k = 1, 2, \dots, M, \quad (4)$$

and

$$\bar{z}_k \equiv \frac{\sum_{z=-N_k}^{+P_k} z n_k^z}{C_k}, \quad k = 1, 2, \dots, M. \quad (5)$$

To account for local variations of the  $C_k$ , a mass balance is written for each component,<sup>1</sup> viz.

$$\frac{\partial C_k}{\partial t} = -\nabla \cdot [v_k^c C_k - \omega_k k_B T \nabla C_k], \\ k = 1, 2, \dots, M, \quad (6)$$

and this forms a set of non-linear electro-diffusional transport equations, coupled through the electric field and the component speciation. In Eqs. (6),  $k_B T$  is the Boltzmann temperature, and  $\omega_k$  is the hydrodynamic mobility of the  $k$ th component (taken here to be independent of component speciation);  $v_k^c$  is the effective component electrophoretic velocity, viz.

<sup>1</sup>The local fluid velocity is not included in this formulation, but a uniform fluid velocity field (such as the mean electroosmotic flow [26,27]) can be accommodated by adopting a frame of reference moving with the fluid velocity.

$$\mathbf{v}_k^c = e\bar{z}_k \omega_k \mathbf{E}, \quad k = 1, 2, \dots, M, \quad (7)$$

where  $\mathbf{E}$  is the local electric field, and  $e$  is the charge on a proton ( $1.6 \times 10^{-19}$  C).

The governing equations are closed by combining Eqs. (3) and (6) to balance the charge; this yields an equation for  $\mathbf{E}$ , i.e.

$$0 = \nabla \cdot \left[ \sigma \mathbf{E} + ek_n T \left( \sum_{i=1}^M \omega_k \nabla \bar{z}_i C_i + \omega_{H^+} \nabla [H^+] - \omega_{OH^-} K_w \nabla [H^+]^{-1} \right) \right], \quad (8)$$

where

$$\sigma = e^2 \left[ \sum_{i=1}^M \bar{z}_i^2 \omega_i C_i + \omega_{H^+} [H^+] + \omega_{OH^-} \frac{K_w}{[H^+]} \right] \quad (9)$$

is the local electrical conductivity. In Eqs. (8) and (9),  $\omega_{H^+}$  and  $\omega_{OH^-}$  are, respectively, the hydrodynamic mobilities of  $H^+$  and  $OH^-$ , and  $\bar{z}_i^2$  is the mean square valence of the  $k$ th component, viz.

$$\bar{z}_k^2 \equiv \frac{\sum_{i=1}^{+P_k} z_i^2 n_i}{C_k}, \quad k = 1, 2, \dots, M. \quad (10)$$

For components that may undergo many protonation or deprotonation reactions (e.g. proteins), dissociation–association equilibrium constants are not necessarily available. In such cases, subspecies concentrations are not calculated, and effective and mean square valences are extracted from titration data. For details on the calculation of effective and mean square valences from titration data, and the calculation of protein mobilities as a function of pH and ionic strength, see Mosher et al. [5].

### 3. Numerical implementation

Standard numerical techniques, when applied to Eqs. (6), and implemented for typical experimental conditions, evince gross instabilities or inefficiencies. The numerical problems arise as the potential gradients exceed 10 V/cm. Electromigrational (or electrophoretic) transport of the ionic solutes dominates diffusion, and the unsteady electro-diffusional trans-

port equations (Eqs. 6) approach a hyperbolic form. As a result, linear finite difference schemes, with second-order and higher spatial accuracy, yield solutions with numerical overshoots, undershoots, or oscillations in the vicinity of sharp concentration gradients (unless an impractically fine mesh is applied). To guarantee numerical monotonicity, a one-dimensional central spatial discretization of Eqs. (6), such as that employed by Palusinski et al. [4] and by Dose and Guiochon [6], requires that

$$Pe_{\Delta x} \equiv \frac{|v^c| \Delta x}{D} < 2 \quad (11)$$

for each component at all times and positions. In (11),  $Pe_{\Delta x}$  is the cell electric Peclet number and  $\Delta x$  is the spatial grid size;  $D$  is the diffusivity and  $|v^c|$  is the magnitude of the local electrophoretic velocity of the component. To satisfy (11), the number of segments  $n_s$  in a discretized domain of length  $L$ , must vary as  $n_s \sim (Pe_{\Delta x})_{max} L / \Delta x \equiv Pe_L$  for a fixed uniform grid. Potential gradients exceeding 10 V/cm typically correspond to  $Pe_L > O(10^3)$ , and this dictates an impractical  $n_s > O(10^3)$  to guarantee monotonic simulations. Ermakov et al. [9,10] developed a numerical scheme employing artificial dispersion, which greatly improved the simple central difference methods. Unfortunately, this method produced oscillatory solutions when simulating electrophoretic separations with  $Pe_L > O(10^4)$ .

Some first-order finite difference schemes, on the other hand, such as the upwind schemes described by Martens et al. [11] and by Ikuta and Hirokawa [12], are monotonic at any  $Pe_{\Delta x}$ , but suffer from excessive numerical diffusion. The lower accuracy of these schemes is generally considered more tolerable than the spurious peaks and distorted concentration profiles generated by the higher-order difference methods. Though the first-order upwind difference methods yield monotonic solutions for any grid spacing, they require an extremely fine mesh to substantially reduce numerical diffusion, and the resultant  $n_s$  is comparable to that required of the central difference schemes to maintain  $Pe_{\Delta x} < 2$ .

Since these numerical difficulties arise when electromigration dominates the electro-diffusional transport of solutes, it seems reasonable to consider the use of numerical methods developed for solving hyperbolic partial differential equations. There is a

class of such methods that apply flux or slope limiters [13] to higher-order difference schemes to prevent the formation of spurious overshoots or undershoots. The limiter is basically a set of rules designed to recognize the formation of a numerical undershoot or overshoot, and to remove it or prevent its formation by limiting the fluxes in these regions. This is done while maintaining a higher-order accurate finite difference approximation throughout the remainder of the simulation domain. Distinct sets of rules, and methods of implementing them, differentiate the various flux limiter methods.

The flux-limiter method of Boris and Book (FCT) employs a multi-step process in which sufficient numerical diffusion is added to a higher-order finite difference solution to ensure monotonicity [15–21]. The numerical diffusion is then removed in an antidiffusion step except where the antidiffusion fluxes are limited by a set of rules to prevent the formation of numerical overshoots or undershoots. Because the FCT method was formulated to yield monotonic solutions to unsteady hyperbolic equations, there is no limit on  $Pe_{\Delta x}$  when applying FCT to unsteady advection–diffusion (or electromigration–diffusion) equations [15–21].

### 3.1. PLPE FCT

In simple tests on unsteady convection problems, an FCT algorithm called Shasta Phoenixal Low Phase Error performed the best of the explicit methods evaluated by Boris and Book [17]. They and co-workers later applied the phoenixal low phase error (PLPE) approach to a second-order central spatial discretization and incorporated the algorithm into several library subroutines [18,19,21]. Since this method employs a second-order central difference spatial discretization, it is a natural choice for modifying the numerical implementation of the electrophoresis model developed by Palusinski et al. [4].

The PLPE FCT method was applied to Eqs. (6) in one space dimension using a second-order Runge–Kutta (RK) time step and central difference spatial discretization, thus creating a scheme which is of second order in both time and space except in the regions where the nonlinear flux correction makes it impossible to determine the order of the truncation

error. Eqs. (6) were solved according to the following algorithm.

**Step 1.** For each component, calculate the concentration  $C_{i,j+1/2}$  at each position  $x_i = i\Delta x$  ( $i = 0, 1, 2, \dots, n_x$ ) at time  $t_{j+1/2} = t_j + 1/2\Delta t$  ( $j = 0, 1, 2, \dots, n_t$ ), where  $t_j = \sum_{m=1}^j (\Delta t)_m$ ;  $\Delta x$  and  $\Delta t$  are, respectively, the discretized spatial and temporal increments, and  $n_t$  is the number of temporal increments. This is done by first determining the transported solution  $C_{i,j+1/2}^T$  (no numerical diffusion), viz.

$$C_{i,j+1/2}^T = C_{i,j} - \frac{\Delta t}{2\Delta x} \left[ v_{i+1/2,j}^c C_{i+1/2,j} - v_{i-1/2,j}^c C_{i-1/2,j} + f_{i+1/2,j}^d - f_{i-1/2,j}^d \right] \quad (12)$$

where the diffusive flux is

$$f_{i+1/2,j}^d = -D \frac{(C_{i+1,j} - C_{i,j})}{\Delta x} \quad (13)$$

and  $v_{i+1/2,j}^c$  and  $C_{i+1/2,j}$  are calculated as the arithmetic average of the values at  $x_i$  and  $x_{i+1}$ . Next numerical diffusion is added to the transported solution to find  $C_{i,j+1/2}^D$ , i.e.

$$C_{i,j+1/2}^D = C_{i,j+1/2}^T - (g_{i+1/2,j}^{nd} - g_{i-1/2,j}^{nd}) \quad (14)$$

where

$$g_{i+1/2,j}^{nd} = -v_{i+1/2,j} (C_{i+1,j} - C_{i,j}) \quad (15)$$

has the form of a discretized diffusion flux multiplied by the ratio of the current time step to the spatial increment.  $v_{i+1/2,j}$  is, in effect, a dimensionless velocity-dependent diffusion coefficient [18]

$$v_{i+1/2,j} = \frac{1}{6} + \frac{1}{3} (\epsilon_{i+1/2,j})^2 \quad (16)$$

with

$$\epsilon_{i+1/2,j} = \frac{\Delta t}{\Delta x} v_{i+1/2,j}^c \quad (17)$$

Finally numerical antidiffusion is applied to find  $C_{i,j+1/2}$ , viz.

$$C_{i,j+1/2} = C_{i,j+1/2}^D - (g_{i+1/2,j}^{ad} - g_{i-1/2,j}^{ad}), \quad (18)$$

where

$$g_{i+\frac{1}{2},j}^{\text{ad}} = L \left\{ \mu_{i+\frac{1}{2},j} \left( C_{i+1,j+\frac{1}{2}}^{\text{T}} - C_{i,j+\frac{1}{2}}^{\text{T}} \right) \right\} \quad (19)$$

$$\mu_{i+\frac{1}{2},j} = \frac{1}{6} - \frac{1}{6} (\epsilon_{i+\frac{1}{2},j})^2, \quad (20)$$

and  $L\{g\}$  is the nonlinear function that applies the flux limiter to  $g$ . In the ZE and ITP simulations, the strong flux limiter described by Boris et al. [21] was applied, and that overall numerical scheme is identified here as PLPE1. This limiter prevents spurious overshoots and undershoots from forming by prohibiting the creation of new extrema, as well as the accentuation of existing extrema, during the antidiffusion stage. In the IEF simulation, two flux limiters were applied—the strong flux limiter of PLPE1 and a weaker limiter (cf. Eqs. (6–14), and (17–18) of Ref. [20]). The weaker flux limiter allows the creation and accentuation of extrema, as long as these extrema do not exceed the values of neighboring nodes from the previous time step. The scheme incorporating this flux limiter is identified here as PLPE2.

**Step 2.** For each component, calculate the concentration  $C_{i,j+1}$  at time  $t_{j+1} = t_j + \Delta t$ . The step begins with a prediction of the velocity  $v_{i+1/2,j+1/2}^c$  and the flux  $f_{i+1/2,j+1/2}^d$ , which are calculated using the values of  $C_{i,j+1/2}$  from Step 1 and Eqs. (2–5), (7–10), and (13). Next, as in Step 1, a transported solution  $C_{i,j+1}^{\text{T}}$  is determined, viz.

$$C_{i,j+1}^{\text{T}} = C_{i,j} - \frac{\Delta t}{\Delta x} \left[ v_{i+\frac{1}{2},j+\frac{1}{2}}^c C_{i+\frac{1}{2},j} - v_{i-\frac{1}{2},j+\frac{1}{2}}^c C_{i-\frac{1}{2},j} + f_{i+\frac{1}{2},j+\frac{1}{2}}^d - f_{i-\frac{1}{2},j+\frac{1}{2}}^d \right] \quad (21)$$

Numerical diffusion is then added to find  $C_{i,j+1}^{\text{D}}$ :

$$C_{i,j+1}^{\text{D}} = C_{i,j+1}^{\text{T}} - (g_{i+\frac{1}{2},j+\frac{1}{2}}^{\text{nd}} - g_{i-\frac{1}{2},j+\frac{1}{2}}^{\text{nd}}) \quad (22)$$

where

$$g_{i+\frac{1}{2},j+\frac{1}{2}}^{\text{nd}} = \nu_{i+\frac{1}{2},j+\frac{1}{2}} (C_{i+1,j} - C_{i,j}). \quad (23)$$

Lastly, numerical antidiffusion is applied to find:

$$C_{i,j+1} = C_{i,j+1}^{\text{D}} - (g_{i+\frac{1}{2},j+\frac{1}{2}}^{\text{ad}} - g_{i-\frac{1}{2},j+\frac{1}{2}}^{\text{ad}}) \quad (24)$$

where

$$g_{i+\frac{1}{2},j+\frac{1}{2}}^{\text{ad}} = L \left\{ \mu_{i+\frac{1}{2},j+\frac{1}{2}} \left( C_{i+1,j+1}^{\text{T}} - C_{i,j+1}^{\text{T}} \right) \right\} \quad (25)$$

Numerical implementation of the remainder of the model follows the method previously described by Palusinski et al. [4]. The second-order RK/FCT algorithm described above replaces the 5th-order Runge–Kutta–Fehlberg (RKF)/2nd-order Central Spatial Difference (CSD) algorithm used to solve Eqs. (6).

### 3.2. Explicit upwinding

To evaluate the performance of the PLPE FCT method for the transient electrophoretic separations model described in Section 2, three benchmark problems were solved, and the solutions compared to solutions derived from two other explicit numerical techniques. One was the RKF/CSD method described by Palusinski et al. [4]. This is a typical higher-order scheme that does not guarantee monotonicity, and includes the same spatial discretization as that used in the PLPE FCT algorithm to find the transported solution. The other method was an explicit first-order upwind scheme that guarantees monotonicity (at the expense of accuracy). These schemes were chosen for comparison to illustrate how FCT combines the second-order accuracy of the RKF/CSD method with the monotonicity of the first-order upwind methods. In the upwinding algorithm, the spatial discretization is equivalent to that in the first-order upwind schemes of Martens et al. [11], but the time derivative is discretized by a forward difference to yield a fully explicit scheme, as are the other schemes examined here. The second-order RK timestep used in the PLPE FCT algorithm is also used in the upwind scheme. The upwinding is done as follows:

For  $v_{i,j}^c < 0$ :

$$C_{i,j+\frac{1}{2}} = C_{i,j} - \frac{\Delta t}{2\Delta x} \left[ v_{i+1,j}^c C_{i+1,j} - v_{i,j}^c C_{i,j} + f_{i+\frac{1}{2},j}^d - f_{i-\frac{1}{2},j}^d \right] \quad (26)$$

$$C_{i,j+1} = C_{i,j} - \frac{\Delta t}{\Delta x} \left[ v_{i+1,j+\frac{1}{2}}^c C_{i+1,j+\frac{1}{2}} - v_{i,j+\frac{1}{2}}^c C_{i,j+\frac{1}{2}} + f_{i+\frac{1}{2},j+\frac{1}{2}}^d - f_{i-\frac{1}{2},j+\frac{1}{2}}^d \right] \quad (27)$$

For  $v_{i,j}^c > 0$ :

$$C_{i,j+\frac{1}{2}} = C_{i,j} - \frac{\Delta t}{2\Delta x} \left[ v_{i,j}^c C_{i,j} - v_{i-1,j}^c C_{i-1,j} + f_{i+\frac{1}{2},j}^d - f_{i-\frac{1}{2},j}^d \right] \quad (28)$$

$$C_{i,j+1} = C_{i,j} - \frac{\Delta t}{\Delta x} \left[ v_{i,j+\frac{1}{2}}^c C_{i,j} - v_{i-1,j+\frac{1}{2}}^c C_{i-1,j} + f_{i+\frac{1}{2},j+\frac{1}{2}}^d - f_{i-\frac{1}{2},j+\frac{1}{2}}^d \right] \quad (29)$$

This scheme is identified here as UPWIND, and the RKF/CSD method will henceforth be identified simply as CSD.

### 3.3. Discretization

In all simulations, the spatial discretization step was prescribed and the time step calculated to meet certain criteria specific to each numerical method. In the PLPE1 and PLPE2 simulations, the time step was calculated to maintain the maximum Courant number,  $Co_{\max} \equiv |\epsilon_{i,j}|_{\max}$ , at 0.45, since numerical monotonicity is only ensured using the PLPE method for  $Co < 0.50$  [21]. Monotonicity for the UPWIND scheme however is guaranteed for  $Co < 1.0$  [16], and thus  $Co$  was maintained at 0.90 for the upwind simulations. In the CSD simulations, the time step was controlled by the RKF algorithm, which adjusts the time step to maintain an estimate of the truncation error within prescribed bounds [28].

The spatial grid was prescribed to permit comparison to previously-published simulation results, and to establish the convergence requirements of each scheme. A reasonable definition of a converged solution might be a solution that changes everywhere by less than 1% of the full-scale value upon doubling the number of segments. However, at typical electric field strengths, component zone boundaries are often reduced to 0.01% of the column length or less. On a fixed uniform grid, a perfect numerical scheme, i.e. one that captures the entire zone boundary in one segment, would require at least 10 000 segments to correctly resolve such transitions, and hence meet the above defined convergence criterion. The numerical schemes studied here require at least 3 segments to

converge in any zone boundary, and therefore even the best of these schemes would require an impractical amount of simulation time to meet this convergence requirement. Therefore, a converged solution is defined here as one which, upon doubling the number of segments, changes everywhere by less than 1% of the full-scale value, except in zone boundaries that are narrower than 0.2% of the column length. In these regions, the zone boundary thicknesses are required only to be resolved to 0.2% of the column length. The zone boundary thickness is defined here as the length over which a dependent variable's value changes from 1% to 99% of the value difference between one plateau value and another. These convergence criteria provide a reasonable basis for comparison of the numerical schemes delineated in this paper. Meeting more stringent convergence criteria efficiently would require the use of adaptive grids, which is beyond the scope of this paper.

### 3.4. Equipment

All simulations were performed on an IBM RISC System/6000 workstation, running the AIX Version 3.2 UNIX operating system and AIXwindows graphical user interface. All computations were coded in FORTRAN 77 and compiled using an AIX XL FORTRAN Compiler/6000 Version 2.3.

## 4. Results and discussion

### 4.1. ZE benchmark

A ZE separation of two weak bases, aniline and pyridine in a uniform buffer, was simulated using each of the numerical techniques described in Section 3. The buffer was composed of 12 mM Tris base and 20 mM acetic acid, and the analytes were introduced as a 5 mm sample plug, 5 mm from the anodic end of a 20 cm long capillary. Initial sample zone boundary thicknesses were approximately 4% of the zone width (~2 segments of fine mesh). The initial analyte concentrations in the sample plug were 1 mM each, and the detector was positioned 10 cm from the anode. The simulation was performed at a constant current density of 2547 A/m<sup>2</sup>, which

corresponded to an initial potential difference of 6564 V applied across the column. In this separation process, the analytes are only an order of magnitude lower in concentration than the background buffer. As a result, the transport of the analytes is fully coupled with the transport of the buffer, and an electric field that is ultimately higher in the analyte zones than in the surrounding buffer generates selfsharpening leading edges of these zones. The sharp transitions advected at high Peclet numbers typically present problems for standard numerical techniques used for parabolic equations.

Computed electropherograms for this ZE separation are presented in Fig. 1. Panel (a) shows the electropherograms calculated using a relatively coarse grid spacing of  $\Delta x = 0.05$  cm. The CSD solution is completely distorted by oscillations and the UPWIND solution produces peaks that are excessively eroded by numerical diffusion. This demonstrates the well known result that upwinding ensures monotonicity at the expense of significant numerical diffusion. The PLPEI solution, however, produces peaks with no oscillations and much less numerical diffusion than the UPWIND scheme. The self-sharpening leading edges of the peaks remain remarkably vertical for such a coarse discretization; the boundary is spread over 2.4 s using the PLPEI method, compared to 14 s with the UPWIND method. Also, the PLPEI method resolves the peak heights to within 7% of the converged values (Fig. 1(b)), but the numerical spreading inherent in the UPWIND scheme has eroded the peaks by half. Numerical results of this separation on the same grid have previously been reported by Ermakov et al. [10], who found minor numerical oscillations at a current density of  $509 \text{ A/m}^2$ ; at the current density simulated here, the Ermakov et al. solution was significantly distorted by numerical oscillations.

Additional electropherograms, calculated on a finer grid ( $\Delta x = 0.01$  cm), for which the PLPEI method has converged, are presented in Fig. 1(b). Again the CSD solution is marred by oscillations. The converged PLPEI solution reveals that the shoulders on the peaks of the course grid are artifacts, probably resulting from the nonlinear behavior of the flux limiter [21]. The peaks generated by the UPWIND scheme are much closer to the converged PLPEI solution, but the numerical diffu-

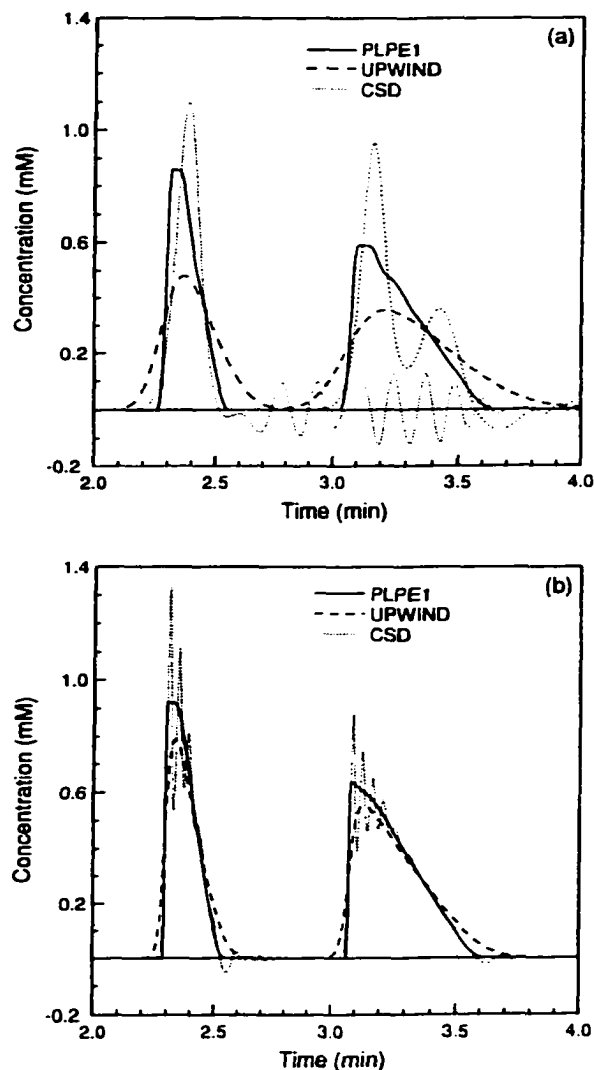


Fig. 1. ZE benchmark electropherograms. Pyridine is eluted first followed by aniline. Constant current,  $2547 \text{ A/m}^2$ ; initial voltage, 6564 V across a 20 cm column. The detector is positioned at the center of the column. Initial buffer concentrations, 12 mM tris base/20 mM acetic acid; initial sample concentrations, 1 mM each. The grid spacing is (a) 0.05 cm and (b) 0.01 cm.

sion has still eroded the peaks to the extent (14% error in peak heights) that the PLPEI solution on the coarse grid (Fig. 1(a)) is closer to the converged solution (Fig. 1(b)). Table 1 lists the peak variances and relative errors in peak variance for PLPEI and

Table 1  
ZE peak variances ( $\sigma^2$ ) and relative errors in peak variance ( $\epsilon$ )<sup>a</sup>

No. of segments	$\sigma^2$ (s <sup>2</sup> )		% $\epsilon$ <sup>b</sup>		
	PLPEI	UPWIND	PLPEI	UPWIND	
Aniline	400	55.8	154.8	12.3	210.0
	2000	<i>49.7</i>	70.9	0.0	42.7
Pyridine	400	11.9	43.9	15.5	326.0
	2000	<i>10.3</i>	16.8	0.0	63.1

<sup>a</sup> *Italicized numbers indicate converged values.*

<sup>b</sup> % $\epsilon$  = 100 ( $\sigma^2$  - Converged  $\sigma^2$ ) / (Converged  $\sigma^2$ ).

UPWIND. CSD was not included in the Table because negative concentrations result in meaningless variances. Note that the relative errors of UPWIND on the *fine* grid are approximately five times those of PLPEI on the *coarse* grid. Ikuta and Hirokawa reported simulating this separation on this grid, using an upwind scheme to obtain numerical stability [12]. Their upwind scheme suffered similarly from the deleterious effects of numerical diffusion.

A summary of the convergence requirements for each scheme is provided in Table 2. Using the PLPEI method, a converged solution was realized in 24 min. The other methods however did not converge on a 10 000 segment grid that required almost 5 h of computation time. All simulation grids were limited to 10 000 segments, so the simulation time required for these 2 methods to converge was not determined.

The converged solution produced by the PLPEI scheme shows the loss of peak resolution that can result from the coupling between the ion transport and the electric field. The flat tops of the converged peaks, particularly the pyridine peak, result from the complicated electric field that develops as the analytes separate in the first minute of separation. The presence of the analytes increases the conductivity,

Table 2  
Convergence requirements for ZE simulation

Scheme	Number of segments	Computation time (min)
PLPEI	2000	24
UPWIND	> 10 000	> 281
CSD	> 10 000	> 268

and thus lowers the electric field in the initial sample zone. This causes the basic buffer component to deplete, and the acidic component to accumulate on the leading edge of the sample zone. Because the pH is much closer to the pK of the acid than the pK of the base, the base has a much higher percent dissociation and thus a much higher effective mobility. As a result, the base depletes much faster than the acid accumulates in this region, causing an increase in the electric field. As the analytes migrate from the initial sample zone, they pass from a low-field region to a higher field region, and are also depleted. A decrease in analyte concentration reduces the depletion of the basic buffer on the leading edge of the analyte zones, which in turn slows the reduction in the analyte concentration. In this way, the concentrations are adjusted until separated analyte zones, lower in concentration than the original zone, are formed. These zones are essentially square because the initial zones are square, but because the basic buffer is depleted, the electric field is now higher in the analyte zones. This results in a self-sharpening leading edge and a broadening trailing edge. Thus a flat top of the analyte zone remains until the broadening edge spreads to the leading edge. The aniline zone is approximately at that stage as it passes the detector (Fig. 1(b)). The shapes of these peaks are not captured by the the UPWIND or CSD schemes, nor by any of the previously-published simulations of this ZE separation, because either numerical diffusion erodes or oscillations distort the profiles.

#### 4.2. ITP benchmark

In an ITP separation, leading and terminating buffers are selected to establish an electric field that ultimately drives a train of sample and buffer zones to move isotachophoretically down the separation column. In accordance with the Kohlrausch condition [29], there are stepwise variations of the electric field in the direction of electrophoretic motion, and self-sharpening boundaries form between the zones where the net diffusive flux of each component is balanced by the net electromigrational flux (when observed from a frame of reference moving at the isotachophoretic velocity). At high electric Peclet numbers, i.e. high electric field

strengths, the zone boundaries must become extremely sharp to allow diffusion to balance the high electromigrational fluxes. This typically presents difficulties for numerical solutions.

To evaluate the performance of the PLPE method on an ITP calculation, an isotachophoretic separation of the two aforementioned weak base analytes was simulated. The leading electrolyte consisted of 18 mM sodium hydroxide and 20 mM acetic acid, and the terminating electrolyte was composed of 40 mM  $\beta$ -alanine and 50 mM acetic acid. Ten mM aniline and pyridine and 20 mM acetic acid were introduced as a 1 mm sample plug, 1 mm from the anodic end of a 40 mm long capillary. Initial zone boundary thicknesses were approximately 4% of the sample zone widths ( $\sim 2$  segments of fine mesh). A separation time of 42 s was simulated at a constant current of 2260 A/m<sup>2</sup>, which corresponded to initial and final potential differences of 576 V and 3280 V, respectively, applied across the column.

The ITP simulation results of the 3 different methods are presented in Fig. 2, with the concentrations of the two sample zones bounded by the leading electrolyte on the right and the terminator on the left. Results are provided for the UPWIND and PLPEI schemes on both coarse ( $\Delta x = 50 \mu\text{m}$ ) and fine ( $\Delta x = 13.3 \mu\text{m}$ ) grids; results of the CSD scheme are reported only on the fine grid because a solution could not be obtained on the coarse grid. Even on the fine grid, the CSD method computes zones that are greatly distorted by spurious oscillations. The PLPEI solution on the fine grid, on the other hand, meets not only the convergence criteria defined in Section 3, but is also converged in the zone boundary between the two analytes. The PLPEI and UPWIND schemes produce non-oscillatory solutions on each grid, but the zone boundaries calculated using the PLPEI method are clearly sharper than those produced by the UPWIND scheme. The zone boundary thickness between the two analytes is plotted in Fig. 3 as a function of the grid spacing for the PLPEI and UPWIND schemes. On the coarse grid, the UPWIND scheme predicts a boundary thickness that is more than six times larger than the 145  $\mu\text{m}$  thickness predicted by the PLPEI scheme. On the fine grid, the PLPEI method converges on a thickness of 40  $\mu\text{m}$ , as compared to 320  $\mu\text{m}$  with the UPWIND method. In fact, the UPWIND method requires an order of

magnitude smaller grid spacing just to resolve this zone boundary as well as the PLPEI method does on the coarse grid. Numerical results of this separation have also been reported by Martens et al. using various implicit upwinding algorithms [11]; the method yielding the best overall simulation results (called DIME) predicted a zone boundary thickness of 120  $\mu\text{m}$  on a mesh finer than that required of the PLPEI method to convergence on the 40  $\mu\text{m}$  boundary thickness. Numerical results of this separation on the coarse grid have also been reported by Ermakov et al. [10], who indicated that numerical oscillations form at a current density of 102 A/m<sup>2</sup>. (Note that their results were obtained using a 1 cm sample plug and a grid spacing of 0.5 mm. Using those lengths and a current density of 2260 A/m<sup>2</sup>, the PLPEI method yielded a non-oscillatory solution, which was self-similar to that represented by the dashed line in Fig. 2(a)).

The convergence requirements for each method applied to the ITP simulation are summarized in Table 3. Again, both the UPWIND and CSD schemes did not converge at the limit of 10 000 segments, and thus would require several days to reach convergence. The PLPEI method, however, converged in less than 9 h of simulation time.

#### 4.3. IEF benchmark

IEF separations include some physics not relevant in ZE or ITP separations. In an IEF separation, amphoteric compounds migrate electrophoretically toward their isoelectric point (iep). As they approach their iep, their electromigrational velocities diminish, thus increasing the role of diffusion in their transport behavior. An IEF simulation thus provides a challenging test of a numerical scheme's ability to handle both diffusion and strong electromigration. This is particularly important as regards FCT, since it was first developed to solve unsteady convection problems with no physical diffusion. The character of each component balance (Eqs. (6)) in an IEF simulation is typically, at the outset, hyperbolic over the entire domain. With time, the components migrate toward their iep, where the component balance laws become locally parabolic. Most components approach their iep from either end of the separation domain, so the iep is a turning point in the com-

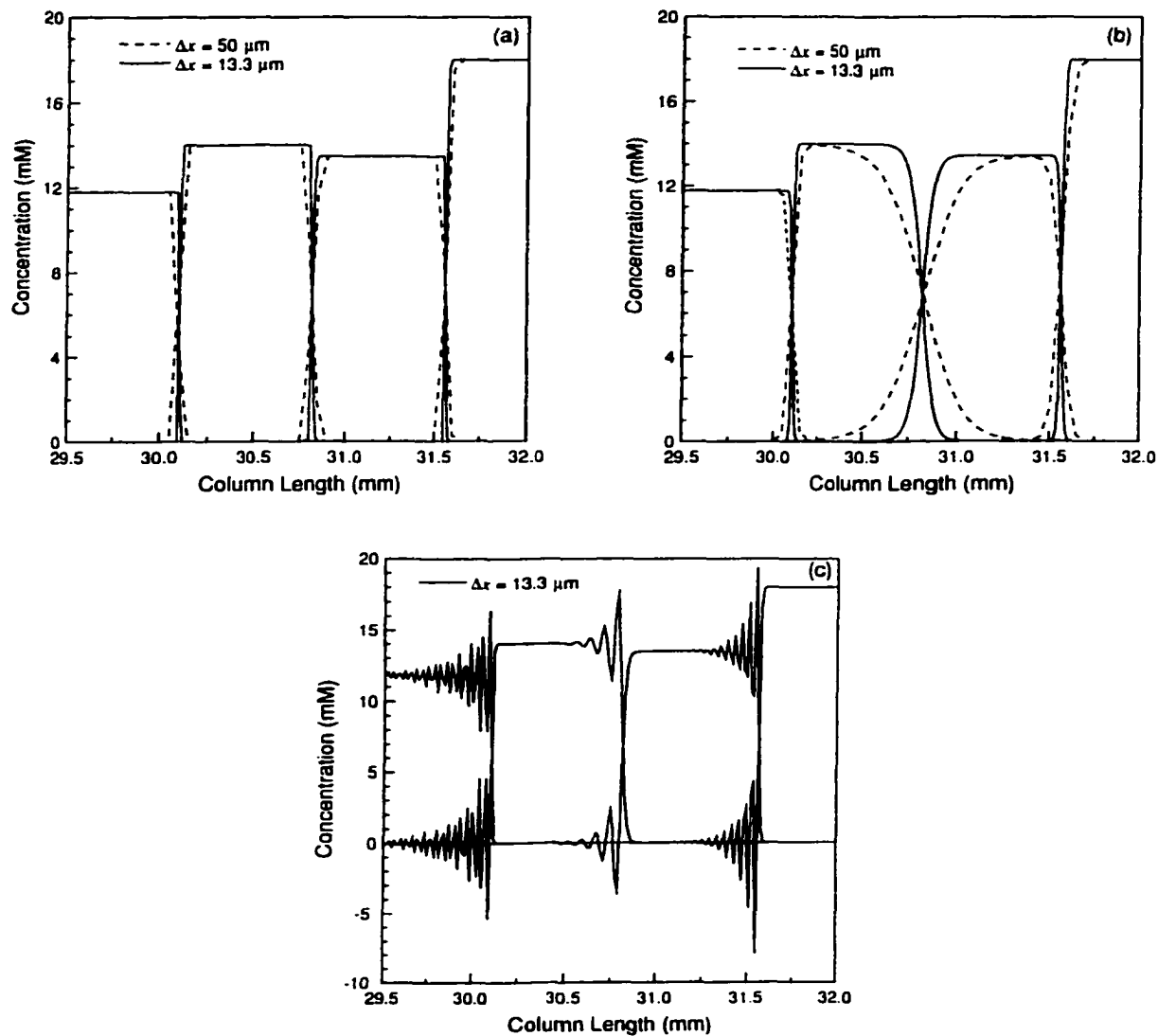


Fig. 2. ITP benchmark sample zone concentration profiles calculated by (a) PLPEI, (b) UPWIND, and (c) CSD. Constant current, 2260  $\text{A}/\text{m}^2$ ; initial voltage, 576 V across a 40 mm column. Initial concentrations: leader, 18 mM NaOH/20 mM HAC; terminator, 40 mM  $\beta$ -alanine/50 mM HAC; sample zone, 10 mM aniline and pyridine in 20 mM HAC. The terminating electrolyte zone is to the left, followed by aniline, pyridine, and the leading electrolyte zone to the right. Anode to the left.

ponent balance law. A numerical scheme applied to an IEF separation must therefore handle the dual hyperbolic/parabolic character of the balance laws, as well as the turning point at the iep.

To evaluate the PLPEI method for IEF, the focusing of a protein in a natural pH gradient

generated by 3 amino acids was simulated. A constant 96.2 V (initial current density  $500 \text{ A}/\text{m}^2$ ) potential difference was applied across a 1 cm separation domain with no-flux boundary conditions at the ends. The initial uniform concentrations of components were 10 mM each of glutamic acid,

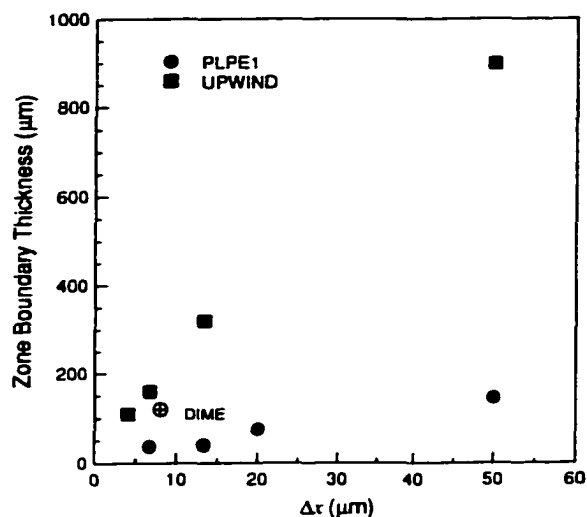


Fig. 3. Predicted ITP steady state boundary thickness between the aniline and pyridine zones as a function of the spatial grid size. The boundary thickness quoted is defined as the distance over which the zone concentrations change from 1% to 99% of their plateau values. Simulation conditions are as for Fig. 2. The DIME data point is from page 56 of Martens et al. [11].

cycloserine, and arginine, and  $7.5 \mu\text{M}$  of bovine serum albumin (BSA). The protein was focused for one min. Results of this simulation conducted at constant current were presented by Mosher et al. for current densities two orders of magnitude lower (for longer times) [5]. Their results show a relatively broad BSA peak occupying approximately 5% to 10% of the simulation domain and similarly broad boundaries between the carrier ampholyte zones. As shown in Figs. 4 and 5, the ampholyte boundaries and the BSA peak are much sharper at the higher field strength.

Fig. 4 shows the carrier ampholyte concentrations computed on coarse ( $\Delta x = 20 \mu\text{m}$ ) and fine ( $\Delta x = 3.33 \mu\text{m}$ ) grids with each numerical technique. As in

Table 3  
Convergence requirements for ITP simulation

	Number of segments	Computation time (h)
PLPE1	3000	8.6
UPWIND	>10 000	>47.5
CSD	>10 000	>33.5

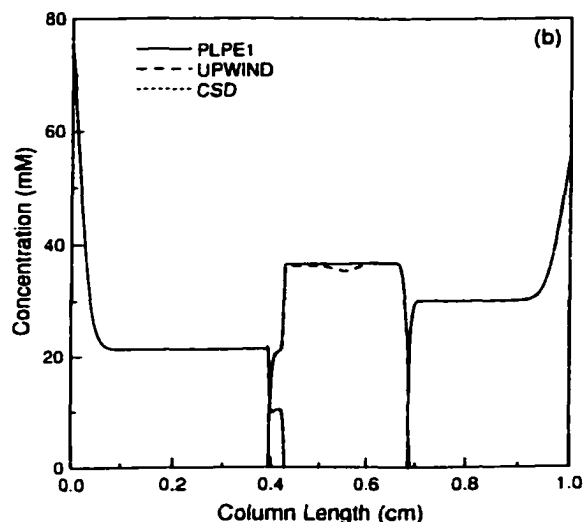
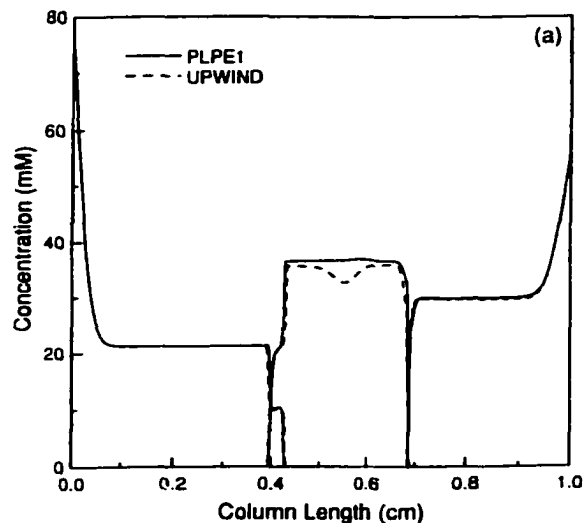


Fig. 4. IEF benchmark carrier ampholyte concentration profiles. The zone on the left boundary is glutamic acid, followed by cycloserine in the center, and the arginine zone on the right boundary. Constant voltage, 96.2 V across a 1 cm column; initial current density,  $500 \text{ A/m}^2$ . Initial carrier ampholyte concentrations, 10 mM each; initial BSA concentration  $7.5 \mu\text{M}$ . The grid spacing is (a)  $20 \mu\text{m}$  and (b)  $3.33 \mu\text{m}$ . Anode to the left.

the ITP simulation, the CSD method would not generate a solution on the coarse grid. The differences between the PLPE1 solutions for the carrier ampholyte concentrations on the coarse and fine

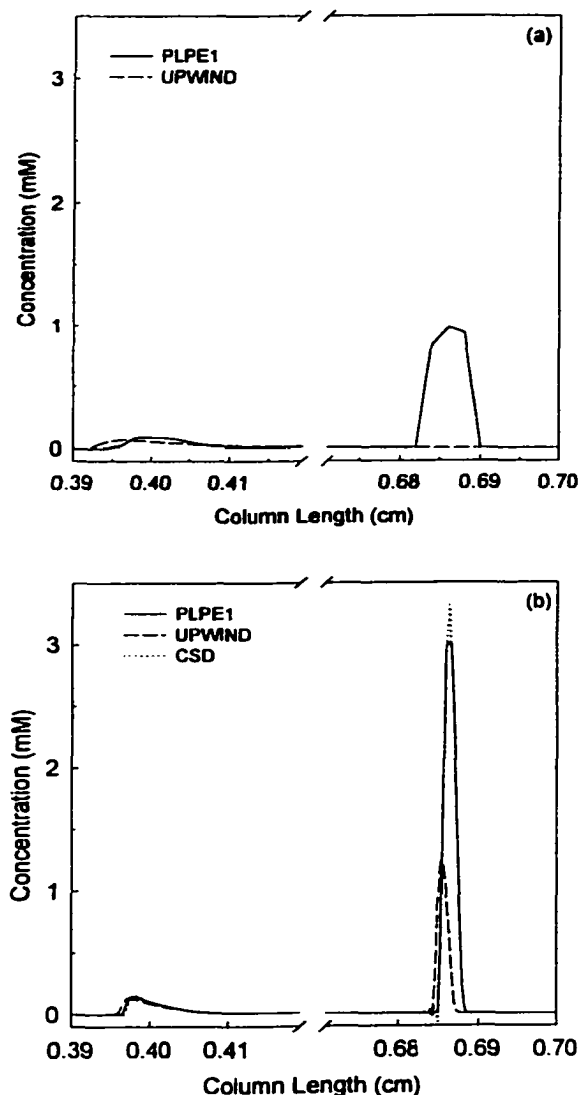


Fig. 5. IEF benchmark BSA concentration profiles. Simulation conditions are as for Fig. 4. The grid spacing is (a) 20  $\mu\text{m}$  and (b) 3.33  $\mu\text{m}$ . Note: results are interpolated linearly between grid points.

grids are barely perceptible on the column length scale, indicating that these components are nearly converged on the coarse grid. The UPWIND solution on the coarse grid exhibits a bit more numerical diffusion, and, more importantly, is flawed with respect to the cycloserine zone concentration. This

results from a mass balance error that occurs where the electrophoretic velocity changes sign (the turning point). The UPWIND scheme approximates the electromigrational derivative at such a point by a forward difference at a node where the velocity is negative and by a backward difference at an adjacent node where the velocity is positive. This results in an inconsistency in the representation of the mass flux for the segments adjacent to the iep. With a sufficiently fine grid, the velocity at these neighboring nodes will approach zero, making the finite difference representation at the turning point irrelevant, and the mass balance error will vanish. On the grids used here, the mass balance error is sufficient to affect the computed concentration field. No such errors occur in the arginine and glutamic acid zones because they accumulate on the ends of the column in approach to their iep, and thus are either positive or negative over the entire simulation domain. On the fine grid, the cycloserine mass balance error is reduced from 4.8% to 1.5%, and a reduction in the zone concentration error is observed. Except for the UPWIND results in the cycloserine zone, the carrier ampholyte concentrations of all three schemes are indistinguishable for the fine grid on the column length scale (Fig. 4(b)).

The protein concentration field is shown in Fig. 5. The separation has not quite reached steady state, as a smaller cathodic peak is migrating toward the anodic peak at the BSA iep. The effect of numerical diffusion on the UPWIND solution on the coarse grid (Fig. 5(a)) can be observed in the small cathodic peak, and mass balance errors by the UPWIND method have completely eliminated the focused protein peak. The BSA mass balance error is far worse than that for cycloserine because the BSA zone is narrow, and thus the BSA electromigrational velocity changes from a significant positive velocity to a significant negative velocity over a short interval. On the fine grid (Fig. 5(b)), the BSA mass balance error is reduced from 74% to 48%, and the focused peak is partially recovered. The PLPE1 solution on the coarse grid accurately predicts the position of the focused protein peak, but the peak height and width change dramatically when calculated on the fine grid. This is not so much a result of numerical diffusion as it is a simple matter of resolution. The BSA zone width predicted on the fine

grid was 30  $\mu\text{m}$ , which is just slightly wider than the 20  $\mu\text{m}$  segment width of the coarse grid. Therefore, even an ideal numerical scheme, which would require 2 segments to resolve a peak positioned with its apex at a node, could not properly resolve the BSA peak on the coarse grid. The PLPE1 solution on the fine grid (Fig. 5(b)) meets all the convergence criteria defined in Section 3 except that the BSA peak concentration changed by more than 1% upon doubling the number of segments. It was estimated that at least a week of simulation time would be required to establish the convergence grid. To converge on the narrow BSA zone with a uniform grid would be inefficient, since computation time would be wasted on thousands of nodes where the concentration would be virtually constant on the segment length scale.

Fig. 5(b) also reveals that the CSD solution for the protein concentration field includes a few small oscillations on the left edge of the focused peak, but this method resolves the peak slightly better than the PLPE1 method. The characteristic 3-node flat top of the PLPE1-generated peak indicates that this results from the 'clipping' phenomenon [20,21], common to flux limiter techniques. The clipping in this case is caused by the strong antidiffusion flux limiter, which does not allow numerical antidiffusion to push the concentration of the peak node above that of neighboring nodes. Fig. 6 shows the BSA peak calculated using the more relaxed flux limiter in the PLPE2 method. With this method, the peak is resolved as well as with CSD method, and no oscillations are formed. Furthermore, this improvement is realized at an insignificant computational cost (4% increase in simulation time), because approximately 80% of the total simulation time is devoted to solving the nonlinear algebraic system of equations governing the pH and component species concentrations. Applying the PLPE2 method, the BSA peak concentration predicted on the fine grid changes by less than 5% upon doubling the number of nodes on this grid.

Fig. 7 shows the pH, conductivity, and electric field computed for this IEF separation on the fine grid using the PLPE2, CSD, and UPWIND schemes. The three methods yield essentially indistinguishable conductivity and pH profiles on the column length scale, as they did for the concentration of the carrier ampholytes. Small pH oscillations on the order of 0.1

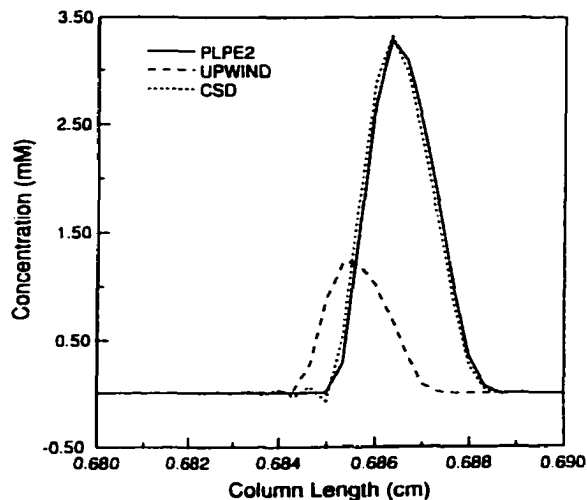


Fig. 6. Improved resolution of the focused BSA peak by the PLPE2 method. Simulation conditions are as for Fig. 4(b). Note: results are interpolated linearly between grid points.

unit, barely visible on this scale, are produced by the CSD method. The CSD method generates substantial oscillations in the electric field (20–30 V/cm amplitude) near the carrier ampholyte zone boundaries. The UPWIND-generated electric field also deviates in the cycloserine zone as a result of the mass balance error.

## 5. Conclusions

The FCT finite difference scheme is an effective method for solving the coupled set of unsteady electromigration–diffusion equations in the electrophoretic separations model. The FCT method yields second-order solutions to these equations, and prevents the formation of numerical oscillations. In contrast to uncorrected higher-order difference schemes, and the artificial dispersion scheme presented by Ermakov et al. [10], there is essentially no Peclet number limit on the stability nor the monotonicity of FCT [15–21]. At  $Pe_L > O(10^3)$ , converged solutions using FCT can typically be realized on coarser grids and in significantly less simulation time than the UPWIND or CSD methods. Also, for the benchmark separations simulated here, the PLPE

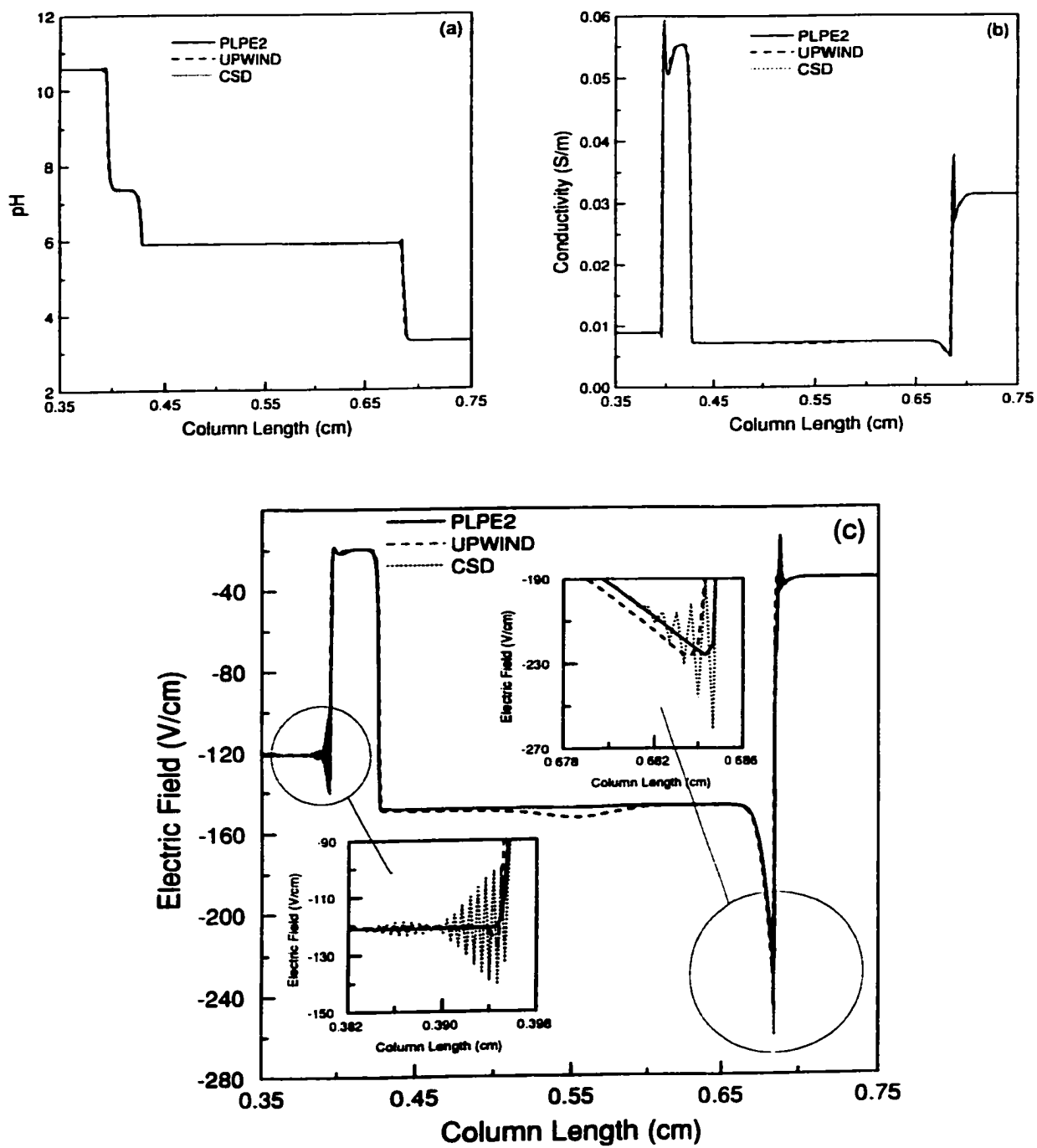


Fig. 7. IEF benchmark pH, conductivity, and electric field profiles. Simulation conditions are as for Fig. 4(b).

method yielded non-oscillatory and significantly more accurate solutions to the electrophoresis model than any of the other published methods. This improved efficiency and the explicit structure of the algorithm will become even more important for two and three dimensional unsteady electrophoresis problems, wherein the simulation time scales as  $n^2$  and  $n^4$  respectively.

In cases such as the IEF benchmark, where convergence was limited by the resolution of the narrow but stationary protein peak, FCT provides only a modest improvement over the CSD method. In no cases studied to date has the FCT method required a finer grid than either the UPWIND or CSD methods; moreover, on coarse grids where CSD fails, one can still use FCT to obtain non-converged solutions that yield such gross features as the position and approximate shape of zone boundaries or peaks.

Finally, for problems such as the IEF benchmark, which are characterized by a disparity in length scales, an adaptive mesh should be developed to provide converged solutions with reasonable efficiency. When combined with an adaptive mesh, the FCT scheme will greatly reduce the number of segments required to converge in regions where sharp gradients are advected at high electric Peclet numbers.

#### Acknowledgements

This work was supported, in part, by the NSF/SRC Center for Environmentally-Benign Semiconductor Manufacturing at The University of Arizona.

#### References

- [1] R. Kniss, *Am. Lab.* 30 (1998) 40.
- [2] M. Bier, O.A. Palusinski, R.A. Mosher, D.A. Saville, *Science* 219 (1983) 1281.
- [3] D.A. Saville, O.A. Palusinski, *AIChE J.* 32 (1986) 207.
- [4] O.A. Palusinski, A. Graham, R.A. Mosher, M. Bier, D.A. Saville, *AIChE J.* 32 (1986) 215.
- [5] R.A. Mosher, D.A. Saville, XV. Thormann, *The Dynamics of Electrophoresis*, VCH, Weinheim, 1992.
- [6] E.V. Dose, G.A. Guiochon, *Anal. Chem.* 63 (1991) 1063.
- [7] C. Schafer-Nielsen, *Electrophoresis* 16 (1995) 1369.
- [8] C. Schwer, B. Gas, F. Lottspeich, E. Kenndler, *Anal. Chem.* 65 (1993) 2108.
- [9] S.V. Ermakov, O.S. Mazhorova, Yu.P. Popov, *Informatica* 3 (1992) 173.
- [10] S.V. Ermakov, M.S. Bello, P.G. Righetti, *J. Chromatogr. A* 661 (1994) 265.
- [11] J.H.P.A. Martens, J.C. Reijenga, J.H.M. ten Thije Boonkamp, R.M.M. Mattheij, F.M. Everaerts, *J. Chromatogr. A* 772 (1997) 49.
- [12] N. Ikuta, T. Hirokawa, *J. Chromatogr. A* 802 (1998) 49.
- [13] P.K. Sweby, *SIAM J. Numer. Anal.* 21 (1984) 995.
- [14] B. van Leer, *J. Comp. Phys.* 14 (1974) 361.
- [15] J.P. Boris, D.L. Book, *J. Comp. Phys.* 11 (1973) 38.
- [16] D.L. Book, J.P. Boris, K. Ham, *J. Comp. Phys.* 18 (1975) 248.
- [17] J.P. Boris, D.L. Book, *J. Comp. Phys.* 20 (1976) 397.
- [18] J.P. Boris, D.L. Book, *Methods in Computational Physics* 16 (1976) 85.
- [19] D.L. Book, J.P. Boris, S.T. Zalesak, in: D.L. Book (Ed.), *Finite-Difference Techniques for Vectorized Fluid Dynamics Calculations*, New York, 1981, Chapter 3, p. 29.
- [20] S.T. Zalesak, *J. Comp. Phys.* 31 (1979) 335.
- [21] J.P. Boris, A.M. Landsberg, E.S. Oran, J.H. Gardner, *LCPFCT – Flux-Corrected Transport Algorithm for Solving Generalized Continuity Equations*, NRL Memorandum Report 6410-93-7192, Naval Research Laboratory, Washington, 1993.
- [22] D. Odstrcil, *J. Comp. Phys.* 91 (1990) 71.
- [23] N. Grandjouan, *J. Comp. Phys.* 91 (1990) 424.
- [24] M.J. Clifton, *Electrophoresis* 14 (1993) 1284.
- [25] S. Blanco, M.J. Clifton, J.L. Joly, G. Pelre, *Electrophoresis* 17 (1996) 1126.
- [26] J.L. Anderson, W.K. Idol, *Chem. Eng. Commun.* 38 (1985) 93.
- [27] R.A. Mosher, C.X. Zhang, J. Caslavka, W. Thormann, *J. Chromatogr. A* 716 (1995) 17.
- [28] H.A. Watts, *Trans. Soc. Computer Simulation* 1 (1985) 15.
- [29] F. Kohrausch, *Ann. Phys.* 62 (1897) 209.

## APPENDIX B

**SIMULATION OF ELECTROPHORETIC SEPARATIONS:  
EFFECT OF NUMERICAL AND MOLECULAR DIFFUSION  
ON pH CALCULATIONS IN POORLY BUFFERED SYSTEMS**

This manuscript has been published in *Electrophoresis* (**21**, 2287-2295, 2000) and is reproduced here with kind permission from WILEY-VCH.

T. L. Sounart  
J. C. Baygents

Department of Chemical and  
Environmental Engineering,  
The University of Arizona,  
Tucson, AZ, USA

## Simulation of electrophoretic separations: Effect of numerical and molecular diffusion on pH calculations in poorly buffered systems

A poorly buffered cationic isotachopheresis separation, first simulated by Reijenga and Kašička, has been revisited to demonstrate that an inconsistent description of solute and charge transport can lead to significant errors in the pH calculation. The separation is first simulated using a second-order finite difference scheme to show that omission of molecular diffusion from the charge balance results in a pH profile with spurious dips in the steady-state zone boundaries. The separation is also simulated using two first-order methods that employ numerical diffusion to stabilize solutions against spatiotemporal oscillations. Similar pH dips are generated by these first-order schemes, even when molecular diffusion is included in the charge balance, if numerical diffusion is not considered amongst the charge transport mechanisms. When numerical diffusion, inherent in the discretization of the component balances, is introduced to the charge balance, the spurious pH dips are eliminated. The results indicate that (i) pH dips originally reported by Reijenga and Kašička are merely artifacts of their numerical model, and (ii) nonoscillatory numerical techniques, such as upwinding and flux limiters, should incorporate artificial transport mechanisms in the charge as well as the solute balances.

**Keywords:** Simulation / Electrophoresis / Diffusion / pH / Upwind

EL 3996

### 1 Introduction

Computer simulations of the classical modes of electrophoretic separation [1] have been used since the mid-1980s to advance our understanding of the dynamics of electrophoresis. To avoid spurious, spatiotemporal oscillations in the calculations, the original numerical studies on electrophoresis were limited to electric field strengths at least an order of magnitude lower than those typically used in practice [1–5]. More recently, upwinding [6, 7] and flux limiter methods [8,9] have been used to suppress numerical oscillations, and this has permitted the investigation of separation phenomena at realistic field strengths (50–500 V/cm).

The balance laws for electrophoretic separations are susceptible to numerical oscillations because, at normal electric field strengths, buffer and analyte transport are domi-

nated by electromigration, except, of course, in regions with sharp spatial transitions. Typical finite-difference representations of the governing equations do not suffice to capture these dramatic transitions, which are characterized by a competition between electromigration and diffusion of the ionic solutes, such as at the boundary between migrating isotachopheretic zones. Flux limiter and upwinding methods accommodate steep gradients, and thus stabilize the computational algorithms against oscillations, by introducing artificial or numerical diffusion – albeit at the expense of some accuracy. The loss of accuracy is generally considered more tolerable than the generation of spurious oscillations, and flux-limited antidiffusion or ultrafine meshes can be used to diminish the loss [9].

While artificial diffusion is certainly an acceptable means to control and avoid numerical instabilities, it is the purpose of the present communication to establish that, without proper accounting for numerical and molecular diffusion, electrophoresis simulations can generate artifactual pH variations. For example, Reijenga and Kašička [10] used a first-order upwind scheme (DIME) to study poorly buffered ITP systems, and reported significant pH dips or peaks (1–2 units) at the steady-state zone boundaries. Reijenga and Kašička refer to these unusual pH variations as discontinuities because one would normally expect pH to vary monotonically between neighboring ITP zones. In the presentation that follows, we show that the

**Correspondence:** Dr. J. C. Baygents, Department of Chemical and Environmental Engineering, The University of Arizona, Tucson, AZ, 85721 USA  
**E-mail:** jcb@maxwell.che.arizona.edu  
**Fax:** +520-621-6048

**Abbreviations:** CSD, central spatial difference; FCT, flux-corrected transport; HOAc, acetic acid; KOAc, potassium acetate; ND, numerical diffusion; RKF, Runge-Kutta-Fehlberg; TEA, tetraethylammonium; UW, upwind

pH discontinuities uncovered by Reijenga and Kašicka are, in fact, artificial and are inherently generated by schemes such as DIME. The pH artifacts are manifested in simulations of poorly buffered systems if upwinding, or other forms of diffusion, are included in the solute balance laws, but not in the charge balance.

After a brief description of the electrophoresis model, we begin by showing that pH discontinuities, analogous to those reported by Reijenga and Kašicka, arise when molecular diffusion is omitted from the charge balance. This is done without employing numerical diffusion and establishes the need for a consistent description of the solute and the charge transport mechanisms. We then demonstrate that inclusion of a numerical diffusion current in the charge balance substantially reduces the pH artifacts generated by a standard upwind scheme. Finally, we present a modified central difference scheme that completely eliminates pH artifacts by treating numerical diffusion in the species and charge balances in a self-consistent way.

Taken together, these results imply that accurate determination of pH requires consistent treatment of diffusion (numerical or molecular) in the charge and species balance laws, especially in poorly buffered systems. That is, pH artifacts can result from either of two errors – one numerical, the other conceptual. The conceptual error involves the mechanisms for charge transport. Electrolyte solutions are ionic conductors, so charge is transported by ohmic and Brownian processes. Omitting the molecular diffusion current from the charge balance, while retaining molecular diffusion in the component balances, can result in substantially flawed results for the local pH, irrespective of the numerical method. The numerical method spawns errors when discrete representations of the spatial gradients in the charge balance differ from those used for the component mass balances.

## 2 Methods

### 2.1 Balance laws for electrophoretic separations

A general set of balance laws, governing the transport of ionic and neutral compounds in electrophoretic separations, includes an unsteady electromigration-diffusion equation for each solutal component, a charge balance, the electroneutrality approximation, expressions for ionogenic dissociation-association equilibria, and a model for calculating protein mobilities as a function of pH and ionic strength [1, 11]. The balance laws are summarized here in a form suited to upwind simulations; a more complete exposition of the notation appears in [9].

At a given instant, ion concentrations, pH, and effective valences are determined by a coupled set of mass-action relations. These include the dissociation of water and the ion dissociation-association equilibria for  $M$  solutal components. Suppose that  $A_k^z$  denotes the subspecies of the  $k$ th component with valence  $z$ , and that  $A_k^0$ , the neutral form of the  $k$ th component, is multiply protonated to form  $P_k$  cationic subspecies and multiply deprotonated to form  $N_k$  anionic subspecies. Then the mass-action equilibrium relations for these protonation-deprotonation reactions are

$$K_k^z \equiv \frac{[H^+]n_k^{z-1}}{n_k^z} \quad \begin{cases} z = N_k + 1, -N_k + 2, \dots, +P_k \\ k = 1, 2, \dots, M \end{cases} \quad (1)$$

where  $n_k^z$  is the concentration of subspecies  $A_k^z$ . It follows from the electroneutrality approximation that

$$0 = \sum_{k=1}^M \bar{z}_k C_k + [H^+] - \frac{K_w}{[H^+]} \quad (2)$$

where  $K_w \equiv [H^+][OH^-]$ , and  $C_k$  is the concentration and  $\bar{z}_k$  is the effective valence of the  $k$ th component, i.e.

$$C_k \equiv \sum_{z=N_k}^{+P_k} n_k^z \quad k = 1, 2, \dots, M \quad (3)$$

and

$$\bar{z}_k \equiv \frac{\sum_{z=N_k}^{+P_k} z n_k^z}{C_k} \quad k = 1, 2, \dots, M \quad (4)$$

To describe local variations of the  $C_k$  with time, a mass balance is written for each component, viz.

$$\frac{\partial C_k}{\partial t} = -\nabla \cdot \mathbf{f}_k^e + \omega_k k_B T \nabla^2 C_k \quad k = 1, 2, \dots, M \quad (5)$$

In Eq. (5),  $k_B T$  is the Boltzmann temperature;  $\omega_k$  and  $\mathbf{f}_k^e$ , respectively, denote the hydrodynamic mobility (taken here to be independent of component speciation) and the electromigrational flux of the  $k$ th component. Accordingly,

$$\mathbf{f}_k^e = \mathbf{v}_k^e C_k = e \bar{z}_k \omega_k \mathbf{E} C_k, \quad k = 1, 2, \dots, M \quad (6)$$

where  $\mathbf{v}_k^e$  is the effective component electrophoretic velocity,  $\mathbf{E}$  is the local electric field, and  $e$  is the charge on a proton ( $1.6 \times 10^{-19}$  C).

The governing equations are closed by combining Eqs. (2) and (5) to balance the charge and obtain an equation for  $\mathbf{E}$ . Since the volume charge density vanishes, the current density must be solenoidal. Thus

$$0 = \nabla \cdot [\sigma \mathbf{E} + \mathbf{i}^d] \quad (7)$$

where

$$\sigma = e^2 \left[ \sum_{k=1}^M \bar{z}_k^2 \omega_k C_k + \omega_H [H^+] + \omega_{OH} \frac{K_w}{[H^+]} \right] \quad (8)$$

is the local electrical conductivity, and

$$\mathbf{i}^d = e k_B T \left( \sum_{k=1}^M \omega_k \nabla \bar{z}_k C_k + \omega_H \nabla [H^+] - \omega_{OH} K_w \nabla [H^+]^{-1} \right) \quad (9)$$

is the current density resulting from component diffusion, i.e., the diffusion current density. In Eqs. (8) and (9),  $\omega_H$  and  $\omega_{OH}$  are, respectively, the hydrodynamic mobilities of  $H^+$  and  $OH^-$ , and  $\bar{z}_k^2$  is the mean square valence of the  $k$ th component,

$$\bar{z}_k^2 \equiv \frac{\sum_{z=-P_k}^{+P_k} N_k z^2 n_k^z}{C_k}, \quad k = 1, 2, \dots, M \quad (10)$$

By including both ohmic ( $\sigma \mathbf{E}$ ) and diffusive ( $\mathbf{i}^d$ ) contributions to the current density, Eq. (7), in principle, ensures that the charge balance is consistent with electroneutrality and the mechanisms postulated for solute transport.

## 2.2 Numerical implementation

The poorly buffered cationic isotachophoretic separation described by Reijenga and Kašicka [10] was simulated with three numerical techniques, including a central spatial discretization scheme and two schemes employing numerical diffusion to guarantee monotonicity. The classical first-order upwind scheme was applied to Eq. (5) with an Euler time step. In this scheme, the spatial discretization is equivalent to that used by Reijenga and Kašicka [10], but the time derivative is discretized by a forward difference to yield a fully explicit scheme. The time derivative was handled in this way because it makes the algorithm straightforward to code; moreover, use of an explicit time step does not substantially alter the results of the simulations.

Equation (5) was solved in one space dimension according to the following algorithm: for each component, the concentration  $C_{i,j+1}$  at each position  $x_i = l \Delta x$  ( $l = 0, 1, 2,$

$\dots, n_x$ ) was calculated at time  $t_{j+1} = t_j + \Delta t$  ( $j = 0, 1, 2, \dots, n_t$ ), where  $t_j = \sum_{m=1}^j (\Delta t)_m$ ;  $\Delta x$  and  $\Delta t$  are, respectively, the discretized spatial and temporal increments, and  $n_x$  and  $n_t$  are, respectively, the number of spatial and temporal increments. The formula for  $C_{i,j+1}$  depends on the sign of  $f_{i,j}^e$ , which here denotes the electromigrational flux at position  $x_i$  and time  $t_j$ . For  $f_{i,j}^e < 0$ ,

$$C_{i,j+1} = C_{i,j} - \Delta t \frac{f_{i,j+1}^e - f_{i,j}^e}{\Delta x} + \Delta t \frac{C_{i,j+1} + 2C_{i,j} + C_{i,j-1}}{(\Delta x)^2} \quad (11)$$

For  $f_{i,j}^e > 0$ ,

$$C_{i,j+1} = C_{i,j} - \Delta t \frac{f_{i,j}^e - f_{i,j-1}^e}{\Delta x} + \Delta t \frac{C_{i,j,j} + 2C_{i,j} + C_{i,j-1}}{(\Delta x)^2} \quad (12)$$

This scheme is identified here as UW.

An alternate first-order scheme, similar to UW, was also implemented. In this scheme, a discretized numerical diffusion term is added to a central difference approximation of the electromigration term; the numerical diffusion added is approximately equal to the numerical diffusion inherent in the UW scheme.  $C_{i,j+1}$  is calculated as

$$C_{i,j+1} = C_{i,j} - \Delta t \frac{f_{i,j+1}^e - f_{i,j-1}^e}{\Delta x} + \frac{1}{2} \epsilon_{i,j+1} (C_{i-1,j} - C_{i,j}) - \frac{1}{2} \epsilon_{i,j-1} (C_{i,j} - C_{i-1,j}) + \Delta t \frac{C_{i,j+1} - 2C_{i,j} + C_{i,j-1}}{(\Delta x)^2} \quad (13)$$

where

$$\epsilon_{i,j} \equiv \frac{|V_{i,j}^e| \Delta t}{\Delta x} \quad (14)$$

is the local Courant number. Any values required at  $x_{i+1/2}$  are calculated as the arithmetic average of those at  $x_i$  and  $x_{i+1}$ . This alternate scheme is identified here as ND.

To establish a basis for assessing the UW and ND schemes, the isotachophoretic separation was also simulated with a Runge-Kutta-Fehlberg (RKF) time-step and a central spatial discretization (CSD) of Eq. (5). This scheme was chosen because it is fifth-order accurate in time and second-order accurate in space, and thus converges on coarser grids than the first-order schemes. This scheme is identified as CSD and is equivalent to that discussed at length in Mosher *et al.* [1]. In all simulations, the spatial discretization step was prescribed and the time step calculated to meet criteria specific to each numerical

**Table 1.** Buffer and separand properties

Component	pK	Mobility ( $10^{-8} \text{ m}^2/\text{Vs}$ )
HOAc	4.76	4.12
K <sup>+</sup>	–	7.61
Na <sup>+</sup>	–	5.19
Li <sup>+</sup>	–	4.01
TEA	–	3.38
H <sup>+</sup>	–	36.27
OH <sup>-</sup>	–	19.87

method. In the UW and ND simulations, the time step was calculated to maintain the maximum Courant number at 0.40. In the CSD simulations, the time step was controlled by the RKF algorithm, which adjusts the time step to maintain an estimate of the truncation error within prescribed bounds [11].

### 3 Results and discussion

Various simulations of the poorly buffered cationic ITP separation, described by Reijenga and Kašicka [10], were implemented and are discussed below; for the sake of brevity, analogous simulations of anionic ITP are not discussed, though similar results were obtained. The leading electrolyte consisted of 10 mM potassium acetate (KOAc) salt, and the terminating electrolyte was composed of 15 mM acetic acid (HOAc). Five mM sodium hydroxide (NaOH), lithium hydroxide (LiOH), and tetraethylammonium (TEA) hydroxide were introduced as a 1 mm sample plug, 1 mm from the anodic end of a 15 mm separation domain. The sample components were dissolved in the terminating electrolyte, which occupied the first 2 mm of the anodic end of the column. The system was simulated for 7.2 s of separation time, at a constant current of 2260 A/m<sup>2</sup>, which corresponded to an initial mean electric field of 390 V/cm. Component properties are provided in Table 1.

We begin by illustrating the effect of omitting the diffusion current from Eq. (7), the charge balance. Figure 1 shows pH profiles in the isotachophoretic sample region, calculated using the CSD method with  $\Delta x = 1.5 \mu\text{m}$ . The results presented in the figure are converged, *viz.* simulation on a grid with twice as many nodes produces no distinguishable change on the length scale shown. When the complete model described in Section 2.1 is solved, no pH dips appear in the zone boundaries. The pH profile steps monotonically from zone to zone, as is typical of ITP separations. When  $i^d$  is omitted from Eq. (7), pH dips similar to those reported by Reijenga and Kašicka [10] are generated at the zone boundaries (Fig. 1, dashed lines). At high electric Peclet numbers, *i.e.*

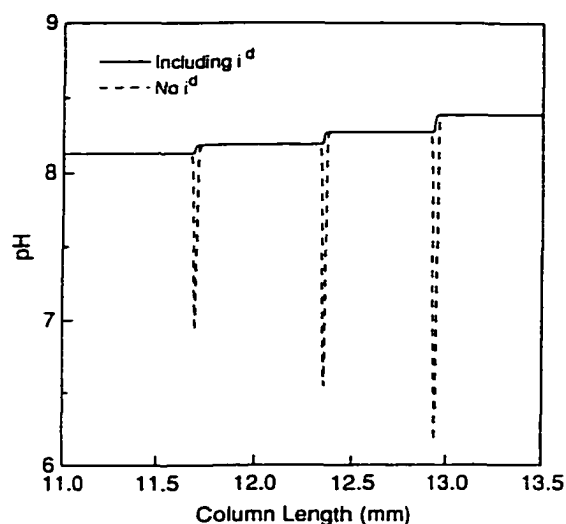


**Figure 1.** pH profiles in sample region, calculated by CSD. Constant current, 2260 A/m<sup>2</sup>; initial mean electric field, 390 V/cm. Initial concentrations: leader, 10 mM KOAc; terminator, 15 mM HOAc; sample zone, 5 mM NaOH, LiOH, and TEA hydroxide in terminator. The TEA zone is to the left, followed by Li<sup>+</sup>, Na<sup>+</sup>, and K<sup>+</sup> to the right. Anode to the left. The grid spacing is 1.5  $\mu\text{m}$ .

$$Pe_e \equiv \left| \frac{v^e L}{\omega k_B T} \right| \gg 1 \quad (15)$$

where  $L$  is the column length, and where  $\omega k_B T$  and  $v^e$  are, respectively, a characteristic diffusivity and electrophoretic velocity, some researchers neglect the diffusion current density [6, 7, 10, 13], and Reijenga and Kašicka do so in their model. Figure 1 indicates that such an omission can result in artificial pH dips at the zone boundaries, even if  $Pe_e \gg 1$ . The spatial gradients in these regions are sufficiently large that diffusion of charge must be considered.

Omission of the diffusion current from the charge balance causes pH errors because the species balances are coupled through mass action and electroneutrality. Accumulation of charge is absent from the charge balance (Eq. 7) inasmuch as the volume charge vanishes everywhere. An electric field, consistent with electroneutrality, is thus calculated from Eq. (7), given the mechanisms of ion transport included in the component balances. When diffusion is included in the component balances but not in the charge balance, the current is not properly reckoned. In other words, the presumed flux of charge is not consistent with the flux of ions. Since the pH is determined directly

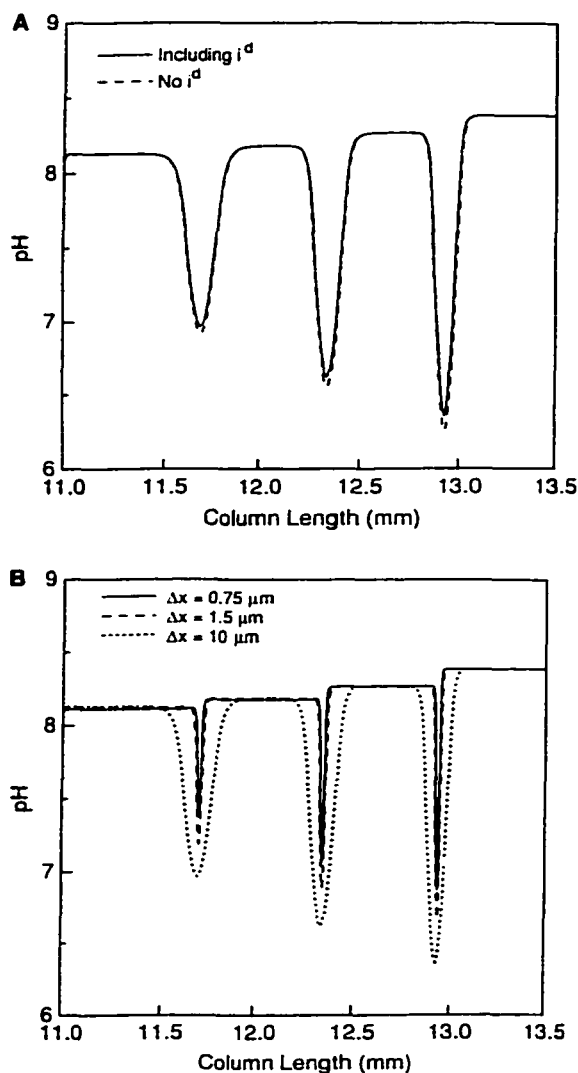


**Figure 2.** pH profiles calculated by UW;  $i^{nd}$  not included in charge balance. Simulation conditions are as for Fig. 1. Anode to the left. (a) Grid spacing is  $10\ \mu\text{m}$ . (b) Refined meshes;  $i^{nd}$  included in the charge balance.

from the electroneutrality approximation (Eq. 2), an erroneous local pH results. In most separations at  $Pe_e \gg 1$ , this inconsistency has little influence on the pH. However, in poorly buffered systems, such as the ITP separation considered here, the pH is extremely sensitive to the concentrations of other ions, meaning small errors in the ion concentrations result in substantial errors in the pH. It is important to note that Reijenga and Kašicka [9] have pre-

viously demonstrated that the pH dip at an ITP boundary vanishes as the buffering capacity of the leading electrolyte or sample cation increases (cf. their Fig. 1 and 4).

The  $Pe_e$  is not a satisfactory criterion for evaluating the importance of the diffusion current because a more appropriate length scale for diffusion in the zone boundaries is the zone boundary thickness. It is not necessary to estimate this length scale, however, as it is known that diffusion is always important in ITP zone boundary regions; the ITP zone boundary length is controlled by a balance between the species diffusive and electromigrational fluxes in the moving isotachophoretic reference frame. Errors introduced by neglecting the diffusion current in these regions may be absorbed by a sufficient buffering capacity of the electrolytes, but it is not always obvious what constitutes "sufficient" buffering capacity. Since it is computationally inexpensive to do so, it seems reasonable to always include the diffusion current in simulations of electrophoretic systems that include dramatic spatial variations of the ion concentrations.

Figure 2 shows the pH profiles calculated using the UW scheme and a grid spacing of  $10\ \mu\text{m}$ . As shown in Fig. 2a, pH dips are produced by this scheme with and without diffusion current in the charge balance; omission of  $i^{nd}$  only slightly increases the magnitude of the pH dips. Figure 2b shows the pH profile calculated on three different grids ( $\Delta x = 10\ \mu\text{m}$ ,  $1.5\ \mu\text{m}$ , and  $0.75\ \mu\text{m}$ ), with the diffusion current included in the model. The pH dips diminish as the mesh is refined, so the solution is not converged – even with 20 000 segments ( $\Delta x = 0.75\ \mu\text{m}$ ) – though presumably the results will converge to that shown in Fig. 1.

The pH dips obtained with the UW scheme are caused primarily by numerical diffusion, or rather by the presence of numerical diffusion in the component balances but not in the charge balance. By their discretization of the electromigration flux in Eq. (5), first-order upwind schemes introduce numerical diffusion to the component balances, which prevents the formation of numerical oscillations in the component concentration profiles. However, this also creates an inconsistency similar to that described for molecular diffusion as it pertains to the charge balance. With upwinding numerical diffusion, the inconsistency results when  $\sigma E$ , the ohmic or electromigrational flux of charge in Eq. (7), is treated differently from  $f_k^e$ , the electromigrational flux of component  $k$  in Eq. (5). The  $\nabla \cdot f_k^e$  are calculated by the upwind difference approximations in Eqs. (11) and (12). However, no difference approximation is required for  $\nabla \cdot (\sigma E)$ , because Eq. (7) can be integrated directly for 1-D problems. Since the current density  $i$  must be independent of  $x$ , Eq. (7) yields

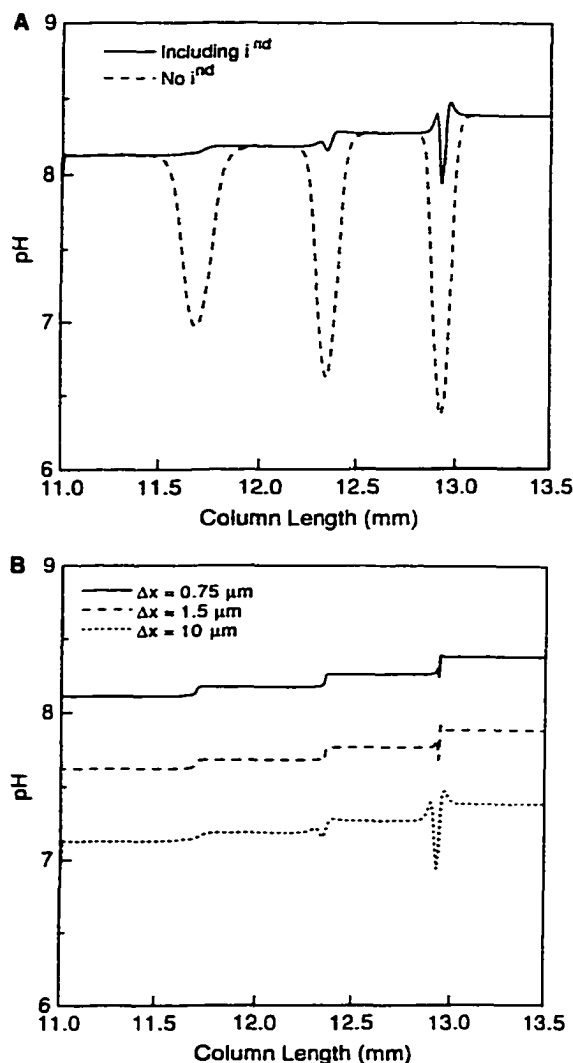


**Figure 3.** pH profiles calculated by UW. Simulation conditions are as for Fig. 1. Anode to the left. (a) Grid spacing is  $10 \mu\text{m}$ . (b) Refined meshes;  $i^d$  and  $i^{nd}$  included in the charge balance. pH profiles in (b) are shifted (dashed line by  $-0.5$  units, dotted line by  $-1.0$  units) for clarity.

$$E = \frac{i - i^d}{\sigma} \quad (16)$$

The solution for the electric field  $E$  thus follows immediately from the charge balance, and incorporates an exact expression for the electromigrational ion fluxes. Conversely, the solutions to Eq. (5) satisfy a discretized ver-

sion of the component balances, which includes the upwind approximations for the electromigrational fluxes; the upwind approximation is equivalent to an exact expression plus a truncation error that, to leading order, has a mathematical form similar to that of molecular diffusion (see below). This numerical diffusion is not included in the charge balance, but contributes (artificially) to the component transport. As a consequence, it has the same effect on the pH calculation as does the inconsistent treatment of molecular diffusion, which was discussed previously in the context of Fig. 1.

The pH artifacts generated by the UW scheme are greatly reduced by including an estimate of the numerical diffusion current in the charge balance. In one dimension, Eq. (5) reads

$$\frac{\partial C_k}{\partial t} = \frac{\partial f_k^e}{\partial x} + \omega_k k_B T \frac{\partial^2 C_k}{\partial x^2} \quad k = 1, 2, \dots, M \quad (17)$$

and the UW finite-difference approximation for  $\partial f_k^e / \partial x$  is

$$\frac{\partial f_k^e}{\partial x} = \begin{cases} [f_k^e(x + \Delta x, t) - f_k^e(x, t)] / \Delta x - \xi_k + O[(\Delta x)^2], & f_k^e(x, t) < 0 \\ [f_k^e(x, t) - f_k^e(x - \Delta x, t)] / \Delta x - \xi_k + O[(\Delta x)^2], & f_k^e(x, t) > 0 \end{cases} \quad k = 1, 2, \dots, M \quad (18)$$

where the numerical error incurred by the approximation is, to leading order,

$$\xi_k = \frac{\partial}{\partial x} \left[ -\frac{\Delta x}{2} \frac{\partial |f_k^e|}{\partial x} \right] = \frac{\partial f_k^{nd}}{\partial x} \quad k = 1, 2, \dots, M \quad (19)$$

By combining Eqs. (6) and (19), one can show

$$f_k^{nd} = \frac{\Delta x e \omega_k}{2} \frac{\partial}{\partial x} [|\bar{z}_k E| C_k] \quad k = 1, 2, \dots, M \quad (20)$$

which has the essential character of a diffusive flux. The flux of charge resulting from these numerical fluxes of ions, *i.e.*, the numerical diffusion current density, is

$$i^{nd} = \frac{\Delta x e^2}{2} \sum_{k=1}^M \omega_k \sum_{z=N_k}^{+P_k} z |z| \frac{\partial}{\partial x} [|\bar{z}_k E| C_k] \quad (21)$$

If this flux is included in the charge balance, then the electric field is calculated as

$$E = \frac{i - i^d - i^{nd}}{\sigma} \quad (22)$$

where  $i^{nd}$  is given by Eq. (21). Equation (22) is not explicit in  $E$ ; therefore  $E$  is calculated by an iterative procedure. At each time  $t_i$  and position  $x_i$ , an estimate of  $i^{nd}$  from the previous time step  $t_{i-1}$  yields an initial guess  $E_{i,i}^0$  for  $E_{i,i}$ , viz.

$$E_{i,i}^0 = \frac{i_{i,i} - i_{i,i}^d - i_{i,i-1}^{nd}}{\sigma} \quad (23)$$

Iterations are then performed by successive substitution until  $E$  converges. At each iteration  $m$ ,  $E_{i,i}^m$  is calculated as

$$E_{i,i}^m = \frac{i_{i,i} - i_{i,i}^d - i_{i,i}^{nd,m-1}}{\sigma} \quad (24)$$

where  $i_{i,i}^{nd,m-1}$  denotes  $i_{i,i}^{nd}$  evaluated at  $E_{i,i}^{m-1}$ . The ITP problem studied here required a maximum of three iterations when the spatial gradient in Eq. (21) was calculated by a fourth-order central difference approximation.

Figure 3 shows the reduction in the pH error when the approximate numerical diffusion is included in the charge balance. As shown in Fig. 3a, for  $\Delta x = 10 \mu\text{m}$ , two of the dips are nearly eliminated, while the error in the boundary between the potassium and sodium zones is significantly reduced. Figure 3b shows that the pH error is essentially eliminated by decreasing the segment length to  $\Delta x = 0.75 \mu\text{m}$ . The maximum error in the pH for  $\Delta x = 1.5 \mu\text{m}$  and  $0.75 \mu\text{m}$  is 0.14 units and 0.06 units, respectively, in contrast to 1.65 units and 1.44 units (Fig. 2b) when the numerical diffusion is not included in the charge balance.

Figure 4 shows the electric and component concentration fields in the sample region, computed by the UW method. Inclusion of numerical diffusion in the charge balance has no noticeable effect on these dependent variables. Omission of the numerical diffusion current, however, results in small errors in the electric and concentration fields, not discernible on the scale of Fig. 4. These small errors produce large errors in the pH profile because  $[\text{H}^+]$  is five orders of magnitude lower than the buffer and separand concentrations, and because the electrolytes have little buffering capacity.

Certain residual error persists in the UW calculation for pH because only an approximation for the numerical diffusion was included in the charge balance. Furthermore, the molecular diffusion flux is calculated at  $x_{i+1/2}$  ( $i = 0, 1, 2, \dots, n_s - 1$ ) in the component balances (Eqs. 11 and 12), and at  $x_i$  ( $i = 0, 1, 2, \dots, n_s$ ) in the charge balance (Eq. 24). This may also contribute to discrepancies in the pH calculation. These errors can be eliminated by use of

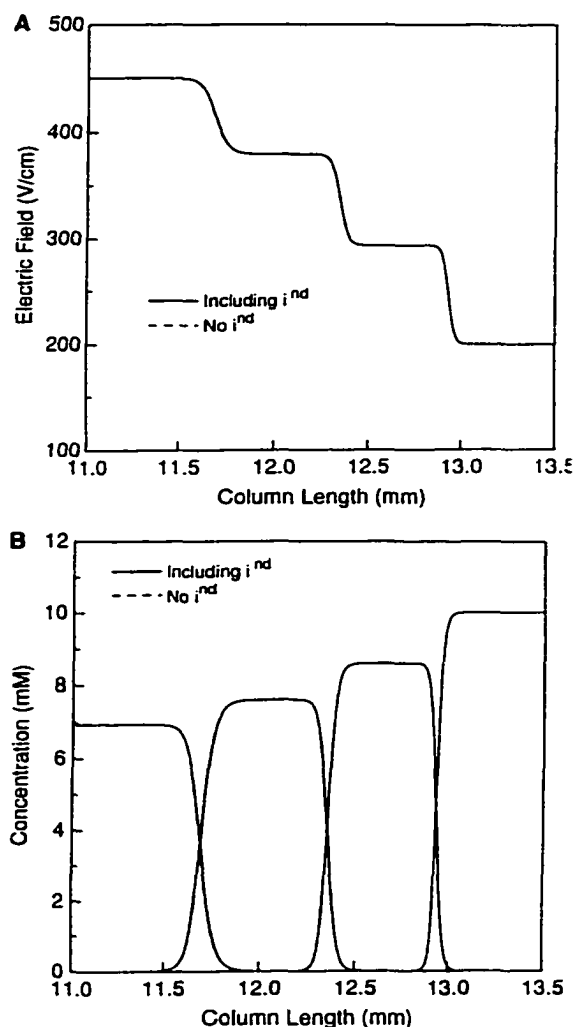


**Figure 4.** (a) Electric and (b) concentration fields in sample region, calculated by UW;  $i^d$  included in the charge balance; grid spacing is  $10 \mu\text{m}$ . Simulation conditions are as for Fig. 1. Anode to the left.

the numerical scheme ND. Numerical diffusion, just sufficient to guarantee monotonicity for any concentration field or  $Pe_s$  [14], is added directly to a central spatial discretization of the component balances. This numerical diffusion is approximately the same as that inherent in the UW scheme, and the ND method is equivalent to the UW method for a uniform velocity field. The advantage of the ND scheme is that the numerical diffusion flux can be included in the charge balance exactly as in the component balances. Moreover, all fluxes are calculated at  $x_{i+1/2}$

( $l = 1, 2, \dots, n_s$ ), and only one iteration is required. For the ND scheme, when numerical diffusion is included in the charge balance,  $E_{l+1/2,l}^0$  is calculated as

$$E_{l+1/2,l}^0 = \frac{i_{l+1/2,l} - i_{l+1/2,l}^d - i_{l+1/2,l}^{nd}}{\sigma} \quad (25)$$

and one iteration is then performed, viz.

$$E_{l+1/2,l} = \frac{i_{l+1/2,l} - i_{l+1/2,l}^d - i_{l+1/2,l}^{nd,0}}{\sigma} \quad (26)$$

where  $i_{l+1/2,l}^{nd,0}$  denotes  $i_{l+1/2,l}^{nd}$  evaluated at  $E_{l+1/2,l}^0$ . The numerical diffusion current density  $i_{l+1/2,l}^{nd}$  is

$$i_{l+1/2,l}^{nd} = \frac{e^2}{2} \sum_{k=1}^M \omega_k \sum_{z=N_k}^{+P_k} z |z E_{l+1/2,l}| [(n_k^z)_{l+1/2,l} - (n_k^z)_{l,l}] \quad (27)$$

where  $(n_k^z)_{l,l}$  denotes  $n_k^z$  at  $x_l$  and  $t_l$ . The difference between  $E_{l+1/2,l}^0$  and  $E_{l+1/2,l}$  is small enough that  $E_{l+1/2,l}^0$  can be used to calculate the numerical diffusion flux in the component balances (Eq. 13) without violating the monotonicity constraint; i.e.,  $C_{l+1/2,l}$  is calculated for each component as

$$C_{l+1/2,l} = C_{l,l} - \Delta t \frac{f_{l+1/2,l}^e - f_{l+1/2,l}^e}{\Delta x} + \frac{1}{2} c_{l+1/2,l}^0 (C_{l+1/2,l} - C_{l,l}) - \frac{1}{2} c_{l+1/2,l}^0 (C_{l,l} - C_{l-1/2,l}) + \Delta t \frac{C_{l+1/2,l} - 2C_{l,l} + C_{l-1/2,l}}{(\Delta x)^2} \quad (28)$$

where  $c_{l+1/2,l}^0$  denotes  $c_{l+1/2,l}$  evaluated at  $E_{l+1/2,l}^0$ . As such, the numerical diffusion fluxes in the component balances are consistent with that in the charge balance.

Figure 5 shows pH profiles produced by the ND scheme. Implementation of this scheme without the numerical diffusion current produces pH profiles very similar to those generated by the UW scheme (Fig. 2). If the numerical diffusion current is included in the charge balance, however, the pH dips are completely eliminated – even with a grid spacing of  $10 \mu\text{m}$  (solid line, panel a). If numerical diffusion is included, but molecular diffusion omitted from the charge balance, pH dips up to two units are obtained. Figure 5a shows that, with  $\Delta x = 10 \mu\text{m}$ , omission of numerical diffusion results in a greater error in the pH than omission of molecular diffusion. Figure 5b shows that, with  $\Delta x = 1.5 \mu\text{m}$ , the effect of omitting molecular diffusion is comparable to that of numerical diffusion. As the mesh is refined, numerical diffusion diminishes because

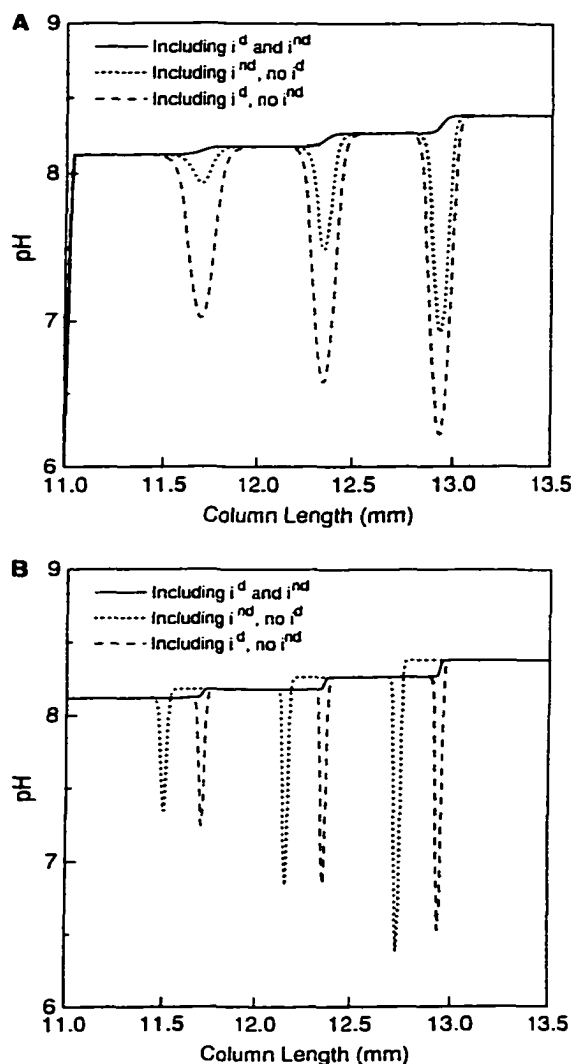


**Figure 5.** pH profiles calculated by ND. Simulation conditions are as for Fig. 1. Anode to the left. Grid spacing is (a)  $10 \mu\text{m}$  and (b)  $1.5 \mu\text{m}$ . Dotted line in (b) shifted by  $-0.2 \text{ mm}$  for clarity.

the numerical diffusivity is  $e\omega_k |z_k E| \Delta x / 2$ . The error due to omitting the molecular diffusion current persists, and to some extent worsens, on finer meshes; the molecular diffusivity is independent of  $\Delta x$ , and sharp gradients are more accurately resolved as  $\Delta x$  diminishes.

Finally, we note that the results in Fig. 5b were calculated using the same grid spacing as the converged CSD results in Fig. 1. The zone boundaries and other transi-

tions in Fig. 5b are not as sharp as those in Fig. 1 because of numerical diffusion in the ND scheme. The utility of the ND scheme is that it yields stable results (no spurious spatiotemporal oscillations) on coarse grids, whereas CSD does not. For example, though CSD has converged on the grid for Fig. 1, the sample zone is completely distorted by oscillations when CSD is applied with  $\Delta x = 10 \mu\text{m}$ . Thus, some form of numerical diffusion is required to stabilize the solution on coarser grids, and if a numerical diffusion current is not included in the charge balance, substantial errors result in the pH calculation.

#### 4 Concluding remarks

A consistent treatment of ion transport processes in the component and charge balance laws is required to obtain reliable pH results from electrophoresis simulations, particularly for poorly buffered systems. Even at high electric Peclet numbers, the diffusion current should be included in the charge balance. Additionally, simulations of electrophoretic separations at normal electric field strengths often employ numerical techniques, such as upwinding and flux limiters, that use numerical diffusion to suppress spurious oscillations. These schemes introduce artificial transport mechanisms to the component balance laws, which must also be included in the charge balance.

*This work was supported, in part, by the NSF/SRC Center for Environmentally Benign Semiconductor Manufacturing at The University of Arizona. We also thank Dr. Wolfgang Thormann at The University of Bern for bringing this problem to our attention.*

Received January 12, 2000

#### 5 References

- [1] Mosher, R. A., Saville, D. A., Thormann, W., *The Dynamics of Electrophoresis*, VCH, Weinheim 1992.
- [2] Palusinski, O. A., Graham, A., Mosher, R. A., Bier, M., Saville, D. A., *AIChE J.* 1986, **32**, 215–223.
- [3] Dose, E. V., Guiochon, G. A., *Anal. Chem.* 1991, **63**, 1063–1072.
- [4] Gas, B., Vacik, J., Zelensky, I., *J. Chromatogr.* 1991, **545**, 225–237.
- [5] Ermakov, S. V., Olga, S. M., Zhukov, M. Y., *Electrophoresis* 1992, **13**, 838–848.
- [6] Martens, J. H. P. A., Reijenga, J. C., ten Thije Boonkamp, J. H. M., Mattheij, R. M. M., Everaerts, F. M., *J. Chromatogr. A* 1997, **772**, 49–62.
- [7] Ikuta, N., Hirokawa, T., *J. Chromatogr. A* 1998, **802**, 49–57.
- [8] Blanco, S., Clifton, M. J., Joly, J. L., Peltre, G., *Electrophoresis* 1996, **17**, 1126–1133.
- [9] Sounart, T. L., Baygents, J. C., *J. Chromatogr. A* 2000, in press.
- [10] Reijenga, J., Kašicka, V., *Electrophoresis* 1998, **19**, 1601–1605.
- [11] Bier, M., Palusinski, O. A., Mosher, R. A., Saville, D. A., *Science* 1983, **219**, 1281–1287.
- [12] Watts, H. A., *Trans. Soc. Computer Simul.* 1985, **1**, 15–25.
- [13] Schafer-Nielsen, C., *Electrophoresis* 1995, **16**, 1369–1376.
- [14] Boris, J. P., Landsberg, A. M., Oran, E. S., Gardner, J. H., *LCPFCT – Flux-Corrected Transport Algorithm for Solving Generalized Continuity Equations*, NRL Memorandum Report 6410-93-7192, Naval Research Laboratory, Washington 1993, pp. 4–7.

## REFERENCES

- [1] Afonso, J.L. and Clifton, M.J., Numerical Model of a Mixed Flow Coupled with Mass and Heat Transfer in Continuous-Flow Electrophoresis, *Computers Chem. Engrng.*, **22**, S323 (1998).
- [2] Afonso, J.L. and Clifton, M.J., Optimization of Protein Separation by Continuous-Flow Electrophoresis: Influence of the Operating Conditions and the Chamber Thickness, *Electrophoresis*, **20**, 2801 (1999).
- [3] Albert, M., Debusschere, L., Demesmay, C., and Rocca, J.L., Large-Volume Stacking for Quantitative Analysis of Anions in Capillary Electrophoresis I. Large-Volume Stacking with Polarity Switching, *J. Chromatogr. A*, **757**, 281 (1997).
- [4] Albert, M., Debusschere, L., Demesmay, C., and Rocca, J.L., Large-Volume Stacking for Quantitative Analysis of Anions in Capillary Electrophoresis II. Large-Volume Stacking without Polarity Switching, *J. Chromatogr. A*, **757**, 291 (1997).
- [5] Altria, K.D., Kelly, M.A., and Clark, B.J., Current Applications in the Analysis of Pharmaceuticals by Capillary Electrophoresis. I, *Trend Anal. Chem.*, **17** 204 (1998).
- [6] Altria, K.D., Kelly, M.A., and Clark, B.J., Current Applications in the Analysis of Pharmaceuticals by Capillary Electrophoresis. II, *Trend Anal. Chem.*, **17**, 215 (1998).
- [7] Altria, K.D., Overview of Capillary Electrophoresis and Capillary Electrochromatography, *J. Chromatogr. A*, **856**, 443 (1999).
- [8] Anderson, J.L. and Idol, W.K., Electroosmosis Through Pores with Nonuniformly Charged Walls, *Chem. Eng. Commun.*, **38**, 93 (1985).
- [9] Andreev, V.P., Dubrovsky, S.G., and Stepanov, Y.V., Mathematical Modeling of Capillary Electrophoresis in Rectangular Channels, *J. Microcolumn Sep.*, **9**, 443 (1997).
- [10] Aris, R., On the Dispersion of a Solute in a Fluid Flowing Through a Tube, *Proc. R. Soc. A*, **235**, 67 (1956).
- [11] Arulanandam, S. and Li, D., Liquid Transport in Rectangular Microchannels by Electroosmotic Pumping, *Colloids Surfaces A: Physicochem. Eng. Aspects*, **161**, 89 (2000).

- [12] Beard, D.A., Taylor Dispersion of a Solute in a Microfluidic Channel, *J. Appl. Phys.*, **89**, 4667 (2001).
- [13] Beckers, J.L. and Boček, P., Sample Stacking in Capillary zone Electrophoresis: Principles, Advantages and Limitations, *Electrophoresis*, **21**, 2747 (2000).
- [14] Beckers, J.L., and Ackermans, M.T., Effect of Sample Stacking on Resolution, Calibration Graphs and pH in Capillary Zone Electrophoresis, *J. Chromatogr. A*, **629**, 371 (1993).
- [15] Belongia, B.M., Electrokinetic and Buoyancy Effects in Colloidal Suspensions, Ph.D. Dissertation, The University of Arizona (1999).
- [16] Belongia, B.M., Haworth, P.D., Baygents, J.C., and Raghavan, S., Treatment of Alumina and Silica Chemical Mechanical Polishing Waste by Electrodecantation and Electrocoagulation, *J. Electrochem. Soc.*, **146**, 4124 (1999).
- [17] van den Berg, A. and Lammerink, T.S.J., Micro Total Analysis Systems: Microfluidic Aspects, Integration Concept and Applications, *Topics in Current Chemistry*, **194**, 21 (1998).
- [18] Bianchi, F., Ferrigno, R., and Girault, H.H., Finite Element Simulation of an Electroosmotic-Driven Flow Division at a T-Junction of Microscale Dimensions, *Anal. Chem.*, **72**, 1987 (2000).
- [19] Bier, M., *Electrophoresis: Theory, Methods and Applications*, Academic Press, New York (1959).
- [20] Bier, M., Palusinski, O.A., Mosher, R.A., and Saville, D.A., Electrophoresis: Mathematical Modeling and Computer Simulation, *Science*, **219**, 1281 (1983).
- [21] Bjorstad, P., Fast Numerical-Solution of the Biharmonic Dirichlet Problem on Rectangles, *SIAM J. Num. Anal.*, **20**, 59 (1983).
- [22] Blanc, P., Larbot, A., Persin, M., and Cot, L., Preparation of Hafnia Ceramic Membranes for Ultrafiltration, *J. Membrane Sci.*, **134**, 109 (1997).
- [23] Blanco, S., Clifton, M.J., Joly, J.L., and Peltre, G., Protein Separation by Electrophoresis in a Nonsieving Amphoteric Medium, *Electrophoresis*, **17** 1126 (1996).
- [24] de Boer, T., de Zeeuw, R.A., de Jong, G.J., and Ensing, K., Selectivity in Capillary Electrokinetic Separations, *Electrophoresis*, **20**, 2989 (1999).
- [25] Book, D.L., Boris, J.P., and Hain, K., Flux-Corrected Transport II: Generalizations of the Method, *J. Comp. Phys.*, **18**, 248 (1975).

- [26] Book, D.L., Boris, J.P., and Zalesak, S.T., in *Finite-Difference Techniques for Vectorized Fluid Dynamics Calculations*, (D.L. Book ed.), Ch. 3, p. 29, New York, (1981).
- [27] Boris, J.P. and Book, D.L., Flux-Corrected Transport. I. SHASTA, A Fluid Transport Algorithm that Works, *J. Comp. Phys.*, **11**, 38 (1973).
- [28] Boris, J.P. and Book, D.L., Flux-Corrected Transport. III. Minimal-Error FCT Algorithms, *J. Comp. Phys.*, **20**, 397 (1976).
- [29] Boris, J.P. and Book, D.L., Solution of Continuity Equations by the Method of Flux-Corrected Transport, *Methods in Computational Physics*, **16**, 85 (1976).
- [30] Boris, J.P., Landsberg, A.M., Oran, E.S., and Gardner, J.H., *LCPFCT - Flux-Corrected Transport Algorithm for Solving Generalized Continuity Equations*, NRL Memorandum Report 6410-93-7192. Naval Research Laboratory, Washington, (1993).
- [31] Bousse, L., Cohen, C., Nikiforov, T., Chow, A., Kopf-Sill, A.R., Dubrow, R., and Parce, J.W., Electrokinetically Controlled Microfluidic Analysis Systems, *Annu. Rev. Bioph. Biom.*, **29**, 155 (2000).
- [32] Bowen, W.R. and Clark, R.A., Electroosmosis at Microporous Membranes and the Determination of Zeta-Potential, *J. Colloid Interface Sci.*, **97**, 401 (1984).
- [33] Brenner, H. and Edwards, D.A., *Macrotransport Processes*, Butterworth-Heinemann, Boston. (1993).
- [34] Bruin, G.J.M., Recent Developments in Electrokinetically Driven Analysis on Microfabricated Devices, *Electrophoresis*, **21**, 3931 (2000).
- [35] Bryden, M.D. and Brenner, H., Multiple-Timescale Analysis of Taylor Dispersion in Converging and Diverging Flows, *J. Fluid Mech.*, **311**, 343 (1996).
- [36] Burgi, D.S. and Chien, R.-L., Optimization in Sample Stacking for High-Performance Capillary Electrophoresis, *Anal. Chem.*, **63**, 2042 (1991).
- [37] Burns, M.A., Johnson, B.N., Brahasandra, S.N., Handique, K., Webster, J.R., Krishnan, M., Sammarco, T.S., Man, P.M. Jones, D., Heldsinger, D., Mas-trangelo, C.H., and Burke, D.T., An Integrated Nanoliter DNA Analysis Device, *Science*, **282**, 484 (1998).
- [38] Canon, E., Bensmina, H., and Valentin, P., On the Modelling of Generalized Taylor-Aris Dispersion in Chromatographs via Multiple Scales Expansions, *Transport in Porous Media*, **36**, 307 (1999).

- [39] Chiem, N.H. and Harrison, D.J., Microchip Systems for Immunoassay: An Integrated Immunoreactor with Electrophoretic Separation for Serum Theophylline Determination, *Clin. Chem.*, **44**, 591 (1998).
- [40] Chien, R.-L. and Burgi, D.S., Field Amplified Sample Injection in High-Performance Capillary Electrophoresis, *J. Chromatogr. A*, **559**, 141 (1991).
- [41] Chien, R.-L. and Burgi, D.S., Field Amplified Polarity-Switching Sample Injection in High-Performance Capillary Electrophoresis. *J. Chromatogr. A*, **559**, 153 (1991).
- [42] Chien, R.-L. and Burgi, D.S., Sample Stacking of an Extremely Large Injection Volume in High-Performance Capillary Electrophoresis. *Anal. Chem.*, **64**, 1046 (1992).
- [43] Cikalo, M.G., Bartle, K.D., Robson, M.M., Myers, P.M., and Euerby, M.R., Capillary Electrochromatography, *Analyst*, **123**, 87R (1998).
- [44] Clifton, M.J., Numerical Simulation of Protein Separation by Continuous-Flow Electrophoresis, *Electrophoresis*, **14**, 1284 (1993).
- [45] Colyer, C.L., Mangru, S.D., and Harrison, D.J., Microchip-Based Capillary Electrophoresis of Human Serum Proteins, *J. Chromatogr. A*, **781**, 271 (1997).
- [46] Corapcioglu, M.O. and Huang, C.P., The Surface Acidity and Characterization of Some Commercial Activated Carbons, *Carbon*, **25**, 569 (1987).
- [47] Creech, J.L., Chauhan, A., Radke, C.J., Dispersive Mixing in the Posterior Tear Film Under a Soft Contact Lens, *Ind. Eng. Chem. Res.*, **40**, 3015 (2001).
- [48] Cummings, E.B., Griffiths, S.K., Nilson, R.H., and Paul, P.H., Conditions for Similitude between the Fluid Velocity and Electric Field in Electroosmotic Flow, *Anal. Chem.*, **72**, 2526 (2000).
- [49] Detwiler, R.L., Rajaram, H., Glass, R.J., Solute Transport in Variable-Aperture Fractures: An Investigation of the Relative Importance of Taylor Dispersion and Macrodispersion, *Water Resources Research*, **36**, 1611 (2000).
- [50] Dolník, V., Liu, S., and Jovanovich, S., Capillary Electrophoresis on Microchip, *Electrophoresis*, **21**, 41 (2000).
- [51] Dose, E.V. and Guiochon, G.A., High-Resolution Modeling of Capillary Zone Electrophoresis and Isotachopheresis, *Anal. Chem.*, **63**, 1063 (1991).
- [52] Dukhin, S.S. *Surface and Colloid Science*, (E. Matijevic ed.), Ch.1, Vol.7, Wiley-Interscience, New York, (1974).

- [53] Edwards, D.A., Shapiro, M., Brenner, H., and Shapira, M., Dispersion of Inert Solutes in Spatially Periodic, 2-Dimensional Model Porous Media, *Transport in Porous Media*, **6**, 337 (1991).
- [54] Effenhauser, C.S., Paulus, A., Manz, A., and Widmer, H.M., High-Speed Separation of Antisense Oligonucleotides on a Micromachined Capillary Electrophoresis Device, *Anal. Chem.*, **66**, 2949 (1994).
- [55] Ermakov, S.V., Bello, M.S., and Righetti, P.G., Numerical Algorithms for Capillary Electrophoresis, *J. Chromatogr. A*, **661**, 265 (1994).
- [56] Ermakov, S.V., Jacobson, S.C., and Ramsey, J.M., Computer Simulations of Electrokinetic Transport in Microfabricated Channel Structures, *Anal. Chem.*, **70**, 4494 (1998).
- [57] Ermakov, S.V., Jacobson, S.C., and Ramsey, J.M., Computer Simulations of Electrokinetic Injection Techniques in Microfluidic Devices, *Anal. Chem.*, **72**, 3512 (2000).
- [58] Ermakov, S.V., Mazhorova, O.S., and Popov, Y.P., Finite-Difference Algorithm for Convection-Diffusion Equation Applied to Electrophoresis Problem, *Informatica*, **3**, 173 (1992).
- [59] Ermakov, S.V., Mazhorova, O.S., and Zhukov, M.Y., Computer Simulation of Transient States in Capillary Zone Electrophoresis and Isotachophoresis, *Electrophoresis*, **13**, 838 (1992).
- [60] Federspiel, W.J. and Fredberg, J.J., Axial-Dispersion in Respiratory Bronchioles and Alveolar Ducts, *J. Applied Physiology*, **64**, 2614 (1988).
- [61] Figeys, D. and Pinto, D., Lab-on-a-Chip: A Revolution in Biological and Medical Sciences, *Anal. Chem.*, **72**, 330A (2000).
- [62] Folkersma, R., van Diemen, A.J.G., and Stein, H.N., Electrophoretic Properties of Polystyrene Spheres, *Langmuir*, **14**, 5973 (1998).
- [63] Freemantle, M., Downsizing Chemistry: Chemical Analysis and Synthesis on Microchips Promise a Variety of Potential Benefits, *Chemical and Engineering News*, **77**, 27 (1999).
- [64] Gas, B., Vacik, J., and Zelensky, I., Computer-Aided Simulation of Electromigration, *J. Chromatogr.*, **545**, 225 (1991).
- [65] Gole, A.M., Sathivel, C., Lachke, A., and Sastry, M., Size Separation of Colloidal Nanoparticles Using a Miniscale Isoelectric Focusing Technique, *J. Chromatogr. A*, **848**, 485 (1999).

- [66] Gottlieb, D., Strang-Type Difference Schemes for Multidimensional Problems, *SIAM J. Num. Anal.*, **9**, 650 (1972).
- [67] Grandjouan, N., The modified Equation Approach to Flux-Corrected Transport, *J. Comp. Phys.*, **91**, 424 (1990).
- [68] Griffiths, S.K. and Nilson, R.H., Band Spreading in Two-Dimensional Microchannel Turns for Electrokinetic Species Transport, *Anal. Chem.*, **72**, 5473 (2000).
- [69] Griffiths, S.K. and Nilson, R.H., Electroosmotic Fluid Motion and Late-Time Solute Transport for Large Zeta Potentials, *Anal. Chem.*, **72**, 4767 (2000).
- [70] Guy, J.H., Kalia, Y.N., and Delgado-Charro, M.B., Iontophoresis: Electrorepulsion and Electroosmosis, *J. Control Release*, **64**, 129 (2000).
- [71] Guzman, N.A. and Majors, R.E., New Directions for Concentration Sensitivity Enhancement in CE and Microchip Technology, *LC-GC*, **19**, 14 (2001).
- [72] Hadd, A.G., Raymond, D.E., Halliwell, J.W., Jacobson, S.C., Ramsey, J.M., Microchip Device for Performing Enzyme Assays, *Anal. Chem.*, **69**, 3407 (1997).
- [73] Hannig, K., *Free-Flow Electrophoresis: An Important Preparative and Analytical Technique for Biology, Biochemistry and Diagnostics*, GIT Verlag, Darmstadt, (1990).
- [74] Harrison, D.J., Manz, A., Fan, Z., Ludi, H., and Widmer, H.M., Capillary Electrophoresis and Sample Injection Systems Integrated on a Planar Glass Chip, *Anal. Chem.*, **64**, 1926 (1992).
- [75] He, B., Ji, J., and Regnier, F.E., Capillary Electrochromatography of Peptides in a Microfabricated System, *J. Chromatogr. A.*, **853**, 257 (1999).
- [76] von Helmholtz, H., Studien Über Electriche Grenschichten, *Ann. Phys.*, **7**, 337 (1879).
- [77] Hempel, G., Strategies to Improve the Sensitivity in Capillary Electrophoresis for the Analysis of Drugs in Biological Fluids, *Electrophoresis*, **21**, 691 (2000).
- [78] Henry, D.C., The Cataphoresis of Suspended Particles. Part I.—The Equation of Cataphoresis, *Proc. Roy. Soc. London Ser. A*, **133**, 106 (1933).
- [79] Herr, A.E., Mohlo, G.I., Santiago, J.G., Mungal, M.G., Kenny, T.W., and Garguilo, M.G., Electroosmotic Capillary Flow with Nonuniform Zeta Potential, *Anal. Chem.*, **72**, 1053 (2000).

- [80] Hirokawa, T., Nishino, M., Aoki, N., Kiso, Y., Sawamoto, Y., Yagi, T., and Akiyama, J.-I., Table of Isotachophoretic Indices. I. Simulated Qualitative and Quantitative Indices of 287 Anionic Substances in the Range pH 3–10, *J. Chromatogr.*, **271**, D1 (1983).
- [81] Hofmann, O., Che, D., Cruickshank, K.A., and Müller, U.R., Adaptation of Capillary Isoelectric Focusing to Microchannels on a Glass Chip, *Anal. Chem.*, **71**, 678 (1999).
- [82] Hu, L., Harrison, J.D., and Masliyah, J.H., Numerical Model of Electrokinetic Flow for Capillary Electrophoresis, *J. Colloid Interface Sci.*, **215**, 300 (1999).
- [83] Hoagland, D.A. and Prud'homme, R.K., Taylor-Aris Dispersion Arising from Flow in a Sinusoidal Tube, *AIChE J.*, **31**, 236 (1985).
- [84] Hunter, R.J., *Introduction to Modern Colloid Science*, Oxford University Press, Oxford, (1993).
- [85] Hunter, R.J., *Zeta Potential in Colloid Science: Principles and Applications*, Academic Press, London, (1981).
- [86] Hutt, L.D., Glavin, D.P., Bada, J.L., and Mathies, R.A., Microfabricated Capillary Electrophoresis Amino Acid Chirality Analyzer for Extraterrestrial Exploration, *Anal. Chem.*, **71**, 4000 (1999).
- [87] Ikuta, N. and Hirokawa, T., Numerical Simulation for Capillary Electrophoresis I. Development of a Simulation Program with High Numerical Stability, *J. Chromatogr. A*, **802**, 49 (1998).
- [88] Issaq, H.J., A Decade of Capillary Electrophoresis, *Electrophoresis*, **21**, 1921 (2000).
- [89] Jacobs, R.A. and Probstein, R.F., Two-Dimensional Modeling of Electroremediation, *AIChE J.*, **42**, 1685 (1996).
- [90] Jacobson, S.C., Culberston, C.T., Daler, J.E., and Ramsey, J.M., Microchip Structures for Submillisecond Electrophoresis, *Anal. Chem.*, **70**, 3476 (1998).
- [91] Jacobson, S.E., Ermakov, S.V., and Ramsey, J.M., Minimizing the Number of Voltage Sources and Fluid Reservoirs for Electrokinetic Valving in Microfluidic Devices, *Anal. Chem.*, **71**, 3273 (1999).
- [92] Jacobson, S.C. and Ramsey, M.J., Microchip Electrophoresis with Sample Stacking, *Electrophoresis*, **16**, 481 (1995).
- [93] Kašička, V., in *Analytical and Preparative Separation Methods of Biomacromolecules*, (A.Y. Hassan ed.), Ch. 3, Marcel Dekker, New York, (1999).

- [94] Keely, C.A., van de Goor, T.A.A.M., and McManigill, D., Modeling Flow Profiles and Dispersion in Capillary Electrophoresis with Nonuniform  $\zeta$  Potential, *Anal. Chem.*, **33**, 4236 (1994).
- [95] Kelsh, D.J. and Parsons, M.W., Department of Energy Sites Suitable for Electrokinetic Remediation, *J. Hazard Mater.*, **55**, 109 (1997).
- [96] Kim, K.J., Fane, A.G., Nystrom, M., Pihlajamaki, A., Bowen, W.R., and Mukhtar, H., Evaluation of Electroosmosis and Streaming Potential for Measurement of Electric Charges of Polymeric Membranes, *J. Membrane Sci.*, **116**, 149 (1996).
- [97] Kniss, R., Revolution of the Drug Discovery Process Using Laboratory-on-a-Chip Technology, *Am. Lab.*, **30**, 40 (1998).
- [98] Kok, W.T., Off-Column Detection with Pressure Compensation in Capillary Electrophoresis, *Anal. Chem.*, **65**, 1853 (1993).
- [99] Koopal, L.K., Vanriemsdijk, W.H., and Roffey, M.G., Surface-Ionization and Complexation Models - A Comparison of Methods for Determining Model Parameters, *J. Colloid Interface Sci.*, **118**, 117 (1987).
- [100] Krull, I.S., Sebag, A., and Stevenson, R., Specific Applications of Capillary Electrochromatography to Biopolymers, Including Proteins, Nucleic Acids, Peptide Mapping, Antibodies, and So Forth, *J. Chromatogr. A*, **887**, 137 (2000).
- [101] Kutter, J.P., Current Developments in Electrophoretic and Chromatographic Separation Methods on Microfabricated Devices, *Trends in Analytical Chemistry*, **19**, 352 (2000).
- [102] Landers, J.P., *Handbook of Capillary Electrophoresis*, CRC Press, Boca Raton, (1997).
- [103] Law, A.W.K., Taylor Dispersion of Contaminants Due to Surface Waves, *Journal of Hydraulic Research*, **38**, 41 (2000).
- [104] Lee, J.H., Choi, O.-K., Jung, H.S., Kim, K.-R., and Chung, D.S., Capillary Electrophoresis of Nonprotein and Protein Amino Acids without Derivatization, *Electrophoresis*, **21**, 930 (2000).
- [105] van Leer, B., Towards an Ultimate Conservative Difference Scheme 2. Monotonicity and Conservation Combined in a Second-Order Scheme, *J. Comp. Phys.*, **14**, 361 (1974).
- [106] Long, D., Stone, H.A., and Ajdari, A., Electroosmotic Flows Created by Surface Defects in Capillary Electrophoresis, *J. Colloid Interface Sci.*, **212**, 338 (1999).

- [107] MacTaylor, C.E. and Ewing, A.G., Critical Review of Recent Developments in Fluorescence Detection for Capillary Electrophoresis, *Electrophoresis*, **18**, 2279 (1997).
- [108] Martens, J.H.P.A., Reijenga, J.C., ten Thije Boonkamp, J.H.M., Mattheij, R.M.M., and Everaerts, F.M., Transient Modelling of Capillary Electrophoresis Isotachophoresis, *J. Chromatogr. A*, **772**, 49 (1997).
- [109] Manz, A., Harrison, D.J., Verpoorte, E.M.J., Fettinger, J.C., Paulus, A., Ludi, H., and Widmer, H.M., Planar Chip Technology for Miniaturization and Integration of Separation Techniques into Monitoring Systems - Capillary Electrophoresis on a Chip, *J. Chromatogr. A*, **593**, 253 (1992).
- [110] Meier, H., Zimmerhackl, E., Zeitler, G., and Menge, P., Correlations of Electrokinetic Properties of Sorption Data of Radionuclides in Site-Specific Samples, *Radiochim. Acta*, **52**, 195 (1991).
- [111] Meloan, C.E., *Chemical Separations: Principles, Techniques, and Experiments*, Wiley, New York, (1999).
- [112] Minor, M., vanderLinde, A.J., vanLeeuwen, H.P., and Lyklema, J., Dynamic Aspects of Electrophoresis and Electroosmosis: A New Fast Method for Measuring Particle Mobilities, *J. Colloid Interface Sci.*, **189**, 370 (1997).
- [113] Mosher, R.A., Saville, D.A., and Thormann, W., *The Dynamics of Electrophoresis*, VCH, Weinheim (1992).
- [114] Muijselaar, P.G., Otsuka, K., and Terabe, S., Micelles as Pseudo-Stationary Phases in Micellar Electrokinetic Chromatography, *J. Chromatogr. A*, **780**, 41 (1997).
- [115] Mullet, M., Fievet, P., Reggiani, J.C., and Pagetti, J., Surface Electrochemical Properties of Mixed Oxide Ceramic Membranes: Zeta-Potential and Surface Charge Density, *J. Membrane Sci.*, **123**, 255 (1997).
- [116] Murphy, E.A., Electrodecantation for Concentrating and Purifying Latex, *Rubber Chem. & Techn.*, **16**, 529 (1943).
- [117] Nair, V., Pillai, O., Poduri, R., and Panchagnula, R., Transdermal Iontophoresis. Part I: Basic Principles and Considerations, *Meth. Find. Exp. Clin.*, **21**, 139 (1999).
- [118] Ng, C.O., Dispersion in Sediment-Laden Stream Flow, *Journal of Engineering Mechanics-ASCE*, **126**, 779 (2000).
- [119] Odstrcil, D., A New Optimized FCT Algorithm for Shock Wave Problems, *J. Comp. Phys.*, **91**, 71 (1990).

- [120] Olgemöller, J., Hempel, G., Boos, J., and Blaschke, G., Determination of (*E*)-5-(2-bromovinyl)-2'-deoxyuridine in Plasma and Urine by Capillary Electrophoresis, *J. Chromatogr. B*, **726**, 261 (1999).
- [121] Osbourn, D.M., Weiss, D.J., and Lunte, C.E., On-Line Preconcentration Methods for Capillary Electrophoresis, *Electrophoresis*, **21**, 2768 (2000).
- [122] Palusinski, O.A., Graham, A., Mosher, R.A., Bier, M., and Saville, D.A., Theory of Electrophoretic Separations. Part II: Construction of a Numerical Scheme and its Applications *AIChE J.*, **32**, 215 (1986).
- [123] Patankar, N.A. and Hu, H.H., Numerical Simulation of Electroosmotic Flow, *Anal. Chem.*, **70**, 1870 (1998).
- [124] Peterson, S.L. and Ballou, N.E., Separation of Micrometer-Size Oxide Particles by Capillary Zone Electrophoresis, *J. Chromatogr. A*, **834**, 445 (1999).
- [125] Petr, J., *Capillary Electrophoresis of Small Molecules and Ions*, VCH, New York, (1993).
- [126] Potoček, B., Gaš, B., Kenndler, E., and Štědrý, M., Electroosmosis in Capillary Zone Electrophoresis with Non-Uniform Zeta Potential, *J. Chromatogr. A*, **709**, 51 (1995).
- [127] Probst, R.F. and Hicks, R.E., Removal of Contaminants from Soils by Electric Fields, *Science*, **260**, 498 (1993).
- [128] Rathore, A.S. and Horváth, Cs., Axial Nonuniformities and Flow in Columns for Capillary Electrochromatography, *Anal. Chem.*, **70**, 3069 (1998).
- [129] Reboiras, M.D., Kaszuba, M., Connah, M.T., and Jones, M.N., Measurement of Wall Zeta Potentials and Their Time-Dependent Changes Due to Adsorption Processes: Liposome Adsorption on Glass. *Langmuir*, **17**, 5314 (2001).
- [130] Reijenga, J. and Kašička, V., Discontinuities of pH at Zone Boundaries in Isotachophoretic Systems with Poorly Buffering Leading Electrolytes, *Electrophoresis*, **19**, 1601 (1998).
- [131] Riviere, J.E. and Heit, M.C., Electrically-Assisted Transdermal Drug Delivery, *Pharmaceut. Res.*, **14**, 687 (1997).
- [132] Russel, W.B., Saville, D.A., and Schowalter, W.R., *Colloidal Dispersions*, Cambridge University Press, Cambridge, (1989).
- [133] Saville, D.A., Electrohydrodynamics: The Taylor-Melcher Leaky Dielectric Model, *Annu. Rev. Fluid Mech.*, **9**, 321 (1997).

- [134] Saville, D.A. and Palusinski, O.A., Theory of Electrophoretic Separations. Part I: Formulation of a Mathematical Model, *AIChE J.*, **32**, 207 (1986).
- [135] Schafer-Nielsen, C. A Computer Model for Time-Based Simulation of Electrophoresis Systems with Freely Defined Initial and Boundary Conditions. *Electrophoresis*, **16**, 1369 (1995).
- [136] Schwer, C., Gas, B., Lottspeich, F., and Kenndler, E., Computer Simulation and Experimental Evaluation of On-Column Sample Preconcentration in Capillary Zone Electrophoresis by Discontinuous Buffer Systems, *Anal. Chem.*, **65**, 2108 (1993).
- [137] Shi, Y., Simpson, P.C., Scherer, J.R., Wexler, D., Skibola, C., Smith, M.T., and Mathies, R.A., Radial Capillary Array Electrophoresis Microplate and Scanner for High-Performance Nucleic Acid Analysis, *Anal. Chem.*, **71**, 5354 (1999).
- [138] Simpson, P.C., Roach, D., Woolley, A.T., Thorsen, T., Johnston, R., Sensabaugh, G.F., and Mathies, R.A., High-Throughput Genetic Analysis Using Microfabricated 96-Sample Capillary Array Electrophoresis Microplates, *Proc. Natl. Acad. Sci. U.S.A.*, **95**, 2256 (1998).
- [139] Transport in Lungs and Branched Estuaries, *J. Fluid Mech.*, **325**, 331 (1996).
- [140] von Smoluchowski, M., Contribution à la Théorie de l'endosmose Électrique et de Quelques Phénomènes Corrélatifs, *Bulletin International de l'Académie des Sciences de Cracovie*, **8**, 182 (1903).
- [141] Sprycha, R. and Szczypa, J., Estimation of Surface-Ionization Constants from Electrokinetic Data, *J. Colloid Interface Sci.*, **102**, 288 (1984).
- [142] Stone, H.A. and Brenner, H., Dispersion in Flows with Streamwise Variations of Mean Velocity: Radial Flow, *Ind. Eng. Chem. Res.*, **38**, 851 (1999).
- [143] Sweby, P.K., High Resolution Schemes Using Flux Limiters for Hyperbolic Conservation Laws, *SIAM J. Numer. Anal.*, **21**, 995 (1984).
- [144] Taylor, G.I., Dispersion of Soluble Matter in Solvent Flowing Slowly Through a Tube, *Proc. R. Soc. London A*, **219**, 186 (1953).
- [145] Thorman, W., Isotachophoresis in Open-Tubular Fused-Silica Capillaries, *J. Chromatogr.*, **516**, 211 (1990).
- [146] Thormann, W., Molteni, S., Stoffel, E., Mosher, R.A., and Chmelík, J., Computer Modeling and Experimental Validation of the Dynamics of Capillary Isoelectric Focusing with Electroosmotic Zone Displacement, *Analytical Methods and Instrumentation*, **1**, 177 (1993).

- [147] Thormann, W., Zhang, C.-X., Caslavská, J., Gebauer, P., and Mosher, R.A., Modeling of the Impact of Ionic Strength on the Electroosmotic Flow in Capillary Electrophoresis with Uniform and Discontinuous Buffer Systems, *Anal. Chem.*, **70**, 549 (1998).
- [148] Todd, P. and Pretlow, T.G., Separation of Living Cells, *ACS Symposium Series*, **464**, 1 (1991).
- [149] Todd, P., Comparison of Methods of Preparative Cell Electrophoresis, *ACS Symposium Series*, **464**, 216 (1991).
- [150] Waters, L.C., Jacobson, S.C., Kroutchinina, N., Khandurina, J., Foote, R.S., Ramsey, J.M., Microchip Device for Cell Lysis, Multiplex PCR Amplification, and Electrophoretic Sizing, *Anal. Chem.*, **70**, 158 (1998).
- [151] Waters, L.C., Jacobson, S.C., Kroutchinina, N., Khandurina, J., Foote, R.S., Ramsey, J.M., Multiple Sample PCR Amplification and Electrophoretic Analysis on a Microchip, *Anal. Chem.*, **70**, 5172 (1998).
- [152] Waters, S.L., Solute Uptake Through Tire Walls of a Pulsating Channel, *J. Fluid Mech.*, **433**, 193 (2001).
- [153] Weinberger, R. and Stevenson, R. Separations Solutions; Capillary Electrophoresis; Stacking: Part 2, *Am. Lab.*, **27**, 26EE (1995).
- [154] Weinberger, R. and Stevenson, R., Separations Solutions; Capillary Electrophoresis; Stacking: Part 1, *Am. Lab.*, **27**, 33U (1995).
- [155] Weinberger, R. and Stevenson, R., Separations Solutions; Capillary Electrophoresis: Sample Preparation, *Am. Lab.*, **32**, 48 (2000),
- [156] Westermeier, R., *Electrophoresis in Practice*, Wiley-VCH, Weinheim, (2001).
- [157] Wey, A.B. and Thormann, W., Head-Column Field-Amplified Sample Stacking in Binary-System Capillary Electrophoresis: The Need for the Water Plug, *Chromatographia*, **49**, S12 (1999).
- [158] Wey, A.B., Zhang, C.-X., and Thormann, W., Head-Column Field-Amplified Sample Stacking in Binary System Capillary Electrophoresis: Preparation of Extracts for Determination of Opioids in Microliter Amounts of Body Fluids, *J. Chromatogr. A*, **853**, 95 (1999).
- [159] Wooley, A.T. and Mathies, R.A., Ultra-High-Speed DNA-Sequencing Using Capillary Electrophoresis Chips, *Anal. Chem.*, **67**, 3676 (1995).

- [160] Woolley, A.T., Sensabaugh, G.F., and Mathies, R.A., High-Speed DNA Genotyping Using Microfabricated Capillary Array Electrophoresis Chips, *Anal. Chem.*, **69**, 2181 (1997).
- [161] Worman, A., Analytical Solution and Timescale for Transport of Reacting Solutes in Rivers and Streams, *Water Resources Research*, **34**, 2703 (1998).
- [162] Yopps, J.A. and Fuerstenau, D.W., Zero Point of Charge of Alpha-Alumina, *J. Colloid Interface Sci.*, **19**, 61 (1964).
- [163] Zalesak, S.T., Fully Multidimensional Flux-Corrected Transport Algorithms for Fluids, *J. Comp. Phys.*, **31**, 335 (1979).
- [164] van der Zande, B.M.I., Dhont, J.K.G., Bohmer, M.R., and Philipse, A.P., Colloidal Dispersions of Gold Rods Characterized by Dynamic Light Scattering and Electrophoresis, *Langmuir*, **16**, 459 (2000).
- [165] de Zeeuw, P.M., Matrix-Dependent Prolongations and Restrictions in a Black-box Multigrid Solver, *J. Comput. Appl. Math.*, **33**, 1 (1990).
- [166] Zhang, C.-X. and Thormann, W., Head-Column Field-Amplified Sample Stacking in Binary System Capillary Electrophoresis: A Robust Approach Providing over 1000-Fold Sensitivity Enhancement, *Anal. Chem.*, **68**, 2523 (1996).
- [167] Zhang, C.-X. and Thormann, W., Head-Column Field-Amplified Sample Stacking in Binary System Capillary Electrophoresis. 2. Optimization with a Preinjection Plug and Application to Micellar Electrokinetic Chromatography, *Anal. Chem.*, **70**, 540 (1998).
- [168] Zoppou, C., Knight, J.H., Analytical Solutions for Advection and Advection-Diffusion Equations with Spatially Variable Coefficients, *Journal of Hydraulic Engineering-ASCE*, **123**, 144 (1997).